ELECTROMAGNETIC FLOWMETERS

FOR LIQUID METALS

by

MAHMOUD TARABAD
B.Sc., M.Sc., D.I.C.

Thesis submitted for the degree
of
Doctor of Philosophy
in the
Faculty of Engineering
of the
University of London

Department of Mechanical Engineering
Imperial College of Science and Technology
London SW7 2BX

1979

ABSTRACT

In this work three types of electromagnetic flowmeters are analysed. These flowmeters have distorted imposed fields in which the distortion is caused either by magnetic property, electrical conductivity or flowrate of fluid.

The first type is the electromagnetic flowmeter for magnetic slurries, where the permeability of fluid affects the imposed field and makes the performance of the meter non-linear. A design is given which has a search coil positioned in the liner which is used as a reference and gives a constant signal for changing fluid permeability and an almost constant one for a limited range of axisymmetric velocity profiles.

The second type of flowmeter is a swept field one where the high magnetic Reynolds number ($R_m = \mu_o \sigma a V_m$) causes the field sweeping. These flowmeters are analysed and their performances are found for three different types of imposed fields. The solution is a numerical finite difference approximation with S.O.R. Also a weight function is found for the swept field flowmeter which is magnetic Reynolds number dependent. And finally a design is given with electrodes displaced downstream. The performance of this meter is effected by conductivity change.

The design which is immune to any conductivity change is the integrated voltage flowmeter for which the theory, and examples for confirming this theory, are given.

Experiments are carried out on swept field flowmeters using an analogue rig and the results obtained are in good agreement with prediction.

Finally pulsed field flowmeters are analysed and a design is given which can measure the flowrate and conductivity of the flow. Performance of this flowmeter is immune to any temperature or conductivity change.

ACKNOWLEDGEMENTS

The author wishes to thank his supervisor, Professor R.C. Baker, for his kind encouragement, guidance and interest in the work.

I wish to express my gratitude and my respect to my parents, who supported me financially and encouraged me in all aspects during my life.

I would like to thank the staff of the Thermal Power Section, especially Mr. W. Lamburn for his valuable help, and Mr. R.D. Bloxham.

Thanks are also due to Miss D. Day, Miss E.M. Archer and Mrs. S.D. Boote of the Mechanical Engineering Department and Miss J. Miles for typing this thesis.

LIST OF CONTENTS

NOMENCLATURE

a	internal radius of pipe, semi-width of channel (in x-direction)
$\underset{\sim}{A}$	magnetic vector potential
$\bar{\underset{\sim}{A}}$	Laplace transformation of $\underset{\sim}{A}$
A_n, A_n'	constant
b	external radius of pipe, semi-depth of channel (in y-direction)
$\underset{\sim}{B}$	magnetic flux density
B_n	constant
C_r	contact resistance number, $(\frac{\sigma_f \tau}{a})$
d	wall conductivity number, $(\frac{\sigma_w w}{\sigma a})$
$\underset{\sim}{ds}$	area element, vector normal to area
d_w	diameter of coil winding
$\underset{\sim}{D}$	electric displacement vector
D_n	constant
$\underset{\sim}{E}$	electric field intensity vector, elliptic integral of second kind
$f(x)$	function
$\underset{\sim}{F}$	vector quantity
h_1, h_2	lattice size in r-direction
h_3	lattice size in z-direction
$\underset{\sim}{H}$	magnetic field intensity vector
i,j,k	Cartesian co-ordinates
i_n	electric current
I	total current vector, total current in coil
$I(x)$	Bessel function of first kind
$I_1(x)$	modified Bessel function of first kind
I_m	virtual current in midplane of pipe
$\underset{\sim}{J}$	current density vector
J_o	current density in primary coil
J_v	virtual current density

R	radius
R	Reynolds number ($\rho_m a V_m/\eta$)
R_c	radius of coil
R_m	magnetic Reynold's number ($\mu \sigma a V_m$)
R_n	electrical resistance
S	sensitivity
s_1, s_2	surfaces around the electrodes
t	time
t_*	non-dimensional time scale ($t/\mu\sigma a^2$)
T	time constant of medium
U	electrical potential
U_o	constant voltage at electrodes
U_v	virtual electric potential
U_v'	virtual electric potential for U_o potential
U^m	voltage induced by motion
$\underset{\sim}{V}$	fluid velocity vector
V_m	mean velocity
w	wall thickness
$\underset{\sim}{W}$	weight vector, weight function
x,y,z	Cartesian co-ordinates
z_1	Cartesian co-ordinate
z'	$\frac{z}{R_c}$
z_1'	$\frac{z_1}{R_c}$
z_n	parameter of Gauss Legendre quandrature

Greek Symbols

α_n	parameter of Gauss Legendre quadrature
β	half angle of coil
$\beta_o=\pi/2-\beta$	angle of coil (in Appendices A, B and C)

β_c	angle
γ	search coil angle
γ_n	constant
δr	lattice size in r-direction
$r\delta\theta$	lattice size in θ-direction
$\delta(z)$	delta function
δ_n	constant
ε	fluid permittivity
ε	induced electric potential in secondary coil
ε_*	$\frac{\sigma R_c \varepsilon}{N_s N_p I\sqrt{2\pi}}$ non-dimensional induced electric potential
η	viscosity of fluid
θ	polar co-ordinate
μ	magnetic permeability
μ'	$\frac{\mu_1}{\mu_2}$
μ_o	permeability of free space, $4\pi \times 10^{-7}$
ρ	polar co-ordinate, fluid density, charge density
ρ_1	dimensionless radius ($\frac{\rho}{R_c}$ or $\frac{\rho}{a}$)
ρ_m	mass density of fluid
σ	electrical conductivity
τ	contact resistance per unit area, time interval, transient time
$d\tau$	volume element
ϕ	magnetic potential function
ϕ_o	magnetic potential at pole faces
ψ	scalar potential
ω	angular velocity

Subscripts

f	value in the fluid
o	imposed or uniform, value at the centre

r,θ,z	cylindrical components
x,y,z	Cartesian components
w	value in the wall
ℓ	value in the flowmeter liner
bar (e.g.$\overline{U}$)	integral value of U in z-direction

$$\overline{U} = \int_{-\infty}^{+\infty} U \, dz$$

CHAPTER 1

INTRODUCTION

The safe operation of the fast breeder reactor (FBR) with liquid sodium cooling necessitates the flow measurement of sodium in a wide range of pipe sizes up to the order of 1m diameter and velocities as high as 10m/sec. Under these conditions the reliability of a flowmeter is more important than the accuracy as an accuracy of a few per cent is sufficient (Hayes 1974).

Electromagnetic flowmeters (induced voltage or induced magnetic field) have been used both in the core, primary and secondary cooling systems of sodium cooled FBR. In the core of the reactor the flow velocity is not high but the operating conditions are severe. High temperature, radiation and inaccessibility encountered here all cause problems and therefore eddy current flowmeters are normally recommended to be used in core flow measurement.

Primary and secondary flow measurements are made using transverse field electromagnetic flowmeters, but the high value of magnetic Reynolds number (R_m) tends to produce distortion of the imposed magnetic field and this makes the performance of these meters non-linear. In this work a design is produced which, although it has an applied magnetic field distorted by the flow, will still provide a linear performance. A problem exists in calibration of the electromagnetic flowmeters for magnetic slurries, where the magnetic property of the slurry causes the distortion of the imposed field and changes the calibration. A flowmeter design is given for the measurement of flow of magnetic slurries, the output of which is not affected by the permeability of the fluid.

The contact method of flow measurement exhibits known disadvantages when used to measure the flowrate of high temperature corrosive fluids.

In particular, the variability of the contact resistance between the electrodes and the medium or the channel walls and the medium gives rise to additional measurement error. In this context a pulsed field flowmeter is analysed and developed which may be used for flow measurement in production of wires, rods, tubes, M.H.D. devices, in the core, the primary and also [illegible] in the secondary cooling circuit of a Fast Breeder Reactor.

1.1 History and Development of Electromagnetic Flowmeters

In 1832 Faraday attempted to measure the induced voltage across the river Thames resulting from the interaction of the water flow and the Earth's magnetic field.

Years after Faraday the principle of electromagnetic flowmeasurement had still only been used for oceanographic applications. Somewhat after it was realised that electromagnetic flowmeasurement could be applied to other fluids than water.

Within the last two decades the electromagnetic flowmeter has been used in the flowmeasurement of, for example, water, chemicals, blood, ionized gases, food stuffs, liquid metals and others. Electromagnetic flowmeters are divided into two distinct categories depending on their mechanism of operation.

a) Induced voltage flowmeters

b) Induced magnetic field flowmeters

1.1.1 Induced voltage flowmeter

The operation of this meter is based on the discovery by Faraday

that voltages are induced in a conductor which moves through a magnetic field. The electric field $\underset{\sim}{E}$ induced by such motion is expressed by the vector equation:

$$\underset{\sim}{E} = \underset{\sim}{V} \times \underset{\sim}{B} \tag{1.1}$$

where $\underset{\sim}{V}$ is the velocity of motion, and $\underset{\sim}{B}$ is the magnetic flux density. Figure 1.1 shows an induced voltage electromagnetic flowmeter in a pipeline configuration. The induced voltage is sensed by two electrodes at diametrically opposite points on the pipe wall.

Williams (1930) performed experiments with a copper sulphate solution flowing in a non-conducting circular pipe, under a uniform transverse magnetic field. The results showed that the induced voltage between the electrodes EE was proportional to the flowrate. The early theory of electromagnetic flowmeters was developed by Thürlemann (1941) and Kolin (1945) who showed that the signal from an electromagnetic flowmeter with point electrodes, non-conducting circular channels and a uniform magnetic field is directly proportional to the flowrate for any axisymmetrical velocity profile. That is

$$\Delta U_{EE} = 2a \; B_o \; V_m \tag{1.2}$$

where ΔU_{EE} is the potential difference between the electrodes, B_o is the uniform magnetic field, V_m is the mean velocity, and 2a is the pipe diameter. Shercliff (1954) introduced the weight function to show how the distribution of velocity affects the performance of the flowmeter. The signal was described as:

$$\Delta U_{EE} = B_o \int_{\text{cross section}} V.W \, ds \tag{1.3}$$

in which W, the weight function, was given by

$$W(r,\theta) = \frac{a^4 + a^2 r^2 \cos 2\theta}{a^4 + 2a^2 r^2 \cos 2\theta + r^4} \tag{1.4}$$

The sensitivity of the flowmeter is defined as

$$S = \frac{\Delta U_{EE}}{2a \, B_o \, V_m} \tag{1.5}$$

Figure 1.2 shows the contours of W, which indicate the contribution of the various parts of the cross-section to the output signal. For axisymmetric velocity profiles equation 1.3 gives a sensitivity of unity, as was obtained by Thürlemann and Kolin, but when the velocity profile is non-axisymmetric the sensitivity can be greater or less than unity and sometimes negative. The sensitivity becomes .5 if the flow concentrates near the side walls. If the flow concentrates near the electrodes the sensitivity can be much greater than unity. Localised reverse flow, may reduce the sensitivity below .5 and could even make it negative.

The sensitivity of the flowmeter, when the magnetic field is non-uniform and flow is rectilinear in the channel cross-section, is expressed in a more general form by Korsunskii (1974).

$$S = \frac{\int_0^a \int_0^{2\pi} V_z(r,\theta).B_y(r,\theta).W(r,\theta) r \, dr \, d\theta}{B_o \int_0^a \int_0^{2\pi} V_z(r,\theta) r \, dr \, d\theta} \tag{1.6}$$

In which B_o here is the magnetic field at the centre of the channel and W is the Shercliff weighting function. If the field is uniform

and flow is axisymmetric the sensitivity again is unity.

In order to remove the effect of velocity profile Rummel and Ketelson (1966) have proposed an electromagnetic flowmeter with a magnetic field inversely proportional to the Shercliff weight function. The magnetic flux distribution everywhere in the channel is defined by the relation:

$$B_y(r,\theta)/B_o = 1/W(r,\theta) \tag{1.7}$$

Bevir (1970,1971) continuing the work of Shercliff has shown that the potential difference between the electrodes can be written in the general form:

$$\Delta U_{EE} = \int_\tau \underset{\sim}{W}.\underset{\sim}{V}\, d\tau \tag{1.8}$$

where τ is the volume and $\underset{\sim}{W}$ denotes the weight vector.

$$\underset{\sim}{W} = \underset{\sim}{B} \times \underset{\sim}{J}_v \tag{1.9}$$

and

$$\underset{\sim}{J}_v = \nabla G$$

G is the solution of the Laplace equation in the region under consideration with given boundary conditions. Bevir refers to $\underset{\sim}{J}_v$ as a virtual current, which would occur if unit current passed between the electrodes with no fluid motion. The condition on $\underset{\sim}{W}$ for an ideal flowmeter which gives a signal proportional to the flowrate irrespective of the velocity distribution was given as:

$$\nabla \times \underset{\sim}{W} = 0 \qquad (1.10)$$

This condition can be satisfied using certain shapes and electrodes. Electromagnetic flowmeter with two point electrodes, in a circular channel cannot have this property, though it can with difficulty be made immune to variation in the profile of a rectilinear flow.

Gammerman and Mezhburd (1971) gave a three dimensional solution for Bevir's weight vector for a cylindrical flowmeter with insulated walls and this work shows that the two dimensional solution by Shercliff is a particular case of the general solution obtained. The solution gives the virtual current distribution for an insulating circular pipe with point or finite electrodes.

Kirshtein and Timofeev (1975,1977) analysed the effect of a non-uniform magnetic field in the direction of flow, on the characteristics of the meter. Their conclusion was that the distribution of the magnetic field along the tube axis has a significant effect on the characteristics of a flowmeter and so approximate designs with shortened magnet systems, which do not take into account the non-uniformity of the magnetic field along the flow can lead to large errors. Thus both the longitudinal and the transverse non-uniformity of the magnetic field must be taken into consideration, when the flowmeter parameters are to be determined. One possible design to give responses proportional to the mean velocity, for an arbitrary velocity distribution in the flowmeter channel, is one in which the magnetic field $\underset{\sim}{B}$ is such as to ensure that the component W_z in the direction of the flow is approximately constant and that all the remaining components of $\underset{\sim}{W}$ vanish.

One of the problems in measuring liquid metal flow by electro-magnetic flowmeters is their high sensitivity to changes in the electrical parameters at the interface of two media, the channel wall and liquid metal. These changes can be caused by the fact that the channel walls

are not wettable, because of the deposition of oxides and precipitates. Velt and Mikaileve (1977) considered the possibility of constructing flowmeters with signals independent of the contact resistance, by introducing a non-uniform magnetic field of a special type. The magnetic field distribution is found from the requirement that the normal current component caused by flow in the magnetic field should vanish at the boundary between the liquid and the wall. The effect of distortion from axial symmetry in the fluid velocity profile was studied by Wenger (1971). A general formula was given for computing the sensitivity for any given rectilinear velocity profile. The solution is in two dimensions and the magnetic field is uniform.

$$S = \frac{\int_0^1 \int_0^{2\pi} K(\rho,\theta)\, V(\rho,\theta)\rho \, d\rho \, d\theta}{\int_0^1 \int_0^{2\pi} V(\rho,\theta)\rho \, d\rho \, d\theta} \tag{1.11}$$

where $K(\rho,\theta)$ the weighting vector is

$$K(\rho,\theta) = \sum_{m=1}^{\infty} \frac{2R^m}{(R^{2m}+1) + \gamma(R^{2m}-1)} \rho^{m-1} \cos(m-1)\theta \sin\frac{m\pi}{2} \tag{1.12}$$

and

$$\gamma = \frac{\sigma_w}{\sigma_f} \qquad \text{and} \qquad R = b/a$$

If $K(\rho,\theta)$ is a constant the flowmeter would be ideal and the sensitivity would be completely independent of the velocity profile. The series expression for $K(\rho,\theta)$ can be expressed in closed form only for a non-conducting pipe wall: i.e.,

$$K(\rho,\theta) = \frac{1 + \rho^2 \cos 2\theta}{1 + 2\rho^2 \cos 2\theta + \rho^4} \qquad (1.13)$$

This result was also obtained by Shercliff (1954). The author shows how to select the flowmeter pipe wall thickness and electrical conductivity to minimize the error in the flow measurement due to uncertainties in the velocity profile. Then the velocity profile distortion produced by the flowmeter itself was analysed for fully developed flow and a Hartmann number range of 1 to 1000. Numerical results were presented in tabular form and used to help to correct flow measurements.

The electromagnetic flowmeters with cylindrical magnets are particularly suitable for measuring flow rates in tubes several hundred millimetres in diameter. The application of a conventional magnetic flowmeter of this size requires a very large magnet system. Modern magnetic materials are capable of operation at temperature up to 600°C. The magnetic flux in these meters is created by a cylindrical permanent magnet, magnetized along its diameter and is placed along the axis of the pipe-line. Loginov (1971) analysed such a meter, and the potential distribution in the walls of the sensor, in the surrounding flow, and in the tubing itself. The solution is analytical and it assumes an infinitly long transverse magnetic field with axisymmetric velocity profile. This author also considers the case when an electrical contact resistance exists between the liquid metal and the solid wall. Kormilov and Loginov (1978) show how the velocity profile effects the sensitivity of the above flowmeter and a correction coefficient for velocity profile is introduced and a table of this coefficient is given.

1.1.2 Induced Magnetic Field Flowmeter

The motion of a fluid in an imposed magnetic field produces an induced magnetic field which is a function of velocity profile and fluid conductivity. Measurement of this induced field is the basis of another technique for flow measurement. The fact of conductivity dependence, makes the measurement uncertain, but if the velocity is known, the method may be used for conductivity measurement (Meyer, 1961). The attraction of the induced field flowmeter is that it requires no electrical connections to or inside the flow channel and therefore no trouble from electrode polarisation and contact resistance exists.

The change in the magnetic field may be measured by a search coil and an a.c. system, the frequency must be low to avoid skin effects in the liquid metal. A device of this kind was first patented by Lehde and Lang (1948) for ship speed measuremnt. This flowmeter consists of a central coil (primary), energized from an alternating current source with a certain frequency, with two identical secondary coils connected differentially at either side of the primary. The coils can be treated as a differential transformer and balanced to zero for stationary fluids (see figure 1.3). The interaction of the flow with the magnetic field of the primary coil creates eddy currents in the fluid. These eddy currents distort the field and generate e.m.f's in the secondary coils which their difference is a function of magnetic Reynolds number. The fluid can either flow through an internal channel or an external channel depending on the particular application.

One type of the induced magentic flowmeter is tested by Kalnin et al (1966). On one side of the flow channel there is a pulsating field inductor, supplied with single-phase alternating current. A receiving inductor is placed on the other side of the channel. An emf is created

at the receiving inductor winding by the flow of fluid through the channel. The disadvantage of the meter is its depedence on the velocity profile, the geometry of the channel and the inductor, the frequency and the conductivity of the fluid. The measurement showed an error of about 2% at $\Delta T = \pm 10^{o}C$ in the range from $+200^{o}$ to $450^{o}C$.

Another type of induced field flowmeter suitable for high magnetic Reynolds number has been suggested and tested for high temperature corrosive media like those in M.H.D. devices at Riga, Latvain S.S.R. Zheigur and Sermons (1965) describe this flowmeter, which in its simplest form consists of two coaxial coils spaced along a pipe (see figure 1.4). The transmitting coil is fed from a generator with rectangular current pulses which induce circular currents in the medium and are convected by the moving liquid. This is accompanied by a displacement of the magnetic field lines induced by the eddy currents and these in turn induce an e.m.f. in the receiving coil. The signal in the receiving coil is a maximum when the eddy current passes the coil. The transit time is a function of velocity and fluid conductivity. If conductivity is constant the velocity becomes the ratio of distance between the coils to transit time:

$$V = \ell/\tau \qquad (1.14)$$

This expression is true only for an ideal case (two circular coils in a moving conducting medium) and high value of magnetic Reynolds number.

1.2 Fast Breeder Reactors

The major development of electromagnetic devices came after the Second World War, with the advent of nuclear power reactors, in particular, the fast breeder system (FBR), where the compactness of the reactor produces problems of extracting heat from the core.

The FBR has been a concept of nuclear physicists from the earliest days of atomic energy. In nuclear reactors when fission occurs the emitted

neutrons are moving at high speeds. In the case of fast breeder reactors no delibrate attempt is made to slow the neutrons down, whereas in a thermal reactor a moderator is introduced, whose function is to absorb the kinetic energy of the neutrons and slow them to thermal energies. Conventional thermal reactors are capable of recovering only 1 per cent of the energy contained in Uranium, while in fast breeder reactors there is potential for recovery of at least 50 per cent of the energy contained in the Uranium and Plutonium.

In the FBR, the fuel is manufactured from Uranium (U-238) and Plutonium (Pu-239). Like the U-238 in a conventional reactor, Pu-239 is a fissionable material; neutrons striking Pu-239 cause its atoms to fission and release heat. But not all the neutrons collide with Plutonium, some hit U-238 causing the Uranium to be transmitted to Plutonium, Pu-239. Compared with a conventional reactor, a breeder therefore has a vital feature. The reactor breeds Plutonium, and the refuelling cycle essentially consists in topping up with U-238. The breeding capability of the FBR will lead to a higher energy potential of the available Uranium and therefore lower consumption for a fixed demand. The prospect of economic power generation, with substantial independence from external fuel supplies as offered by fast breeder reactors, has provided a strong incentive for several countries to initiate development programmes on this type of reactor.

High ratings and surface heat fluxes are inherent in the core design of a fast reactor. These requirements give rise to very severe cooling problems. Furthermore, the choice of coolant is dictated by the fact that it is undesirable to introduce neutron-moderating materials into the core, so that water or hydrogenous materials are not suitable. This limitation and the inadequacy of a gas as a heat transfer medium directed attention in the early days of development to the consideration of liquid metals as reactor coolants. The alkali metals proved most suitable and sodium or sodium potassium alloys have emerged as pre-eminent. It is interesting to note the properties

of sodium which have led to its choice as a coolant for the fast reactor:

1) Good resistance to irradiation damage.
2) High boiling point, which permits high operating temperatures and therefore high thermal efficiency in the steam cycle.
3) High thermal conductivity leading to good heat transfer coefficients, which in turn permit high rates of heat transfer from the surfaces of the fuel elements. It has also a reasonably high specific heat and density which enables the required heat transport rates to be obtained with acceptable coolant velocities and temperature rise across the core.
4) It is cheap and a large supply is readily obtainable. Thus sodium has a combination and range of physical properties which make it particularly suitable for a fast reactor coolant (Moore et al, 1961).

1.3 Electromagnetic Flowmeters for Fast Breeder Reactors

The typcial large fast reactor under construction or active design today employs mixed oxide $(Pu,U)O_2$ fuel helium bonded to stainless steel clad jackets having a diameter of about .6cm. The fuel elements are close-packed into a core having an average composition of about 35% fuel, 45% sodium and 20% steel (Simnad, 1971). Between the radioactive primary system sodium and the steam generators is an intermediate sodium heat exchanger and secondary sodium system. Typical average core exit coolant temperatures are 540-600°C; the core temperature (ΔT) is about 170°C. Primary system pumps are usually mechanical. Three or six primary system loops are usually

considered, although as few as two have been proposed. The major early designs had two choices of primary system: the loop system, in which coolant is piped from the reactor vessel to the pump and intermediate exchanger, which are located in inter atmosphere cells; or the pool system in which the entire primary system lies submerged in a large vessel. Examples of loop and pool systems are illustrated in figures 1.5 and 1.6 respectively and table 1.1 shows which of the reactors under construction or already operating have loop, and which have pool type primary circuits (Campbell, 1973).

The safe operation of FBR requires reliable instruments for monitoring the sodium in core, primary and secondary circuits. The problems of designing such instruments are severe. These include for example, high temperature; radiation; restricted access; hydraulic shock and reliability (Duncombe and Thomasson, 1970). All these qualities, and more, are possessed by the electromagnetic flowmeter, which has now become a standard fitting in liquid metal circuits such as those in fast breeder reactors Hess et al (1975) give a survey of measurement methods and the variety of appropriate instrumentation developed and tested for primary and secondary systems of fast breeder reactors. Baker (1977) considers various types of electromagnetic flowmeters which have been used for primary and secondary circuits. For primary, both flow through type and probe type electromagnetic flowmeters, have been proposed while in the secondary the high magnetic Reynolds numbers cause field sweeping and this has led to the use of the long saddle coil flowmeter. Flux distortion (eddy current) flowmeters, either flow through or probe types, have been discussed for monitoring the primary circuit flow.

1.3.1 Core Flow Measurements

The space available in the control rod guide tube puts restrictions on the size and type of the flowmeter which may be used in core flow measurements. This space is dictated by the .53m long, 5cm diameter flow channel in the guide tube. The instrument should respond to 10% change in flowrate over a 10 second period and must operate satisfactorily in molten sodium at temperature up to 700°C in the presence of high radiation levels (Dean et al 1970). The electromagnetic flowmeter in which a magnetic flux is produced by a permanent magnet may be used for either flow through or probe type, but the difficulty is to find magnetic materials with stability up to 700°C. Modern magnetic materials are capable of operating at high temperature and some of these designs have been tested by Popper and Glass (1967), Foster (1971, 1973) and Yada (1970). At the present time, with the difficulties surrounding the permanent magnet flowmeters, the eddy current (flux distortion) flowmeters seem to be favoured for core flow measurements.

The probe type eddy current flowmeter is shown in figure 1.8 and is inserted coaxially into a duct where the sodium flows through the annulus between the probe and the duct wall. This flowmeter has been developed and selected in British prototype fast reactor for protection against the loss of coolant incident and for primary circuit flow monitoring (Dean et al, 1970). A theoretical model has been illustrated by Hirayama (1977) and its validity has been confirmed by experiments using a moving aluminium cylinder as a fluid. Wiegand (1967,1969) describe the flow through eddy current flowmeter (see figure 1.7), and a numerical solution is given by Feng et al (1975) employing a finite difference relaxation method and complex

notation for quadrature signal. Calculations were made for various axially symmetric arrangements of coils, and experiments have been carried out using mercury as the conducting fluid. There was a good agreement between measured and computed values and the conclusion was that, for a reasonable accuracy, a low frequency should be used to allow for skin effects.

As explained earlier, the primary system could be a loop or a pool system. The probe type eddy current flowmeter is used in the pool system, which can be pushed down into the discharge pipe (see Dean et al 1970). Besides the eddy current flowmeter, the induced voltage electromagnetic flowmeter may also be used. Problems arise in the primary (with the loop system) and secondary circuit, where the flow rates, sodium conductivity and channel size produce a high magnetic Reynolds number ($R_m = \mu\sigma\ a\ V_m$).

1.3.2 Primary (loop system) and Secondary Circuit Flow Measurement

The high magnetic Reynolds number in the primary and secondary circuit causes the field of a conventional flowmeter to be swept away from the midplane of a meter downstream by the flow and results in a non-linear characteristic. Turner (1960) has shown that the non-linearity of a flowmeter at high magnetic Reynolds number is due to the distortion of the magnetic field caused by the eddy currents flowing in the sodium. He suggested two methods for obtaining a nearly linear output from large electromagnetic flowmeters:

1) make the pole-face-length/pipe-diameter ratio large, or
2) move the electrodes to a location downstream from the centre of the magnet assembly.

The flowmeter with a long field may be used so that at the centre of the meter the effect of sweeping becomes negligible. Increasing the pole-face length does not appear promising since, the pole-face length would have to increase by a factor of eight or greater if the pipe diameter were doubled and a permanent magnet of this size becomes massive and it leads to handling and space problems. The non-linear output was also observed by Meshii and Ford (1969), in calibration of flowmeters located on the .36m lines of the primary loop of the Enrico Fermi atomic power plant. In this case the permanent magnet had a length-to-diameter ratio of .7. Pfister and Dunham (1957) have noticed this effect in their experiments and they indicate that the non-linearity depends on sodium conductivity as well as flow rate.

Thatcher et al (1970) have developed the concept of the saddle coil electromagnetic flowmeter. This saddle coil has a sufficient length (2.34m), to reduce the effects of sweeping and is illustrated in figure 1.10. It is mounted outside the .3m stainless steel pipe having .64cm wall thickness. The maximum sodium flow rate is .455 m^3/s at $400^{\circ}C$ and produces the R_m of 5. The coil has a diameter 2.5 times that of the flow pipe and produces a uniform magnetic field across the pipe cross-section. The field distribution is assumed to be in a trapezoidal form and for this field profile the correction factor for field distortion is obtained but it is not valid for gross field distortion where the departure from linearity is greater than a few per cent. The disadvantage of this meter is that it requires a long system of straight pipes which are not always available. Therefore there is a need for flowmeters which fit into short pipe sections and operate for a wide range of magnetic Reynolds number with linear characteristics. The design proposed by Turner

(1960) is the short magnetic field with electrodes located downstream which gives nearly linear outputs. The performance is linear at a constant temperature and any temperature fluctuation will affect the linearity as a result of conductivity change. Komori et al (1974) suggested the use of more than one pair of electrodes along the pipe to overcome the uncertainty caused by magnetic field distortion.

1.4 Electromagnetic Flowmeter for Magnetic Slurries

Distortion of the imposed magnetic field also occurs in electromagnetic flowmeters used for magnetic slurries. These meters are used to measure the flow rate of magnetic iron ore. The magnetic property of fluid flow modifies the imposed magnetic field and changes the sensitivity of the flowmeter. Mannhers et al (1968) employed a reference coil to reduce the change in sensitivity when the magnetic permeability of slurry varied. This flowmeter is shown in figure 1.9, where the reference coil is located at right angles to the electrodes. The induced voltage in this coil is proportional to the magnetic flux through the conducting medium. The ratio of output signal to the reference voltage was found to be less sensitive to the magnetic property of the slurry.

1.5 Outline of Thesis

Electromagnetic flowmeters are described and a review is given. The applications in the FBR are explained and the problems are defined. The theory of electromagnetic flowmeters comes in Chapter 2 where the governing equations are derived and the simple forms of magnetic field and flowmeter equations are given. In Chapter 3 the flowmeter

for magnetic slurries is analysed. In Chapter 4 the swept field flowmeter is analysed and to find the performance of the flowmeter, magnetic field and flowmeter equations are solved numerically using the finite difference approximation and the Successive Over Relaxation method. In Chapter 5 the swept field flowmeter has been approached by using weight function theory. A weight function is derived for swept field flowmeters. This is a first attempt to find the weight function for distorted field induced voltage flowmeters. Chapter 6 deals with integrated voltage flowmeters where an original theoretical solution is given for this meter and two different approaches are carried out (flowmeter equation and weight function). Several examples are given to prove this theory.

Chapter 7 covers the experimental work where the validity of the numerical solution obtained in Chapter 4 is checked using an analogue sodium rig. A permanent magnet is used in this experiment as an imposed field source. The pulsed field flowmeter is analysed in Chapter 8. The vector potential equation is solved by a time marching technique using the finite difference approximation and S.O.R. method. Employing this solution the performance of this flowmeter is predicted and a new design is given which is only sensitive to flowrate.

Appendices A, B and C give analytical solutions for three different air core coils (saddle coil concentric type, diamond coil and saddle coil) which are used in the calculations in Chapter 4.

To what extent is this chapter direct quotation from refs ?

CHAPTER 2

THEORY

2.1 Introduction

Electromagnetic flowmeters vary in their construction depending on the application, but they all operate in basically the same manner. The principle of operation is based on the interaction between the moving conducting medium and an imposed magnetic flux. Electric currents are induced when the flow passes through an imposed magnetic field, or it may be induced by changes in magnetic field with time. There are two consequences:

1) Perturbation of the imposed magnetic field by the induced magnetic field associated with those currents;
2) Perturbation of the flow by the electromagnetic force due to the interaction of currents and magnetic field.

The second effect exists in M.H.D. devices, where the imposed magnetic flux is strong and perturbes the flow. $M^2/R = B^2 a/\rho_m V_m$ gives the magnitude of the perturbations, where M is the Hartmann number and R is the Reynolds number. In electromagnetic flowmeters the imposed magnetic flux is not strong and therefore the Hartmann number is very small, hence we can neglect the perturbation of velocity caused by the imposed field. This study of electromagnetic flowmeters is concerned with the first phenomenon only.

The imposed magnetic field is affected by many different parameters, these are outlined below:

a) Permeability of the media (μ):

The permeability of the fluid alters the signal by modifying

the imposed magnetic field in the flowmeter section. In Chapter 3 this effect is examined and a design is produced which gives a signal constant for changing fluid permeability and almost constant for a limited range of axisymmetric velocity profiles.

b) Magnetic Reynolds number ($R_m = \mu\sigma a V_m$):

Magnetic Reynolds number gives the ratio of induced field (produced by induced currents in the fluid) to imposed field and shows the extent to which the imposed field is distorted. This parameter is very important in the design of flowmeters for liquid metals where the electrical conductivity is high.

c) Skin effect ($S^2 = \mu\sigma\omega a^2$):

The alternating magnetic field or time dependent velocity induces an alternating current. Then, if the frequency is high, the induced current and electric field distributions will be seriously upset by self-inductance. In extreme cases this excludes the imposed magnetic field from the bulk of the fluid, so rendering electromagnetic flow measurement impossible. Here ω is the frequency of change of the fluid velocity or the magnetic field. We assume that this is small so that the self-inductance effects may be ignored, obviously it will vanish in d.c. flowmeters. With electrolytic conductors little restriction on ω is necessary due to the very low conductivity, but with liquid metals self-inductance effects are severe and it is wise to use a d.c. field.

d) Permittivity (ε):

The dielectric liquids such as oil have high permittivity which introduce the displacement current ($\partial D/\partial t$) which may be higher than the conduction current. In this work we are not studying this effect (see Cushing, 1958). We neglect the displacement

current in comparison with the conduction current ($\omega\varepsilon/\sigma<<1$).

2.2 Governing Equations

In a material of conductivity σ moving with velocity $\underset{\sim}{V}$ relative to a system in which the electric and magnetic fields are $\underset{\sim}{E}$ and $\underset{\sim}{B}$ respectively the current density will be:

$$\underset{\sim}{J} = \sigma(\underset{\sim}{E} + \underset{\sim}{V} \times \underset{\sim}{B}) \qquad (2.1) \qquad \text{(Ohm's Law)}$$

The Maxwell equations are used in the following form:

$$\nabla \times \underset{\sim}{E} = -\partial \underset{\sim}{B}/\partial t \qquad (2.2)$$

$$\nabla . \underset{\sim}{B} = 0 \qquad (2.3)$$

$$\nabla \times \underset{\sim}{H} = \underset{\sim}{J} \qquad (2.4)$$

Where:

$\underset{\sim}{H}$ = magnetic intensity

t = time

The medium is taken to be linear and isotropic, but not homogeneous. In a linear and isotropic medium the following relations between $\underset{\sim}{B}$ and $\underset{\sim}{H}$ hold:

$$\underset{\sim}{B} = \mu \underset{\sim}{H} \tag{2.5}$$

2.2.1 Induced Voltage Flowmeter

For a steady magnetic field the inductance term, $\partial \underset{\sim}{B}/\partial t$ is zero, therefore the Maxwell's equations lead to:

$$\nabla \times \underset{\sim}{E} = 0 \tag{2.6}$$

$$\nabla \times \underset{\sim}{B}/\mu = \underset{\sim}{J} \tag{2.7}$$

Since $\nabla \times \underset{\sim}{E} = 0$, then $\underset{\sim}{E}$ is the gradient of some scalar function U, such that:

$$\underset{\sim}{E} = -\nabla U \tag{2.8}$$

Equation 2.7 describes how the imposed magnetic field is affected by the induced current in the fluid. The object of this chapter is to present the simple form of the governing equations for electromagnetic flowmeters, therefore it is assumed that the induced currents are small and have no effect on the applied magnetic field:

$$\nabla \times \underset{\sim}{B}/\mu = 0 \qquad (2.9)$$

Since $\nabla \times \underset{\sim}{B}/\mu = 0$, then we may define the potential function ϕ as:

$$\nabla\phi = \underset{\sim}{B}/\mu \qquad (2.10)$$

Now taking the divergence of equation 2.10 and assuming the permeability to be uniform the magnetic potential equation becomes:

$$\nabla^2\phi = 0 \qquad (2.11)$$

This equation is solved in Chapter 3 for a moving fluid with uniform permeability but with a higher permeability than that of free space (μ_o).

The flowmeter equation can be derived by taking the divergence of equation 2.1 and applying equation 2.8 with σ constant:

$$\nabla^2 U = \nabla.(\underset{\sim}{V} \times \underset{\sim}{B}) \qquad (2.12)$$

Using a vector identity we may rewrite 2.12 as

$$\nabla^2 U = \underset{\sim}{B}.\nabla \times \underset{\sim}{V} - \underset{\sim}{V}.\nabla \times \underset{\sim}{B} \qquad (2.13)$$

The second term on the right hand side may be neglected if the magnetic field is not affected, the importance of this term is the subject of Chapter 4 and 5. Then,

$$\nabla^2 U = \underset{\sim}{B}.\nabla \times \underset{\sim}{V} \qquad (2.14)$$

The second order differential equations 2.11 and 2.14 require a single electrical and magnetic boundary condition. Part of the boundary usually consists of hypothetical surfaces where the fluid enters and leaves the region of interest. These may be chosen to be sufficiently remote for all electrical and magnetic disturbances to have fallen to negligible proportions, unless the relevant boundary condition is obvious from symmetry of the problem. Within this region there may be interfaces separating liquid and solid conductors over which two electrical boundary conditions must be specified.

One simple solution of equation 2.14 for an axisymmetric velocity profile V(r), nonconducting pipe wall and very long field is given by Baker (1968b).

$$U = \frac{1}{2} \int_{\cdot}^{r} \{V(\sqrt{\rho}\, r + V(a\sqrt{\rho/r})\} \; B_\theta (\rho, \theta) \, d\rho \qquad (2.15)$$

If the magnetic field $B_\theta(r, \pi/2)$ is uniform the potential difference between two electrodes is (see figure 1.1):

$$\Delta U_{EE} = 2 a B V_m \qquad (2.16)$$

Shercliff (1962) discussed how a conducting tube affects the signal due to shorting the current in the pipe wall, and also the drop due to the contact resistance between the fluid and the pipe wall. The sensitivity is reduced for a uniform field flowmeter to

$$S = \frac{2a^2}{(a^2 + b^2) + \frac{\sigma_w}{\sigma} (1 + \frac{\sigma \tau}{a}) (b^2 - a^2)} \qquad (2.17)$$

Where σ_w is the wall conductivity, σ is the fluid conductivity, τ is the contact resistance between fluid and wall, 2a is the inside diameter of tube, and 2b is the outside diameter of the tube wall.

The equation 2.17 simplifies if the wall thickness, w is small in comparison with a, ($w<<a$) giving equation (2.18).

$$S = \frac{1}{1 + \frac{\sigma_w w}{\sigma a}\left(1 + \frac{\sigma \tau}{a}\right)} \qquad (2.18)$$

2.2.2 Induced Magnetic Field Flowmeter

In analysing the induced field flowmeter it is common to use the magnetic vector potential which is expressed as:

$$\underset{\sim}{B} = \nabla \times \underset{\sim}{A} \qquad (2.19)$$

Equations 2.1 may be substituted into equation 2.4 to give

$$\nabla \times \underset{\sim}{H} = \sigma(\underset{\sim}{E} + \underset{\sim}{V} \times \underset{\sim}{B}) \qquad (2.20)$$

$$\nabla \times \underset{\sim}{E} = - \frac{\partial}{\partial t} (\nabla \times \underset{\sim}{A}) \qquad (2.21)$$

or $$\nabla \times \underset{\sim}{E} = -\nabla \times \frac{\partial \underset{\sim}{A}}{\partial t} \qquad (2.22)$$

or $$\underset{\sim}{E} = - \partial \underset{\sim}{A}/\partial t - \nabla \psi \qquad (2.23)$$

The term ψ is a scalar potential. The coil may be driven by a voltage generator with an applied voltage ψ and an internal resistivity $1/\sigma$. However for the purpose of the pulse field flowmeter the driving function is expressed as a step current density of $J_o(t)$ rather than applied potential (in fact this applied current may have a pulse or alternating form) where:

$$(- \sigma \nabla \psi) = \underset{\sim}{J}_o(t) \qquad (2.24)$$

This provides a current which is not affected by induced voltages or the presence of other coils.

Making this substituion gives:

$$\sigma \underset{\sim}{E} = - \sigma \partial \underset{\sim}{A}/\partial t + \underset{\sim}{J}_o(t) \qquad (2.25)$$

Substituting equations 2.5 and 2.19 into the left hand side of equation 2.20 and equation 2.25 into the right hand side of equation 2.20 gives:

$$\nabla \times (\frac{1}{\mu} \nabla \times \underset{\sim}{A}) = \sigma (-\frac{\partial \underset{\sim}{A}}{\partial t}) + \underset{\sim}{J}_o(t) + \sigma \underset{\sim}{V} \times (\nabla \times \underset{\sim}{A}) \qquad (2.26)$$

The vector identities:

$$\nabla \times (\psi \underset{\sim}{F}) = \nabla\psi \times \underset{\sim}{F} + \psi \nabla \times \underset{\sim}{F} \tag{2.27}$$

and

$$\nabla \times \nabla \times \underset{\sim}{F} = \nabla(\nabla . \underset{\sim}{F}) - \nabla^2 \underset{\sim}{F} \tag{2.28}$$

could be used to obtain the differential equation for A ie:

$$\nabla \times (\frac{1}{\mu})(\nabla \times \underset{\sim}{A}) = \nabla \frac{1}{\mu} \times (\nabla \times \underset{\sim}{A}) + \frac{1}{\mu} \nabla \times (\nabla \times \underset{\sim}{A}) \tag{2.29}$$

or

$$\nabla \times (\frac{1}{\mu})(\nabla \times \underset{\sim}{A}) = \nabla(\frac{1}{\mu}) \times (\nabla \times \underset{\sim}{A}) + \frac{1}{\mu}\nabla(\nabla . \underset{\sim}{A}) - \frac{1}{\mu} \nabla^2 \underset{\sim}{A} \tag{2.30}$$

In the original definition of the vector potential the divergence of the vector potential was not specified, so it can be chosen to be anything convenient. It is assumed that $\nabla . \underset{\sim}{A}$ is zero, equation 2.30 will then yield the following results when substituted in equation 2.26.

$$\nabla(\frac{1}{\mu}) \times (\nabla \times \underset{\sim}{A}) - \frac{1}{\mu} \nabla^2 \underset{\sim}{A} = -\sigma \frac{\partial \underset{\sim}{A}}{\partial t} + \underset{\sim}{J}_o(t) + \sigma \underset{\sim}{V} \times (\nabla \times \underset{\sim}{A}) \tag{2.31}$$

or

$$\nabla^2 \underset{\sim}{A} = -\mu \underset{\sim}{J}_o(t) + \mu\sigma \frac{\partial \underset{\sim}{A}}{\partial t} + \mu \nabla(\frac{1}{\mu}) \times (\nabla \times \underset{\sim}{A}) - \mu\sigma \underset{\sim}{V} \times (\nabla \times \underset{\sim}{A}) \tag{2.32}$$

Dodd and Deeds (1967) solved this equation for a stationary conductor with sinusoidal and also pulsed applied current. It was found that the computed and measured values are in good agreement.

Feng et al (1975) give a numerical solution for a sinusoidal applied current density and an axisymmetric velocity distribution.

Thatcher (1971) has solved the vector potential equation numerically when the permeability is uniform. The applied current density appears in the boundary condition at the primary coils instead of in the vector potential equation:

$$\left(\frac{A}{r} + \frac{\partial A}{\partial r}\right)_2 - \left(\frac{A}{r} + \frac{\partial A}{\partial r}\right)_1 = \mu_r \mu_o J_o \qquad (2.33)$$

Baker (1977) gives a finite difference analysis with a time marching solution, he uses a magnetic function approach instead of the magnetic vector potential. He also discusses a method using current rings to divide up the conducting material. By considering the interaction of all the rings, the current distribution and hence the magnetic field can be found.

We assume permeability is constant at any point in the medium and is equal to the permeability of free space ($\mu = \mu_o$), therefore equation 2.32 becomes:

$$\nabla^2 \underset{\sim}{A} = -\mu_o J_o(t) + \mu_o \sigma \frac{\partial \underset{\sim}{A}}{\partial t} - \sigma \mu_o \underset{\sim}{V} \times (\nabla \times \underset{\sim}{A}) \qquad (2.34)$$

With axial symmetry of coils and flow, there is only one componenet of $\underset{\sim}{A}$ (for non-symmetric coils the problem requires a three dimensional solution).

CHAPTER 3

THE PERFORMANCE OF ELECTROMAGNETIC FLOWMETER WITH MAGNETIC SLURRIES*

3.1 Introduction

In this Chapter the effect of a magnetic fluid on the response of a particular design of electromagnetic flowmeter is examined. Aqueous based fluids are considered in which the conductivity is that for an electrolyte and therefore low enough to ensure that the currents circulating in the fluid will be small enough to have a negligible effect on the applied magnetic field.

Magnetic slurries have been observed to have a considerable effect on the flowmeter calibration. The cause of this, which will be discussed later, is the change in the permeability of the magnetic circuit. The material between the pole-pieces changes from a relative permeability of unity to something higher and the flux density is accordingly increased. The flux distribution may also be modified since not all the permeability will be changed in the same ratio. The consequences of these changes in flux density and distribution is to change the size of the voltage generated by the flow.

---

* The work in this Chapter has been reported by R.C. Baker and M. Tarabad (1978).

The effect of magnetic slurries does not appear to have been analysed, but a method for compensating for the increased signal level was proposed and patented (Mannherz and Schmoock 1968). The idea incorporated in this patent was to use a search coil which would monitor the field size, and the signal from this could be used to eliminate the effect of changing flux by taking the ratio of generated voltage to search coil signal. Of course the idea of using a ratio to eliminate effects due to fluctuation of field caused by mains voltage is common practice. However the usual method is to sample the field current, rather than as suggested in the patent mentioned above, to sample the flux density. The inventors assumed the use of as uniform a field as possible. This is seldom the case actually and the change in flux distribution means that even with the use of a search coil, the calibration will not necessarily be retained. One outcome of this work will be to recommend a design having a constant calibration for a wide range of slurry permeability.

The governing equations given in Chapter 2 are used to obtain the solutions for the particular geometry selected. The results are discussed including a simple model to confirm the behavioural trends, and limitations of the analysis are considered.

3.2 Theory

It was assumed that the conductivity would not be enough to permit circulating currents of sufficient size to modify the applied magnetic field appreciably.

It was also assumed that the effects of changing magnetic field will be eliminated by careful design of the flowmeter (Baker 1968a) so that the electric field will satisfy equation 2.6. Using these

assumptions the flowmeter equation 2.14 was obtained.

The boundary conditions can be obtained from equation 2.1 for a non-conducting boundary as

$$\frac{\partial U}{\partial n} = - (\underset{\sim}{v} \times \underset{\sim}{B})_{\perp} \qquad (3.1)$$

where n is the co-ordinate perpendicular ($\perp$) to the boundary.

In this work the attention will be confined to the "long-flowmeter" where variation is considered to exist only for r and θ. The solution for this case has been obtained (Baker 1968b) and is given below (see figure 3.1 for the geometry).

$$\Delta U_{EE} = 2\int_{a}^{o} v(\sqrt{ra}) \quad B_{\theta}(r,\pi/2)\ dr \qquad (3.2)$$

where ΔU_{EE} is the potential difference generated between diametrically opposed electrodes ($\theta = \pi/2$), a is the pipe radius, v(r) is an axisymmetric velocity profile, and B_{θ} is the azimuthal component of the magnetic field.

The change in signal which will be considered arises from a redistribution of the magnetic field. The flowmeter layout which is convenient for this analysis is one suggested by Bevir (1969) in which the field coils lie in the flowtube surface only separated from the fluid by the presence of the non-conducting liner (figure 3.2). This geometry has also been analysed by Baker (1973). In this work it will be assumed that the relative permeability of the tube (which behaves as the magnet yoke) will be very large compared with the relative permeability of the slurry. So referring to figure 3.2 there are three regions of differing permeability, the yoke, the slurry and the insulating liner with relative permeability of unity.

The solution of magnetic potential equation 2.11 is obtained in the three regions to match the appropriate boundary conditions. The boundary conditions to be satisfied are that

$$\mu_1 \left(\frac{\partial\phi}{\partial n}\right)_1 = \mu_2 \left(\frac{\partial\phi}{\partial n}\right)_2 \tag{3.3}$$

where 1 and 2 refer to two different regions and

$$\phi_1 = \phi_2 \tag{3.4}$$

These are all the equations needed to solve the problem and the solution for the magnetic field making use of ϕ was obtained. Then applying this to equation 3.2 the solution for a long flow-meter was found.

3.3 Solution

It is assumed that the value of ϕ on the surface of the tube will be unaffected by the magnetic slurry and so only two regions need to be considered, the tube lining where on the outer boundary ϕ will be given and the slurry in the tube.

The general solution for the magnetic potential function in the liner in cylindrical co-ordinates is

$$\phi_\ell(r,\theta) = \sum_{n=0}^{\infty} (A_n r^n + B_n r^{-n}) \mathrm{Cos}n\theta \tag{3.5}$$

and for the slurry in the tube is

$$\phi_f(r,\theta) = \sum_{n=0}^{\infty} (C_n r^n + D_n r^{-n}) \text{Cosn}\theta \qquad (3.6)$$

where A_n, B_n, C_n and D_n are arbitrary constants. D_n in equation 3.6 must be zero as the value of magnetic potential function at $r = 0$ is finite. Using the boundary conditions of $r = a$ (equations 3.3 and 3.4) give

$$C_n = A_n + B_n a^{-2n} \qquad (3.7)$$

and

$$C_n = \frac{1}{\mu'} (A_n - B_n a^{-2n}) \qquad (3.8)$$

At $r = b$ we have:

$$\sum_{n=0}^{\infty} (A_n b^n + B_n b^{-n}) \text{Cosn}\theta = \phi_\ell(b,\theta) \qquad (3.9)$$

Using the Fourier Cosine transformation we obtain:

$$A_n b^n + B_n b^{-n} = \frac{1}{\pi} \int_{-\pi}^{\pi} \text{Cosn}\theta \, \phi_\ell (b,\theta) \, d\theta \qquad (3.10)$$

or

$$A_n b^n + B_n b^{-n} = \frac{2}{\pi n} \text{Sin}(n\beta)(1 - \text{Cosn}\pi) \, \phi_o \qquad (3.11)$$

where $\phi_o = I$

From equations (3.7), (3.8) and (3 .11) the values of A_n, B_n, C_n can be calculated as:

$$A_n = \frac{-2I}{\pi n} \frac{\mathrm{Sin}(n\beta)\ (1 - \mathrm{Cos}n\pi)\ (\mu' + 1)\ (b/a^2)^n}{(\mu' - 1) - (b/a)^{2n}\ (\mu' + 1)} \tag{3.12}$$

and

$$B_n = \frac{2I}{\pi n} \frac{\mathrm{Sin}(n\beta)\ (1 - \mathrm{Cos}n\pi)\ (\mu' - 1)\ b^n}{(\mu' - 1) - (b/a)^{2n}\ (\mu' + 1)} \tag{3.13}$$

and

$$C_n = \frac{-4I}{\pi n} \frac{\mathrm{Sin}(n\beta)\ (1 - \mathrm{Cos}n\pi)\ (b/a^2)^n}{(\mu' - 1) - (b/a)^{2n}(\mu' + 1)} \tag{3.14}$$

when $n = 2m$, A_m, B_m and C_m are zero, therefore the magnetic potential function distributions for the liner and the slurry regions will be as follows:

$$\phi_\ell(r,\theta) = \frac{-4I}{\pi} \sum_{m=o}^{\infty} \frac{\sin(2m + 1)\beta\ \cos(2m + 1)\theta}{(2m + 1)\{(\mu' - 1) - (b/a)^{2(2m + 1)}\ (\mu' + 1)\}}$$

$$\times \{(\mu' + 1)\ (\frac{br}{a^2})^{(2m + 1)} - (\mu' - 1)\ (\frac{r}{b})^{-(2m + 1)}\} \tag{3.15}$$

and

$$\phi_f(r,\theta) = -\frac{8I}{\pi} \sum_{m=0}^{\infty} \frac{\mathrm{Sin}(2m + 1)\beta\ \cos(2m + 1)\theta}{(2m + 1)\{(\mu' - 1) - (\frac{b}{a})^{2(2m + 1)}\ (\mu' + 1)\}} (\frac{br}{a^2})^{2m+1} \tag{3.16}$$

where the geometry is given in figure 3.2, and I is equal to the current turns in the slot. In particular β is the half angle of

the pole pieces and a and b the inner and outer radii of the insulating liner. μ' is the ratio of permeabilities of fluid and liner, which on the assumption that the relative permeability of the liner is unity will be equal to the relative permeability of the slurry.

The Θ component of magnetic flux density may be calculated as:

$$B_{\theta f}(r,\theta) = \frac{\mu_f}{r} \frac{\partial \phi_f(r,\theta)}{\partial \theta} \tag{3.17}$$

Using equation 3.16 gives,

$$B_{\theta f}(r,\theta) = \frac{8\mu_f I}{\pi r} \sum_{m=0}^{\infty} \frac{\sin(2m+1)\beta \sin(2m+1)\theta}{\{(\mu'-1) - (b/a)^{2(2m+1)}(\mu'+1)\}} \left(\frac{br}{a^2}\right)^{2m+1} \tag{3.18}$$

Equation 3.18 can be applied in equation 3.2 and gives,

$$\Delta U_{EE} = \frac{16\mu_f I}{\pi} \sum_{m=0}^{\infty} \frac{(-1)^m \sin(2m+1)\beta}{\{(\mu'-1) - (\frac{a}{b})^{2(2m+1)}(\mu'+1)\}} \int_o^a \frac{v(\sqrt{ra})}{r} \left(\frac{br}{a}\right)^{2m+1} dr \tag{3.19}$$

For two special cases the following results are obtained.

(a) Uniform Profile

In this case v is constant and equal to v_m, and equation 3.19 reduces to:

$$\Delta U_{EE} = \frac{16\mu_f v_m I}{\pi} \sum_{m=0}^{\infty} \frac{(-1)^m \sin(2m+1)\beta}{(2m+1)(\mu'-1) - (\frac{b}{a})^{2(2m+1)}(\mu'+1)} \left(\frac{b}{a}\right)^{2m+1} \tag{3.20}$$

(b) Parabolic profile

The expression for v(r) is

$$v = 2v_m\left(1 - \left(\frac{r}{a}\right)^2\right) \tag{3.21}$$

and equation 3.19 reduces to

$$\Delta U_{EE} = \frac{16\mu_f v_m I}{\pi} \sum_{m=0}^{\infty} \frac{(-1)^m \sin(2m+1)\beta}{(m+1)(2m+1)\{(\mu'-1) - \left(\frac{b}{a}\right)^{2(2m+1)}(\mu'+1)\}} \left(\frac{b}{a}\right)^{2m+1} \tag{3.22}$$

One further quantity will be required. To obtain an output signal which is independent of fluid permeability, the generated voltage will be divided by the signal from a search coil in the insulating liner which measures the radial component of magnetic field at r=a and $\theta=\gamma$. Various values of γ will be tested. The best search coil position angle will then be found.

The field at this point is given by

$$B_r(a,\gamma) = \frac{-8\mu_f I}{\pi a} \sum_{m=0}^{\infty} \frac{\sin(2m+1)\beta\cos(2m+1)\gamma}{\{(\mu'-1) - \left(\frac{b}{a}\right)^{2(2m+1)}(\mu'+1)\}} \left(\frac{b}{a}\right)^{2m+1} \tag{3.23}$$

3.4 Results

The first results show the effect on the signal of increasing fluid permeability assuming that the signal is taken as a ratio of voltage generated to field current. The field current, magnetic

flux density and magnetic potential at the pole piece are related by:

$$I = \int_{o}^{b} \frac{B_r}{\mu} (r,0)_{dr} = \phi(b,\theta) \qquad (3.24)$$

$\phi(b,\theta)$ is, of course, constant for the pole piece. The results are given by the ratio $\Delta U_{EE}/(\mu_\ell I v_m)$ which can be considered as a flowmeter sensitivity (Shercliff, 1962).

Figure 3.3 shows the signal variation with μ' obtained from equations 3.20 and 3.22 for two velocity profiles and four field coil angles.

The next results in figure 3.4 show the effect of taking the ratio of voltage generated to search coil signal. These are obtained from equations 3.20 and 3.22 using equation 3.23 for the coil signal. Again the variation of the signal with μ' is shown for two velocity profiles and, in this case, three search coil angles. The ratio used, $\Delta U_{EE}/(2aB_r v_m)$, where B_r is the field at the search coil, is also a sort of sensitivity.

3.5 Discussion

In discussing these results some apology for the approach is not out of place. It is reasonable to expect a weight-function analysis to be applied to the behaviour of the electromagnetic flowmeter. In nearly all situations this appears to be the best approach since it provides a clear picture of the effect of any particular region of flow on the signal. It is not immediately obvious how a change of complete profile will affect the signal, but this can be calculated with

relative ease given the weight function and a computer.

The essential different in this situation of changing permeability is that because the magnetic flux distribution will change the weight function distribution will also change. The weight function will continue to be valuable in providing an indication of the effect of varying velocity profile but only for a given permeability.

Since the effect on the signal level is to be considered it is chosen to examine the effect on output signal of changing permeability for the two extreme profiles; parabolic to give the laminar end of the range and uniform as an extreme limit of a turbulent profile.

Long flowmeters with axisymmetric flow profile are to be considered so the more extensive problem of non-axisymmetric profiles is excluded.

3.5.1 Operation with Constant Field Current

The most common method used to compensate for supply voltage variation, which would otherwise upset the calibration by altering the magnetic field strength, is to divide the flow induced voltage by a signal proportional to the field current. The variation of signal with permeability for a conventional variety of flowmeter will result. Figure 3.3 indicates first a rapid increase in signal followed by an asymptotic behaviour. It is assumed in this work that the fluid permeability will always be much less than the yoke permeability, so this will not be a true asymptote. However, the reason for this trend can be understood from a simple argument based on an idealisation of the magnetic circuit. The magnetic reluctance in the fluid will generally be much greater than the magnetic reluctance in the liner since the distances will be greater in the

fluid. As the fluid permeability increases, however, the fluid reluctance will decrease until for the limit of fluid permeability much greater than unity, the fluid reluctance will be negligible compared with the liner magnetic reluctance. The field will then jump the liner by the shortest path and the liner reluctance will control the field strength. Thus the asymptotic-like behaviour will result.

The critical point at which this behaviour starts will be related to the ratio of liner thickness to pipe radius. The larger this ratio the sooner it will occur. This of course overlooks the change in the distribution of the flux which introduces separate factors.

It is possible to calculate the value of the induced voltage when the fluid permeability is also very high. This calculation may be simplified by making the following approximations: the value of ϕ on the inner surface of the liner will be zero and on the outer surface will be I for $0 \leqslant \theta \leqslant \beta$ and will be zero for $\beta < \theta \leqslant \pi/2$; the value of B_r at the inner surface of the liner will be $\mu_\ell I/t$ for $0 \leqslant \theta < \beta$ and zero for $\beta < \theta \leqslant \pi/2$, where t is thickness of the liner. The first approximation is adequate provided the ratio of liner thickness to permeability is very much greater than the ratio of tube radius to the 'inifinite' permeability of tube and fluid. The second approximation will only be valid for an infinitely thin liner, but simplifies the analysis greatly.

The flow signal is given by equation (3.2) which for a uniform profile is

$$\Delta U_{EE} = 2v_m \int_a^0 B_\theta(r,\pi/2)\, dr \qquad (3.25)$$

Since all the flux entering at the circumference must cross the electrode diameter

$$\int_a^0 B_\theta(r,\pi/2)\,dr = a\int_0^\beta B_r(a,\theta)\,d\theta \qquad (3.26)$$

or

$$\frac{\Delta U_{EE}}{\mu_\ell I v_m} = \frac{2a\beta}{t} \qquad (3.27)$$

For $\beta = 69^\circ$ and $t/a = 0.2$, the value of $\Delta U_{EE}/(\mu_\ell I v_m) = 12$ which agrees well with the value given in figure 3.3.

The design which is considered is not entirely typical, but the trends which have been obtained should generally be applicable to commercial designs. The effect on signal of variation of the flow profile at different permeabilities (Figure 3.3) is likely to be the aspect of the behaviour least able to be applied to the other designs.

It can be seen from Figure 3.3 that while for lower values of the field coil angle the parabolic velocity profile results in a higher singal than the uniform profile and for higher values the reverse, a value of $\beta = 69^\circ$ gives the same signal for both profiles.

One change not calculated here is the inductance of the circuit resulting in a lower field current for the same supply voltage. Mannherz and Schmook (1968) note that for water a meter had a magnet current of 1.37 amps while for a slurry containing 32.5 of magnetite by weight the magnet current dropped to 1.27 amps. For the same change the ratio of signal voltage over flow rate was found to increase from 1.836 millivolts per gallon per minute to 2.175 millivolts per gallon per minute.

3.5.2 Operation with a Search-Coil Reference Voltage

Mannherz and Schmook (1968) using a search coil to measure their approximately uniform magnetic field and dividing their signal voltage by this search coil voltage were able to keep this ratio constant to about 1% for the change given in section 3.5.1.

Figure 3.4 shows the possibilities for the design which have been considered for compensating for increased permeability of fluid using a search coil positioned at the edge of the insulating liner. The search coil angle has been varied to examine the effect on the ratio with changing permeability and flow profile.

It is apparent from Figure 3.4 that with a search coil angle of $\gamma = 40^{\circ}$ the ratio of flow signal to search coil signal is virtually independent of relative permeability. However there is a small change of about 2% when the profile changes from parabolic to uniform. Using a field coil angle $\beta = 69^{\circ}$ and a search coil angle $\gamma = 34^{\circ}$, the variation was much reduced.

It seems likely that a similar analysis for any design will equally yield a best layout. Equally it does not seem necessary to retain the uniform field limitation of Mannherz and Schmook since the fields which are considered have been far from uniform.

3.6 Conclusions

The behaviour of electromagnetic flow meters with magnetic slurries has been illustrated using a convenient design of long flow meter having a non- uniform field.

The signal variation with constant field excitation current has been calculated and an explanation in terms of simple magnetic

circuit concepts advanced.

The use of a search coil to provide a reference signal has been discussed and the constancy of the ratio of flow signals to search coil signal has been plotted for certain parameter variations. It was suggested that a suitable layout should be obtainable which would ensure a constant signal for any design regardless of the field uniformity, for the restricted range of axisymmetric velocity profiles represented by the parabolic and uniform profiles.

CHAPTER 4

SWEPT FIELD ELECTROMAGNETIC FLOWMETERS

4.1 Introduction

The motion of a conducting fluid in a magnetic field induces currents in the fluid. The induced currents were ignored in non-metallic liquids because of the low conductivity, but in liquid metals with high conductivity the effects are significant. Two major phenomena associated with these currents are:

1) The distortion of imposed magnetic fields by the induced currents.
2) The body forces produced by interaction of the imposed field and the induced currents, which affects the fluid dynamics, disrupt the velocity profile and add to the pressure drop. The Hartmann number $M(= Ba\sqrt{\sigma/\eta})$, which is the ratio of the electromagnetic forces to the viscous forces in the fluid is small in electromagnetic flowmeasurements. Therefore the effect of self-induced velocity profile distortion by the flowmeter is considered to be negligible. Wenger (1971) has shown the effect of Hartmann number on flowmeter sensitivity for a Hartmann number range from 1 to 1000. The results enable the experimenter to correct flow measurements for the effect of velocity profile distortion produced by the flowmeter itself.

In this chapter we study the first phenomena to see the extent to which the imposed magnetic field is distorted by the induced currents.

The output voltage of an ideal electromagnetic flowmeter with infinitely long, unifrom magnetic field and axisymmetric velocity profile was given by equation 1.2. For flowmeters representative of present industrial practice, where the magnetic field is neither infinite nor uniform an allowance must be made for reduction in voltage. Hartmann (1937) realised that the induced voltage in the fluid decreases where the magnetic field falls off, allowing short-circuit currents in planes parallel to the direction of flow at the edge of the magnetic field. Boucher and Ames (1961) showed how these end currents produce losses in d.c. MHD generators and Shercliff (1962) gave a simple explanation for edge effects (see figure 4.1). For an imposed magnetic field which is not perturbated too greatly, the edge current density is of order σBV_m circulating at the edges of the field at which the field perturbation will be a maximum. The magnetic field induced by the circular currents at upstream is of order $\mu\sigma aBV_m$ and therefore the induced magnetic field will distort the imposed field at the upstream edge of the magnet by a fraction of the order $\sigma\mu aV_m$, (the magnetic Reynolds number). At the downstream edge the field will be reinforced by a similar fraction. The resultant field profile is shown in figure 4.2. The flow of liquid metal tends to sweep the imposed field downstream and the characteristics of the flowmeter becomes non-linear. The magnetic field distortion will vary with magnetic Reynolds number.

The short meter with electrodes displaced downstream or a combination of electrodes are the alternatives to the long transverse field meter with point electrodes in the midplane. The main steps to analyse this meter will be:

a) To analyse the field in a circular pipe for high magnetic

Reynolds number.

b) To predict the response for the best electrode arrangements.

4.2 Magnetic Field Analysis

The extent to which the imposed field is distorted by the induced currents is given by equation 2.7. From equation 2.1 and equation 2.7 it follows that

$$\nabla \times \frac{\underset{\sim}{B}}{\mu} = \sigma(\underset{\sim}{E} + \underset{\sim}{V} \times \underset{\sim}{B}) \tag{4.1}$$

If we take the curl of both sides of equation 4.1 we obtain:

$$\nabla \times \nabla \times \frac{\underset{\sim}{B}}{\mu} = \sigma(\nabla \times \underset{\sim}{E} + \nabla \times (\underset{\sim}{V} \times \underset{\sim}{B})) \tag{4.2}$$

For steady magnetic field and uniform permeability we have

$$\nabla \times \nabla \times \underset{\sim}{B} = \mu\sigma \nabla \times (\underset{\sim}{V} \times \underset{\sim}{B}) \tag{4.3}$$

or

$$\nabla(\nabla.\underset{\sim}{B}) - \nabla^2 \underset{\sim}{B} = \mu\sigma \nabla \times (\underset{\sim}{V} \times \underset{\sim}{B}) \tag{4.4}$$

Using equation 2.3 this gives

$$\nabla^2 \underset{\sim}{B} = -\mu\sigma \nabla \times (\underset{\sim}{V} \times \underset{\sim}{B}) \tag{4.5}$$

The following assumptions are made in deriving equation 4.5

a) σ, the electrical conductivity is constant

b) μ, the magnetic permeability is constant and is equal to the permeability of free space (μ_o).

If the velocity is axisymmetric along the axis of the pipe, the equation 4.5 leads to

$$\nabla^2 \underset{\sim}{B} = -\mu_o \sigma \nabla \times (-V_z(r) B_\theta \underset{\sim}{r} + V_z(r) B_r \underset{\sim}{\theta}) \tag{4.6}$$

where B_r and B_θ are the magnetic field components.

It follows therefore that:

$$\nabla^2 \underset{\sim}{B} = \mu_o \sigma V_z(r) \frac{\partial B_r}{\partial z} \underset{\sim}{r} + \mu_o \sigma V_z(r) \frac{\partial B_\theta}{\partial z} \underset{\sim}{\theta}$$

$$- \mu_o \sigma \{\frac{1}{r} (\frac{\partial}{\partial r} (r V_z(r) B_r) + V_z(r) \frac{\partial B_\theta}{\partial \theta} \underset{\sim}{z}\} \tag{4.7}$$

The expression $\nabla^2 B$ is given in Appendix E and from that the following differential equations can be derived for the r and θ components of an induced magnetic field:

$$\frac{\partial^2 B_r}{\partial r^2} + \frac{1}{r} \frac{\partial B_r}{\partial r} + \frac{1}{r^2} \frac{\partial^2 B_r}{\partial \theta^2} + \frac{\partial^2 B_r}{\partial z^2} - \frac{B_r}{r^2} - \frac{2}{r^2} \frac{\partial B_\theta}{\partial \theta}$$

$$= \mu_o \sigma V_z(r) \frac{\partial B_r}{\partial z} \tag{4.8}$$

and

$$\frac{\partial^2 B_\theta}{\partial r^2} + \frac{1}{r}\frac{\partial B_\theta}{\partial r} + \frac{1}{r^2}\frac{\partial^2 B_\theta}{\partial \theta^2} + \frac{\partial^2 B_\theta}{\partial z^2} - \frac{B_\theta}{r} + \frac{2}{r^2}\frac{\partial B_r}{\partial \theta}$$

$$= \mu_o \sigma V_z(r) \frac{\partial B_\theta}{\partial z} \qquad (4.9)$$

To express the above equations in non-dimensional form, the following definitions are used:

$$R_m = \mu \sigma a V_m, \quad r_1 = r/a \quad \text{and} \quad z_1 = z/a$$

Substituting the above definitions into equation 4.9 gives

$$\frac{\partial^2 B_r}{\partial r_1^2} + \frac{1}{r_1}\frac{\partial B_r}{\partial r_1} + \frac{1}{r_1^2}\frac{\partial^2 B_r}{\partial \theta^2} + \frac{\partial^2 B_r}{\partial z_1^2} - \frac{B_r}{r_1^2} - \frac{2}{r_1^2}\frac{\partial B_\theta}{\partial \theta} = R_m \frac{V_z(r_1)}{V_m}\frac{\partial B_r}{\partial z_1} \qquad (4.10)$$

and

$$\frac{\partial^2 B_\theta}{\partial r_1^2} + \frac{1}{r_1}\frac{\partial B_\theta}{\partial r_1} + \frac{1}{r_1^2}\frac{\partial^2 B_\theta}{\partial \theta^2} + \frac{\partial^2 B_\theta}{\partial z_1^2} - \frac{B_\theta}{r_1^2} + \frac{2}{r_1^2}\frac{\partial B_r}{\partial \theta} = R_m \frac{V_z(r_1)}{V_m}\frac{\partial B_\theta}{\partial z_1} \qquad (4.11)$$

The effect of the induced current is expressed by the terms on the right hand side of both equations 4.10 and 4.11. This is the term which produces field distortion and it will vanish for low conducting fluids or zero flow.

An analytical solution of equations 4.10 and 4.11 is not generally available and this is particularly so when the equations are applied to situations complicated by flow profile, pipe geometry or imposed field configuration. Therefore with the help of a numerical technique a solution is obtained for an arbitrary imposed field.

4.2.1 Numerical Techniques

To solve the magnetic field equations we use the finite difference approximation. The individual terms in equations 4.10 and 4.11 can be approximated in finite difference form:

$$f(x + h_1) = f(x) + h_1 f'(x) + \frac{h_1^2}{2!} f''(x) + \frac{h_1^3}{3!} f'''(x) + \ldots.$$

$$f(x - h_2) = f(x) - h_2 f'(x) + \frac{h_2^2}{2!} f''(x) - \frac{h_2^3}{3!} f'''(x) + \ldots.$$

From the above equations it is possible to find the first and second derivatives of f(x) in terms of values of the function of points x, $x + h_1$ and $x - h_2$.

$$f''(x) = \frac{h_2 f(x + h_1) + h_1 f(x - h_2) - (h_1 + h_2) f(x)}{\frac{h_1 h_2}{2}(h_1 + h_2)} + O(h^2) \tag{4.12}$$

$$f'(x) = \frac{h_2^2 f(x + h_1) - h_1^2 f(x - h_2) - (h_2^2 - h_1^2) f(x)}{h_1 h_2 (h_1 + h_2)} + O(h^2) \tag{4.13}$$

After the various terms in equations 4.10 and 4.11 have been approximated in cylindrical co-ordinates with a particular lattice size, as shown in Figure 4.3 it follows that:

$$\begin{aligned} B_r(i,j,k) &= A_2(i) B_r(i - 1,j,k) + A_3(i)\, B_r(i+ 1,j,k) \\ &+ A_4(i)\,(B_r(i,j - 1,k) + B_r(i,j + 1,k)) + A_6(i) B_r(i,j,k - 1) \\ &+ A_7(i)\, B_r(i,j,k + 1) + A_8(i)\,(B_\theta(i,j - 1,k) - B_\theta(i, j + 1,k))/A_1(i) \end{aligned} \tag{4.14}$$

and

$$\begin{aligned} B_\theta(i.j.k) &= (A_2(i) B_\theta(i - 1,j,k) + A_3(i) B_\theta(i + 1,j,k) + A_4(i) \\ &(B_\theta(i,j - 1,k) + B_\theta(i, j + 1,k)) + A_6(i) B_\theta(i.j.k - 1) + A_7(i) \\ &B_\theta(i,j,k + 1) + A_8(i)\,(B_r(i.j - 1,k) - B_r(i,j + 1,k))/A_1(i) \end{aligned} \tag{4.15}$$

where

$$A_1(i) = \left(\frac{2}{h_1 h_2} + \frac{h_2 - h_1}{r_1(i) h_1 h_2} + \frac{2}{(r_1(i)\delta\theta)^2} + \frac{2}{h_3^2} + \frac{1}{r_1(i)^2}\right)$$

$$A_2(i) = \left(\frac{2}{h_2(h_1 + h_2)} - \frac{h_1}{r_1(i) h_2(h_1 + h_2)}\right)$$

$$A_3(i) = \left(\frac{2}{h_1(h_1 + h_2)} + \frac{h_2}{r_1(i) h_1(h_1 + h_2)}\right)$$

$$A_4(i) = \frac{1}{(r_1(i)\delta\theta)^2}$$

$$A_6(i) = \left(\frac{1}{h_3^2} + \frac{R_m V_z(i)}{2h_3 V_m}\right)$$

$$A_7(i) = \left(\frac{1}{h_3^2} - \frac{R_m V_z(i)}{2h_3 V_m}\right)$$

$$A_8(i) = \frac{1}{r_1(i)^2 \delta\theta}$$

Equation 4.14 gives the r component of the magnetic field at every point in terms of its value at the nearest six neighbours to that point and the θ component of the magnetic field at the two nearest neighbours (see figure 4.3). Equation 4.15 gives the θ-component of the magnetic field.

It is not possible to solve the equations 4.14 and 4.15 separately, therefore an iteration method with Successive Over Relaxation method (S.O.R) has been used to solve these two equations simultaneously.

4.2.2 Successive Over Relaxation

A direct method of successive elimination cannot be applied to solve the magnetic field equations (coupled equations), therefore an iterative method must be used to handle the system of equations. Using this method it is first necessary to set the boundary conditions and the initial guesses for all the other points in the field. From equation 4.14 it is then possible to calculate the new value of $B_r^{n+1}(i,j,k)$, however iteration can be accelerated by imposing a greater change in $B_r^{n+1}(i,j,k)$.

$$\Delta B_r(i,j,k) = B_r^{n+1}(i,j,k) - B_r^{n}(i,j,k) \tag{4.16}$$

The new value of $B_r^{n+1}(i,j,k)$ used is then:

$$B_r^{n+1}(i,j,k) = B_r^{n}(i,j,k) + R \cdot \Delta B_r(i,j,k) \tag{4.17}$$

where R is the relaxation factor.

In general, the higher the value of R, the faster convergence is obtained, but values of R above an optimum value will give oscillation in successive values of $B_r(i,j,k)$ and excessively high values of R will give total instability.

Once the calculation has been carried out to find the new values of B_r at all the other points the new value of B_r obtained is used to replace the old value for quick convergence.

After one sweep the new values of B_r are obtained at each point, using these values we continue to find the new value for B_θ by the same method from equation 4.15. After one sweep for B_θ, we repeat the process all over again until the convergence criteria is satisfied

for both B_θ and B_r. Convergence usually takes place rapidly once a system has begun to converge. The convergence criteria should normally be somewhere in the range of 10^{-4} - 10^{-7}, which is sufficient for most purposes. There are several methods of convergence that can be used:

1) Maximum absolute residual
2) Average absolute residual
3) Maximum absolute weighted residual
4) Mean absolute weighted residual

The last method has been employed in this investigation to check for the convergence, i.e.:

$$\text{Mean absolute weighted residual: } \frac{\sum_{n=1}^{nt} |B_r^{\,n} - B_r^{\,n-1}|}{\sum_{n=1}^{nt} |B_r^{\,n}|}$$

4.2.3 Boundary Conditions

The imposed magnetic field is normally symmetric about the pipe centre line and the coils producing this field are placed at the top and bottom part of the pipe. Some of these coils are analysed in Appendices A, B and C. When the velocity distribution is axisymmetric and the imposed field has the symmetrical configuration, it is sufficient to analyse only 1/4 of the pipe, for non-symmetric velocity distribution or imposed field the whole section must be considered. The spacing of lattices is illustrated in figure 4.4. The boundary conditions for B_r and B_θ are defined as follows. Since the finite difference terms become infinite at the centre of the pipe, the equations fail at the

centre. To overcome this it is assumed that the magnetic field components have flat curves (i.e. not changed) near the centre and a half spaced lattice at the centre is used.

$$B_r(0,\theta,z) = B_r(\frac{\delta r}{2},\theta,z)$$

and

$$B_\theta(0,\theta,z) = B_\theta(\frac{\delta r}{2},\theta,z)$$

The r component of magnetic field is mirrored by the plane at $\theta = 0$, the θ component of magnetic field is zero at this plane, and is also mirrored by the plane but in the opposite direction (see figure 4.5). The θ component of magnetic field is mirrored by the plane at $\theta = \pi/2$, the r component of magnetic field is zero at this plane, and is mirrored by this plane in the opposite direction. Magnetic field components at upstream and downstream remote from edges of imposed field are set to zero. It is assumed that magnetic field components at r = b, (the surface close to the imposed magnetic field coil or permanent magnet pole faces) are not affected by the induced currents and are equal to the imposed field. Later the extent of the error produced by this approximation is investigated.

4.3 Induced Voltage

Equation 2.12 is the general form of the flowmeter equation, for an rectilinear velocity profile the equation becomes:

$$\nabla^2 U = -B_\theta \frac{\partial V_z(r)}{\partial r} - V_z(r) \ (\nabla \times B)_z \qquad (4.18)$$

From equation 2.7 we have

$$(\nabla \times \underset{\rightharpoonup}{B})_z = \mu J_z \tag{4.19}$$

and from Ohm's Law we have

$$J_z = \sigma(-\frac{\partial U'}{\partial z}) \tag{4.20}$$

Combining the last three equations (4.18, 4.19 and 4.20) gives:

$$\nabla^2 U = -B_\theta \frac{\partial V_z(r)}{\partial r} + \mu \sigma V_z(r) \frac{\partial U}{\partial z} \tag{4.21}$$

or

$$\frac{\partial^2 U}{\partial r^2} + \frac{1}{r}\frac{\partial U}{\partial r} + \frac{1}{r^2}\frac{\partial^2 U}{\partial \theta^2} + \frac{\partial^2 U}{\partial z^2} = -B_\theta \frac{\partial V_z(r)}{\partial r} + \mu \sigma V_z(r)\frac{\partial U}{\partial z} \tag{4.22}$$

In non-dimensional form this equation becomes:

$$\frac{\partial^2 U}{\partial r_1^2} + \frac{1}{r_1}\frac{\partial U}{\partial r_1} + \frac{1}{r_1^2}\frac{\partial^2 U}{\partial \theta^2} + \frac{\partial^2 U}{\partial z_1^2} = -a\, B_\theta \frac{\partial V_z(r_1)}{\partial r_1} + \mu \sigma a\, V_z(r_1)\frac{\partial U}{\partial z_1} \tag{4.23}$$

Using the finite difference approximation in cylindrical co-ordinate gives the equation:

$$U(i,j,k) = (A'_2(i)U(i-1,j,k) + A'_3(i)U(i+1,j,k) + A'_4(i)(U(i,j-1,k) + U(i,j+1,k)) + A'_6(i)U(i,j,k-1) + A'_7(i)U(i,j,k+1) - a\, B_\theta(i,j,k)\frac{\partial V_z(i)}{\partial r_1})/A'_1(i) \tag{4.24}$$

where

$$A'_1(i) = \left(\frac{2}{h_1 h_2} + \frac{h_2 - h_1}{r_1(i) h_1 h_2} + \frac{2}{(r_1(i)\delta\theta)^2} + \frac{2}{h_3^2}\right)$$

and A'_2, A'_3, A'_4, A'_6 and A'_7 are the same as A_2, A_3, A_4, A_6 and A_7, given before in Section 4.2.1.

The induced voltage at any point, U(i,j,k) is in terms of the values of induced voltage at the six nearest neighbours. We use the same method (S.O.R) as used for calculation of the magnetic field equation to solve the induced voltage equation.

4.3.1 Boundary Conditions

The partial differential equation governing the distribution of U the induced voltage requires a single electrical boundary condition specified at all points along the boundary of the conducting region. Part of the boundary of the region of interest consists of hypothetical surfaces. These surfaces are where the fluid enters and leaves, which may be chosen to be sufficiently remote for all electrical disturbances to have fallen to negligible proportions and the assumption of $\frac{\partial U}{\partial z} = 0$ is quite correct. From symmetry it is obvious that $\frac{\partial U}{\partial \theta} = 0$ at $\theta = \pi/2$ and the induced voltage is constant at $\theta = 0$, and it may be set to zero for convenience. The boundary condition at r=a the fluid and pipe interface, depends on wall conductivity and contact resistance between the wall and fluid.

It is possible to use the numerical solution of the induced voltage equation in the wall as well as in the fluid and satisfy the boundary condition at wall and fluid interface from these two solutions. However to save computing time it is assumed that the pipe is thin

e.g. the wall conductivity number is much smaller than unity:

$$d\left(= \frac{w\sigma_w}{a\sigma_f}\right) << 1$$

4.3.2 Thin-wall Boundary Conditions

Let σ_w the conductivity of the pipe material be uniform and the contact resistance between the fluid and the wall be τ. Here it is assumed that τ is also uniform, although in practice it is well known to be very variable, both in time and space (Shercliff, 1962). It is not even always realistic to take the contact voltage drop as proportional to normal current density. However, use of a constant τ enables us to explore the effect of contact resistance without too much mathematical complication. Figure 4.6 shows a portion of thin wall, the flow being in the z-direction.

Let J_w denote the total current in the wall at any point per unit length of pipe, it therefore follows:

$$\underset{\sim}{J}_w = (J_{\theta w}\, \underset{\sim}{\theta} + J_{zw}\, \underset{\sim}{z}) \tag{4.25}$$

where

$$J_{\theta w} = -\frac{w\sigma_w}{a}\frac{\partial U_w}{\partial \theta} \tag{4.26}$$

and

$$J_{zw} = -w\sigma_w \frac{\partial U_w}{\partial z} \tag{4.27}$$

leading to:

$$\underset{\sim}{J}_w = w\left(-\frac{\sigma_w}{a}\frac{\partial U_w}{\partial \theta}\,\underset{\sim}{\theta} - \sigma_w \frac{\partial U_w}{\partial z}\,\underset{\sim}{z}\right) \tag{4.28}$$

The electrical current is continuous at the fluid and wall interface and $\underset{\sim}{J}_w$ varies in accordance with the equation:

$$\frac{1}{a}\frac{\partial J_{\theta w}}{\partial \theta} + \frac{\partial J_{zw}}{\partial z} = J_{rf} \tag{4.29}$$

J_{rf} is the current density in the r-direction in the fluid at the fluid/wall interface. Combining equations 4.26, 4.27 and 4.29 results in equation 4.30 below:

$$\frac{1}{a}\frac{\partial}{\partial \theta}\left(-\frac{w\,\sigma_w}{a}\frac{\partial U_w}{\partial \theta}\right) + \frac{\partial}{\partial z}\left(-w\,\sigma_w\frac{\partial U_w}{\partial z}\right) = J_{rf} \tag{4.30}$$

or

$$d\left(\frac{1}{a^2}\frac{\partial^2 U_w}{\partial \theta^2} + \frac{\partial^2 U_w}{\partial z^2}\right) = \frac{1}{a}\left(\frac{\partial U_f}{\partial r} + V_z(r)\,B_\theta\right) \tag{4.31}$$

At the interface between the fluid and the wall there is a voltage difference where the normal current traverses the contact resistance. This is expressed by the equation:

$$U_f - U_w = \tau\, J_{rf} \tag{4.32}$$

or

$$U_w = U_f + \tau\,\sigma_f\left(\frac{\partial U_f}{\partial r} + V_z(r)\,B_\theta\right) \tag{4.33}$$

From equations 4.31 and 4.33 we obtain the partial differential equation for induced voltage at the fluid/wall interface.

$$\frac{d}{a^2}\,\frac{\partial^2}{\partial\theta^2}\left(U_f + \tau\,\sigma_f\left(\frac{\partial U_f}{\partial r} + V_z(r)\,B_\theta\right)\right)$$

$$+\,d\,\frac{\partial^2}{\partial z^2}\left(U_f + \tau\,\sigma_f\left(\frac{\partial U_f}{\partial r} + V_z(r)\,B_\theta\right)\right) = \frac{1}{a}\left(\frac{\partial U_f}{\partial r} + V_z(r)\,B_\theta\right) \tag{4.34}$$

If $C_r = \frac{\tau\,\sigma}{a}$ is the contact resistance number equation 4.34 becomes:

$$d\,\frac{\partial^2}{\partial\theta^2}\left(U_f + C_r\left(\frac{\partial U_f}{\partial r_1} + V_z(r_1)\,a\,B_\theta\right)\right)$$

$$+\,d\,\frac{\partial^2}{\partial z_1^2}\left(U_f + C_r\left(\frac{\partial U_f}{\partial r_1} + V_z(r_1)\,a\,B_\theta\right)\right) = \frac{\partial U_f}{\partial r_1} + V_z(r_1)\,a\,B_\theta \tag{4.35}$$

To represent the boundary condition more accurately at r = a a central difference formula is used:

$$\frac{\partial U}{\partial r} = \frac{U(a + \delta r) - U(a - \delta r)}{2\,\delta r}$$

where $U(a + \delta r)$ is the fictitious voltage at the external mesh point. The voltage $U(a + \delta r)$ is unknown and necessitates another equation. This is obtained by assuming that the induced voltage equation is satisfied at r = a. Now by rewriting equation 4.35 in terms of

$U(a + \delta r, \Theta, z)$, fictitious voltage and induced voltage equation at $r = a$ we can calculate the induced voltage at the external mesh point:

$$U(i_1 + 2,j,k) = (Q_1.U(i_1 + 1,j,k) - Q_2.U(i_1,j,k) +$$

$$Q_3.(U(i_1 + 1,j,k) + U(i_1 + 1,j - 1, k)) + Q_4.(U(i + 1,j,k + 1)$$

$$+ U(i_1 + 1,j,k - 1)) + Q_5.(U(i_1 + 2,j + 1,k) + U(i_1 + 2,j - 1,k)$$

$$-U(i_1,j + 1,k) - U(i_1,j - 1,k_1)) + Q_6.(U(i_1 + 2,j,k + 1)$$

$$+ U(i_1 + 2,j,k - 1) - U(i_1,j,k + 1) - U(i_1,j,k - 1)) + Q_7)/Q_2$$

(4.36)

where

$$Q_1 = -2\ d\left(\frac{1}{\delta\Theta^2} + \frac{1}{\delta z_l^2}\right)$$

$$Q_2 = \frac{d\ C_r}{\delta r_l}\left(\frac{1}{\delta\Theta^2} + \frac{1}{\delta z_l^2}\right) + \frac{1}{2\delta r_l}$$

$$Q_3 = \frac{d}{\delta\Theta^2}$$

$$Q_4 = \frac{d}{\delta z_l^2}$$

$$Q_5 = \frac{d\ C_r}{2\delta r_l\ \delta\Theta^2}$$

$$Q_6 = \frac{d\ C_r}{2\delta r_l\ \delta z_l^2}$$

$$Q_7 = (d\, C_r\, V_z\, (i_1 + 1)\, a)$$

$$\left[\frac{(B_\theta(i_1 + 1,j + 1,k) + B_\theta(i_1 + 1,j - 1,k) - 2B_\theta(i_1 + 1,j,k))}{\delta\theta^2} \right.$$

$$\left. + \frac{(B_\theta(i_1 + 1,j,k + 1) + B_\theta(i_1 + 1,j,k - 1) - 2B_\theta(i_1 + 1,j,k)}{\delta z_1^2} \right]$$

$$- V_z(i_1 + 1)\, a\, B_\theta(i_1 + 1,j,k)$$

4.4 Results

A computer program has been written to solve magnetic field equations utilising the S.O.R. method and employing several accelerated convergence techniques. The program can handle an axisymmetric velocity profile and symmetrical imposed field. The values of magnetic field close to the coil are calculated from direct analyses of the coils (rectangular or diamond) and in the case of permanent magnets the measured values are given as boundary values. The effect of relaxation factor on convergence is shown by figures 4.7, 4.8 and 4.9. These are plots of the mean weighted absolute residual as the iteration proceeds for a number of relaxation factors. The optimum relaxation factor in calculating the magnetic field components is about 1.6, while the induced voltage equation converges most rapidly with a value of about 1.4. A relaxation factor of 2 or

greater makes the system of equations unstable.

The numerical solution of induced magnetic field and induced voltage equations makes it possible to analyse any flowmeter with symmetrical imposed field. The solution is valid for a wide range of magnetic Reynolds number and axisymmetric velocity profiles. The effect of wall conductivity and wall contact resistance can also be predicted. Here the flow of sodium in the .356m diameter pipes of a fast breeder reactor with a typical sodium temperature of $400^{\circ}C$ and the maximum R_m of 5 is studied.

4.4.1 Saddle Coil (Concentric Type) Flowmeter

The configuration of the coil is illustrated in Appendix A where an analytical formula for induced magnetic field is derived. This solution will provide the magnetic field components at the boundary, where r = b. The specifications of the coil are

coil diameter = three times the pipe inside diameter

coil length = two times the pipe inside diameter

half coil angle = 80°

magnetic field strength at the centre of coil = 3.404 mT

no contact resistance (C_r = 0) and wall conductivity number (d) = .044

The coil has 100amps and 26 turns per component coil.

The results of this analysis are presented in figure 4.11 to figure 4.18. Figure 4.11 shows the magnetic field distribution in the plane $\theta = 0$. The high magnetic Reynolds number ($R_m = 5$) has swept the imposed field downstream. Figure 4.12 shows how the size of magnetic Reynolds number affects the distortion of magnetic field and magnitude of induced field. The change in sodium temperature affectsthe distortion, since a change in temperature would cause a change in the sodium conductivity, causing a change in the magnitude of the eddy currents. The magnetic field distribution was then used to obtain the induced voltage and is illustrated in figure 4.13. The induced voltage at the inner and outer surface of the pipe is equal, because the contact resistance between sodium and wall is ignored.

Figure 4.14 shows the induced voltage distribution along the pipe for point electrodes at $\theta = \pi/2$ and $r = a$ and various values of magnetic Reynolds number. The effects of velocity profile are shown in figure 4.15. The results indicate that there is a position of electrodes that gives an equal signal for uniform and parabolic velocity profile and downstream of that position the signal is higher for uniform velocity and upstream of that the signal is higher for parabolic velocity. Figure 4.16 illustrates how the wall conductivity number d, causes a drop in signal and there is also a further drop due to the contact resistance number C_r, and the voltage drops are maximum at one diameter downstream of flow. This is because the end currents enter the wall at maximum rate at this section of pipe. The induced voltage is non-linear for electrodes in the midplane of the flow-meter and this is shown in figure 4.17. Figure 4.18 shows the induced voltage from six electrode locations, and the signal is nearly linear for electrodes positioned at one diameter downstream.

The sensitivity defined as:

$$S = \frac{\Delta U}{2 a V_m B_o}$$

(where B_o is the magnetic field at the centre of the flowmeter for no flow), is calculated for two positions of the electrodes and two velocity profiles and three values of R_m. The results are given in table 4.1.

4.4.2 Diamond Coil Flowmeter

The configuration of this coil is shown in figure C.1 and the analytical formula for induced magnetic field is derived in Appendix C. The specifications of the diamond coil flowmeter are identical to the saddle coil used in section 4.4.1. The magnetic field at the centre of the coil is B_o = 2.44 mT.

The distortion of magnetic field is shown in figure 4.19. The induced voltage distribution along the pipe for point electrodes at $\theta = \pi/2$ and $r = a$ and three values of magnetic Reynolds number is shown in figure 4.20. The effect of velocity profile is shown in figure 4.21.

The induced signals from six electrode locations are shown in figure 4.22, and the signal is nearly linear for the electrode positioned at one diameter downstream. Again the sensitivity of the flowmeter for two positions of electrodes, two velocity profiles and three values of R_m are calculated and are given in table 4.2.

4.5 Discussion

Earlier it was assumed that the magnetic field at the surface close to the coil was not affected by the induced currents. This surface has a radius of b and is not so close to the coils as to make the calculation of imposed field impossible at this surface. Generally the distance of two or three wire diameters are sufficient. To see the magnitude of the error produced by this assumption a very simple method is used. The end currents have a maximum radius of a (the radius of the pipe) and this is shown in figure 4.10. The magnetic field at the centre line of this current loop is

$$B_i = \frac{\mu_o I a^2}{2(a^2 + r^2)^{3/2}} \qquad (4.37)$$

This equation shows how the induced field drops with r, the distance from the axis of the current loop. Therefore the ratio of induced field at r, the distance from the centre of circle, to induced field at the centre of circle is

$$\frac{B_i}{B_{io}} = \frac{1}{(1 + (\frac{r}{a})^2)^{3/2}} \qquad (4.38)$$

The calculation gives B_{io} = 2.1 mtesla for a magnetic Reynolds number of 5. The radius of the coil is three times the pipe radius and hence the equation 4.38 suggests an induced field of .066 mtesla at the surface. This is only 1.7% of the imposed field at this point. This error is less for lower values of R_m. The nature of end currents is to increase the imposed field downstream of the coil and to reduce the field upstream and this introduces a maximum error of +1.7%

downstream and -1.7% upstream. The opposite sign of the error at the two ends will produce practical errors less than 1.7% for a magnetic Reynolds number of 5.

4.6 Conclusions

The magnetic field and flowmeter equations have been presented for the case when the effect of magnetic Reynolds number may not be ignored.

In addition the magnetic field equation is solved numerically in three dimensions, using a cylindrical co-ordinate system and taking into account the effect of magnetic Reynolds number. The flowmeter equation is also solved numerically using the magnetic field distribution obtained in the first part of this chapter (Section 4.2).

Two types of short air cored coil, namely saddle coil (concentric type) and diamond coil are examined.

The results show that the performance of flowmeters with electrodes located in the middle of the coil, becomes non-linear with increasing magnetic Reynolds number. The results also show that linearity can be achieved by displacing the electrodes downstream of the midplane. This was also observed by Turner (1960) and the theoretical results obtained here confirm his experimental observation.

The only disadvantage of this method is that the linearity is obtained with respect to magnetic Reynolds number not the flow rate and therefore any change in fluid temperature will affect the performance of the flowmeter. This type of flowmeter is capable of working, over a wide range of flow rate. However, where the problems of field sweeping exist, the change of temperature must be small, unless a continuous check on fluid temperature is maintained.

In Chapter 6 a method is established for eliminating the effect of fluid temperature.

Note on uncertainty due to unknown σ

If σ is unknown but R_m is known to be given by

$$0 < R_m < 5$$

the sensitivity for the saddle coil flowmeter (for example) with electrodes one diameter downstream and uniform profile will be in the range

$$.676 < S < .802$$

CHAPTER 5

WEIGHT FUNCTION FOR SWEPT FIELD FLOWMETER

5.1 Introduction

The previous weight function approach on the induced voltage electromagnetic flowmeter was concerned with low conducting fluids, where the induced currents in the fluid are negligible and the induced magnetic field by these currents is not strong enough to influence the imposed field significantly. For the case of liquid metals however, the conductivity is high and therefore the induced currents will distort the imposed magnetic field. In this chapter a weight function is derived for the induced voltage flowmeter with a distorted field. This weight function will be a function of magnetic Reynolds number, but a position of the electrodes is to be found where a weight function distribution independent of magnetic Reynolds number occurs.

5.2 Theory

Bevir (1970) gives the relation for the flowmeter signal (see equation 1.8). This equation has been derived with no restriction on magnetic field shape and fluid conductivity and therefore it is still valid when the induced currents are not ignored. Volume of integration is restricted to the moving fluid because V=0 outside it. $\underset{\sim}{J}_v$ the virtual current density is determined by the electrode shape, electrical condition on the flowmeter wall and the conductivity distribution of fluid if this is non-uniform. Bevir (1970) assumed that the induced currents were negligible and calculated the magnetic field distribution from the following equation:

$$\nabla^2 F = 0 \tag{5.1}$$

where

$$\underset{\sim}{B} = \nabla F \tag{5.2}$$

But when the conductivity of the fluid is high the induced currents cannot be ignored and therefore we used the magnetic field distribution found numerically in Chapter 4.

The virtual current is expressed by the equation:

$$\underset{\sim}{J}_v = -\sigma \nabla U_v \tag{5.3}$$

If we take the divergence of virtual current and assume that conductivity of the fluid is uniform we obtain:

$$\nabla^2 U_v = 0 \tag{5.4}$$

The distribution of the virtual current may be found from the 'virtual voltage' equation 5.4.

5.2.1 Boundary Conditions

The boundary condition of r = a is the same as equation 4.34 when the fluid velocity is zero.

$$d \frac{\partial^2}{\partial \theta^2} (U_{vf} + C_r \frac{\partial U_{vf}}{\partial r_1}) + d \frac{\partial^2}{\partial z_1^2} (U_{vf} + C_r \frac{\partial U_{vf}}{\partial r_1}) = \frac{\partial U_{vf}}{\partial r_1} \tag{5.5}$$

The definition of virtual current requires a unit current density at the electrodes, but for easy computation it is assumed that the induced voltage is constant (U_o) at electrodes, therefore from equation 4.33 we have

$$U_{vf} - U_o = C_r\left(-\frac{\partial U_{vf}}{\partial r_1}\right) \tag{5.6}$$

The virtual voltage downstream and upstream (and sufficiently remote from electrodes) is chosen to be zero. From symmetry it is obvious that $\frac{\partial U_v}{\partial \theta} = 0$ at $\theta = \pi/2$, the virtual voltage is constant at $\theta = 0$ and is taken to be zero for convenience. With the help of these boundary conditions and the numerical technique, successive over relaxation (S.O.R.), the Laplace equation for virtual voltage in three dimensions has been solved. The real virtual voltage at any point when unit current density is set at the eletrodes is given by:

$$U_v = \frac{U'_v}{I_m} \tag{5.7}$$

where U'_v is the virtual voltage when the voltage at electrodes is U_o. I_m is the current in the midplane of the pipe:

$$I_m = 4 \int_o^a \int_o^\infty J \, dr \, dz \tag{5.8}$$

At the midplane the current perpendicular to this plane is J_θ (see figure 5.1). Hence from equation 5.8 it follows that:

$$I_m = 4 \int_o^a \left(\int_o^\infty J_{\theta f} \, dr + J_{\theta w} \right) dz \tag{5.9}$$

where

$$J_{\theta w} = - \frac{\sigma_w W}{a} \frac{\partial U_{vw}}{\partial \theta} \tag{5.10}$$

putting this in equation 5.9 gives:

$$I_m = 4 a \sigma_f \int_0^{\infty} (a \int_0^1 \frac{J_{\theta f}}{\sigma_f} dr_1 - d \frac{\partial U_{vw}}{\partial \theta}) dz_1 \tag{5.11}$$

where

$$\frac{J_{\theta f}}{\sigma_f} = - \frac{1}{a} \frac{\partial U_{vf}}{\partial r_1} \quad \text{at } r_1 = 0$$

and

$$\frac{J_{\theta f}}{\sigma_f} = - \frac{1}{a r_1} \frac{\partial U_{vf}}{\partial \theta} \qquad \text{for } o < r_1 \leq 1$$

If the velocity consists of a z-component only it follows from equation 1.8 that:

$$\Delta U = \int_{\tau} V_z \cdot W_z \, d\tau \tag{5.12}$$

And for a velocity independent of z we obtain:

$$\Delta U = \int_{s} V_z \cdot \overline{W}_z \, dS \tag{5.13}$$

where $\overline{W}_z = \int_{-\infty}^{+\infty} W_z \, dz$ is called the mean weight function and

$$W_z = (\underset{\sim}{B} \times \underset{\sim}{J}_v)_z \tag{5.14}$$

or

$$W_z = (B_r J_{\theta v} - B_\theta J_{rv}) \tag{5.15}$$

putting the virtual current density components from equation 5.3 in equation 5.15 gives:

$$W_z = \sigma_f \left(B_r \frac{1}{r} \frac{\partial U_v}{\partial \theta} - B_\theta \frac{\partial U_v}{\partial r}\right) \tag{5.16}$$

At $\theta = 0$ it follows that $B_\theta = 0$ from the symmetry of meter, and therefore:

$$W_z = \sigma_f B_r \left(\frac{1}{r} \frac{\partial U_v}{\partial \theta}\right) \tag{5.17}$$

At $\theta = \pi/2$ we have $B_r = 0$ giving:

$$W_z = \sigma_f B_\theta \left(-\frac{\partial U_v}{\partial r}\right) \tag{5.18}$$

At the centre of the pipe equation 5.18 has been used when W_z is calculated.

5.3 Results

The finite difference approximation and successive over relaxation method has been employed again to solve equation 5.4 giving the weight vector distribution. The virtual voltage is a maximum in the plane of electrodes and drops rapidly along the

z-axis shown in figure 5.1. Therefore to find a more accurate weight vector the grid must be finer in the z-direction. Finer grids are used in calculating the virtual voltage. "Lagrangian interpolation" (see Appendix D) is applied to calculate magnetic field components which can then be found from coarser grids. The mean weight function distribution has been found for different positions of the electrodes along the pipe and is presented by figure 5.2 through 5.6.

Figure 5.2 shows the mean weight function at the cross-section of the conducting pipe with wall conductivity number of .044 and the electrodes positioned at the midplane of meter and no flow. The imposed field is produced by the short saddle coil identical to the one used in Chapter 4. A similar plot when the magnetic Reynolds number is 5 is illustrated in figure 5.3. Figure 5.3 for $R_m = 5$ shows that the high value of magnetic Reynolds number has changed the mean weight function distribution from the form presented by Shercliff, which is similar to figure 5.2 when $R_m = 0$. This change of distribution produces a non-linear signal, this being observed from results obtained in induced voltage analysis. The calculation shows that with electrodes shifted to the edge of the coil (one diamter downstream) the mean weight function distribution becomes identical for a magnetic Reynolds number range of 0 to 5 and the signal becomes linear. This is shown in figure 5.4. This again gives the expected results which were found in Chapter 4 with a different method of analysis. The effects of wall conductivity and imposed field configuration are shown in figures 5.5 to 5.6. If we compare figure 5.2 and 5.6 we can see that the diamond coil flowmeter is less sensitive to velocity profile than the saddle coil meter as it gives a more uniform mean weight function distribution. Figure 5.5 shows that a non-conducting wall produces a smaller mean weight function at the wall and shows that by

increasing the wall conductivity it is possible to obtain a more uniform mean weight function as observed by Bevir (1970) when he used large electrodes.

5.4 Conclusions

The weight function analysis is more useful in flowmeter design because adjustments can be made to the electrode or field configuration, to obtain a flowmeter with a uniform mean weight function and therefore one independent of velocity distribution. Here it is shown that the flowmeter with point electrode , positioned at the middle of the field gives a non-linear signal, and moving the electrodes to the edge of field gives a linear signal which is not affected by magnetic Reynolds number. The flowmeter with electrodes positioned at the edge of field cannot be accepted as the final design as a change in temperature will affect the fluid conductivity, magnetic Reynolds number and therefore the signal. The results show that a design with series of electrodes along the pipe integrated voltage flowmeter is immume to conductivity changes. In the next chapter it is shown that the integrated voltage flowmeter will have a mean weight function which is unaffected by changes in the flowrate or fluid conductivity and a signal proportional to flowrate.

CHAPTER 6

INTEGRATED-VOLTAGE FLOWMETERS

6.1 Introduction

It has been shown that swept field flowmeters, with electrodes displaced one diameter downstream, have a linear characteristic but are affected by changes in conductivity. Therefore the aim of this part of the work is to design a flowmeter which gives a linear performance and is immune to any conductivity change due to temperature variation.

The end currents downstream will induce a field in the direction of the imposed field which adds to the field, but the end currents upstream induce the field in the opposite direction to the imposed field and therefore reduce the field (see figure 4.2). The distortion of the imposed-field leads to a distorted induced voltage and gives a non-linear signal. Therefore an increase in field downstream increases the induced voltage and a reduction of field upstream reduces the induced voltage. Shercliff (1962) suggested integration of the signal along the pipe to eliminate the effect of the non-uniformity of the transverse field. In this chapter a theory for integrated-voltage flowmeters is given and it is proved by two independent methods that they have a linear performance which is not affected by the conductivity change. Finally a few examples are given to confirm the theory.

6.2 Induced Voltage Solution

6.2.1 Theory

In analysing the ordinary flowmeter it is assumed that induced currents have no effect on the applied magnetic field ($\nabla \times B = 0$), and therefore the magnetic field distribution may be found from a potential function equation 2.11. In liquid metal flowmeters the induced currents cannot be ignored as they have a significant effect and they modify the applied field. The z-component of induced current density is given by equations 4.19 and 4.20 and from these equations it follows:

$$(\nabla \times B)_z = \mu \sigma \left(-\frac{\partial U}{\partial z}\right) \qquad (6.1)$$

Expanding equation 6.1 gives

$$\frac{1}{r}\left(\frac{\partial}{\partial r}(r B_\theta) - \frac{\partial B_r}{\partial \theta}\right) = \mu \sigma \left(-\frac{\partial U}{\partial z}\right) \qquad (6.2)$$

The integral of the magnetic field components is defined as:

$$\overline{B}_\theta = \int_{-\infty}^{+\infty} B_\theta \, dz \qquad (6.3)$$

and

$$\overline{B}_r = \int_{-\infty}^{+\infty} B_r \, dz \qquad (6.4)$$

The integral of equation 6.2 from $z = -\infty$ to $z = +\infty$ is

$$\frac{1}{r}\left\{\frac{\partial}{\partial r}\left(r\int_{-\infty}^{+\infty} B_\theta \, dz\right) - \frac{\partial}{\partial \theta}\int_{-\infty}^{+\infty} B_r \, dz\right\} = \mu\,\sigma\left(-\int_{-\infty}^{+\infty}\frac{\partial U}{\partial z}\, dz\right) \qquad (6.5)$$

In the derivation of equation 6.5 it was assumed that the velocity had only a z-component and fluid permeability and fluid conductivity are constant in that direction. The induced voltage at $z = \pm\infty$ is zero as the magnetic field is zero, therefore equation 6.5 becomes

$$\frac{1}{r}\left(\frac{\partial}{\partial r}\left(r\,\bar{B}_\theta\right) - \frac{\partial \bar{B}_r}{\partial \theta}\right) = 0 \qquad (6.6)$$

Equation 6.6 proves that the following relation between the scalor $\bar{\phi}$ (integral of potential function) and $\bar{B}$ (integral of magnetic field) exists

$$\bar{B}/\mu = \nabla\,\bar{\phi} \qquad (6.7)$$

or

$$\bar{B}/\mu = \frac{\partial \bar{\phi}}{\partial r}\,\underset{\sim}{r} + \frac{1}{r}\,\frac{\partial \bar{\phi}}{\partial \theta}\,\underset{\sim}{\theta} + \int_{-\infty}^{+\infty}\frac{\partial \phi}{\partial z}\,\underset{\sim}{dz} \qquad (6.8)$$

ϕ may be assumed equal to zero at $z = \pm\infty$ and hence the equation 6.8 becomes:

$$\bar{B}/\mu = \frac{\partial \bar{\phi}}{\partial r}\,\underset{\sim}{r} + \frac{1}{r}\,\frac{\partial \bar{\phi}}{\partial \theta}\,\underset{\sim}{\theta} \qquad (6.9)$$

The integral of equation 2.3 from $z = -\infty$ to $z = +\infty$ leads to:

$$\nabla . \underset{\sim}{\overline{B}} = 0 \tag{6.10}$$

and from equations 6.7 and 6.10 the following equation results:

$$\nabla^2 \overline{\phi} = 0 \tag{6.11}$$

The solution of equation 6.11 gives the integral of magnetic field components. The solution is in two dimensions and is independent of the z-axis. The boundary condition for the differential equation 6.11 is, in an integral form:

$$\overline{\phi}_o = \int_{-\infty}^{+\infty} \phi_o \, dz \tag{6.12}$$

ϕ_o is the value of the magnetic potential at the pole-pieces of flowmeter. The differential equation for induced voltage was given by equation 4.22 and the integral of induced voltage along the z-axis is defined as:

$$\overline{U} = \int_{-\infty}^{+\infty} U \, dz \tag{6.13}$$

As $z \to \pm\infty$ outside the field, U and $\frac{\partial U}{\partial z}$ tend to zero and therefore

$$\int_{-\infty}^{+\infty} \frac{\partial U}{\partial z} \, dz = 0 \tag{6.14}$$

and

$$\int_{-\infty}^{+\infty} \frac{\partial^2 U}{\partial z^2} \, dz = 0 \tag{6.15}$$

The integral of equation 4.22 along the z-axis after the substition of equations 6.3, 6.13, 6.14 and 6.15 is

$$\frac{\partial^2 \bar{U}}{\partial r^2} + \frac{1}{r} \frac{\partial \bar{U}}{\partial r} + \frac{1}{r^2} \frac{\partial^2 \bar{U}}{\partial \theta^2} = -\bar{B}_\theta \frac{\partial V_z(r)}{\partial r} \tag{6.16}$$

The r-component of current density at r = a is

$$J_r = \sigma(- \frac{\partial U}{\partial r} - V_z(a) \, B_\theta) \tag{6.17}$$

The integral of equation 6.17 is

$$\int_{-\infty}^{+\infty} J_r \, dz = \sigma(- \frac{\partial \bar{U}}{\partial r} - V_z(a) \, \bar{B}_\theta) \tag{6.18}$$

Equation 6.18 for a non-conducting wall becomes

$$\frac{\partial \bar{U}}{\partial r} = - V_z(a) \, \bar{B}_\theta \tag{6.19}$$

6.2.2 Solution

The following solutions have been found for a flowmeter with

point electrodes, and an infinitely long transverse field, are used to find the signal for the integrated-voltage flowmeter with a short imposed field.

Baker (1968b)

The solution of the induced voltage equations for a non-uniform magnetic field in the cross-section of a pipe with point electrodes was given by Baker (1968b):

$$U = -\frac{1}{2}\int_{o}^{r} \{V_z(\sqrt{\rho r}) + V_z(a\sqrt{\rho/r})\}\, B_\theta\,(\rho,\theta)\, d\rho \qquad (6.20)$$

Using this equation for an integrated-voltage flowmeter gives:

$$\overline{U} = -\frac{1}{2}\int_{o}^{r} \{V_z(\sqrt{\rho r}) + V_z(a\sqrt{\rho/r})\}\, \overline{B_\theta}\,(\rho,\theta)\, d\rho \qquad (6.21)$$

The signal for electrodes at r = a and $\theta = \pi/2$ will be

$$\overline{\Delta U} = 2\int_{o}^{a} V_z(\sqrt{\rho a})\, \overline{B_\theta}\,(\rho,\pi/2)\, d\rho \qquad (6.22)$$

Integrated-voltage flowmeters with magnetic slurries

In Chapter 3 a solution was given for a flowmeter with point electrodes and a reference coil, which had a performance immune from fluid permeability changes. The solution was obtained assuming that

the conductivity is not so high as to permit induced currents to modify the imposed magnetic field. This restriction for conductivity is not necessary any more. Instead of using equation 2.11 to find the magnetic field distribution equation 6.11 can be used, which has no conductivity limitation. Therefore equation 3.18 becomes

$$\overline{B}_{\theta f}(r,\theta) = \frac{8\mu_f \bar{\phi}_o}{\pi r} \sum_{m=0}^{\infty} \frac{\sin(2m+1)\beta \sin(2m+1)\theta}{\{(\mu'-1) - (\frac{b}{a})^{2(2m+1)}(\mu'+1)\}} (\frac{br}{a^2})^{2m+1} \tag{6.23}$$

where

$$\bar{\phi}_o = 2\ell I \tag{6.24}$$

and 2ℓ is the length of pole pieces.

Put equation 6.23 in equation 6.22

$$\overline{\Delta U} = \frac{32\mu_f \ell I}{\pi} \sum_{m=0}^{\infty} \frac{(-1)^m \sin(2m+1)\beta}{\{(\mu'-1) - (\frac{a}{b})^{2(2m+1)}(\mu'+1)\}} \int_o^a \frac{V(\sqrt{ra})}{r} (\frac{br}{a^2})^{2m+1} dr \tag{6.25}$$

For a uniform velocity profile equation 6.25 reduces to

$$\overline{\Delta U} = \frac{32\mu_f V_m \ell I}{\pi} \sum_{m=0}^{\infty} \frac{(-1)^m \sin(2m+1)\beta}{(2m+1)\{(\mu'-1) - (\frac{b}{a})^{2(2m+1)}(\mu'+1)\}} (\frac{b}{a})^{2m+1} \tag{6.26}$$

and for a parabolic velocity profile equation 6.25 reduces to

$$\overline{\Delta U} = \frac{32\mu_f V_m \ell I}{\pi} \sum_{m=0}^{\infty} \frac{(-1)^m \mathrm{Sin}(2m+1)}{(m+1)(2m+1)\{(\mu'-1) - (\frac{b}{a})^{2(2m+1)}(\mu'+1)\}} (\frac{b}{a})^{2m+1} \tag{6.27}$$

The integral of the r-component of magnetic field at r = a and $\theta = \gamma$ is

$$\overline{B_r}(a,\gamma) = \frac{-16\mu_f \ell I}{\pi a} \sum_{m=0}^{\infty} \frac{\mathrm{Sin}(2m+1)\beta \mathrm{Cos}(2m+1)\gamma}{\{(\mu'-1) - (\frac{b}{a})^{2(2m+1)}(\mu'+1)\}} (\frac{b}{a})^{2m+1} \tag{6.28}$$

The value of $\overline{B_r}(a,\gamma)$ may be found by fitting a search coil at r = a and $\theta = \gamma$ and extended along the pipe. The sensitivity of this flowmeter is defined as:

$$S = \frac{\overline{\Delta U}}{(2a\ \overline{B_r}\ V_m)} \tag{6.29}$$

Equations 6.26, 6.27 and 6.28 are similar to equations 3.20, 3.22 and 3.23 in Chapter 3 with an extra term, 2ℓ, the length of the pole pieces. The design explained in Chapter 3 with infinitely long pole pieces may be changed to one with short pole pieces, length 2ℓ, infinitely long integrating electrodes and a search coil at r=a and $\theta = \gamma$ which is long enough in the z-direction to integrate the r-component of magnetic field along the pipe. This design with coil half angle $\beta = 69^\circ$ and a search coil angle $\gamma = 34^\circ$ gave a sensitivity which is proportional to the length of the pole pieces.

(see figure 6.1).

Thatcher (1971)

The field distortion and its effect on sensitivity was investigated for the rectangular transverse uniform field and the flow of liquid metals in a channel with insulated walls (see figure 6.2). It was assumed that the applied field was uniform for all x and z less than ℓ but greater than $-\ell$ and having only a y-component. The imposed field is zero everywhere else. The velocity is uniform and is in the z-direction. The solution given by Thatcher does not seem to be correct, while the correct formulae for induced voltage distribution are as follows:

$$U = \frac{2V_m B_o}{a} \left\{ \sum_{n=1}^{\infty} \frac{(-1)^n \delta_n \operatorname{Sin} a_n x \left(e^{\gamma_n (z - \ell)} - e^{\gamma_n (z + \ell)}\right)}{a^2 n \left(\gamma_n - \delta_n\right)} \right\} \tag{6.30}$$

$$U = \frac{2V_m B_o}{a} \left\{ \sum_{n=1}^{\infty} \frac{(-1)^n \delta_n \operatorname{Sin} a_n x \; e^{\gamma_n (z - \ell)}}{a^2_n \left(\gamma_n - \delta_n\right)} - \frac{ax}{2} \right.$$

$$\left. - \sum_{n=1}^{\infty} \frac{(-1)^n \gamma_n \operatorname{Sin} a_n x \cdot e^{\delta_n (z + \ell)}}{a^2_n \left(\gamma_n - \delta_n\right)} \right\} \tag{6.31}$$

$$U = \frac{2V_m B_o}{a} \left\{ \sum_{n=1}^{\infty} \frac{(-1)^n \gamma_n \operatorname{Sin} a_n x \left(e^{\delta_n (z - \ell)} - e^{\delta_n (z + \ell)}\right)}{a^2_n \left(\gamma_n - \delta_n\right)} \right\} \tag{6.32}$$

where

$$\gamma_n a = (R_m + (R_m^2 + 4(a_n a)^2)^{\frac{1}{2}})/2$$

$$\delta_n a = (R_m - (R_m^2 + 4(a_n a)^2)^{\frac{1}{2}})/2$$

and

$$a_n a = (2n - 1)\,\pi/2$$

The induced voltage for electrodes at $x = \pm a$ will be

$$\Delta U = U(-a) - U(a) \tag{6.33}$$

and from equation 6.33 and 6.30 the following is obtained:

$$\Delta U = \frac{4V_m B_o}{a} \left\{ \sum_{n=1}^{\infty} \frac{\delta_n (e^{\gamma_n (z - \ell)} - e^{\gamma_n (z + \ell)}}{a^2{}_n (\gamma_n - \delta_n)} \right. \tag{6.34}$$

for $z < -\ell$

and from equation 6.33 and 6.31 the following is obtained:

$$\Delta U = \frac{4V_m B_o}{a} \left\{ \sum_{n=1}^{\infty} \frac{\delta_n e^{\gamma_n (z - \ell)}}{a^2{}_n (\gamma_n - \delta_n)} + \frac{a^2}{2} - \sum_{n=1}^{\infty} \right.$$

$$\left. \frac{\gamma_n e^{\delta_n (z + \ell)}}{a^2{}_n (\gamma_n - \delta_n)} \right\} \tag{6.35}$$

for $-\ell < z < \ell$

and from equation 6.33 and 6.32 it follows that:

$$\Delta U = \frac{4V_m B_o}{a} \sum_{n=1}^{\infty} \frac{\gamma_n (e^{\delta_n (z-\ell)} - e^{\delta_n (z+\ell)})}{a_n^2 (\gamma_n - \delta_n)} \qquad (6.36)$$

for $z > \ell$

The signal from the integrated voltage can be calculated by integrating equations 6.34, 6.35 and 6.36 along the channel.

The result after integration is a very simple term given by equation 6.37.

$$\Delta \bar{U} = 4 B_o V_m a\ell \qquad (6.37)$$

and from equation 6.37 the sensitivity is given by:

$$\bar{S} = 2\ell \qquad (6.38)$$

which 2ℓ is the extent of uniform applied field.

The above result could be found directly from the differential equation, which is, (See Thatcher 1971)

$$\frac{\partial^2 U}{\partial x^2} + \frac{\partial^2 U}{\partial z^2} = \mu \sigma V_m \frac{\partial U}{\partial z} \qquad (6.39)$$

and the boundary conditions are:

$$\frac{\partial U}{\partial x} = \frac{\partial U}{\partial z} = 0 \qquad \text{at } z = \pm\infty$$

and $U = 0$ at $z = \pm\infty$

$$\frac{\partial U}{\partial x} = - V_m B_o \qquad \text{at} \quad x = \pm a \qquad \text{for } -\ell < z < \ell$$

and

$$\frac{\partial U}{\partial x} = 0 \qquad \text{at } x = \pm a \qquad \text{for } z < \ell \text{ and } z > -\ell$$

The integrals of differential equation and boundary conditions using equation 6.13 are

$$\frac{\partial^2 \overline{U}}{\partial x^2} = 0 \tag{6.40}$$

and

$$\frac{\partial \overline{U}}{\partial x} = 2\ell V_m B_o \qquad \text{at} \quad x = \pm a$$

The solution of the differential equation 6.40 with the above boundary condition is

$$\overline{U} = -2\ell V_m B_o x \tag{6.41}$$

and the signal for the electrodes at $x = \pm a$, using equation 6.33, is:

$$\Delta\overline{U} = 4a\ell B_o V_m$$

which gives the sensitivity as found before in equation 6.38.

Numerical Example

In Chapter 4 the induced voltage distribution was found for a short saddle coil. The integral of the signal, for electrodes at $\theta = \pi/2$ and $r = a$, along the pipe was calculated for different values of magnetic Reynolds number and uniform or parabolic velocity profiles. The sensitivity of the integrated-voltage flowmeter based on these calculations is given in table 6.1. Table 6.1 shows that the sensitivity of a saddle coil flowmeter is constant for different values of magnetic Reynolds number and the slight difference for R_m of 5 is due to computational errors.

The change of velocity profile has little effect on the sensitivity. The table also shows that for two cases with magnetic Reynolds numbers of 5, one with a conductivity double the other and a mean velocity half of the other, the senstivity is the same. This proves that the sensitivity is not affected by fluid conductivity. The effect of wall conductivity number (d) and contact resistance number (C_r) on sensitivity is given in table 6.2. Table 6.2 shows that the results from the numerical solution are in very good agreement with those found from Equation 2.18.

Table 6.3 gives the sensitivity of a diamond coil flow meter for three values of magnetic Reynolds number and two velocity profiles.

6.3 Weight Function Solution

It is more useful to use the concept of the weight function when analysing electromagnetic flowmeters. Shercliff (1962) and Bevir (1970) have done this for flowmeters where the imposed magnetic

field is not distorted by the induced currents. In the following section this is extended for integrated-voltage flowmeters used with liquid metals.

The divergence theorem of Gauss is:

$$\int_{\tau} \nabla . \underset{\sim}{A} \; d\tau = \int_{s} \underset{\sim}{A} . d\underset{\sim}{s} \tag{6.42}$$

and from this equation it follows that:

$$\int_{s_1+s_2} (U^m \underset{\sim}{J}_v - U_v \underset{\sim}{J}^m) . d\underset{\sim}{s} = \int_{\tau} \{\nabla . (U^m \underset{\sim}{J}_v) - \nabla . (U_v \underset{\sim}{J}^m)\} \; d\tau \tag{6.43}$$

where s_1 and s_2 are the surfaces around the electrodes and τ is the entire volume of the meter.

From equation 2.5 it follows that:

$$\nabla . \underset{\sim}{J}_v = 0 \tag{6.44}$$

$$\nabla . \underset{\sim}{J}^m = 0 \tag{6.45}$$

$\underset{\sim}{J}_v$ is the virtual current and U_v is the virtual voltage, which would occur if unit current entered at $r = a$ and $\theta = \pi/2$ and left at $r = a$ and $\theta = -\pi/2$ with no fluid motion. $\underset{\sim}{J}^m$ is the induced current density and U^m is the induced voltage, with fluid motion.

Substitutions of equations 6.44 and 6.45 in equation 6.43 leads to:

$$\int_{S_1+S_2} (U^m \underset{\sim}{J}_V - U_V \underset{\sim}{J}^m) . \underset{\sim}{ds} = \int_{\tau} (\underset{\sim}{J}_V . \nabla U^m - \underset{\sim}{J}^m . \nabla U_V) \, d\tau \tag{6.46}$$

The virtual current is zero everywhere on the outer surface of wall except at the electrodes where it is unity and J^m is zero because no current is drawn during the operation of the flowmeter. Therefore the left hand side of equation 6.46 becomes:

$$\int_{S_1+S_2} (U^m \underset{\sim}{J}_V - U_V \underset{\sim}{J}^m) . \underset{\sim}{ds} = \int_{-\infty}^{+\infty} (U_2{}^m - U_1{}^m) dz \tag{6.47}$$

and

$$\Delta\overline{U} = \int_{-\infty}^{+\infty} (U_2{}^m - U_1{}^m) dz \tag{6.48}$$

The right hand side of equation 6.48 will lead to equation 6.49 if Ohm's Law is used.

$$\Delta\overline{U} = \int_{\tau} -\sigma (\underset{\sim}{V} \times \underset{\sim}{B}) . \nabla U_V \, d\tau \tag{6.49}$$

Applying Ohm's Law to the virtual current density in equation 6.49 gives:

$$\Delta\overline{U} = \int_{\tau} (\underset{\sim}{V} \times \underset{\sim}{B}) . \underset{\sim}{J}_V \, d\tau \tag{6.50}$$

Equation 6.50 may be written in the following form:

$$\Delta\overline{U} = \int_{\tau} \underset{\sim}{V}.(\underset{\sim}{B} \times \underset{\sim}{J}_v)\, d\tau \qquad (6.51)$$

where $\underset{\sim}{W} = \underset{\sim}{B} \times \underset{\sim}{J}_v$ and is called the weight vector by Bevir (1970). For an integrated-voltage flowmeter the distribution of J_v, the virtual current is two dimensional and is not a function of z. If the velocity is a function of θ and r we obtain:

$$\Delta\overline{U} = \int_{s} \underset{\sim}{V}.\underset{\sim}{\overline{W}}\, d\, s \qquad (6.52)$$

where $\underset{\sim}{\overline{W}} = \int_{-\infty}^{+\infty} \underset{\sim}{W}\, dz$ is the mean weight function and can be found from equation 6.53.

$$\overline{W} = \overline{B}_r\ J_{v\theta} - \overline{B}_\theta\ J_{vr} \qquad (6.53)$$

where $\overline{B_r}$ and $\overline{B_\theta}$ are defined by equations 6.3 and 6.4 respectively and are calculated from equation 6.11. The distribution of virtual current density may be found from equation 6.54.

$$\nabla^2 \overline{U}_v = 0 \qquad (6.54)$$

The mean weight function for the integrated voltage flowmeter is not affected by velocity profile, flowrate or conductivity of the

fluid and if the mean weight function is uniform the signal is proportional to flowrate.

6.4 Method for Integrating the Signal

The integral could be evaluated experimentally with reasonable precision from readings taken at a small number of electrodes along the pipe. One way of combining the readings would be to use two passive networks of resistance (high compared with the fluid but low compared with the voltage measuring device), this is shown in figure 6.3. If U is the output signal and U_n is the voltage for the electrode at z_n then it follows from Ohm's equation:

$$U_1 - U = i_1 R_1$$

$$U_2 - U = i_1 R_2$$

$$U_3 - U = i_3 R_3$$

. .

. .

. .

$$U_n - U = i_n R_n \qquad (6.55)$$

Because no current is drawn out of the meter during the operation, it follows that (Kirchhoffs Law):

$$i_1 + i_2 + i_3 + \ldots + i_n = 0 \qquad (6.56)$$

and from equations 6.55 and 6.56 we obtain

$$U\left(\frac{1}{R_1} + \frac{1}{R_2} + \frac{1}{R_3} \ldots + \frac{1}{R_n}\right) = \frac{U_1}{R_1} + \frac{U_2}{R_2} + \frac{U_3}{R_3} \ldots \frac{U_n}{R_n} \tag{6.57}$$

or in general equation 6.57 becomes

$$U = \frac{\sum_{n=1}^{N} \left(\frac{U_n}{R_n}\right)}{\sum_{n=1}^{N} \left(\frac{1}{R_n}\right)} \tag{6.58}$$

The values of R_n can be calculated and depends on the method of integration. For example, if a simple method of adding the signal is used, for which the resistances are equal, then equation 6.59 becomes

$$U = \frac{\sum_{n=1}^{N} U_n}{N} \tag{6.59}$$

and the integral is

$$\overline{U} = N\,U \tag{6.60}$$

The Gauss-Legendre quadrature method can be used which gives

$$\int_{-1}^{+1} f(x)\,dx = \sum_{n=1}^{N} \alpha_n\, f(z_n) \tag{6.61}$$

In equation 6.58 it is necessary to find the value of $\sum_{n=1}^{N} (\frac{U_n}{R_n})$ which is the integral of the signal. The values of R_n and the positions of the electrodes with respect to each other can then be found by selecting the number of electrodes from the the values of α_n and z_n.

6.5 Conclusions

It has been shown that the integrated voltage flowmeter may be used wherever the problem of field distortion and induced voltage distortion exists, due to field sweeping, because of the short length of imposed magnetic field and high magnetic Reynolds number. This flowmeter will give a signal proportional to flowrate and is not affected by conductivity changes in the fluid. It was also shown that the non-linearity because of the magnetic property of the fluid can be overcome by using a reference coil at the appropriate position at the liner but long enough to integrate the field along the pipe at that angle.

CHAPTER 7

SWEPT FIELD FLOWMETER EXPERIMENTS

7.1 Introduction

The experimental rig described in this chapter gives an analogue of sodium flow in the FBR and was designed to simulate flow up to a maximum magnetic Reynolds number of about 1.5, with reasonably steady measuring conditions. Measurements were also carried out for R_m greater than 1.5 but the velocity was not steady and therefore higher errors resulted. A sketch of the rig is shown in figure 7.1. A 5cm diameter aluminium rod was used to simulate a uniform flow of sodium in a non-conducting pipe. The rod was driven through a system of belts and pulleys, the pulleys in turn being driven by a pneumatic cylinder. The aluminium rod was supported on an aerostatic track and has coaxial guides. The complete driven system, rod, pulley, belts and track were contained in a common support frame.

The system of pulleys situated near the centre of the frame transmitted the drive from belts fitted to the double ended pneumatic piston to belts attached to the rod. This design is a modification of the rig built to investigate flux distortion flowmeters (see Baker et al 1974).

The objective of the experiments reported in this chapter is to verify the predictions obtained numerically in chapter 4. The aluminium rod needs to be moved at high speed for a short time, and many of the design problems were due to the high acceleration and

deceleration needed to achieve a constant rod velocity over a short period. This was overcome with an effective braking system at the end of the stroke.

The design of electrodes also created a problem, the contacts of the electrodes with the surface of the rod would cause corrosion and signal noise. Various ideas were tried and the final design is the carbon brushes. Electrodes are spring loaded for constant contact with the rod to measure the induced voltage across the diameter of the rod.

7.2 Mechanical Design

The experimental rig consists of:

1. Base Frame
2. Pneumatic Drive Cylinder
3. Drive Belts and Gears
4. Aluminium Rod
5. Flowmeter Assembly

7.2.1 Base Frame

The total length of the base frame is about seven metres and consists of eight hexagonal loops connected lengthwise by two square and two rectangular section steel members. The pneumatic cylinder, gears, pulleys, aluminium rod guides and permanent magnets are supported by this frame (figure 7.2).

Care was taken in the design to avoid steel in the vicinity of the magnet assembly and the hexagonal frames at that point are made of wood. The shocks from the sudden accelerations and decelerations due to high speed operation were reduced by supporting the frame on foam

pads.

7.2.2 Pneumatic Drive Cylinder

This is operated from the shop air supply of about 7 bar. This is fed into a reservoir which in turn feeds a four-way solenoid-operated control sequence valve attached to the cylinder inlet, the outlet or exhaust is controlled by a variable flow control ratio valve. This controls the overall speed of the drive system. The cylinder is of the through rod type which enables the toothed belt to be driven in either direction. The cylinder stroke is .58 metres which allows the aluminium rod to travel 1.16 metres.

7.2.3 Drive Belts and Gears

Two types of belting were used, toothed and flat section. The toothed belts could only be obtained up to a certain length and in consequence the remaining belt length was made up with a glass fibre belt. This combination of belts gave a good performance. The belts were joined to the drive cylinder eccentrically and with an adjustment to allow for the gear wheel diameters. The fibre belt was bolted to the rod and were tightened by using alloy plates with series of holes. Then the belts were linked through a series of toothed gears. Two sets of these gears transmitted the drive from the belts connected to the piston. The third set was not used.

Figure 7.3 shows the gear arrangement. The large diameter carry the belts from the rod and the smaller gears carry the belts from the piston end. The gear ratio is 2 and therefore the speed of the rod

is twice that of the piston.

7.2.4 Aluminium Rod

The aluminium rod was used to simulate the sodium flow, this rod has a minimum diameter of 5.037cm and a maximum diameter of 5.044cm. The average diameter was used in calculations. The rod is mounted on an air bearing to obtain smooth linear movement. These air bearings consist of a laminated wooden base on which the two supports for the rod run. In the base of each support an array of holes supplies air to the surface. In addition to this bearing two further wooden guides ensure that the rod is concentric.

Problems arise from the high deceleration necessary to bring the aluminium rod to rest at the end of the piston stroke. To prevent sudden shocks braking the belts, a brake system was added and can be seen in figure 7.4. This brake makes sure that the aluminium rod will not hit the magnet and electrode support. Therefore the rod is stopped independently of the piston as the latter comes to the end of its stroke.

The surge of air into the piston caused a rod peak velocity of about 2.5m/sec followed by a fluctuation which smoothed out towards the end of the stroke to give reasonably steady measuring conditions at about 1.5m/sec.

7.2.5 Flowmeter Assembly

Figure 7.5 shows the flowmeter design where the position of electrodes, electrode support and the permanent magnet can be seen. Figure 7.5 also shows a sectional view of the meter. The electrode

support is made out of non-conducting material (polyvinyl chloride) with resistivity of 10^{16} ohm/cm. It has nine pairs of holes diametrically opposite each other at 2.54cm intervals, the inner diameter of support is 5.33cm and the outer diameter is 7.32cm.

The main problem associated with voltage measurement was the design of a system for picking up the voltage from the surface of the moving aluminium rod. Various methods were tried and each one of them had its own problem. Small brass wheels were tried but they did not revolve smoothly at high R.P.M. Small steel balls caused scratching of the rod surface and also produced a high level of noise comparable with the actual signal. Finally the best solution considered was the use of carbon brushes similar to the ones used in electrical machines. The electrodes were made out of cylindrical carbon brushes and were inserted in the electrode support. The electrodes were loaded by springs and were secured to the support to allow a reasonable amount of play as the aluminium rod moved through the support tube.

The permanent magnet is shown in figure 7.5 which is 10cm long and has replaceable pole faces. The pole faces were machined to accomodate the electrode support. The gap between poles is 7.32cm at the midplane and the support was held in position by screws through the pole-face. The magnet was lined up with the rod and supported by the base frame (see figure 7.6). The magnetic field strength at the centre of the magnet was .03T(300 gauss).

7.3 Electrical Operation

The electrical equipment is shown in figure 7.7 and it consists of the following parts.

7.3.1 Cylinder Control and Trigger Controls

The pneumatic cylinder were controlled by electrical solenoids and two push button switches control the solenoid operation for the firing stroke and the return stroke.

When the fire stroke button was pressed two timing circuits start to work. One timer triggered the oscilloscope to store the trace of the signal for the duration of the movement and it was set to trigger instantaneously. The second timer triggered both digital counter and digital voltmeter and was also used to give a trace on the oscilloscope to show the point at which the recordings were made.

The delay time could be varied by selection of capacitance and changing the variable resistance in the timer circuit, and therefore the time at which the measurements were made could be varied to obtain a satisfactory point during the rod movement.

7.3.2 Speed Measurement

An encoder is keyed to the shaft of one of the gear wheels, this is shown in figure 7.3. The encoder has a disc with 500 lines and gives 2000 pulses for every revolution of the disc. Its rotation is directly linked to the movement of the rod. One revolution of the shaft was equivalent to a linear movement of .381 metres. The timing interval could be selected from a seven position switch which gave factors of ten for each position change and for a given position, four selection dials allowed ranges up to 9999. Therefore the counting time may be found from the following equation:

$$t = (10)^{n-3} (N_1) \qquad (7.1)$$

where t is in ms, n is the position on the seven position switch and N_1 is the selection dial.

The incoming encoder pulses were counted for a given time period and the final number could then be converted to a value representing the speed of the rod.

$$V_m = \frac{(\text{counts in 100ms})}{524.9} \qquad (7.2)$$

where V_m is in m/sec.

Time periods of 100ms were used for the low velocities, where there was enough smooth movement of rod and for higher velocities 50ms and 25ms periods were used.

7.3.3 Signal Amplifier

A differential amplifier was built with a fixed gain and this was calibrated with a standard digital voltmeter. The calibration curve is shown in figure 7.8. The signal picked up by the electrodes was transmitted to the amplifier and then to a digital voltmeter which gave a full scale reading for 199.9mV D.C. The output of the amplifier was also connected to an oscilloscope with a storage facility.

7.3.4 Earth Connections

The earth connections are shown in figure 7.9. All signal earths originated from the amplifier output. The power earths of the triggering circuits, counter and oscilloscope, base frame and aluminium rod all had a common earth. No earth screens were used

between the trigger and oscilloscope.

7.4 Magnetic Field Measurements

In order to predict the performance of the permanent magnet flowmeter it was necessary to measure the magnetic field components (B_r and B_θ) near the pole faces. The field was measured in 10° intervals in the θ-direction and 1.27cm intervals in the z-direction by means of a Hall probe. Figure 7.10 shows the probe and how it was positioned for field measurement.

About a 100mA current was supplied to the probe and the resulting voltage across the probe was measured. The measurement also was carried out by turning the probe 180°, and then the magnetic field was deduced from the average of these two measurements. The probe was calibrated and the calibration factor was found with an accuracy of ±2.6%.

The magnitude of the emf induced in the probe is proportional to the product of the current and the field and was found from the following expression.

$$e_H = \frac{I\ B}{4742} \qquad (7.3)$$

where e_H in mV, I in mA and B in gauss.

The magnetic field components were found from these measured values and were used as boundary values in the numerical solution described in Chapter 4.

7.5 Rod Conductivity

The suppliers of the aluminium bar do not provide a conductivity

value. Measurements were therefore made of the bar conductivity after it was machined and was ready to fit in the rig. A current was passed from one end of the rod to the other end at opposite ends of a diameter. This current was measured using an avometer. The voltage between the two knife edges on which the rod rested, was taken at the same time. Knowing the distance apart of the knife edges and the rod dimensions the value of conductivity was obtained:

$$\sigma_{Al} = 2.93 \times 10^{7} \text{ mho/m}$$

This is 20% less than the conductivity of the pure aluminium.

7.6 Theoretical Prediction

The performance of the flowmeter assembled in the experimental rig was obtained by using the numerical solution in Chapter 4 together with the measured values of the magnetic field components near the pole faces*. Figure 7.11 shows the magnetic field distribution along the aluminium rod for different values of magnetic Reynolds numbers. Figure 7.12 shows the induced voltage distribution along the pipe for various values of magnetic Reynolds numbers. The induced voltage from six electrode locations is shown in figure 7.13. The signal is nearly linear for the position of electrode at 5cm downstream.

7.7 Test Procedure

Tests were run for nine different positions of electrodes along the rod at 2.54cm intervals. For each test a range of speeds was used and for each speed the run was repeated eight times or more. For each new speed, adjustments were made for delay time to ensure

*The theoretical assumed requirement of a distant field boundary will clearly introduce an error for this case.

that the triggering pulse occured at the point in the rod movement at which the output signal was acceptably constant. The photographs were taken of the signal displayed on the oscilloscope to study the signal and its changes during the counting. One of these photographs is shown in figure 7.14.

7.8 Test Results

The results for nine different positions of electrodes are given in tables 7.1 to 7.9. For each position of the electrodes, the tables give the number of counts in 100ms, the signal displayed on the digital voltmeter, velocity, the equivalent magnetic Reynolds number and the output signal of the flowmeter. The results are also plotted in figure 7.15, 7.16 and 7.17 and are compared with the prediction obtained from the analysis of Chapter 4. The best curve is fitted through the results and from this the distribution of the signal along the rod is found for R_m =.5, 1. and 1.5. Figure 7.18 shows the computed distribution and the experimental curve. The distribution of magnetic field along the z-axis at the centre of rod, when there is no movement of rod is shown figure 7.19 and measured values are compared with computed results.

7.9 Experimental Errors

These errors are caused by a number of sources - speed, signal , magnetic field measurements and non-symmetry of the permanent magnet.

7.9.1 Error in Speed Measurement

Belt stretching can be neglected and therefore the rotation of the encoder disc will give an accurate indication of the linear movement of the rod. The counter will produce an error of ±1.2% at low speed and ±.4% at the highest speed. On top of that, an uncertainty of ±2 in the last digit of the counter will give an error of about ±2.3% for the slow runs and ±8% for the highest speed. However each experiment was repeated eight times or more and this would eliminate these errors.

The signal trace had a variation over the period during which pulses were received by the counter. The trace for four different runs is shown in figure 7.14. The picture shows that there is a variation of ±4% in signal for $R_m = 1.5$ and a careful study of the trace during the counting period shows that the average velocity for slow speed, and for $R_m = 2.5$ the trace shows that the signal drop during the counting is 8% and therefore the signal is overestimated by 4%.

7.9.2 Error in Signal Measurement

The digital voltmeter had a full scale input range of 199.9mV with the option of 1 decimal and this produced the error of ±.8% at the lowest speed and ±1% at the highest speed.

7.9.3 Errors in Magnetic Field Measurement

The errors in magnetic field measurement are due to the calibration factor for the Hall probe and positioning the probe during the measurements. The magnetic field is nearly uniform in the magnet gap and it drops outside the gap. The variation of magnetic field components are a maximum at $\theta = 40^{\circ}$ which makes errors a maximum at this point. The error estimated as a results of inaccurately positioning the probe with respect to the magnet in the θ direction is ±1%, in the z-direction ±.4% and in the radial direction ±.14%. The calibration

factor of the Hall probe was found using a standard magnet. There is a change of ±2.6% in magnetic field strength in the gap of a standard magnet, therefore there was an uncertainty of ±2.6% in the calibration factor. The error produced by a standard DVM for reading the current input to the probe was ±.01% while the induced voltage reading gave an error of ±.013%. Hence the total error in magnetic field measurement was ±4.16%. This error will appear in the numerical results, as the measured values were used in the numerical calculations.

7.9.4 Non-Symmetry of the Magnetic Field

The major error was introduced by the shape of the permanent magnet. In the numerical solution a symmetrical imposed magnetic field was assumed and the magnetic field was measured at the surface S (see figure 7.5) and then used as boundary value. The shape of magnet assembly suggests that the magnetic field is not symmetrical, the region near the core of the magnet having a higher magnetic flux density.

The measurements also show that the magentic field at point a is 15% less than that at point b (figure 7.5). Hence it will be realistic to expect the measured values to be about 10% more than the computed values as a result of non-symmetry of the imposed magnetic field.

7.9.5 Error in Conductivity Measurement

The error in the conductivity measurement will result from the error in dimensional measurement of ±.054%, the error of ±.13% in measuring the current and the error of ±1.2% in voltage measurement, giving a total error of ±1.4%.

7.10 Discussion

Figures 7.10, 7.11 and 7.12 show the numerical solution and experimental results. It was stated that the experimental values should be higher than the numerical values, 10% of the difference being due to non-symmetry of the imposed magnetic field. The numerical results were calculated with an accuracy of ±4.16%, while there is an uncertainty in velocity measurement which produces an error of ±2% for R_m = 1.5 and ±1% for R_m = .5. The speed measurement error was more when the measurement was made for R_m greater than 1.5. These measurements were taken at the peak speed of the rod immediately after acceleration (see figure 7.14) and the trace shows that the voltage drop is 8% during the counting. This will cause a 4% overestimation. At slower speeds the measurement was made in the region where the speed was more steady. Although the magnetic Reynolds number which could be reached experimentally was not as high as exists in the FBR where there is high distortion and non-linearity (as shown numerically in figure 7.11 and 7.12), there is a measureable amount of distortion in figure 7.18.

In figure 7.19 the magnetic field distribution is shown and it can be seen that the measured field is higher than the computed value and this was expected due to non-symmetry of magnet.

7.11 Conclusion

The experiments were carried out with an analogue sodium rig, and the experimental results were in good agreement with the computed values. The uncertainty in speed measurement was reduced by repeating the experimental runs more than eight times, but the variation of

speed during measurements produced a ±2% error at high speed and less than ±1% at the lowest speed. The non-symmetry of the imposed magnetic field produced an expected 10% difference between the experimental results and numerical values. The experimental results give confidence in the numerical solution obtained in Chapter 4 which can be used to predict the performance of swept field flow-meters.

CHAPTER 8

PULSED FIELD FLOWMETERS

8.1 Previous Work

Non-contact methods of measuring the velocity and flowrate of liquid metals are well known in magnetohydrodynamic (MHD) measurements and there is a considerable amount of work in the Russian literature. Sermons (1964, 1966), and Sermons and Zheigur (1964) studied the propagation of an electromagnetic field pulse in a moving conducting medium, and showed the possibility of using a pulsed field to measure the flowrate of a conducting fluid.

The flowmeter consists of two coaxial coils spaced along a pipe. The primary coil is supplied by a generator with rectangular current pulses which induce circular currents in the moving conducting liquid. The displacement of the magnetic field lines induced by the currents in turn induce a voltage in the secondary coil due to is decay and due to its motion. The induced signal due to motion is a maximum when the current rings reach the secondary coil. The operating principle of this device can be appreciated from figure 1.4.

Zheigur and Sermons (1965) gave an analytical solution for an induced voltage in the secondary coil, when a step current is applied between two circular circuits in a moving conducting medium:

$$\varepsilon_* = t_*^{-3/2}\, e^{-1/t_*}\, I(1/t_*) \exp\{-\frac{1}{2t_*}(\ell_* - V_* t_*)^2\} \qquad (8.1)$$

where the following quantities are introduced as dimensionless

parameters:

$$\varepsilon_* = \frac{\sigma R_c \varepsilon}{I\sqrt{2\pi}}, \quad t_* = \frac{2t}{\sigma \mu_o R_c^2}, \quad V_* = \frac{1}{2} \sigma \mu_o R_c V_m$$

and $$\ell_* = \frac{\ell}{R_c}$$

The condition for maximization of the function defined by equation 8.1 is:

$$t_* = \frac{\ell_*}{V_*} \qquad \text{or} \qquad t = \frac{\ell}{V} \tag{8.2}$$

The curves plotted in figure 8.1 were calculated from equation 8.1 and they show that relation 8.2 is satisfied with a reasonable degree of accuracy when $V^* \geq 8$ i.e. for a comparatively high value of the magnetic Reynolds number. The reason for this is the time constant of the medium:

$$T = 1/4 \, \mu_o \sigma R_c^2 \tag{8.3}$$

The distance between the coils for the corresponding velocity, V must be chosen with allowance for the time constant of the medium to satisfy the inequality:

$$\ell < VT \tag{8.4}$$

or

$$V_* > 2\ell_* \tag{8.5}$$

Equation 8.2 which enables the velocity of the medium to be determined regardless of the conductivity of the medium is only applied for idealized cases, i.e. when allowance is not made for the velocity distribution, the effect of the channel walls etc. The theoretical investigation of problems in which allowances are made simultaneously for all factors is difficult and has not been tackled before. In this chapter we apply a numerical technique together with a finite difference approximation to solve the problem.

8.2 Governing Equation

Expanding the component of equation 2.34 gives:

$$\frac{\partial^2 A}{\partial r^2} + \frac{1}{r}\frac{\partial A}{\partial r} - \frac{A}{r^2} + \frac{\partial^2 A}{\partial z^2} = -\mu_o J_o(t) + \mu_o \sigma \frac{\partial A}{\partial t}$$

$$- \sigma \mu_o \underset{\sim}{V} \times (\nabla \times \underset{\sim}{A}) \qquad (8.6)$$

If the velocity of the fluid be axisymmetric, $V_z(r)$ then:

$$\frac{\partial^2 A}{\partial r^2} + \frac{1}{r}\frac{\partial A}{\partial r} - \frac{A}{r^2} + \frac{\partial^2 A}{\partial z^2} = -\mu_o J_o(t) + \mu_o \sigma \frac{\partial A}{\partial t}$$

$$+ \mu_o \sigma V_z(r) \frac{\partial A}{\partial z} \qquad (8.7)$$

The term $\sigma \mu_o V_z(r) \frac{\partial A}{\partial t}$ is the only one containing the velocity and is the one responsible for the effect produced by motion. We define $r_1 = r/a$, $z_1 = z/a$ and $t_1 = t/(\mu_o \sigma_f a^2)$ (where σ_f is the conductivity of fluid and a is the radius of the pipe) then we have:

$$\frac{\partial^2 A}{\partial r_1^2} + \frac{1}{r_1}\frac{\partial A}{\partial r_1} - \frac{A}{r_1^2} + \frac{\partial A}{\partial z_1^2} - \mu_o a \sigma V_z(r_1)\frac{\partial A}{\partial z_1} =$$

$$\frac{\sigma(r_1)}{\sigma_f}\frac{\partial A}{\partial t_1} - \mu_o a^2 J_o(t) \qquad (8.8)$$

If $I_o(t)$ is the current in the primary coil, then

$$J_o(t) = \frac{I_o(t)}{a^2 \delta r_1 \delta z_1}$$

where δr_1 and δz_1 are the lattice spacings.

It follows from this that

$$\frac{\partial^2 A}{\partial r_1^2} + \frac{1}{r_1}\frac{\partial A}{\partial r_1} - \frac{A}{r_1^2} + \frac{\partial^2 A}{\partial z_1^2} - \mu_o \sigma a V_z(r_1)\frac{\partial A}{\partial z_1}$$

$$= \frac{\sigma(r_1)}{\sigma_f}\frac{\partial A}{\partial t_1} - \frac{\mu_o I_o(t)}{\delta r_1 \delta z_1} \qquad (8.9)$$

8.3 Boundary Conditions for Thin Wall Channels

It is assumed that the thickness of wall, w is much smaller than the radius of pipe, and therefore, at $r = a$ we have a current sheet with density of J_w. The integral form of Maxwell's equation is:

$$\oint H.dl = \mu_o I \qquad (8.10)$$

Taking a portion of wall with length dz and using equation

8.10 gives:

$$(H_z^{I} - H_z^{II})\,dz = \mu_o\, w\, J_w\, dz \tag{8.11}$$

We know from equation 2.29 that $J_w = \sigma_w(-\frac{\partial A}{\partial t})$ and $H_z = \frac{A}{r} + \frac{\partial A}{\partial r}$, therefore:

$$(H_z^{I} - H_z^{II})_{r = a} = \mu_o\, w\, \sigma_w(-\frac{\partial A}{\partial t}) \tag{8.12}$$

The vector potential is continuous at r = a, i.e.

$$(A^{I})_{r = a} = (A^{II})_{r = a} \tag{8.13}$$

Therefore we obtain the condition at r = a as:

$$\frac{\partial A^{I}}{\partial r_1} - \frac{\partial A^{II}}{\partial r_1} = d(\frac{\partial A}{\partial t_1})_{r = a} \tag{8.14}$$

8.4 Time Marching Solution

The magnetic vector potential is a time dependent variable and to find this the solution must be a function of time as well as z and r-directions. The individual terms in equation 8.9 may be written in finite difference form as:

$$\frac{\partial^2 A(r_1,z_1,t_1)}{\partial r_1^{2}} = \frac{A(r_1 + \delta r_1,z_1,t_1) + A(r_1 - \delta r_1,z_1,t_1) - 2A(r_1,z_1,t_1)}{\delta r_1^{2}}$$

and

$$\frac{\partial^2 A}{\partial z_1^2} = \frac{A(r_1, z_1 + \delta z_1, t_1) + A(r_1, z_1 - \delta z_1, t_1) - 2A(r_1, z_1, t_1)}{\delta z_1^2}$$

and

$$\frac{1}{r_1} \frac{\partial A}{\partial r_1} = \frac{1}{r_1} \frac{A(r_1 + \delta r_1, z_1, t_1) - A(r_1 - \delta r_1, z_1, t_1)}{2\,\delta r_1}$$

and

$$\frac{\partial A}{\partial z_1} = \frac{A(r_1, z_1 + \delta z_1, t_1) - A(r_1, z_1 - \delta z_1, t_1)}{2\,\delta z_1}$$

The time derivative term is:

$$\frac{\partial A}{\partial t_1} = \frac{A(r_1, z_1, t_1) - A(r_1, z_1, t_1 - \tau)}{\tau}$$

where

δr_1 is the size of lattice in r-direction

δz_1 is the size of lattice in z-direction

τ is the time step.

Using these finite difference approximations yields:

$$\frac{A(r_1 + \delta r_1, z_1, t_1) + A(r_1 - \delta r_1, z_1, t_1) - 2A(r_1, z_1, t_1)}{\delta r_1^2} +$$

$$\frac{1}{r_1} \frac{A(r_1 + \delta r_1, z_1, t_1) - A(r_1 - \delta r_1, z_1, t_1)}{2\,\delta r_1} - \frac{A(r_1, z_1, t_1)}{r_1^2}$$

$$+ \frac{A(r_1, z_1 + \delta z_1, t_1) + A(r_1, z_1 - \delta z_1, t_1) - 2A(r_1, z_1, t_1)}{\delta z_1^2}$$

$$- \sigma(r_1) a\, V_z(r_1) \frac{A(r_1, z_1 + \delta z_1, t_1) - A(r_1, z_1 - \delta z_1, t_1)}{2\, \delta z_1}$$

$$= \frac{\sigma(r_1)}{\sigma_f} \left(\frac{A(r_1, z_1, t_1) - A(r_1, z_1, t_1 - \tau)}{\tau} \right) - \frac{\mu_o\, I_o(t)}{\delta r_1\, \delta z_1} \qquad (8.15)$$

and hence

$$A(r_1, z_1, t_1) = (A(r_1 - \delta r_1, z_1, t_1) C_2 + A(r_1 + \delta r_1, z_1, t_1) C_3$$

$$+ A(r_1, z_1 - \delta z_1, t_1) C_4 + A(r_1, z_1 + \delta z_1, t_1) C_5$$

$$+ A(r_1, z_1, t_1 - \tau) C_6 + C_7) / C_1 \qquad (8.16)$$

where

$$C_1 = \frac{2}{\delta r_1^2} + \frac{1}{r_1^2} + \frac{2}{\delta z_1^2} + \frac{\sigma(r_1)}{\sigma_f \tau}$$

$$C_2 = \frac{1}{\delta r_1^2} - \frac{1}{2 r_1\, \delta r_1}$$

$$C_3 = \frac{1}{\delta r_1^2} + \frac{1}{2 r_1\, \delta r_1}$$

$$C_4 = \frac{1}{\delta z_1^2} + \frac{\sigma(r_1) \mu_o\, a\, V_z(r_1)}{2\, \delta z_1}$$

$$C_5 = \frac{1}{\delta z_1^2} - \frac{\sigma(r_1) \mu_o\, a\, V_z(r_1)}{2\, \delta z_1}$$

$$C_6 = \frac{\sigma(r_1)}{\sigma_f\, \tau}$$

$$C_7 = \frac{\mu_o\, I_o(t_1)}{\delta r_1\, \delta z_1}$$

Using the finite difference approximation for the boundary condition at a conducting wall gives:

$$A(r_1,z_1,t_1) = (A(r_1 - \delta r_1,z_1,t_1) + A(r_1 + \delta r_1,z_1,t_1) + \frac{d\,\delta r_1}{\tau} A(r_1,z_1,t_1 - \tau)/(2 + \frac{d\,\delta r_1}{\tau}) \qquad (8.17)$$

The velocity was assumed to be independent of θ, z and t. In solving for this vector potential, it is sufficient to solve the problem in one half plane only, due to the axial symmetry. Equation 8.16 will simplify somewhat depending on the location of the particular point. For example, $V_z = 0$ and $\sigma = 0$ everywhere, except in the medium and conducting wall, $I_o(t) = 0$ everywhere except in the primary coils. Along the boundaries of the mesh the values of A(r,z,t) are held to zero. The magnetic potential along the axis is constant, (for convenience this is taken to be zero), and the remaining boundary should be far enough away to approximate to infinity. The current in the primary coils, $I_o(t)$ can be approximated (in time) to any current wave form. The solution will have to start where $I_o(t)$ is a constant and $\frac{\partial A}{\partial t} = 0$, then the vector potential equation can be solved independent of time with appropriate boundary condition for z and r. The calculations then proceed to values of t where $I_o(t)$ varies. This method of solution in which the results at one time step are used in calculation for the next time step is called a 'time marching' solution as the calculations march with time step by step.

8.5 Computer Results

A computer program has been written which employs the numerical technique explained in chapter 4 together with the finite difference approximation. The program handles the solution of the vector potential equation for a rotationally symmetric system, such as flow of fluids with axisymmetric velocity profiles inside a conducting pipe. The current in the primary coils can be sinusoidal or any other pulse form. The coils can be positioned inside or outside the pipe.

The computer starts at a point in the mesh (see figure 8.2) and works through point by point using the Successive Over Relaxation (S.O.R.) method. The optimization procedure shows that the best relaxation factor is 1.5 for parabolic and 1.6 for uniform velocity profiles. The accuracy of the results depends on the mesh size, the finer the mesh, the greater the accuracy and longer and more expensive the solution.

The computer program is tested against some special cases, e.g. the stationary conductor and two circular coils placed in a moving sodium pool with uniform velocity. The results are in good agreement with the analytical solution of Zheigur and Sermons (1965). For stationary fluid Smythe (1968) gives an expression for the potential induced by a coil with current I and radius R. (This is mentioned by Baker (1977)).

$$A = \frac{\mu I}{\pi R} \left(\frac{R}{r}\right)^{\frac{1}{2}} \left\{ \left(1 - \frac{k^2}{2}\right) K - E \right\} \qquad (8.18)$$

where K and E are complete elliptic integrals of the first and second kind.

$$k^2 = \frac{4Rr}{(R + r)^2 + z^2} \tag{8.19}$$

The Elliptic integrals are given by Dwight (1961) in the form:

$$K = \frac{\pi}{2}(1 + m)\left\{1 + \frac{1^2}{2^2} m^2 + \frac{1^2 . 3^2}{2^2 . 4^2} m^4 + \frac{1^2 . 3^2 . 5^2}{2^2 . 4^2 . 6^2} m^6 + \ldots.\right\} \tag{8.20}$$

and

$$E = \frac{\pi}{2(1 + m)}\left\{1 + \frac{m^2}{2^2} + \frac{1^2}{2^2 . 4^2} m^4 + \frac{1^2 . 3^2}{2^2 . 4^2 . 6^2} + m^6 + \ldots.\right\} \tag{8.21}$$

where $m = (1 - k')/(1 + k')$

and $k' = \sqrt{1 - k^2}$

The induced signal in a coil at radius r is

$$\varepsilon = 2\pi r\left(-\frac{\partial A}{\partial t}\right) \tag{8.22}$$

Calculations show that the induced voltage from equation 8.22 is in good agreement with the computed values from finite difference solutions. The difference is due to errors which arise because of the lattice size.

Figure 8.3 shows the matrix plot of the vector potential at difference time steps, at t = 0 the constant current in the primary induces the magnetic field distribution which is a maximum in the plane of the primary coil. When the current is switched off the circular currents form and move with the fluid. The plot shows the magnetic field moving and damping with time, which is

caused of conductivity of the medium. The higher the conductivity the slower is the damping. The induced voltage can be found from the following expression:

$$\varepsilon = 2\pi r E_{\theta} \tag{8.23}$$

where

$$E_{\theta} = -\frac{\partial A}{\partial t}$$

or

$$\varepsilon = 2\pi r \frac{\partial A}{\partial t}$$

and in finite difference form:

$$\varepsilon = \pi r \frac{(A(r,z,t+\tau) - A(r,z,t-\tau))}{\tau} \tag{8.24}$$

8.6 Flowmeter Design

The design considered consists of three coaxial coils and is illustrated in figure 8.4. The centre coil is the primary or excitation coil. The two end secondary coils are connected together (series opposing), as in a differential transformer arrangement. Because of the symmetry of the system, the output signals of the coils are zero when the fluid is stationary.

If I_o is the primary current, N_p the primary turns and N_s the secondary turns the output signal is:

$$\varepsilon = (\varepsilon_1 - \varepsilon_2)\, N_p\, N_s\, I_o \qquad (8.25)$$

ε_1 and ε_2 are the signal in the secondary coils for unit current pulse in the primary coil. Figure 8. 5 shows how the induced voltage in the secondary system of coils changes with time for different values of magnetic Reynolds numbers. Figure 8.6 shows the induced signal when the velocity is parabolic. The transient time is longer and the signal is smaller for the parabolic velocity profile. The reason is that the signal induced is influenced mostly by the induced current rings near the wall rather than those close to the centre of the pipe. In the flow of a fluid with parabolic velocity profile the velocity of fluid near the wall is less than the average velocity and therefore the induced current rings move slower compared with uniform flow.

The conducting wall will affect the signal by delaying the transient time. The current induced in the wall delays the maximum signal by enforcing the signal in the secondary coil. This effect is shown in figure 8.7 (for d = 0, .0154 and .077).

The characteristics of the flowmeter are shown in figure 8.8 for two extreme cases of velocity profile, parabolic velocity profile which represents laminar flow and uniform velocity profile for turbulent flow. The results show a linear characteristic line but with different slope depending on the velocity profile. The characteristic becomes non-linear at low values of magnetic Reynolds number and this is because decay dominates the response at low R_m. Figure 8.9 exhibits the use of an induced signal as a measure of magnetic Reynolds number, but the characteristic is not linear. The results obtained so far explain how the transit time changes with magnetic Reynolds number. The magnetic Reynolds number is proportional

to fluid conductivity as well as mean velocity. As the electrical conductivity of liquid metals is dependent on temperature (see figure 8.10) this factor must be allowed for when calibrating the meter. In practice, if the measurement is to be made accurately, fluid conductivity needs to be specified at the time of measurement. The technique for finding the conductivity of the fluid is described below. This method can be applied in any system with moving conductive medium for conductivity measurement.

8.7 Eddy Current Method for Conductivity Measurement

If a magnetic field is suddenly applied to a conductor, eddy currents are caused to flow in the conductor. The magnetic field created by these currents is in opposition to the externally applied field. The induced field damps with time, and the rate of damping is a function of the conductivity of the conductor. The higher the conductivity of the medium the slower the damping of the magnetic field. This method is described by Bean et al (1959) for measuring the resistivity of metallic specimens. The measurement is made by noting the rate of decay of flux from a bar situated in an external magnetic field that has been rapidly reduced to zero (see figure 8.11).

Nagao and Ishibashi (1976) used the same method to measure the resistivity of NaCl solution, an alternative to the Kohlaush-Bridge method which is more commonly used.

For a moving conducting medium the common practice for conductivity measurement is to employ an alternating field. This has limitations as a result of skin effect. It is shown that the eddy current method may equally be applied for the conductivity measurement of a

moving medium. The sudden change of field in the primary coil induces eddy currents in the moving liquid and the eddy currents induce a signal in any circular coil perpendicular to the flow due to is motion and decay. The signal produced by motion has a positive sign downstream of the eddy current and negative sign upstream, while the part of the signal due to the decay is always positive. By placing a solenoid around the pipe the induced signal along the pipe may be integrated and therefore the part of the signal induced by motion will vanish. The final signal will be a function of conductivity.

The equation of vector potential in a fluid region was (see figure 8.12):

$$\frac{\partial^2 A_1}{\partial r^2} + \frac{1}{r}\frac{\partial A_1}{\partial r} - \frac{A_1}{r^2} + \frac{\partial^2 A_1}{\partial z^2} = \mu_o \sigma_f V_z \frac{\partial A_1}{\partial z} + \mu_o \sigma_f \frac{\partial A_1}{\partial t} \qquad (8.26)$$

defining

$$\overline{A} = \int_{-\infty}^{+\infty} A \, dz \qquad (8.27)$$

to be an integral transform of the vector potential, and applying this in equation 8.26 gives:

$$\frac{\partial^2 \overline{A_1}}{\partial r^2} + \frac{1}{r}\frac{\partial \overline{A_1}}{\partial r} - \frac{\overline{A}}{r^2} = \mu_o \sigma_f \frac{\partial \overline{A_1}}{\partial t} \qquad (8.28)$$

where the first term on the right hand side of equation 8.26 is dropped as its integral is zero.

The first derivatives of the vector potential is zero at $z = \pm\infty$ (remote from the primary coils), and the vector potential is

constant at $z = \pm\infty$ and is assumed to be zero. The output signal from the solenoid is of the form:

$$\bar{\varepsilon} = \int_{-\infty}^{+\infty} \varepsilon \, dz \tag{8.29}$$

or

$$\bar{\varepsilon} = - 2\pi R \frac{\partial \bar{A}}{\partial t} \tag{8.30}$$

Let

$$\bar{\bar{A}} = \int_{o}^{\infty} \bar{A} \, e^{-st} \, d t \tag{8.31}$$

be the Laplace transformation of $\bar{A}$, using this transformation in equation 8.28 gives:

$$\frac{\partial^2 \bar{\bar{A}}_1}{\partial r^2} + \frac{1}{r} \frac{\partial \bar{\bar{A}}_1}{\partial r} - \frac{\bar{\bar{A}}_1}{r^2} = \sigma_f \mu_o S \, \bar{\bar{A}}_1 \tag{8.32}$$

This equation for region 2 and 3 outside the pipe where the conductivity is zero becomes:

$$\frac{\partial^2 \bar{\bar{A}}_2}{\partial r^2} + \frac{1}{r} \frac{\partial \bar{\bar{A}}_2}{\partial r} - \frac{\bar{\bar{A}}_2}{r^2} = 0 \tag{8.33}$$

Hence, the equation for the vector potential in the fluid region is:

$$\frac{\partial^2 \bar{\bar{A}}_1}{\partial r^2} + \frac{1}{r} \frac{\partial \bar{\bar{A}}_1}{\partial r} - (\gamma^2 + \frac{1}{r^2}) \bar{\bar{A}}_1 = 0 \qquad (8.34)$$

where

$$\gamma^2 = \sigma_f \mu_o S$$

The general solution of equation 8.34 has the form

$$\bar{\bar{A}}_1 = C_1 I_1 (\gamma r) + C_2 K_1 (\gamma r) \qquad (8.35)$$

The value of K_1 leads to infinity as $r \to 0$, hence C_2 must be zero. The solution of the differential equation 8.33 for region 2 and 3 is:

$$\bar{\bar{A}}_2 = C_3 r + \frac{C_4}{r} \qquad (8.36)$$

and

$$\bar{\bar{A}}_3 = C_5 r + \frac{C_6}{r} \qquad (8.37)$$

For $r \to \infty$ the value of A_3 becomes infinite and hence C_5 must be zero.

$$\bar{\bar{A}}_3 = \frac{C_6}{r} \qquad (8.38)$$

8.7.1 Boundary Conditions

The vector potential is continuous at r = a and r = R_c, i.e.

$$\bar{\bar{A}}_1 \Big|_{r = a} = \bar{\bar{A}}_2 \Big|_{r = a}$$

and

$$\bar{\bar{A}}_2 \Big|_{r = R_c} = \bar{\bar{A}}_3 \Big|_{r = R_c}$$

for non-conducting channel walls we have

$$\frac{1}{r} \frac{\partial (r\bar{\bar{A}}_1)}{\partial r} \Big|_{r = a} = \frac{1}{r} \frac{\partial (r\bar{\bar{A}}_2)}{\partial r} \Big|_{r = a}$$

The boundary condition at the primary coil is

$$\frac{1}{r} \frac{\partial}{\partial r} (r\bar{\bar{A}}_2) \Big|_{r = R_c} - \frac{1}{r} \frac{\partial}{\partial r} (r\bar{\bar{A}}_3) \Big|_{r = R_c} = \mu_o J_o(t) \delta(z) \qquad (8.39)$$

Using the transformation for z we obtain

$$\frac{1}{r} \frac{\partial}{\partial r} (r\bar{\bar{A}}_2) \Big|_{r = R_c} - \frac{1}{r} \frac{\partial}{\partial r} (r\bar{\bar{A}}_3) \Big|_{r = R_c} = \frac{\mu_o N_p I_o(t)}{S} \qquad (8.40)$$

where $J_o(t)$ is the current density, $I_o(t)$ is the current in the primary coil and N_p is the number of turns in the primary coil.

The Laplace tranformation of equation 8.40 becomes:

$$\frac{1}{r}\frac{\partial}{\partial r}(r\bar{\bar{A}}_2)\Big|_{r=R_c} - \frac{1}{r}\frac{\partial}{\partial r}(r\bar{\bar{A}}_3)\Big|_{r=R_c} = \frac{\mu_o N_p I_o}{S} \tag{8.41}$$

The current density in the primary is taken to be a step function. Applying the boundary conditions leads to:

$$C_1 I_1(\gamma a) = C_3 a + \frac{C_4}{a}$$

$$C_1 \frac{\partial I_1(\gamma r)}{\partial r}\Big|_{r=a} = C_3 - \frac{C_4}{a^2}$$

$$C_3 R_c + \frac{C_4}{R_c} = \frac{C_6}{R_c}$$

$$C_3 - \frac{C_4}{R_c} + \frac{C_6}{R_c} = \frac{\mu_o I_o N_p}{S}$$

Solving the above equations gives C_1, C_3, C_4 and C_6:

$$C_1 = \frac{\mu_o I_o N_p}{S}\left(\frac{1}{\frac{I_1(\gamma a)}{a} + \frac{\partial I_1(\gamma r)}{\partial r}\Big|_{r=a}}\right) \tag{8.42}$$

$$C_3 = \frac{\mu_o I_o N_p}{2S} \tag{8.43}$$

$$C_4 = \frac{\mu_o I_o N_p}{S}\left(\frac{a^2 I_1(\gamma a)}{I_1(\gamma a) + a\frac{\partial I_1(\gamma r)}{\partial r}\Big|_{r=a}} - \frac{a^2}{2}\right) \tag{8.44}$$

$$C_6 = \frac{\mu_o I_o N_p}{S}\left(\frac{a^2 I_1(\gamma a)}{I_1(\gamma a) + a\frac{\partial I_1(\gamma r)}{\partial r}\Big|_{r=a}} - \frac{a^2}{2} + \frac{R_c^2}{2}\right) \tag{8.45}$$

Finally the equations for the transformed vector potential in region 1, 2 and 3 are:

$$\bar{\bar{A}}_1(s) = \frac{\mu_o I N_p}{S} \left(\frac{a I_1(\gamma a)}{I_1(\gamma a) + a \left. \frac{\partial I_1(\gamma r)}{\partial r} \right|_{r=a}} \right) I_1(\gamma r) \qquad (8.46)$$

and

$$\bar{\bar{A}}_2(s) = \frac{\mu_o I_o N_p}{2S} r + \frac{\mu_o I_o N_p}{Sr} \left(\frac{a^2 I_1(\gamma a)}{I_1(\gamma a) + a \left. \frac{\partial I_1(\gamma r)}{\partial r} \right|_{r=a}} - \frac{a^2}{2} \right) \qquad (8.47)$$

and

$$\bar{\bar{A}}_3(s) = \frac{\mu_o I_o N_p}{Sr} \left(\frac{a^2 I_1(\gamma a)}{I_1(\gamma a) + a \frac{\partial I_1(\gamma r)}{\partial r}_{r=a}} - \frac{a^2}{2} + \frac{R_c^2}{2} \right) \qquad (8.48)$$

The induced signal in the solenoid may be found by the inverse Laplace tranform of $\bar{\bar{A}}(s)$ and the methods of complex variable theory.

$$\bar{A} = \frac{1}{2\pi i} \lim_{T \to \infty} \int_{c-iT}^{c+iT} e^{st} \bar{\bar{A}}(s) \, dS \qquad (8.49)$$

where c is chosen so that all the singular points of $\bar{\bar{A}}(s)$ lie to the left of the line $R_e(s) = c$ in the complex plane.

The inverse Laplace transform of $\bar{\bar{A}}(s)$ is difficult to find and it is in a complicated form, while the numerical solution of equation 8.28 is easier to obtain. Here the induced signal distribution

obtained in section 8.5 has been integrated in z-direction to find the signal induced in solenoid for conductivity measurement. The results show that the signal in the solenoid is not affected by velocity, and has only one non-dimensional plot which is shown in figure 8.13. Therefore the conductivity of the medium can be found from this curve and knowing the magnetic Reynolds number from previous calculations the mean velocity can be obtained. Figure 8.14 illustrated the flowmeter which provides the mean velocity and fluid conductivity.

8.8 Conclusions

The pulsed field flowmeter has been analysed and a time marching solution given using the finite difference approximations and S.O.R. methods. The effects of wall conductivity and fluid velocity profile are considered.

The results show that the flowmeter with one primary and two secondary coils gives the flowrate of fluid but its performance is dependent on the velocity profile and the temperature of fluid flow. The flowmeter shown in figure 8.14 is designed to cancel the temperature dependence and it is capable of measuring the magnetic Reynolds number and conductivity of fluid flow.

CHAPTER 9

CONCLUSIONS AND FURTHER WORK

In this thesis electromagnetic flowmeters are reviewed and analysed. The following problems exist in their design and calibration;

a) Variations in calibration due to changes in the permeability of the fluid.

b) Short axial length transverse field flowmeters, when used in a flow with high R_m, suffer from field sweeping. This sweeping produces a non-linear output signal from electrodes positioned in the mid-plane of the flowmeter.

c) Variations in calibration due to changes in contact resistance between the fluid and the pipe wall.

The first problem exists in electromagnetic flowmeters with magnetic slurries. In Chapter Three a long flowmeter with concentric pole-pieces was examined and a solution given for the induced signal and magnetic distribution signal varies with changes of permeability. It was found that using a search coil positioned in the insulating liner to act as a reference, gives a constant signal for changing fluid permeability, and an almsot constant one for a limited range of axisymmetric velocity profiles. The solution was found for uniform fluid permeability in the fluid-region, but in practice a non-uniform distribution of permeability may occur, and also the conductivity may be high enough to affect the imposed magnetic field. Therefore the numerical solution may be applied to more general cases by taking into account the non-uniform permeability, effect of conductivity and the length of the applied magnetic field.

Swept field flowmeters were analysed in Chapter Four where the magnetic field and flowmeter equations were solved numerically in three-dimensions, using a cylindrical co-ordinate system and taking into account the effect of magnetic Reynolds number. The flow was assumed to be rectilinear in a thin conducting pipe ($\frac{w\sigma_w}{a\sigma_f} << 1$) with a constant contact resistance between the pipe wall and the fluid. The numerical solution uses a finite difference approximation with S.O.R. The computer program (SWEPT) can deal with a symmetrically imposed magnetic field, and requires the distribution of the imposed magnetic field at the surface, (r = b) as a boundary condition. The magnetic field at this surface is assumed to be unaffected by the flow of the fluid. This assumption produces some error, however, the estimated error in Chapter Four where b = 3a and R_m = 5 was less than 1.7%.

The performance of a swpet field flowmeter was found for three different types of imposed magnetic fields (saddle coil, diamond coil, and permanent magnet). The results show that high values of R_m sweep the imposed magnetic field downstram and produce a non-linear signal for point electrodes positioned at the mid-plane. The results also show that for electrodes positioned one pipe diameter downstream the signal is nearly linear for magnetic Reynolds numbers from 0 to 5 (see figures 4.18, 4.22 and 7.13).

The weight function is more useful in designing a flowmeter, the aim being to find a flowmeter with a uniform weight function. Changes in electrode shape and field configuration can produce this uniform weight function. This is the first time that weight function theory has been applied to the swept field flowmeter. The weight function distribution is affected by the magnetic Reynolds number. In Chapter Five the weight vector is derived for similar conditions specified in Chapter Four (rectilinear flow, thin wall, constant contact

resistance). A numerical solution is obtained using a finite difference approximation with S.O.R. The weight function distribution is found for different electrode positions along the pipe. The results show that the weight function is dependent on R_m, but for electrodes displaced one diameter downstream the weight function distribution becomes unchanged for R_m over the range from 0 to 5.

The computer program can be used to find a uniform weight function by changing the electrodes shape and field configuration. The results obtained by the weight function solution are a check for results obtained by direct solution of the flowmeter equation. The weight function distributions show that;

(i) a diamond coil flowmeter has a more uniform weight function compared to a saddle coil flowmeter.

(ii) a flowmeter with a conducting wall has a more uniform weight function than one with a non-conducting wall.

This shows that the flowmeter with large electrodes and a tailored field can give a uniform weight function. Experiments carried out on the swept field flowmeter are described in Chapter Seven, where an aluminium rod was used to simulate the uniform flow domain. Although the experiments were for low values of R_m (less than 2), the results showed good agreement with the numerical predictions. More experimental work can be carried out with the actual sodium rig for higher values of R_m to confirm the theoretical work. -

The swept field flowmeter has the advantage of a short axial length but suffers from conductivity dependence. To overcome the latter disadvantage an integrated voltage flowmeter was designed (patent 119243). This design of flowmeter has a short imposed magnetic field and electrodes integrating the signal in the flow direction. The signal

is independent of the conductivity of the liquid. The theory of this flowmeter is given in Chapter Six. It was discovered that if all the quantities in the flowmeter equation (2.12) were integrated in the flow direction ($\overline{U} = \int_{-\infty}^{+\infty} U dz$) then the form of the flowmeter equation is the same as that of the flowmeter equation for low conductivity fluids in two-dimensions. The importance of this observation is that this equation is susceptible to all the analytical techniques used for the two-dimensional form of the equation.

The practical consequences are:

a) The signal from the flowmeter is not affected by conductivity of the fluid.

b) The signal is a linear function of the flowrate and is dependent on velocity profile.

c) It may be possible to optimise the magnetic field distribution and electrode shape in the cross-sectional plane, so that such a flowmeter has a low sensitivity to changes in flow profile.

An alternative design is given in Chapter Six, in which a search coil is placed in the liner as a reference, and electrodes integrating the signal along the pipe (see figure 6.1). This flowmeter can operate for fluids with a wide range of conductivity and permeability and gives a linear signal with flowrate.

The last type of flowmeter which has been anlysed is a pulsed field flowmeter. A time marching solution is given using a finite difference approximation with S.O.R. The computer program (ECFM) is written for this numerical solution. It is assumed that the flow is rectilinear in a thin conducting pipe. A design with a primary and two secondary coils spaced symmetrically on either side of the primary, gives an output signal dependent on the velocity profile and conductivity of

the fluid. It is shown that by integrating the vector potential equation in the z-direction ($\bar{A} = \int_{-\infty}^{+\infty} A dz$), we obtain an equation which has no velocity term. The induced signal ($\bar{\varepsilon} = \int_{-\infty}^{+\infty} \varepsilon dz$) obtained from this equation is not velocity dependent and is a function of the conductivity of the fluid. Therefore a solenoid was placed around the pipe to integrate the induced signal along the pipe. The output signal of this solenoid was used to calculate the conductivity of the fluid (see figure 8.13). The magnetic Reynolds number was found from the three coil arrangement and hence the flowrate can be found. The disadvantage of this flowmeter is its velocity profile dependence, this can be seen in figure 8.8.

APPENDIX A

CALCULATION OF INDUCED MAGNETIC FIELD FOR SADDLE-TYPE COILS (CONCENTRIC)

In the saddle coils flowmeter the magnetic field is generated by two saddle shaped, series connected, air cored coils, supplied with a constant current and installed around the liquid metal containing duct. A special coil former in two separable halves supports the coil cables. The coils are fitted diametrically opposite to each other over the duct and work in relatively cool ambient conditions (see figure A.1). The calculations of field distribution were made for a coil with finite length and the windings replaced by a cylindrical conductor at β_o (angle of coil). The magnetic induction due to a current flowing in the conductor can be calculated using Biot-Savart's law for each part of the conductor.

Biot-Savart's law for magnetic induction due to a current NI, flowing in a conductor of length ds at a point $P(\rho,\phi,z)$ illustrated in figure A.2 is defined as:

$$\underset{\sim}{dB} = \frac{\mu_o NI}{4\pi} \frac{\underset{\sim}{ds} \times \underset{\sim}{r}_1}{|r^2|} \qquad (A.1)$$

or

$$\underset{\sim}{dB} = -\frac{\mu_o NI}{4\pi} \frac{\underset{\sim}{ds} \times \underset{\sim}{r}}{|r^3|} \qquad (A.2)$$

where the variables are

$\underset{\sim}{ds}$ = an element of conductor carrying current NI

$\underset{\sim}{dB}$ = induced magnetic field at point $P(\rho,\phi,z)$

$\underset{\sim}{r}_1$ = unit vector directed toward point $P(\rho,\phi,z)$ at point $M(R_c,\beta,z')$

$\underset{\sim}{r}$ = vector joining P to M

I = electrical current

N = number of turns per coil element

Applying the above law to part 5 of conductor gives the result:

$$\underset{\sim}{ds} = (R_c\, d\beta\, \cos\beta)\, i - (R_c\, d\beta\, \sin\beta)\, j \qquad (A.3)$$

Where R_c is the radius of saddle coils and

$$\underset{\sim}{r} = (R_c \sin\beta - \rho \sin\phi)\, i + (R_c \cos\beta - \rho \cos\phi)\, j + (L - z)\, k \qquad (A.4)$$

Rearranging equations A.2, A.3 and A.4 gives the following equation for $\underset{\sim}{dB}$

$$\underset{\sim}{dB} = \frac{-\mu_o NI}{4\pi} \frac{(R_c\, d\beta \cos\beta\, i - R_c\, d\beta \sin\beta\, j) \times \{(R_c \sin\beta - \rho \sin\phi)\, i + (R_c \cos\beta - \rho \cos\phi)\, j + (L - z)\, k\}}{\{(R_c \sin\beta - \rho \sin\phi)^2 + (R_c \cos\beta - \rho \cos\phi)^2 + (L - z)^2\}^{3/2}} \qquad (A.5)$$

alternatively it can be written as,

$$\underset{\sim}{dB} = \frac{\mu_o NI}{4\pi} \frac{R_c \sin\beta\, (L - z)\, d\beta\, i + R_c \cos\beta\, (L - z)\, d\beta\, j - (R_c^2 - \rho R_c \cos(\beta - \phi))\, d\beta\, k}{\{(R_c \sin\beta - \rho \sin\phi)^2 + (R_c \cos\beta - \rho \cos\phi)^2 + (L - z)^2\}^{3/2}} \qquad (A.6)$$

Introducing the following definitions, equation A.6 can be rewritten, giving equation A.7

$$\rho_1 = \frac{\rho}{R_c}$$

$$\ell = \frac{L}{R_c}$$

and $$z_1 = \frac{z}{R_c}$$

Therefore:

$$\underset{\sim}{dB} = \frac{\mu_o NI}{4\pi R_c} \frac{\mathrm{Sin}\beta(\ell - z_1)d\beta\ i + \mathrm{Cos}\beta(\ell - Z_1)d\beta\ j - (1 - \rho_1\mathrm{Cos}(\beta - \phi)d\beta\ k}{\{(\mathrm{Sin}\beta - \rho_1\mathrm{Sin}\phi)^2 + (\mathrm{Cos}\beta - \rho_1\mathrm{Cos}\phi)^2 + (\ell - z_1)^2\}^{3/2}} \tag{A.7}$$

To find the magnitude of the induced magnetic field from part 5 of conductor at point P we integrate over the angle β from β_o to $\pi - \beta_o$:

$$\underset{\sim}{B}_5 = \frac{\mu_o NI}{4\pi R_c} \int_{\beta_o}^{\pi - \beta_o} \left\{ \frac{\mathrm{Sin}\beta(\ell - Z_1)i + \mathrm{Cos}\beta(\ell - z_1)j - (1 - \rho_1\mathrm{Cos}(\beta - \phi))\ k}{\{(\mathrm{Sin}\beta - \rho_1\mathrm{Sin}\phi)^2 + (\mathrm{Cos}\beta - \rho_1\mathrm{Cos}\phi)^2 + (\ell - z_1)^2\}^{3/2}} \right\} d\beta \tag{A.8}$$

$\underset{\sim}{B}_6$, $\underset{\sim}{B}_7$ and $\underset{\sim}{B}_8$ induced field at point P by parts of conductor which is curved at $z = \pm L$ can be found by substitution of the following expressions into equation A.8

$\underset{\sim}{B}_5$	$\underset{\sim}{B}_6$	$\underset{\sim}{B}_7$	$\underset{\sim}{B}_8$
I	-I	-I	I
$\beta_o<\beta<\pi-\beta_o$	$\beta_o<\beta<\pi-\beta_o$	$\pi+\beta_o<\beta<2\pi-\beta_o$	$\pi+\beta_o<\beta<2\pi-\beta_o$
$\ell=\ell$	$\ell=-\ell$	$\ell=\ell$	$\ell=-\ell$

Therefore the magnetic induction at point $P(\rho,\phi,z)$ by the parts of the conductor at $z_1 = \pm\ell$ will be

$$\underset{\sim}{B} = \underset{\sim}{B}_5 + \underset{\sim}{B}_6 + \underset{\sim}{B}_7 + \underset{\sim}{B}_8 \qquad (A.9)$$

Now the magnetic induction from the straight parts of conductor may be calculated. It follows that:

$$\underset{\sim}{ds} = dz'\ k \text{ and } M(R_c\ \mathrm{Sin}\beta_o,\ R_c\ \mathrm{Cos}\beta_o,\ z')$$

Because

$$\underset{\sim}{r} = (R_c\mathrm{Sin}\beta_o - \rho\mathrm{Sin}\phi)\,i + (R_c\mathrm{Cos}\beta_o - \rho\mathrm{Cos}\phi)\,j + (z'-z)\,k \qquad (A.10)$$

and using the Biot-Savart law it follows that:

$$\underset{\sim}{dB} = \frac{\mu_o NI}{4\pi}$$

$$\frac{(R_c \, Cos\beta_o - \rho Cos\phi)\, i \, dz' - (R_c \, Sin\beta_o - \rho Sin\phi)\, j \, dz'}{\{(R_c \, Sin\beta_o - \rho Sin\phi)^2 + R_c \, Cos\beta_o - \rho Cos\phi)^2 + (z' - z)^2\}^{3/2}}$$

(A.11)

The magnetic induction by part 1 of the conductor at point P is the integral of above equation from -L to +L.

$$\underset{\sim}{B}_1 = \frac{\mu_o NI}{4\pi} \int_{-L}^{L}$$

$$\left\{\frac{(R_c \, Cos\beta_o - \rho Cos\phi)\, i - (R_c \, Sin\beta_o - \rho Sin\phi)\, j}{\{(R_c \, Sin\beta_o - \rho Sin\phi)^2 + (R_c \, Cos\beta_o - \rho Cos\phi)^2 + (z' - z)^2\}^{3/2}}\right\} dz'$$

(A.12)

substituting for $z'_1 = z'/R_c$ and the other dimensions defined as before it follows that

$$\underset{\sim}{B}_1 = \frac{\mu_o NI}{4\pi R_c} \int_{-\ell}^{+\ell}$$

$$\left\{\frac{(Cos\beta_o - \rho_1 Cos\phi)\, i - (Sin\beta_o - \rho_1 \, Sin\phi)\, j}{\{(Sin\beta_o - \rho_1 Sin\phi)^2 + (Cos\beta_o - \rho_1 Cos\phi)^2 + (z'_1 - z_1)^2\}^{3/2}}\right\} dz'$$

(A.13)

The result of the integration is

$$\underset{\sim}{B}_1 = \frac{\mu_o NI}{4\pi R_c} \frac{(B_1\, i - A_1\, j)}{(A_1^2 + B_1^2)} \left\{ \frac{E_1}{(A_1^2 + B_1^2 + E_1^2)^{\frac{1}{2}}} + \frac{E_2}{A_1^2 + B_1^2 + E_2^2)^{\frac{1}{2}}} \right\} \qquad (A.14)$$

where

$$E_1 = \ell + z_1$$

$$E_2 = \ell - z_1$$

$$A_1 = \mathrm{Sin}\beta_o - \rho_1 \mathrm{Sin}\phi$$

$$A_2 = \mathrm{Sin}\beta_o + \rho_1 \mathrm{Sin}\phi$$

$$B_1 = \mathrm{Cos}\beta_o - \rho_1 \mathrm{Cos}\phi$$

$$B_2 = \mathrm{Cos}\beta_o + \rho_1 \mathrm{Cos}\phi$$

$\underset{\sim}{B}_2$, $\underset{\sim}{B}_3$ and $\underset{\sim}{B}_4$ can be calculated from the following alternatives in equation A.14,

$\underset{\sim}{B}_1$	$\underset{\sim}{B}_2$	$\underset{\sim}{B}_3$	$\underset{\sim}{B}_4$
I	-I	-I	I
$\beta_o = \beta_o$	$\beta_o = \pi - \beta_o$	$\beta_o = \pi + \beta_o$	$\beta_o = 2\pi - \beta_o$

The total magnetic induction at point $P(\rho,\phi,z)$ by the saddle coil is the sum of the fields induced by the individual parts of the conductor, i.e.

$$\underset{\sim}{B} = \sum_{i=1}^{8} \underset{\sim}{B}_i \qquad (A.15)$$

The calculations were made for coil diameter 1.067m and pipe diameter .356m and coil half length .356m. The electrical current in winding was 110 amps and number of windings per coil element was 26. The results are plotted in figure A.3 through A.6.

Figure A.3 shows the magnetic field distribution along z-axis at the centre of the saddle coil for three coil angles. The magnetic field distribution along z-axis at $\phi = \pi/2$ and $R = 2.7a$ is shown in figure A.4. The values of magnetic field at this surface were used as boundary value for finite difference calculations, and it was assumed that it is not affected by the flow of fluid. Figure A.5 shows the magnetic field distribution at $z = 0$, along y-axis and figure A.6 shows the distribution along x-axis.

APPENDIX B

CALCULATION OF MAGNETIC FIELD DISTRIBUTION OF SADDLE-TYPE COILS

These coils are illustrated in figure B.1 and the calculations of field distribution were made for a coil with finite length and the windings replaced by continuous current sheets. The top and bottom part of each is divided into four elements to make the calculations easier (see figure B.2).

N is the total number of coil turns and are placed in the θ-direction as shown in figure B.3. Therefore β_c is:

$$\beta_c = \frac{d_w N_1}{R_c} \tag{B.1}$$

where R_c is the radius of coil and d_w is the diameter of the cable. The model is considered as a conductor with thickness of $n_1 d_w$ in the r-direction and current density of J in the z-direction which can be calculated as

$$IN = J d_w \beta_c R_c n_1 \tag{B.2}$$

or

$$J = \frac{I}{d^2_w} \tag{B.3}$$

If L is the half length of the coil winding in the z-direction for the winding placed at angle β_o and L_o is the half length of the coil winding in z-direction for the winding placed at angle $\beta_o + \beta_c$ then:

$$L_o = L - \frac{\beta_c R_c n_1}{n_2} \tag{B.4}$$

Biot-Savart's law for a magnetic field induced by element $d\tau$ with current density of J at point $P(\rho,\phi,z)$ is:

$$\underset{\sim}{dB} = \frac{\mu_o}{4\pi} \frac{\underset{\sim}{J} \times \underset{\sim}{r}_1}{|r^2|} \quad d\tau \tag{B.5}$$

where

$$d\tau = (R_c n_1 d_w)\, d\beta\, dz' \tag{B.6}$$

The co-ordinate of the volume element $(d\tau)$ is

$$M(R_c,\beta,z')$$

Therefore:

$$\underset{\sim}{r} = \underset{\sim}{PM} = (R_c \operatorname{Sin}\beta - \rho \operatorname{Sin}\phi)i + (R_c \operatorname{Cos}\beta - \rho \operatorname{Cos}\phi)j + (z' - z)k \tag{B.7}$$

and

$$\underset{\sim}{r}_1 = \frac{-\underset{\sim}{r}}{|\underset{\sim}{r}|} \tag{B.8}$$

where

$$|\underset{\sim}{r}| = \{(R_c \operatorname{Sin}\beta - \rho \operatorname{Sin}\phi)^2 + (R_c \operatorname{Cos}\beta - \rho \operatorname{Cos}\phi)^2 + (z' - z)^2\}^{\frac{1}{2}} \tag{B.9}$$

It therefore follows that:

$$\underset{\sim}{dB} = \frac{-\mu_o J k}{4\pi} \times$$

$$\frac{\{(R_c \sin\beta - \rho \sin\phi) i + (R_c \cos\beta - \rho \cos\phi) j + (z' - z) k\} R_c n_1 d_w d\beta dz'}{\{(R_c \sin\beta - \rho \sin\phi)^2 + (R_c \cos\beta - \rho \cos\phi)^2 + (z' - z)^2\}^{3/2}}$$

(B.10)

or

$$\underset{\sim}{dB} = \frac{\mu_o J}{4\pi}$$

$$\frac{\{(R_c \cos\beta - \rho \cos\phi) i - (R_c \sin\beta - \rho \sin\phi) j\ R_c d_w n_1 d\beta dz'}{\{(R_c \sin\beta - \rho \sin\phi)^2 + (R_c \cos\beta - \rho \cos\phi)^2 + (z' - z)^2\}^{3/2}}$$

(B.11)

Substituting the non-dimensional parameters in equation B.11 leads to:

$$\underset{\sim}{dB} = \frac{\mu_o J d_w n_1}{4\pi R_c}$$

$$\frac{\{(\cos\beta - \rho_1 \cos\phi) i + (\sin\beta - \rho_1 \sin\phi) j\}\ d\beta\ dz_1'}{\{(\sin\beta - \rho_1 \sin\phi)^2 + (\cos\beta - \rho_1 \cos\phi)^2 + (z_1' - z_1)\}^{3/2}}$$

(B.12)

Using the value of J from equation (B.3) gives:

$$\underset{\sim}{dB} = \frac{\mu_o NI}{4\pi \beta_c R_c}$$

$$\frac{\{(\cos\beta - \rho_1\cos\phi)\,i - (\sin\beta - \rho_1\sin\phi)\,j\}\,d\beta\,dz_1'}{\{(\sin\beta - \rho_1\sin\phi)^2 + (\cos\beta - \rho_1\cos\phi)^2 + (z_1' - z_1)^2\}^{3/2}} \tag{B.13}$$

To find the induced magnetic field by element (1) of the top winding, equation (B.13) is integrated giving,

$$\underset{\sim}{B}_1 = \frac{\mu_o NI}{4\pi \beta_c R_c} \int_{\beta_o}^{\beta_o + \beta_c} \int_{-\ell_z}^{\ell_z}$$

$$\frac{\{(\cos\beta - \rho_1\cos\phi)\,i - (\sin\beta - \rho_1\sin\phi)\,j\}\,d\beta\,dz_1'}{\{(\sin\beta - \rho_1\sin\phi)^2 + (\cos\beta - \rho_1\cos\phi)^2 + (z_1' - z_1)^2\}^{3/2}} \tag{B.14}$$

where ℓ_z is the half length of the cable which is placed at an angle of β and can be obtained from the following relation:

$$\ell_z = \frac{n_1}{n_2}\beta + \ell + \frac{n_1}{n_2}\beta_o \tag{B.15}$$

After integrating the following expression is obtained:

$$\underset{\sim}{B}_1 = \frac{\mu_o NI}{4\pi \beta_c R_c} \int_{\beta_o}^{\beta_o + \beta_c}$$

$$\frac{\{(\cos\beta - \rho_1\cos\phi)\,i - (\sin\beta - \rho_1\sin\phi)\,j\}}{\{(\sin\beta - \rho_1\sin\phi)^2 + (\cos\beta - \rho_1\cos\phi)^2\}}$$

$$\{\frac{\ell_z - z_1}{\{(\mathrm{Sin}\beta - \rho_1\mathrm{Sin}\phi)^2 + (\mathrm{Cos}\beta - \rho_1\mathrm{Cos}\phi)^2 + (\ell_z - z_1)^2\}^{\frac{1}{2}}} +$$

$$\frac{\ell_z + z_1}{\{(\mathrm{Sin}\beta - \rho_1\mathrm{Sin}\phi)^2 + (\mathrm{Cos}\beta - \rho_1\mathrm{Cos}\phi)^2 + (\ell_z + z_1)^2\}^{\frac{1}{2}}}\}d\beta \qquad (B.16)$$

$\underset{\sim}{B}_2$, $\underset{\sim}{B}_3$ and $\underset{\sim}{B}_4$ can be found by substitution of the following expression into equation B.16 in turn.

$\underset{\sim}{B}_1$	$\underset{\sim}{B}_2$	$\underset{\sim}{B}_3$	$\underset{\sim}{B}_4$
I	-I	-I	I
$\ell_z = \frac{n_1}{n_2}\beta + \ell + \frac{n_1}{n_2}\beta_o$	$\ell_z = \frac{n_1}{n_2}\beta + \ell - \frac{n_1}{n_2}(\pi - \beta_o)$	$\ell_z = \frac{n_1}{n_2}\beta + \ell + \frac{n_1}{n_2}(\pi + \beta_o)$	$\ell_z = \frac{n_1}{n_2}\beta + \ell - \frac{n_1}{n_2}(2\pi - \beta_o)$
$\beta_o < \beta < \beta_o + \beta_c$	$\pi - \beta_o - \beta_c < \beta < \pi - \beta_o$	$\pi + \beta_o < \beta < \pi + \beta_o + \beta_c$	$2\pi + \beta_o - \beta_c < \beta < 2\pi - \beta_o$

Now the induced magnetic field by the parts of the coil winding which they are in the Θ-direction around the pipe is calculated (see figure B.4).

The current density may be expressed in the form of:

$$\underset{\sim}{J} = J\,\mathrm{Cos}\beta\ i + J\,\mathrm{Sin}\beta\ j \qquad (6.17)$$

Using the Biot-Savart's law we obtain:

$$\underset{\sim}{dB} = \frac{-\mu_o}{4\pi}$$

$$\frac{\{(J\,\mathrm{Cos}\beta\; i - J\,\mathrm{Sin}\beta\; j) \times \{(R_c\,\mathrm{Sin}\beta - \rho\mathrm{Sin}\phi)i + (R_c\mathrm{Cos}\beta - \rho\mathrm{Cos}\phi)j + (z'-z)k\}d\tau}{\{(R_c\,\mathrm{Sin}\beta - \rho\mathrm{Sin}\phi)^2 + (R_c\,\mathrm{Cos}\beta - \rho\mathrm{Cos}\phi)^2 + (z'-z)^2\}^{3/2}}$$

(B.18)

where $d\tau = R_c\, d_w\, n_2\, d\beta\, dz'$

Therefore:

$$\underset{\sim}{dB} = \frac{\mu_o\, J\, n_2\, d_w\, R_c}{4\pi}$$

$$\frac{\{\mathrm{Sin}\beta(z'-z)i + \mathrm{Cos}\beta(z'-z)j - (R_c - \rho\mathrm{Cos}(\beta-\phi))k\}d\beta\, dz'}{\{(R_c\mathrm{Sin}\beta - \rho\mathrm{Sin}\phi)^2 + (R_c\mathrm{Cos}\beta - \rho\mathrm{Cos}\phi)^2 + (z'-z)^2\}^{3/2}}$$

(B.19)

Substituting for non-dimensional parameters and value of J from equation B.2 gives

$$\underset{\sim}{dB} = \frac{\mu_o\, IN\, n_2}{4\pi\, \beta_c\, R_c\, n_1}$$

$$\frac{\{\mathrm{Sin}\beta(z_1'-z_1)i + \mathrm{Cos}\beta(z_1'-z_1)j - (1 - \rho_1\mathrm{Cos}(\beta-\phi))k\}\, d\beta\, dz_1'}{\{\mathrm{Sin}\beta - \rho_1\mathrm{Sin}\phi)^2 + (\mathrm{Cos}\beta - \rho_1\mathrm{Cos}\phi)^2 + (z_1' - Z_1)^2\}^{3/2}}$$

(B.20)

$\underset{\sim}{B}_5$ the induced magnetic field is calculated by integrating the above equation.

$$\underset{\sim}{B}_5 = \frac{\mu_o \, IN \, n_2}{4\pi \, \beta_c \, R_c \, n_1} \int_{\ell_o}^{\ell} \int_{\phi_1}^{\phi_2} \frac{\{\mathrm{Sin}\beta(z_1' - z_1)i + \mathrm{Cos}\beta(z_1' - z_1)j - (1 - \rho_1 \mathrm{Cos}(\beta - \phi))k\} \, d\beta \, dz_1'}{\{(\mathrm{Sin}\beta - \rho_1 \mathrm{Sin}\phi)^2 + (\mathrm{Cos}\beta - \rho_1 \mathrm{Cos}\phi)^2 + (z_1' - z_1)^2\}^{3/2}} \tag{B.21}$$

ϕ_1 and ϕ_2 are the half angles of coil winding at z_1'.

where

$$\phi_2 = \pi - \phi_1 \tag{B.22}$$

and

$$\phi_1 = -\frac{n_2}{n_1} z_1' + \beta_o + \frac{n_2}{n_1} \ell \tag{B.23}$$

and

$$\ell_o = \ell - \frac{n_1}{n_2} \beta_c \tag{B.24}$$

$\underset{\sim}{B}_6$, $\underset{\sim}{B}_7$ and $\underset{\sim}{B}_8$ can be calculated by the following alternatives in equation B.21.

$\underset{\sim}{B}_5$	$\underset{\sim}{B}_6$	$\underset{\sim}{B}_7$	$\underset{\sim}{B}_8$
I	-I	-I	I
$\ell_o < z_1' < \ell$	$-\ell < z_1' < -\ell_o$	$\ell_o < z_1' < \ell$	$-\ell < z_1' < -\ell_o$
$\phi_1 < \beta < \phi_2$	$\phi_3 < \beta < \phi_4$	$\phi_5 < \beta < \phi_6$	$\phi_7 < \beta < \phi_8$
$\phi_2 = \pi - \phi_1$	$\phi_4 = \pi - \phi_3$	$\phi_6 = 3\pi - \phi_5$	$\phi_8 = 3\pi - \phi_7$
$\phi_1 = \frac{n_2}{n_1} z_1' + \beta_o + \frac{n_2}{n_1}\ell$	$\phi_3 = \frac{n_2}{n_1} z_1' + \beta_o + \frac{n_2}{n_1}\ell$	$\phi_5 = \frac{n_2}{n_1} z_1' + \pi + \beta_o + \frac{n_2}{n_1}\ell$	$\phi_7 = \frac{n_2}{n_1} z_1' + \beta_o + \frac{n_2}{n_1}\ell + \pi$

The computed field distribution of a short saddle coil in the x, y and z direction are shown in figures B.5, B.6 and B.7.

The geometry of the coil used here is identical with the one which was used in Appendix A. The coil angle was 10° (β_o).

Figure B.5 shows the magnetic field distribution at the centre line of coil at $\phi = \pi/2$ and three different types of saddle coil windings. The results show that the field strength is higher for the design in which the winding is presented as a single winding, similar to the design explained in Appendix A. Figure B.6 and B.7 shows the field distribution along y and x axis respectively.

APPENDIX C

CALCULATION OF MAGNETIC FIELD DISTRIBUTION FOR DIAMOND-TYPE COILS

The magnetic field is generated by two diamond shaped air cored coils supplied with a constant current and installed around the fluid containing duct. This is shown in figure C.1.

Vector $\underset{\sim}{ds}$ in Biot-Savart's equation (A.1) can have the following form

$$\underset{\sim}{ds} = a\,i + b\,j + c\,k \qquad (C.1)$$

From equation A.2, A.4 and C.1 we obtain the expression for induced magnetic field as:

$$\underset{\sim}{dB} = \frac{-\mu_o NI}{4\pi R_c} \left\{ \frac{(a\,i + b\,j + c\,k) \times \{(R_c \sin\beta - \rho\sin\phi)i + (R_c \cos\beta - \rho\cos\phi)j + (z' - z)k\}}{\{(R_c \sin\beta - \rho\sin\phi)^2 + (R_c \cos\beta - \rho\cos\phi)^2 + (z' - z)^2\}^{3/2}} \right\}$$

(C.2)

Substituting for the non-dimensional parameters as before, and $a' = a/R_c$, $b' = b/R_c$, $c' = c/R_c$ and simplify the above equation leads to the equation C.3:

$$\underset{\sim}{dB} = \frac{-\mu_o NI}{4\pi R_c}$$

$$\frac{\{b'(z_1' - z_1) - c'(\cos\beta - \rho_1\cos\phi)\}\,\underset{\sim}{i} + \{c'(\sin\beta - \rho_1\sin\phi) - a'(z_1' - z_1)\}\,\underset{\sim}{j}}{\{(\sin\beta - \rho_1\sin\phi)^2 + (\cos\beta - \rho_1\cos\phi)^2 + (z_1' - z_1)^2\}^{3/2}}$$

$$+ \{a'(\cos\beta - \rho_1\cos\phi) - b'(\sin\beta - \rho_1\sin\phi)\}\,\underset{\sim}{k}$$

(C.3)

The aim is to find the magnetic field contribution of every individual part of the coil at point $P(\rho,\phi,z)$. Therefore each part of the coil is labelled with a number. To calculate the total magnetic field at point P due to for example wire 1 it is necessary to know the form of element ds, relationship between z_1' and β and the limits of integral, because

$$\underset{\sim}{B} = \int_{\beta_1}^{\beta_2} \underset{\sim}{dB} \qquad \text{(C.4)}$$

Figure C.2 shows a plane view of diamond coil and it follows that:

$$L_2 = R_c(\pi/2 - \beta_o) \qquad \text{(C.5)}$$

and

$$z' = \frac{L_1\,(L_2 - L_z)}{L_2} \qquad \text{(C.6)}$$

From figure C.2 we have:

$$L_z = R_c(\pi/2 - \beta) \tag{C.7}$$

therefore

$$z' = \frac{L_1 R_c(\beta - \pi/2) + L_1 L_2}{L_2} \tag{C.8}$$

or in non-dimensional form

$$z_1' = \frac{\ell_1(\beta - \pi/2) + \ell_1 \ell_2}{\ell_2} \tag{C.9}$$

where $\ell_1 = \frac{L_1}{R_c}$ and $\ell_2 = \frac{L_2}{R_c}$

Figure C.3 shows the element $d\underset{\sim}{s}$ in the different wires. In the wire where $d\underset{\sim}{s}$ appears in the opposite direction to the current, $-d\underset{\sim}{s}$ is used.

It follows therefore for:

Wire 1

$$\underset{\sim}{ds} = R_c\, d\beta \cos\beta\, \underset{\sim}{i} - R_c\, d\beta \sin\beta\, \underset{\sim}{j} + dz'\, \underset{\sim}{k}$$

$$z_1' = \frac{\ell_1(\beta - \pi/2) + \ell_1 \ell_2}{\ell_2}$$

$$\underset{\sim}{B}_1 = \int_{\beta_o}^{\pi/2} d\underset{\sim}{B}$$

Wire 2

$$\underset{\sim}{ds} = R_c\, d\beta\, \text{Cos}\beta\ \underset{\sim}{i} - R_c\, d\beta\, \text{Sin}\beta\ \underset{\sim}{j} - dz'\ \underset{\sim}{k}$$

$$z_1' = \frac{\ell_1(\pi/2 - \beta) + \ell_1\ell_2}{\ell_2}$$

$$\underset{\sim}{B}_2 = \int_{\pi/2}^{\pi - \beta_o} \underset{\sim}{dB}$$

Wire 3

$$-\underset{\sim}{ds} = -(R_c\, d\beta\, \text{Cos}\beta\ \underset{\sim}{i} - R_c\, d\beta\, \text{Sin}\beta\ \underset{\sim}{j} + dz'\ \underset{\sim}{k})$$

$$z_1' = -\frac{\ell_1(\pi/2 - \beta) + \ell_1\ell_2}{\ell_2}$$

$$\underset{\sim}{B}_3 = \int_{\pi/2}^{\pi - \beta_o} \underset{\sim}{dB}$$

and for

Wire 4

$$-\underset{\sim}{ds} = -(R_c\, d\beta\, \text{Cos}\beta\ \underset{\sim}{i} - R_c\, d\beta\, \text{Sin}\beta\ \underset{\sim}{j} - dz'\ \underset{\sim}{k})$$

$$z_1' = -\frac{\ell_1(\beta - \pi/2) + \ell_1\ell_2}{\ell_2}$$

$$\underset{\sim}{B}_4 = \int_{\beta_o}^{\pi/2} \underset{\sim}{dB}$$

Figure C.4 shows the configuration of element $\underset{\sim}{ds}$ for the bottom coil.

Similarly it follows for

Wire 5

$$-\underset{\sim}{ds} = -(R_c\, d\beta\, \cos\beta\, i - R_c\, d\beta\, \sin\beta\, j - dz'\, k)$$

$$z_1' = \frac{\ell_1(\frac{3\pi}{2} - \beta) + \ell_1\ell_2}{\ell_2}$$

$$\underset{\sim}{B}_5 = \int_{\frac{3\pi}{2}}^{2\pi - \beta_o} \underset{\sim}{dB}$$

Wire 6

$$-\underset{\sim}{ds} = (R_c\, d\beta\, \cos\beta\, i - R_c\, d\beta\, \sin\beta\, j + dz'\, k)$$

$$z_1' = \frac{\ell_1\,(\beta - \frac{3\pi}{2}) + \ell_1\ell_2}{\ell_2}$$

$$\underset{\sim}{B}_6 = \int_{\pi + \beta_o}^{\frac{3\pi}{2}} \underset{\sim}{dB}$$

Wire 7

$$\underset{\sim}{ds} = (R_c\, d\beta\, \mathrm{Cos}\beta\ \underset{\sim}{i} - R_c\, d\beta\, \mathrm{Sin}\beta\ \underset{\sim}{j} - dz'\ \underset{\sim}{k})$$

$$z_1' = -\frac{\ell_1\ (\beta - \frac{3\pi}{2}) + \ell_1 \ell_2}{\ell_2}$$

$$\underset{\sim}{B}_7 = \int_{\pi + \beta_o}^{\frac{3\pi}{2}} \underset{\sim}{dB}$$

and

Wire 8

$$\underset{\sim}{ds} = (R_c\, d\beta\, \mathrm{Cos}\beta\ \underset{\sim}{i} - R_c\, d\beta\, \mathrm{Sin}\beta\ \underset{\sim}{j} + dz'\ \underset{\sim}{k})$$

$$z_1' = -\frac{\ell_1\ (\frac{3\pi}{2} - \beta) + \ell_1 \ell_2}{\ell_2}$$

$$\underset{\sim}{B}_8 = \int_{\frac{3\pi}{2}}^{2\pi - \beta_o} \underset{\sim}{dB}$$

A computer program has been written to find the integral of equation C.3, numerically for different wires. The program is being tested for special cases such as straight wires (when ℓ_1 is very large) and circular coils (when ℓ_1 is very small).

The diamond coil used in the following has the similar geometry with saddle coil given in Appendix A.

Figures C.5 shows the magnetic field distribution along z-axis

at the centre of diamond coil for three coil angles. The field distribution along z-axis and R = 2.7a is shown in figure C.6. The distribution at this surface is used as boundary values in finite difference solution. The magnetic field distribution at z = 0, along y-axis of diamond coil for three coil angles are shown in figure C.7 and distribution along x-axis is shown in figure C.8.

APPENDIX D

LAGRANGIAN INTERPOLATION

In the general case the polynomial P(x) of degree n passing through the tabular points is given by

$$P(x) = \sum_{k=0}^{n} L_k(x)\, f_k \tag{D.1}$$

where

$$L_k(x) = \prod_{r\neq k} (x - x_r) / \prod_{r\neq k} (x_k - x_r) \tag{D.2}$$

P(x) is known as the Larangian interpolation polynomial of degree n. Since

$$L_k(x_i) = \begin{cases} 0 , & i\neq k \\ 1 , & i=k \end{cases} \tag{D.3}$$

it follows that $P(x_k) = f_k$, that is, the polynomial P(x) has the same values as the function f(x) at the tabular points.

APPENDIX E

$\nabla^2 f$

The expression for $\Delta f = \nabla^2 f$, where f is a vector field is given by N. Kemmer (1977) in cylindrical polars:

$$\Delta f = \left(\frac{\partial}{\partial r}\left(\frac{1}{r}\frac{\partial}{\partial r}(rf_r)\right) + \frac{1}{r^2}\frac{\partial^2 f_r}{\partial \theta^2} + \frac{\partial^2 f_r}{\partial z^2} - \frac{2}{r^2}\frac{\partial f_\theta}{\partial \theta}\right)\underset{\sim}{r}$$

$$+\left(\frac{\partial}{\partial r}\left(\frac{1}{r}\frac{\partial}{\partial r}(rf_\theta)\right) + \frac{1}{r^2}\frac{\partial^2 f_\theta}{\partial \theta^2} + \frac{\partial^2 f_\theta}{\partial z^2} + \frac{2}{r^2}\frac{\partial f_r}{\partial \theta}\right)\underset{\sim}{\theta}$$

$$+\left(\frac{1}{r}\frac{\partial}{\partial r}\left(r\frac{\partial f_z}{\partial r}\right) + \frac{1}{r^2}\frac{\partial^2 f_z}{\partial \theta^2} + \frac{\partial^2 f_z}{\partial z^2}\right)\underset{\sim}{z} \qquad \text{(E.1)}$$

Reactor	Country	MWt	MWe	pool or loop	Operation
Experimental					
BR-5	Russia	5	...	loop	1959
DFR	Great Britain	72	15	loop	1959
EBR-II	United States	62.5	20	pool	1963
FERMI	United States	200	67	loop	1963
RAPSODIE	France	40	...	loop	1967
BR-60(BRO)	Russia	60	...	loop	1970
JOYO	Japan	100	...	loop	1974
FFTF	United States	400	...	loop	1975
Power Producing					
BN-350	Russia	1000	350	loop	1973
PFR	Great Britain	600	250	pool	1973
Phenix	France	600	250	pool	1973
BN-600	Russia	1500	600	pool	1976
SNR-300	Debenelux	730	300	loop	1978
MONJU	Japan	714	300	loop	1978

Table 1.1 List of experimental and power producing Fast Breeder Reactors

Electrode location	midplane		one diameter downstream	
Velocity profile	uniform	parabolic	uniform	parabolic
$R_m = 1$	.955	.934	.757	.729
3	.677	.695	.802	.765
5	.463	.509	.676	.661

Table 4.1 Sensitivity of saddle coil flowmeter for two positions of electrode location

Electrode location	midplane		one diameter downstream	
Velocity profile	uniform	parabolic	uniform	parabolic
$R_m = 1$	.903	.891	.599	.61
3	.602	.63	.685	.662
5	.38	.447	.575	.572

Table 4.2 Sensitivity of diamond coil flowmeter for two positions of electrode location

Saddle Coil

		Sensitivity, $\bar{S}$	
R_m	V_m m/sec	Uniform velocity	Parabolic velocity
1.	.985	.825	.817
3.	2.954	.825	.816
5.	4.924	.815	.807
.1	.0985	.826	-
5.	2.462	.815	.807

Table 6.1 Sensitivity of integrated voltage flowmeter for different flowrate and velocity profile wall conductivity number (d = .044) and contact resistance number (C_r = 0)

Saddle Coil

Sensitivity, $\bar{S}$

	d = 0 C_r = 0	d = .022 C_r = 0	d = .044 C_r = .0	d = .044 C_r = .5
numerical solution (3-D)	.853	.834	.815	.796
from equation 2.21 (2-D)	.853	.835	.817	.8

Table 6.2 Effect of wall conductivity number d, and contact resistance number C_r, on the sensitivity.

Diamond Coil

R_m	V_m m/sec	Sensitivity, $\bar{S}$	
		Uniform Velocity	Parabolic Velocity
1.	.985	.662	.668
3.	2.954	.657	.664
5.	4.924	.646	.653

Table 6.3 Sensitivity of integrated voltage flowmeter for different flow rate and velocity profile

Counts in 100 mS	Amplifier output mV	Speed m/sec	Magnetic Reynolds Number	Flowmeter Output mV
0	2.1000	0	0	0
86	5.2000	.1638	.1523	.0819
95	5.6000	.1810	.1683	.0925
94	5.0000	.1791	.1665	.0766
94	5.3000	.1791	.1665	.0846
92	4.5000	.1753	.1629	.0634
95	5.0000	.1810	.1683	.0766
95	5.0000	.1810	.1683	.0766
95	4.6000	.1810	.1683	.0661
97	4.6000	.1848	.1718	.0661
201	7.3000	.3829	.3560	.1374
201	7.6000	.3829	.3560	.1453
200	7.8000	.3810	.3542	.1506
201	7.4000	.3829	.3560	.1401
201	7.9000	.3829	.3560	.1533
201	7.9000	.3829	.3560	.1533
201	7.6000	.3829	.3560	.1453
201	7.8000	.3829	.3560	.1506
201	7.6000	.3829	.3560	.1453
347	10.4000	.6611	.6146	.2193
347	10.6000	.6611	.6146	.2246
346	11.5000	.6592	.6128	.2484
346	11.1000	.6592	.6128	.2378
346	11.4000	.6592	.6128	.2458
346	10.9000	.6592	.6128	.2326
346	11.1000	.6592	.6128	.2378
346	11.4000	.6592	.6128	.2458
346	10.4000	.6592	.6128	.2193
443	14.4000	.8440	.7846	.3251
486	14.6000	.9259	.8608	.3303
466	13.0000	.8878	.8253	.2881
448	13.6000	.8535	.7935	.3039
444	13.6000	.8459	.7864	.3039
466	13.2000	.8878	.8253	.2933
510	14.7000	.9716	.9033	.3330
496	13.5000	.9449	.8785	.3013
504	14.6000	.9602	.8926	.3303
612	15.6000	1.1659	1.0839	.3568
604	15.9000	1.1507	1.0698	.3647
620	15.8000	1.1812	1.0981	.3621
616	16.5000	1.1736	1.0910	.3805
624	17.0000	1.1888	1.1052	.3938
636	15.8000	1.2117	1.1264	.3621
568	16.7000	1.0821	1.0060	.3858
608	15.6000	1.1583	1.0768	.3568
568	17.1000	1.0821	1.0060	.3964
776	18.9000	1.4784	1.3744	.4440
764	19.0000	1.4555	1.3531	.4466
764	19.3000	1.4555	1.3531	.4545
716	17.8000	1.3641	1.2681	.4149
736	18.5000	1.4022	1.3035	.4334
724	18.4000	1.3793	1.2823	.4308
800	18.9000	1.5241	1.4169	.4440
784	19.7000	1.4936	1.3886	.4651
756	18.7000	1.4403	1.3390	.4387
864	22.1000	1.6460	1.5302	.5285
920	23.5000	1.7527	1.6294	.5655
868	24.0000	1.6536	1.5373	.5788
904	25.9000	1.7222	1.6011	.6290
952	25.0000	1.8137	1.6861	.6052
928	27.2000	1.7680	1.6436	.6633
876	22.8000	1.6689	1.5515	.5470
936	26.4000	1.7832	1.6578	.6422
1116	30.5000	2.1261	1.9766	.7505
1140	31.3000	2.1718	2.0191	.7717
1132	30.7000	2.2338	2.0768	.7522

Table 7.1 Experimental results for electrodes positioned at

$z = -10.16$cm

Counts in 100 mS	Amplifier output mV	Speed m/sec	Magnetic Reynolds Number	Flowmeter output mV
0	2.1000	0	0	0
86	5.2000	.1638	.1523	.0819
81	5.6000	.1543	.1435	.0925
78	5.2000	.1486	.1381	.0819
77	5.4000	.1467	.1364	.0872
78	5.5000	.1486	.1381	.0899
79	5.5000	.1505	.1399	.0899
80	5.9000	.1524	.1417	.1004
80	5.8000	.1524	.1417	.0978
80	5.6000	.1524	.1417	.0925
208	12.2000	.3963	.3684	.2669
210	12.3000	.4001	.3719	.2696
211	12.4000	.4020	.3737	.2722
210	12.3000	.4001	.3719	.2696
210	13.1000	.4001	.3719	.2907
211	12.4000	.4020	.3737	.2722
211	12.6000	.4020	.3737	.2775
210	12.4000	.4001	.3719	.2722
212	12.6000	.4039	.3755	.2775
356	19.2000	.6782	.6305	.4519
362	19.1000	.6897	.6411	.4493
361	18.2000	.6878	.6394	.4255
362	18.7000	.6897	.6411	.4387
364	18.6000	.6935	.6447	.4360
326	17.8000	.6401	.5951	.4149
352	18.7000	.6706	.6234	.4387
346	18.4000	.6592	.6128	.4308
366	20.0000	.6973	.6482	.4730
506	23.2000	.9640	.8962	.5576
472	22.0000	.8992	.8360	.5259
512	23.6000	.9754	.9068	.5682
502	24.7000	.9564	.8891	.5973
498	24.9000	.9488	.8820	.5761
506	23.1000	.9640	.8962	.5550
502	24.6000	.9564	.8891	.5946
504	23.9000	.9602	.8926	.5761
500	23.9000	.9526	.8856	.5761
620	28.6000	1.1812	1.0981	.7003
624	29.2000	1.1888	1.1052	.7162
620	29.5000	1.1812	1.0981	.7241
624	28.1000	1.1888	1.1052	.6871
620	29.0000	1.1812	1.0981	.7109
616	27.9000	1.1736	1.0910	.6818
624	28.8000	1.1888	1.1052	.7056
608	27.9000	1.1583	1.0768	.6818
624	28.5000	1.1888	1.1052	.6977
800	37.8000	1.5241	1.4169	.9434
808	36.9000	1.5393	1.4311	.9197
788	37.1000	1.5012	1.3956	.9249
828	35.0000	1.5774	1.4665	.8695
764	32.0000	1.4555	1.3531	.7902
732	34.5000	1.3946	1.2965	.8562
784	34.3000	1.4936	1.3886	.8510
732	33.5000	1.3946	1.2965	.8298
952	44.7000	1.8137	1.6861	1.1258
976	46.4000	1.8594	1.7286	1.1707
936	45.7000	1.7832	1.6578	1.1522
992	47.6000	1.8899	1.7569	1.2024
932	45.8000	1.7756	1.6507	1.1549
936	46.6000	1.7832	1.6578	1.1760

Table 7.2 Experimental results for electrodes positioned at z = -6.45cm.

Counts in 100 mS	Amplifier output mV	Speed m/sec	Magnetic Reynolds Number	Flowmeter output mV
0	2.1000	0	0	0
84	8.1000	.1600	.1488	.1586
86	7.9000	.1638	.1523	.1533
89	8.3000	.1696	.1576	.1638
89	8.4000	.1696	.1576	.1665
90	8.5000	.1715	.1594	.1691
91	8.4000	.1734	.1612	.1665
91	8.8000	.1734	.1612	.1771
92	9.2000	.1753	.1629	.1876
93	9.3000	.1772	.1647	.1903
202	18.6000	.3848	.3578	.4360
201	18.1000	.3829	.3560	.4228
201	18.7000	.3829	.3560	.4387
202	18.6000	.3848	.3578	.4360
201	18.1000	.3829	.3560	.4228
201	18.4000	.3829	.3560	.4308
201	18.4000	.3829	.3560	.4308
201	18.6000	.3829	.3560	.4360
201	18.3000	.3829	.3560	.4281
325	29.0000	.6192	.5756	.7109
328	28.3000	.6249	.5809	.6924
327	28.1000	.6230	.5792	.6871
326	28.4000	.6211	.5774	.6950
327	27.6000	.6230	.5792	.6739
327	28.5000	.6230	.5792	.6977
327	28.0000	.6230	.5792	.6845
327	28.6000	.6230	.5792	.7003
324	28.3000	.6173	.5738	.6924
508	44.4000	.9678	.8997	1.1179
496	42.2000	.9449	.8785	1.0597
490	42.6000	.9335	.8678	1.0703
456	39.8000	.8687	.8076	.9963
490	43.3000	.9335	.8678	1.0888
502	42.6000	.9564	.8891	1.0703
508	43.2000	.9678	.8997	1.0862
512	42.8000	.9754	.9068	1.0756
524	43.6000	.9983	.9281	1.0967
616	51.4000	1.1736	1.0910	1.3029
616	52.4000	1.1736	1.0910	1.3293
628	50.5000	1.1964	1.1123	1.2791
596	48.6000	1.1355	1.0556	1.2289
608	52.6000	1.1583	1.0768	1.3346
624	53.4000	1.1888	1.1052	1.3557
620	51.2000	1.1812	1.0981	1.2976
620	51.5000	1.1812	1.0981	1.3055
620	51.2000	1.1812	1.0981	1.2976
824	64.5000	1.5698	1.4594	1.6490
808	63.5000	1.5393	1.4311	1.6226
836	65.6000	1.5927	1.4807	1.6781
800	64.4000	1.5241	1.4169	1.6464
740	58.4000	1.4098	1.3106	1.4878
824	65.3000	1.5698	1.4594	1.6702
800	63.8000	1.5241	1.4169	1.6305
788	64.2000	1.5012	1.3956	1.6411
800	61.5000	1.5241	1.4169	1.5698
992	79.7000	1.8899	1.7569	2.0507
1004	80.3000	1.9127	1.7782	2.0666
1012	80.4000	1.9280	1.7924	2.0692

Table 7.3 Experimental results for electrodes positioned at z = -5.08cm.

Counts in 100 mS	Amplifier output mV	Speed m/sec	Magnetic Reynolds Number	Flowmeter Output mV
0	2.1000	0	0	0
86	10.6000	.1638	.1523	.2246
86	10.5000	.1638	.1523	.2220
88	10.7000	.1677	.1559	.2273
90	11.0000	.1715	.1594	.2352
93	11.3000	.1772	.1647	.2431
83	10.6000	.1581	.1470	.2246
89	10.7000	.1696	.1576	.2273
90	11.3000	.1715	.1594	.2431
90	11.2000	.1715	.1594	.2405
206	23.9000	.3925	.3649	.5761
205	23.5000	.3906	.3631	.5655
205	23.5000	.3906	.3631	.5655
205	23.2000	.3906	.3631	.5576
205	23.5000	.3906	.3631	.5655
205	23.7000	.3906	.3631	.5708
205	23.6000	.3906	.3631	.5682
204	23.1000	.3886	.3613	.5550
205	23.4000	.3906	.3631	.5629
337	36.5000	.6420	.5969	.9091
337	36.4000	.6420	.5969	.9064
339	36.6000	.6458	.6004	.9117
332	36.2000	.6325	.5880	.9012
342	36.7000	.6516	.6057	.9144
341	36.7000	.6496	.6040	.9144
338	36.9000	.6439	.5986	.9197
339	36.5000	.6458	.6004	.9091
338	36.6000	.6439	.5986	.9117
468	46.8000	.8916	.8289	1.1813
464	47.3000	.8840	.8218	1.1945
494	48.9000	.9411	.8749	1.2368
450	46.2000	.8573	.7970	1.1654
492	50.5000	.9373	.8714	1.2791
480	47.7000	.9145	.8501	1.2051
448	46.2000	.8535	.7935	1.1654
490	50.6000	.9335	.8678	1.2817
436	46.3000	.8306	.7722	1.1681
608	65.6000	1.1583	1.0768	1.6781
600	61.8000	1.1431	1.0627	1.5777
700	63.8000	1.1431	1.0627	1.6305
600	62.6000	1.1431	1.0627	1.5988
600	62.6000	1.1431	1.0627	1.5988
604	61.3000	1.1507	1.0698	1.5645
604	60.1000	1.1507	1.0698	1.5328
588	60.7000	1.1202	1.0414	1.5486
604	61.2000	1.1507	1.0698	1.5618
776	74.2000	1.4784	1.3744	1.9054
792	77.5000	1.5089	1.4027	1.9926
800	79.4000	1.5241	1.4169	2.0428
716	73.4000	1.3641	1.2681	1.8842
784	78.5000	1.4936	1.3886	2.0190
788	79.1000	1.5012	1.3956	2.0349
808	77.3000	1.5393	1.4311	1.9873
800	77.6000	1.5241	1.4169	1.9952
800	77.0000	1.5241	1.4169	1.9794
944	101.3000	1.7984	1.6719	2.6216
996	102.9000	1.8975	1.7640	2.6638
988	102.7000	1.8823	1.7499	2.6586
912	101.0000	1.7375	1.6153	2.6136
1008	104.4000	1.9204	1.7853	2.7035
916	100.3000	1.7451	1.6223	2.5951

Table 7.4 Experimental results for electrodes positioned at z = -2.45cm.

Counts in 100 mS	Amplifier output mV	Speed m/sec	Magnetic Reynolds Number	Flowmeter output mV
0	2.1000	0	0	0
87	13.2000	.1657	.1541	.2933
83	12.3000	.1581	.1470	.2696
86	11.6000	.1638	.1523	.2511
89	13.6000	.1695	.1575	.2881
91	12.9000	.1734	.1612	.2854
91	12.2000	.1734	.1612	.2669
93	11.7000	.1772	.1647	.2537
92	11.9000	.1753	.1629	.2590
94	12.7000	.1791	.1665	.2801
206	26.0000	.3925	.3649	.6316
206	25.2000	.3925	.3649	.6105
206	25.8000	.3925	.3649	.6263
206	25.6000	.3925	.3649	.6210
207	25.2000	.3944	.3666	.6105
206	25.3000	.3925	.3649	.6131
204	24.9000	.3886	.3613	.6025
205	25.5000	.3906	.3631	.6184
205	25.6000	.3906	.3631	.6210
327	37.9000	.6230	.5792	.9461
328	38.0000	.6249	.5809	.9487
327	37.8000	.6230	.5792	.9434
328	38.3000	.6249	.5809	.9567
328	37.7000	.6249	.5809	.9408
327	39.0000	.6230	.5792	.9752
327	38.6000	.6230	.5792	.9646
324	38.8000	.6173	.5738	.9699
332	38.8000	.6325	.5880	.9699
486	55.9000	.9259	.8608	1.4218
476	54.5000	.9068	.8431	1.3848
492	56.9000	.9373	.8714	1.4218
484	56.5000	.9221	.8572	1.4076
472	53.5000	.8992	.8360	1.3684
484	53.7000	.9221	.8572	1.3636
472	56.0000	.8992	.8360	1.3990
490	57.5000	.9335	.8678	1.4641
468	55.7000	.8916	.8289	1.4165
624	72.7000	1.1888	1.1052	1.8658
622	70.3000	1.1850	1.1016	1.8023
630	73.2000	1.2002	1.1158	1.8790
626	71.0000	1.1926	1.1087	1.8420
636	75.0000	1.2117	1.1264	1.9265
612	70.3000	1.1659	1.0839	1.8023
620	71.7000	1.1812	1.0981	1.8393
636	73.6000	1.2117	1.1264	1.8895
610	69.4000	1.1621	1.0804	1.7785
790	89.0000	1.5050	1.3992	2.2965
776	83.8000	1.4784	1.3744	2.1591
712	77.5000	1.3564	1.2610	1.9926
772	85.9000	1.4708	1.3673	2.2146
788	85.6000	1.5012	1.3956	2.2067
760	81.7000	1.4479	1.3460	2.1036
780	84.0000	1.4860	1.3815	2.1644
772	85.4000	1.4708	1.3673	2.2278
732	82.9000	1.3946	1.2965	2.1353
960	103.3000	1.8289	1.7003	2.8330
960	107.6000	1.8289	1.7003	2.7081
956	111.6000	1.8213	1.6932	2.8938
948	105.9000	1.8061	1.6790	2.7431
952	106.9000	1.8137	1.6861	2.7696
944	98.2000	1.7984	1.6719	2.5396
916	90.9000	1.7451	1.6223	2.3457
856	93.2000	1.6308	1.5161	2.4075
930	95.6000	1.8570	1.7267	2.4874
1012	100.7000	1.9280	1.7924	2.6057
972	94.7000	1.8518	1.7215	2.4471
932	91.1000	1.7756	1.6507	2.3520
940	90.4000	1.8061	1.6790	2.4656
948	95.0000	1.7908	1.6649	2.4551
1144	124.0000	2.1795	2.0262	3.2215
1164	107.9000	2.0271	1.8845	2.7960
1196	125.4000	2.2823	2.0474	3.2585
1104	116.1000	2.1033	1.9553	3.0127
1160	124.6000	2.2089	2.0545	3.3095
1112	118.7000	2.1185	1.9685	3.0814
1096	115.0000	2.0890	1.9411	3.0048
1096	115.8000	2.0890	1.9411	3.0048
1200	124.9000	2.2861	2.1253	3.2452
1204	128.1000	2.2938	2.1324	3.3298
1040	102.4000	1.9813	1.8420	2.6506
1104	113.7000	2.1033	1.9553	2.9493

Table 7.5 Experimental results for electrodes positioned at z = 0.

Counts in 100 mS	Amplifier output mV	Speed m/sec	Magnetic Reynolds Number	Flowmeter output mV
0	2.1000	0	0	0
88	12.5000	.1677	.1559	.2748
88	12.3000	.1677	.1559	.2696
88	12.3000	.1677	.1559	.2695
88	11.8000	.1677	.1559	.2563
87	12.3000	.1657	.1541	.2696
87	12.3000	.1657	.1541	.2696
88	12.5000	.1677	.1559	.2748
87	12.6000	.1657	.1541	.2775
88	12.3000	.1677	.1559	.2696
210	25.7000	.4001	.3719	.6237
210	25.5000	.4001	.3719	.6184
209	25.4000	.3982	.3702	.6158
210	25.7000	.4001	.3719	.6237
209	25.4000	.3982	.3702	.6158
210	25.8000	.4001	.3719	.6263
210	25.1000	.4001	.3719	.6078
209	22.7000	.3982	.3702	.5444
209	22.6000	.3982	.3702	.5418
334	39.1000	.6363	.5916	.9778
333	36.9000	.6344	.5898	.9197
333	38.3000	.6344	.5898	.9567
333	36.7000	.6344	.5898	.9144
332	37.5000	.6325	.5880	.9355
332	37.3000	.6325	.5880	.9302
333	38.0000	.6344	.5898	.9487
333	37.1000	.6344	.5898	.9249
330	36.2000	.6287	.5845	.9012
490	55.5000	.9335	.8678	1.4112
494	55.1000	.9411	.8749	1.4006
494	54.6000	.9411	.8749	1.3874
494	54.2000	.9411	.8749	1.3768
492	56.0000	.9373	.8714	1.4244
486	53.8000	.9259	.8608	1.3663
488	54.8000	.9297	.8643	1.3927
496	55.5000	.9449	.8785	1.4112
456	55.0000	.8687	.8076	1.3980
612	69.5000	1.1659	1.0839	1.7812
620	70.4000	1.1812	1.0981	1.8050
618	70.5000	1.1774	1.0946	1.8076
634	74.8000	1.2078	1.1229	1.9212
604	67.2000	1.1507	1.0698	1.7204
614	69.8000	1.1697	1.0875	1.7891
610	70.6000	1.1621	1.0804	1.8103
616	70.4000	1.1736	1.0910	1.8050
602	68.1000	1.1469	1.0662	1.7442
774	85.8000	1.4746	1.3708	2.2119
780	87.2000	1.4860	1.3815	2.2489
760	86.3000	1.4479	1.3460	2.2252
788	85.8000	1.5012	1.3956	2.2119
772	88.1000	1.4708	1.3673	2.2727
788	87.0000	1.5012	1.3956	2.2437
780	84.2000	1.4860	1.3815	2.1697
772	85.6000	1.4708	1.3673	2.2067
772	85.3000	1.4708	1.3673	2.1987
944	112.9000	1.7984	1.6719	2.9281
992	114.1000	1.8899	1.7569	2.9598
976	115.7000	1.8594	1.7286	3.0021
976	113.7000	1.8594	1.7236	2.9493
972	113.0000	1.8518	1.7215	2.9308
960	114.5000	1.8289	1.7003	2.9704

Table 7.6 Experimental results for electrodes positioned at z = 2.54cm.

Counts in 100 mS	Amplifier output mV	Speed m/sec	Magnetic Reynolds Number	Flowmeter output mV
0	2.1000	0	0	0
90	11.5000	.1715	.1594	.2484
91	11.0000	.1734	.1612	.2352
93	11.1000	.1772	.1647	.2376
95	11.7000	.1810	.1683	.2537
95	10.8000	.1810	.1683	.2299
94	10.9000	.1791	.1665	.2326
93	10.8000	.1772	.1647	.2299
94	11.2000	.1791	.1665	.2405
94	10.9000	.1791	.1665	.2326
210	21.4000	.4001	.3719	.5100
212	21.8000	.4039	.3755	.5206
211	21.7000	.4020	.3737	.5180
212	22.2000	.4039	.3755	.5312
212	21.8000	.4039	.3755	.5206
213	22.2000	.4058	.3772	.5312
214	22.2000	.4077	.3790	.5312
214	22.3000	.4077	.3790	.5338
214	22.1000	.4077	.3790	.5285
332	34.3000	.6325	.5880	.8510
335	34.3000	.6382	.5933	.8510
333	34.1000	.6344	.5898	.8457
334	34.3000	.6363	.5916	.8510
334	34.8000	.6363	.5916	.8642
333	34.5000	.6344	.5898	.8562
334	34.6000	.6363	.5916	.8589
333	34.2000	.6344	.5898	.8483
340	35.3000	.6477	.6022	.8774
482	48.4000	.9183	.8537	1.2236
496	47.2000	.9449	.8785	1.1919
484	46.7000	.9221	.8572	1.1786
484	47.4000	.9221	.8572	1.1971
484	47.9000	.9221	.8572	1.2104
486	49.3000	.9259	.8608	1.2474
484	47.9000	.9221	.8572	1.2104
486	47.2000	.9259	.8608	1.1919
488	47.8000	.9297	.8643	1.2077
608	60.9000	1.1583	1.0768	1.5539
616	62.5000	1.1736	1.0910	1.5962
636	63.2000	1.2117	1.1264	1.6147
602	60.0000	1.1459	1.0662	1.5301
592	60.5000	1.1278	1.0485	1.5433
630	62.8000	1.2002	1.1158	1.6041
592	59.6000	1.1278	1.0485	1.5196
598	60.6000	1.1393	1.0591	1.5460
622	63.1000	1.1850	1.1016	1.6121
776	75.0000	1.4784	1.3744	1.9265
756	75.5000	1.4403	1.3390	1.9397
776	76.6000	1.4784	1.3744	1.9688
749	74.6000	1.4250	1.3248	1.9160
716	71.7000	1.3641	1.2681	1.8393
772	76.1000	1.4708	1.3673	1.9556
788	77.2000	1.5012	1.3956	1.9847
760	75.6000	1.4479	1.3460	1.9424
756	74.4000	1.4403	1.3390	1.9107
1000	98.5000	1.9051	1.7711	2.5476
948	96.9000	1.8061	1.6790	2.5053
952	98.3000	1.8137	1.6861	2.5423
996	97.7000	1.8975	1.7640	2.5264
976	98.1000	1.8594	1.7286	2.5370

Table 7.7 Experimental results for electrodes positioned at z = 5.08cm

Counts in 100 mS	Amplifier output mV	Speed m/sec	Magnetic Reynolds Number	Flowmeter output mV
0	2.1000	0	0	0
84	7.0000	.1600	.1488	.1295
89	7.5000	.1696	.1576	.1427
90	7.4000	.1715	.1594	.1401
90	7.2000	.1715	.1594	.1348
92	7.4000	.1753	.1629	.1401
93	7.2000	.1772	.1647	.1348
94	7.7000	.1791	.1665	.1480
95	7.5000	.1810	.1683	.1427
95	7.4000	.1810	.1683	.1401
213	14.6000	.4058	.3772	.3303
213	14.5000	.4058	.3772	.3277
214	14.4000	.4077	.3790	.3251
214	14.2000	.4077	.3790	.3198
215	14.2000	.4096	.3808	.3198
214	14.3000	.4077	.3790	.3224
216	14.7000	.4115	.3826	.3330
215	15.0000	.4096	.3808	.3409
215	14.6000	.4096	.3808	.3303
337	22.2000	.6420	.5969	.5312
338	22.9000	.6439	.5986	.5497
339	23.6000	.6458	.6004	.5682
339	23.5000	.6458	.6004	.5655
339	23.3000	.6458	.6004	.5603
340	23.8000	.6477	.6022	.5735
338	23.9000	.6439	.5986	.5761
335	22.7000	.6382	.5933	.5444
344	22.5000	.6554	.6093	.5391
482	30.2000	.9183	.8537	.7426
482	31.2000	.9183	.8537	.7690
490	31.6000	.9335	.8678	.7796
486	31.5000	.9259	.8608	.7770
481	31.3000	.9104	.8519	.7717
458	29.3000	.8725	.8112	.7188
456	29.7000	.8687	.8076	.7294
482	30.9000	.9183	.8537	.7611
456	29.3000	.8687	.8076	.7188
592	37.2000	1.1278	1.0485	.9276
606	37.5000	1.1545	1.0733	.9355
596	38.4000	1.1355	1.0556	.9593
606	38.4000	1.1545	1.0733	.9593
608	37.1000	1.1583	1.0768	.9249
604	38.2000	1.1507	1.0698	.9540
612	38.8000	1.1659	1.0839	.9699
596	37.4000	1.1355	1.0556	.9329
594	38.0000	1.1316	1.0520	.9487
788	50.1000	1.5012	1.3956	1.2685
762	47.9000	1.4517	1.3496	1.2104
786	49.9000	1.4974	1.3921	1.2632
796	50.2000	1.5165	1.4098	1.2711
762	47.7000	1.4517	1.3496	1.2051
792	51.1000	1.5089	1.4027	1.2949
790	50.4000	1.5050	1.3992	1.2764
784	50.4000	1.4936	1.3886	1.2764
780	52.0000	1.4860	1.3815	1.3187
986	66.3000	1.8785	1.7463	1.6966
972	66.1000	1.8518	1.7215	1.6913
932	64.8000	1.7756	1.6507	1.6570
976	67.1000	1.8594	1.7286	1.7178
976	67.2000	1.8594	1.7286	1.7204

Table 7.8 Experimental results for electrodes positioned at z = 6.45cm.

Counts in 100 mS	Amplifier output mV	Speed m/sec	Magnetic Reynolds Number	Flowmeter output mV
0	2.1000	0	0	0
86	3.8000	.1638	.1523	.0449
89	3.7000	.1696	.1576	.0423
89	3.6000	.1696	.1576	.0396
88	4.3000	.1677	.1559	.0581
90	3.8000	.1715	.1594	.0449
90	3.9000	.1715	.1594	.0476
88	3.8000	.1677	.1559	.0449
89	3.8000	.1696	.1576	.0449
87	4.4000	.1657	.1541	.0608
209	7.7000	.3982	.3702	.1480
210	7.5000	.4001	.3719	.1427
211	7.3000	.4020	.3737	.1374
211	8.5000	.4020	.3737	.1691
212	8.5000	.4039	.3755	.1691
212	7.7000	.4039	.3755	.1480
212	7.6000	.4039	.3755	.1453
212	7.6000	.4039	.3755	.1453
213	8.0000	.4058	.3772	.1559
342	11.9000	.6516	.6057	.2590
336	11.9000	.6401	.5951	.2590
339	12.0000	.6458	.6004	.2616
340	12.4000	.6477	.6022	.2722
342	11.9000	.6516	.6057	.2590
341	12.3000	.6496	.6040	.2696
334	12.2000	.6363	.5916	.2669
344	13.0000	.6554	.6093	.2881
346	12.2000	.6592	.6128	.2669
442	16.4000	.8421	.7828	.3779
506	18.3000	.9640	.8962	.4281
526	18.1000	1.0021	.9316	.4228
504	18.1000	.9602	.8926	.4228
482	17.7000	.9183	.8537	.4123
500	17.8000	.9526	.8856	.4149
518	19.6000	.9869	.9174	.4625
516	18.9000	.9830	.9139	.4440
528	17.7000	1.0059	.9352	.4123
636	22.0000	1.2117	1.1264	.5259
592	24.4000	1.1278	1.0485	.5893
608	22.7000	1.1583	1.0768	.5444
620	22.1000	1.1812	1.0981	.5285
628	21.7000	1.1964	1.1123	.5180
608	24.2000	1.1583	1.0768	.5840
608	23.4000	1.1583	1.0768	.5629
632	22.2000	1.2040	1.1193	.5312
618	21.8000	1.1774	1.0946	.5206
720	29.0000	1.3717	1.2752	.7109
680	24.7000	1.2955	1.2044	.5973
700	25.3000	1.3336	1.2398	.6131
700	25.5000	1.3336	1.2398	.6184
684	23.9000	1.3031	1.2114	.5761
686	24.0000	1.3107	1.2185	.5788
700	26.4000	1.3336	1.2398	.6422
732	26.7000	1.3946	1.2965	.6501
680	23.3000	1.2955	1.2044	.5603
924	34.9000	1.7603	1.6365	.8668
972	34.4000	1.8518	1.7215	.8536
904	34.7000	1.7222	1.6011	.8615
900	33.2000	1.7146	1.5940	.8219
960	34.6000	1.8289	1.7003	.8589
932	35.6000	1.7756	1.6507	.8853

Table 7.9 Experimental results for electrodes positioned at z = 10.16cm.

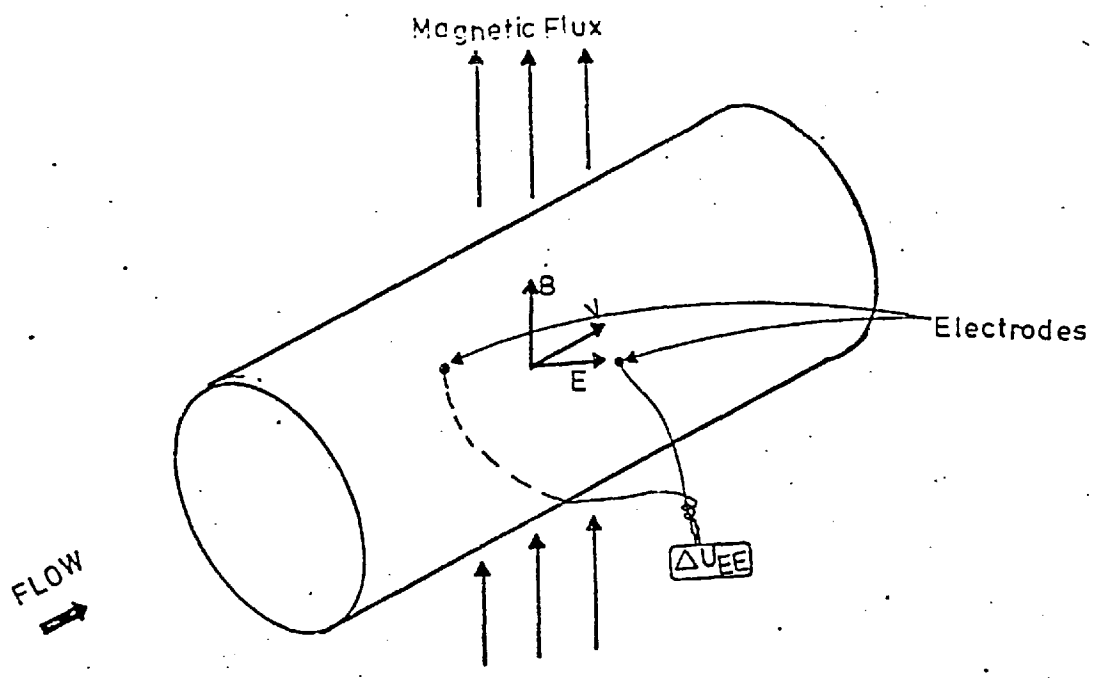

Figure 1.1 Schematic of induced voltage electromagnetic flowmeter

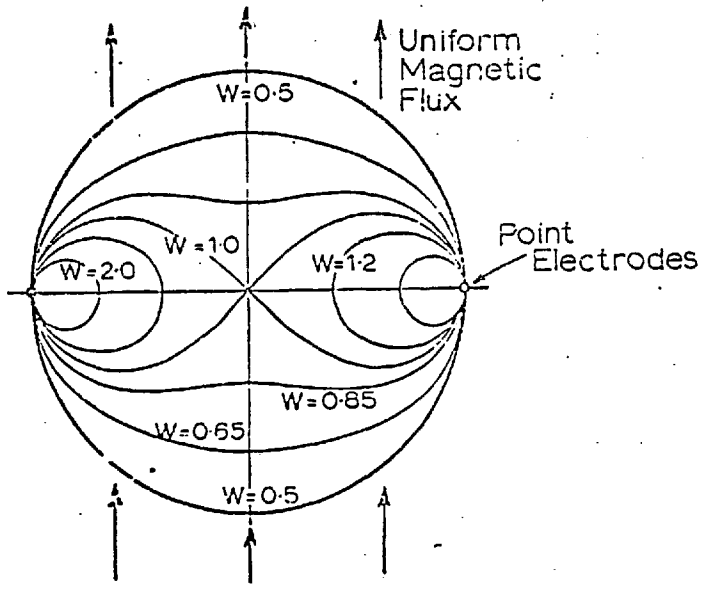

Figure 1.2 Shercliff weight function for uniform field and point electrode flowmeter

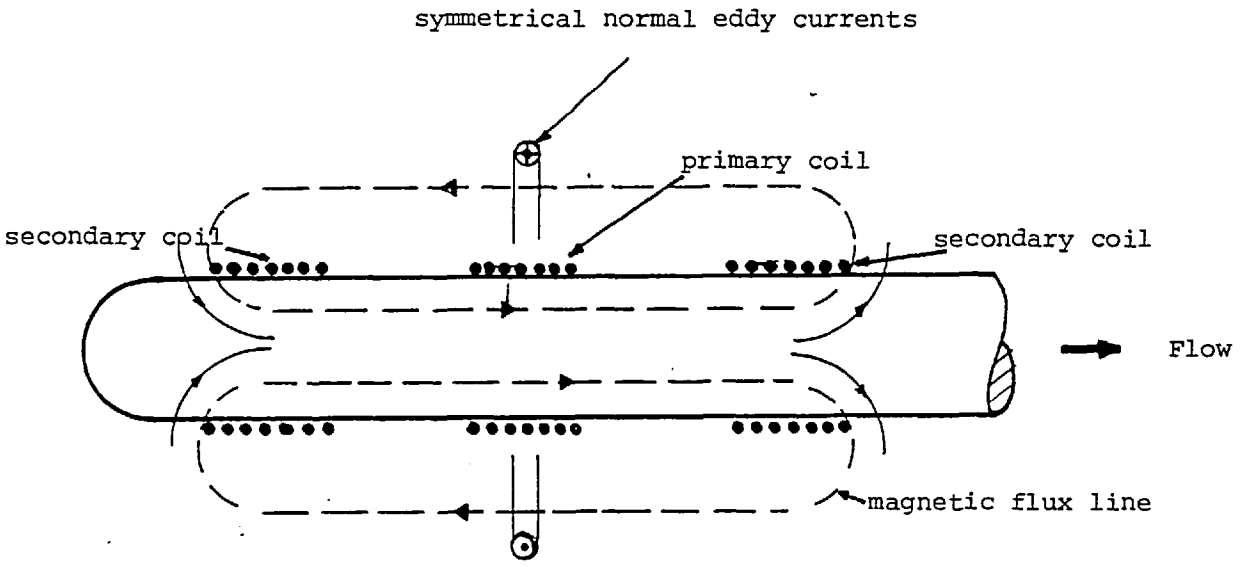

a) Symmetrical normal eddy currents induced in static and moving sodium

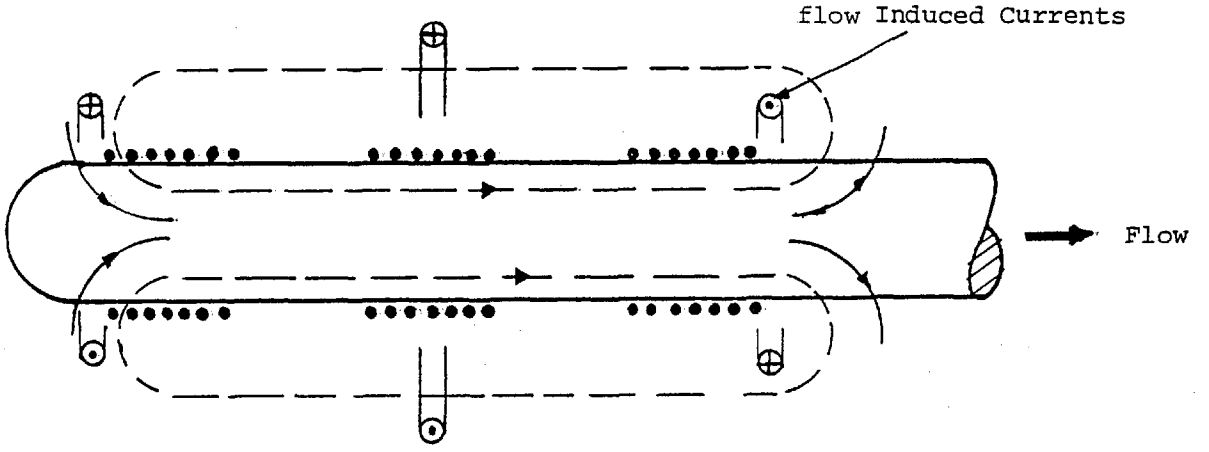

b) Flow induced currents produce secondary fields which effectively distort the primary field in the direction of the flow.

Figure 1.3 Principle of eddy current flowmeter

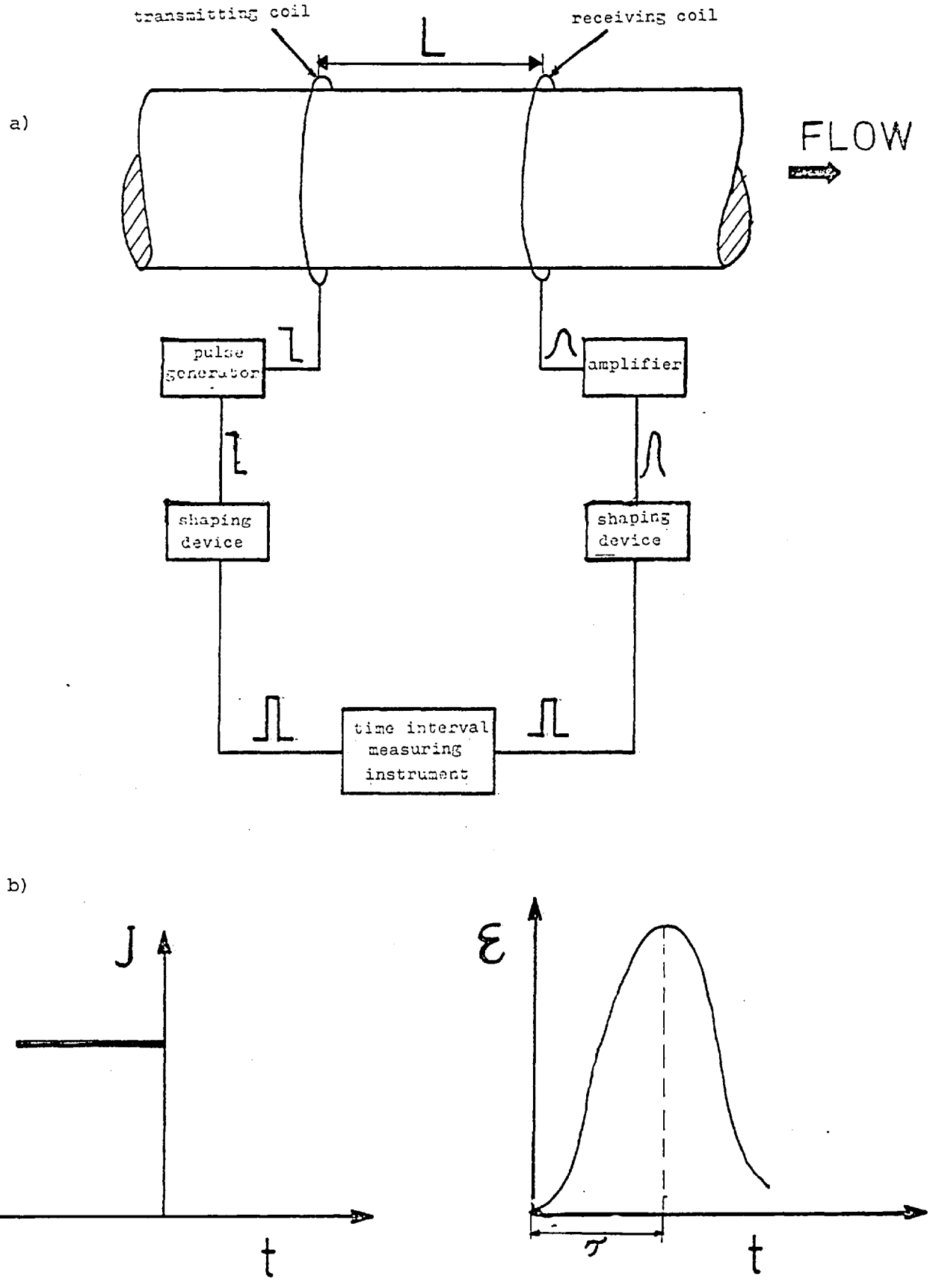

Figure 1.4 Block diagram of pulsed field flowmeter operating on the principle of recording the shift in the peak of the emf induced in the measuring coil; a – position of the coils, b – curves of the current and emf in the transmitting and receiving coils.

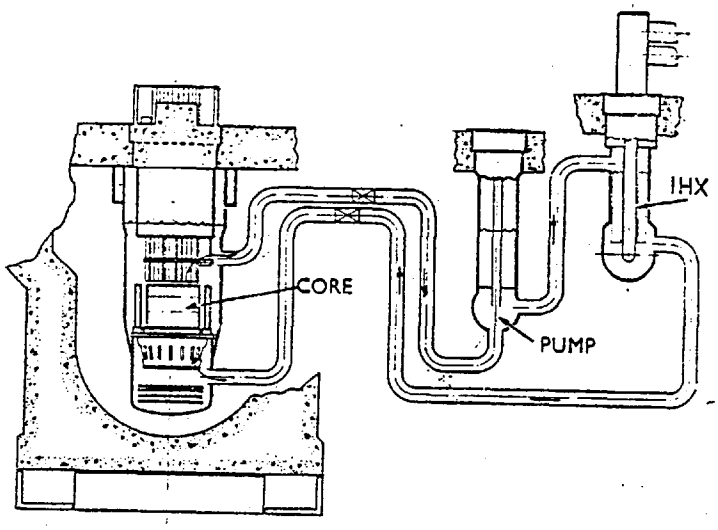

Figure 1.5 A loop-type primary system

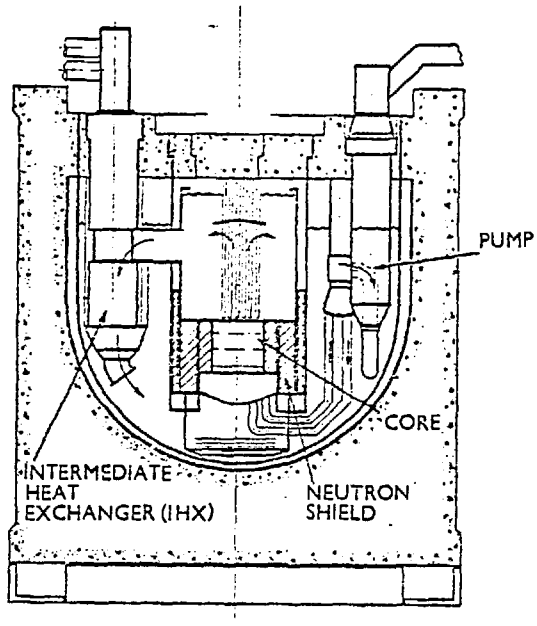

Figure 1.6 A pool-type primary system

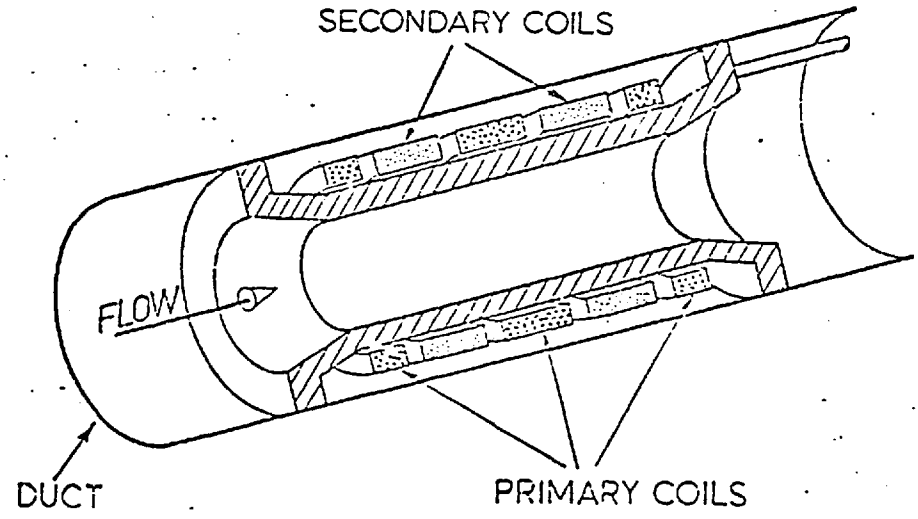

Figure 1.7 Eddy current flow through type flowmeter

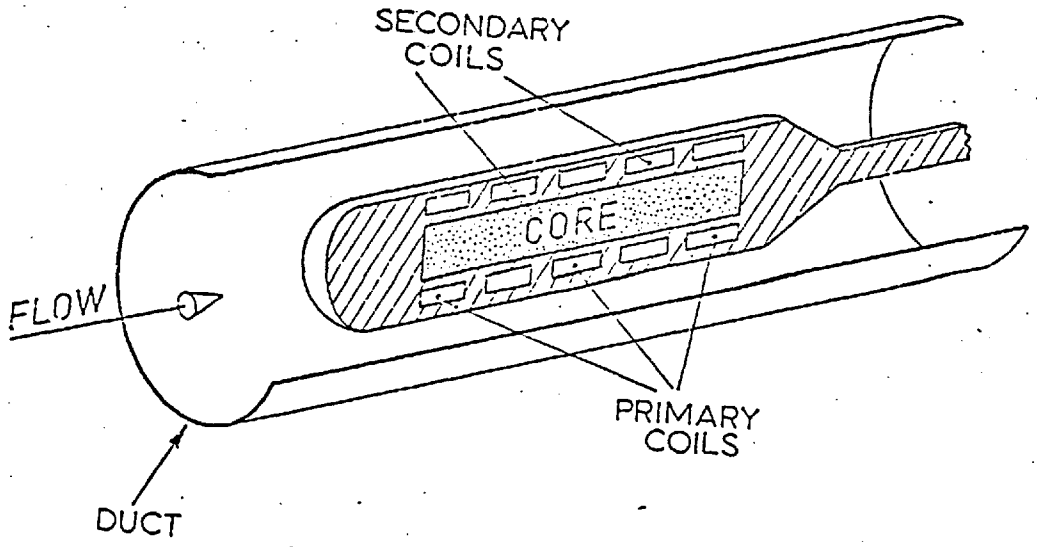

Figure 1.8 Eddy current probe-type flowmeter

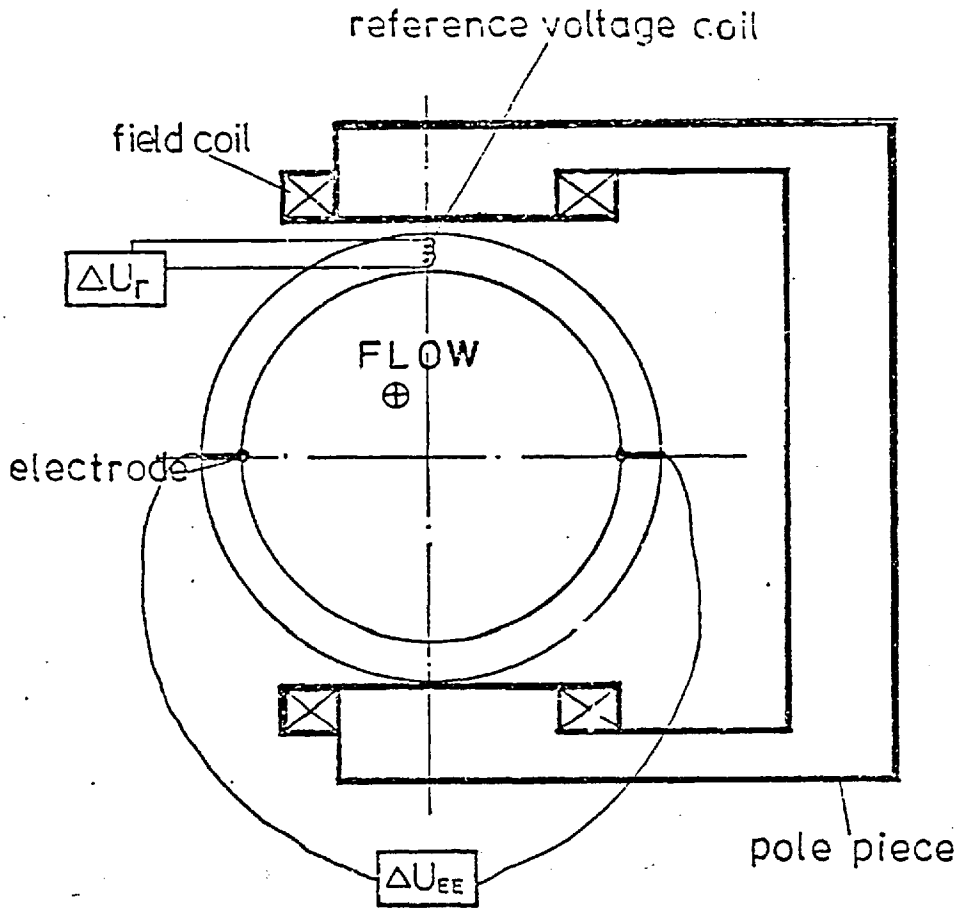

Figure 1.9 Flowmeter for magnetic slurries (Mannherz and Schmook 1968)

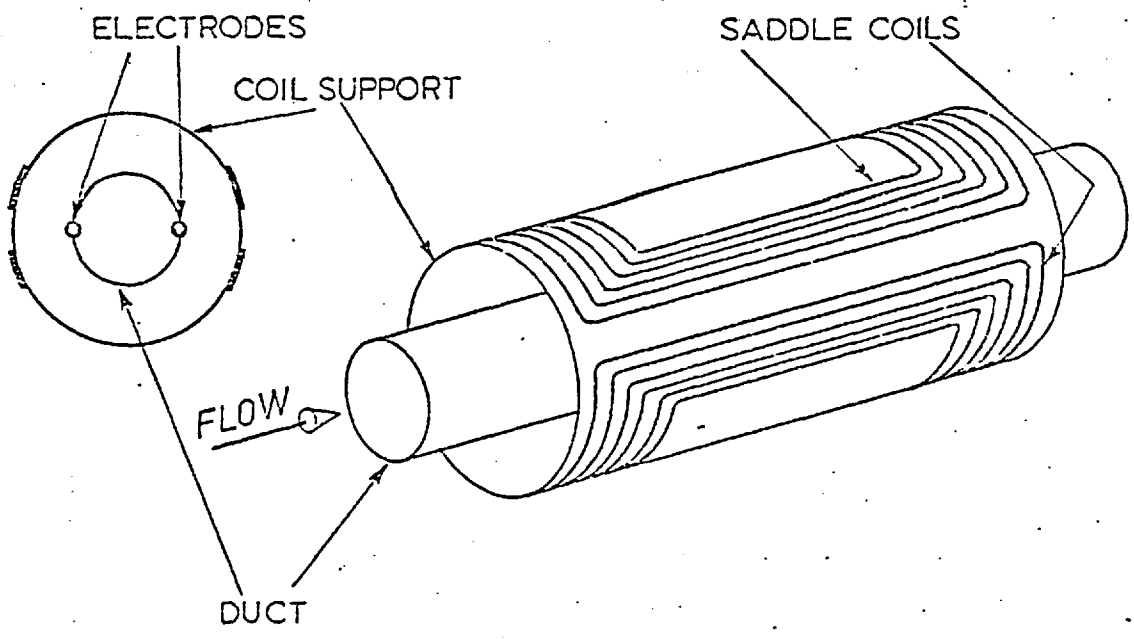

Figure 1.10 Saddle coil flowmeter

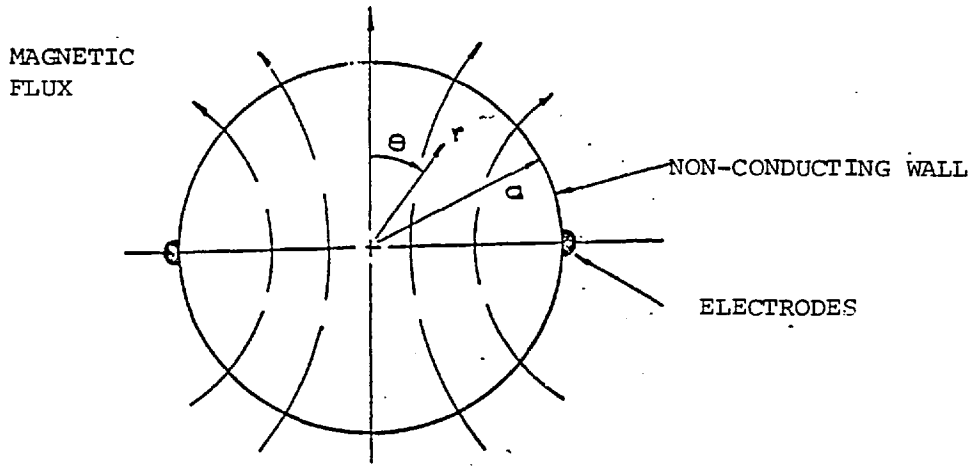

Figure 3.1 Flowmeter geometry

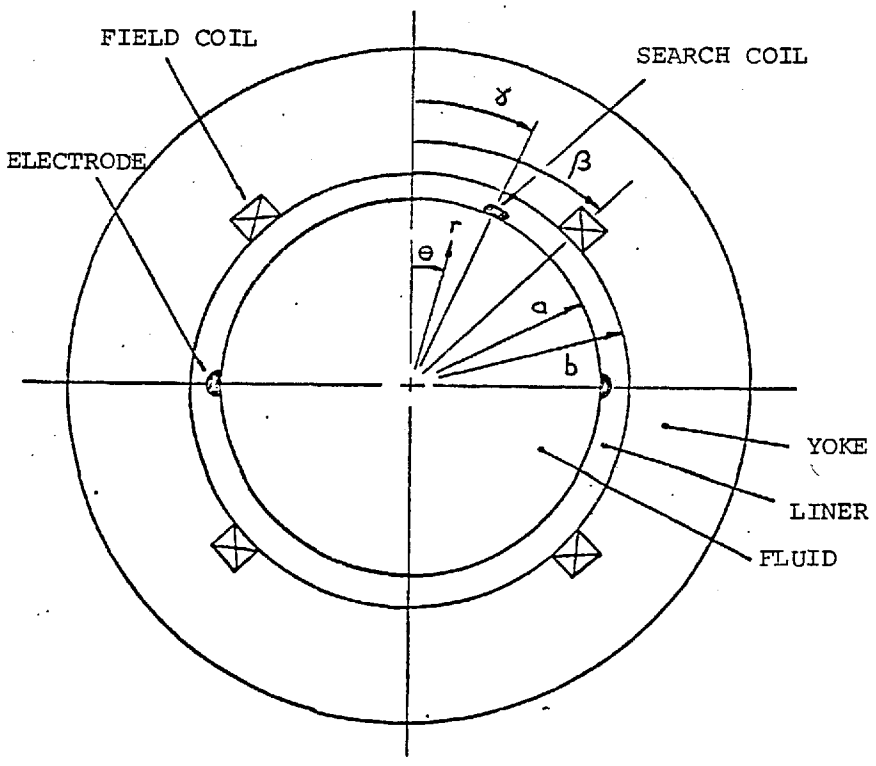

Figure 3.2 Two dimensional flowmeter for magnetic slurries

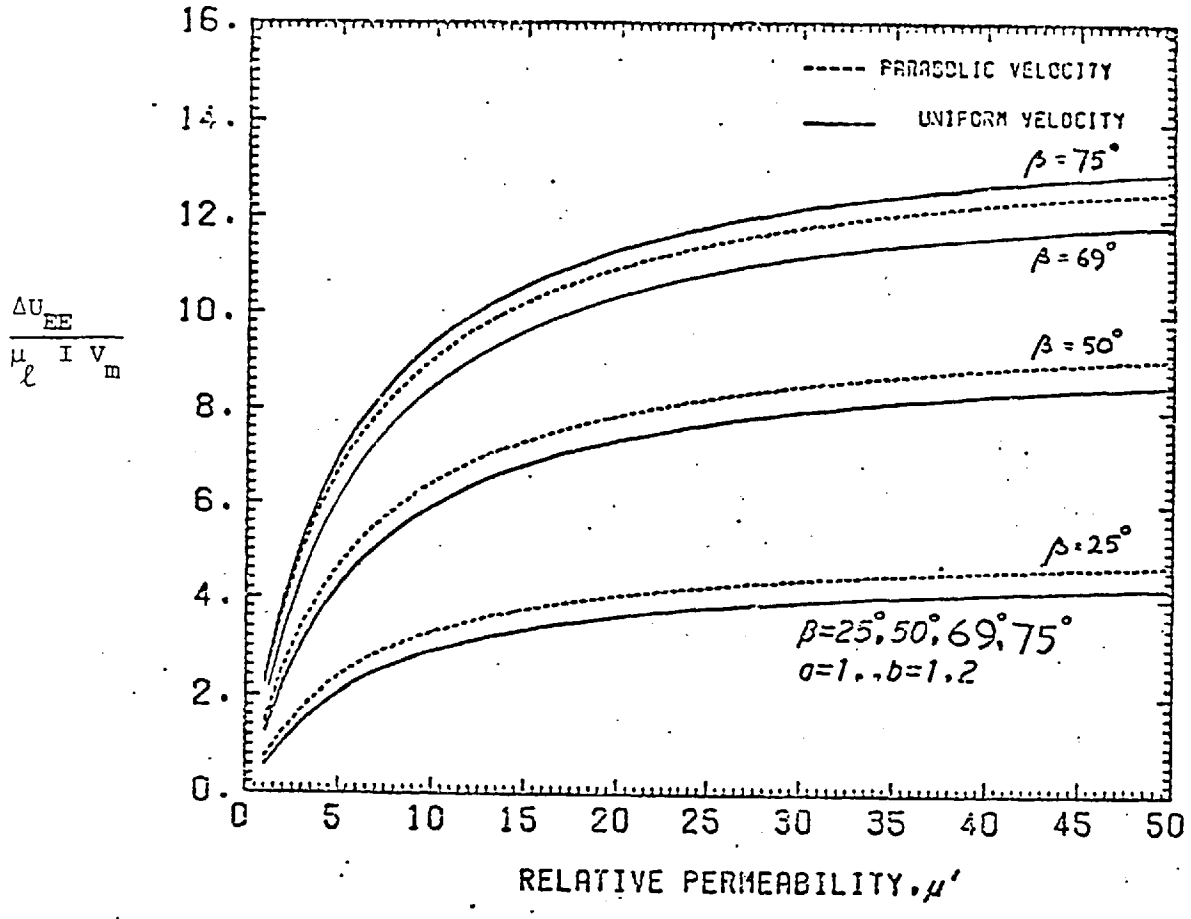

Figure 3.3 Variation with fluid permeability of the ratio (flow signal/ field current) for four field coil angles

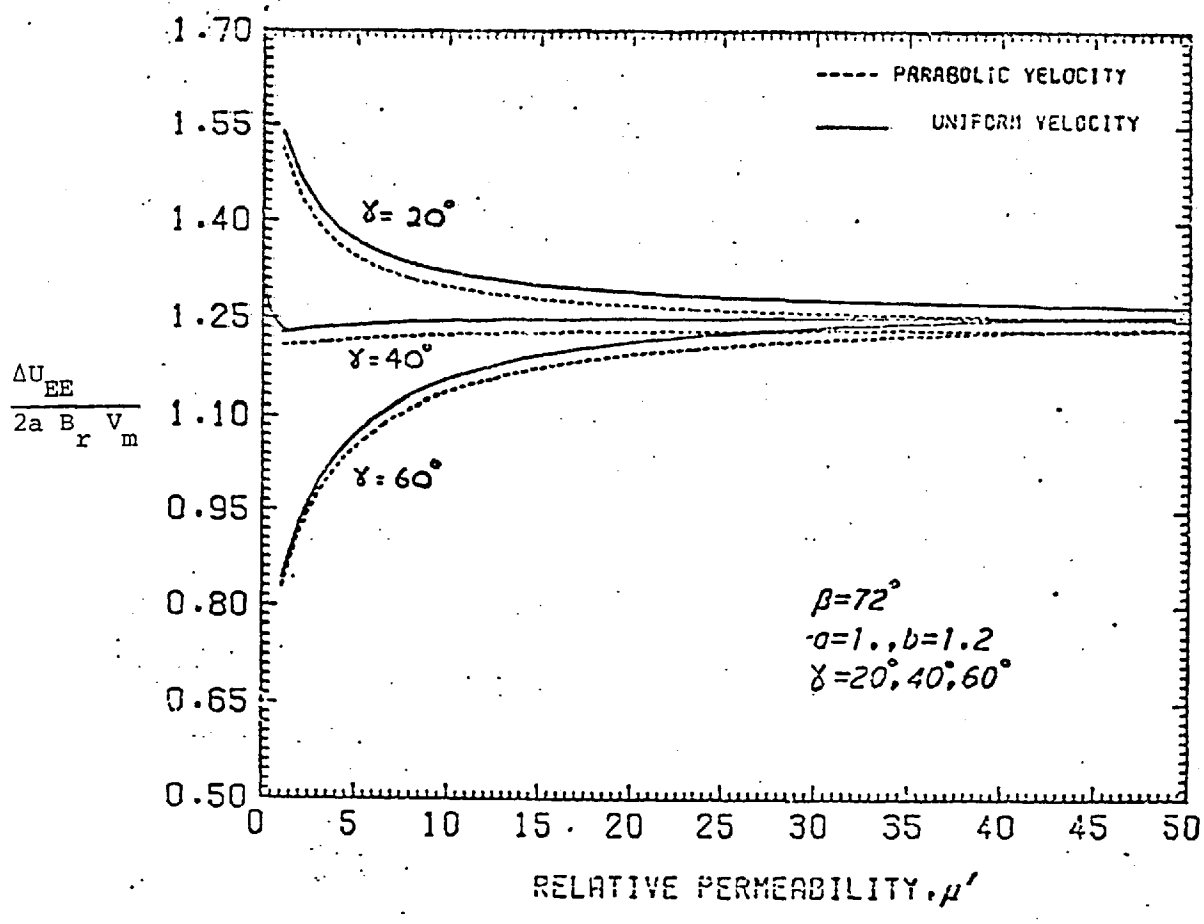

Figure 3.4 Variation with fluid permeability of the ratio (flow signal/ magnetic field search coil) for three values of search coil angles

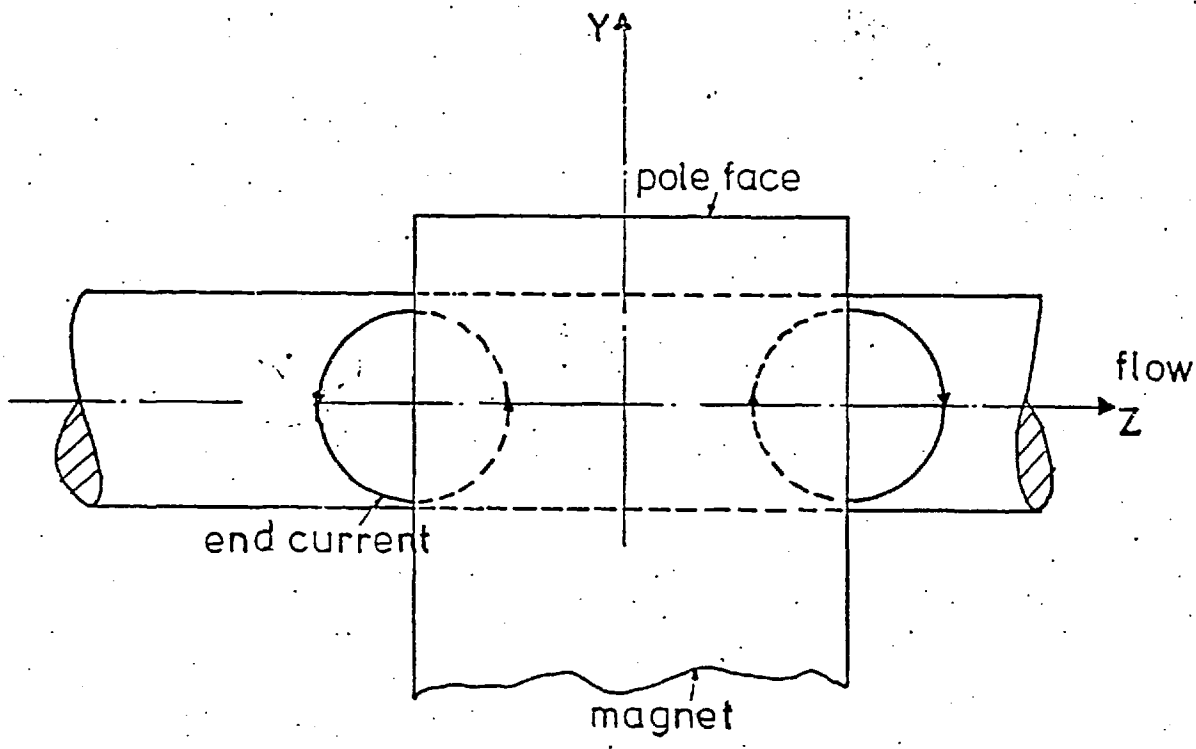

Figure 4.1 Side view of flowmeter showing current loops at the edges of the field

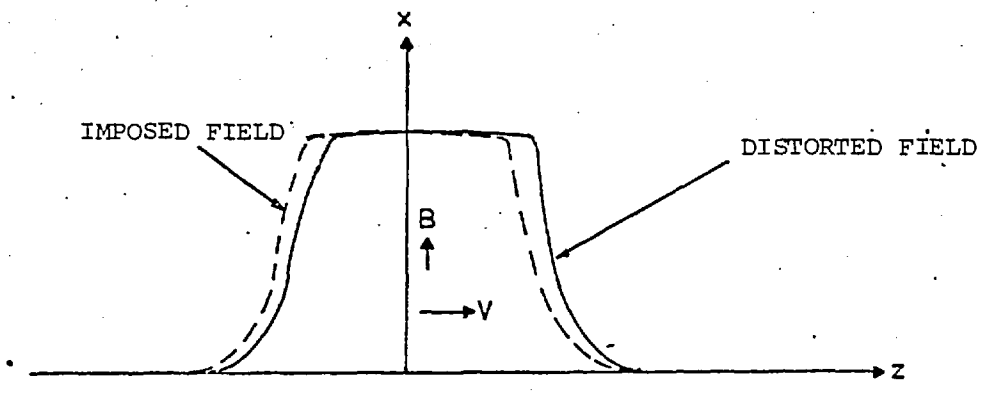

Figure 4.2 Distortion of transverse magnetic field

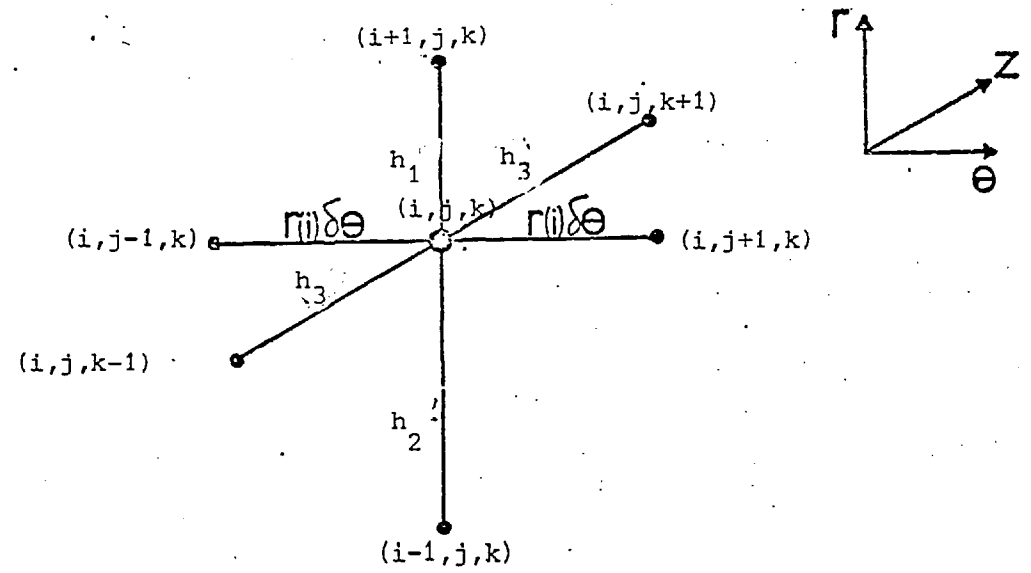

a)

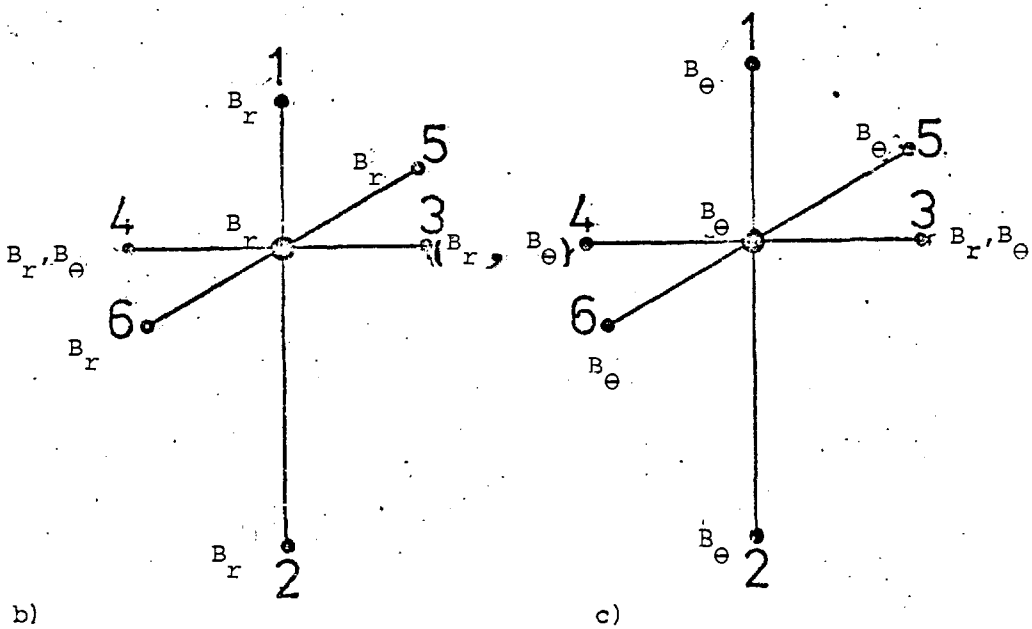

b) c)

Figure 4.3 Lattice configuration a) lattice configuration for calculating the magnetic field components, b) and c) diagram showing the magnetic field components required at neighbouring points to calculate the magnetic field components at the centre point

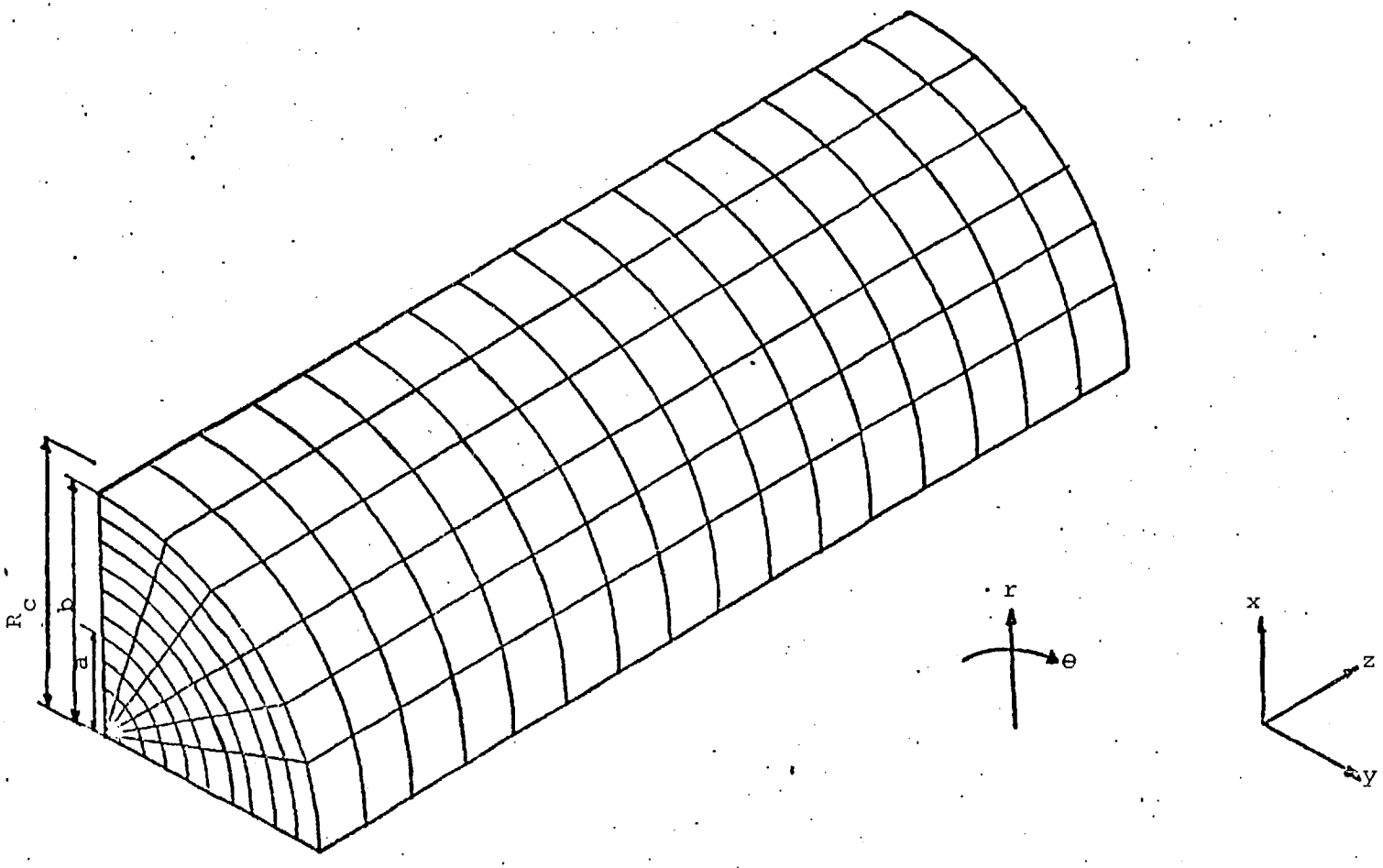

Figure 4.4 Typical lattice arrangement for numerical analysis

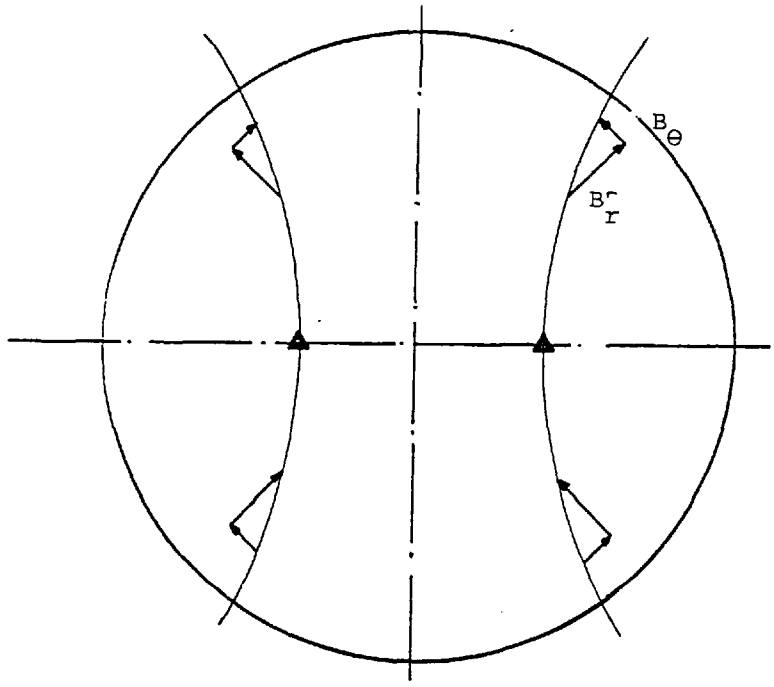

Figure 4.5 To show the direction and symmetry of magnetic field components at cross-section of coil

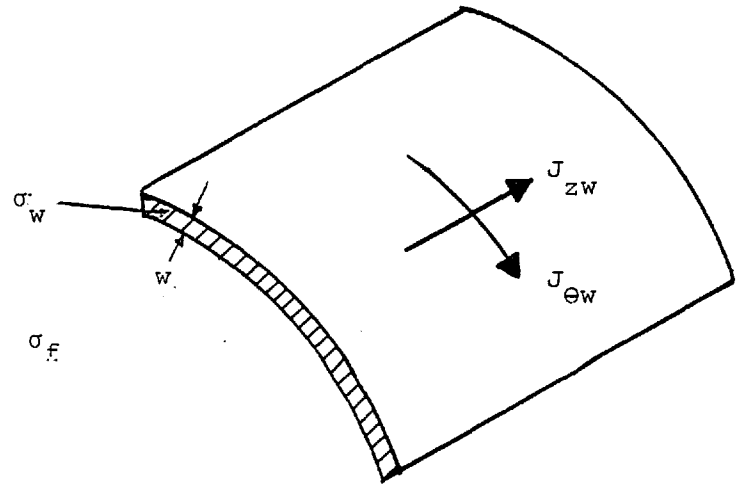

Figure 4.6 Portion of the thin conducting wall

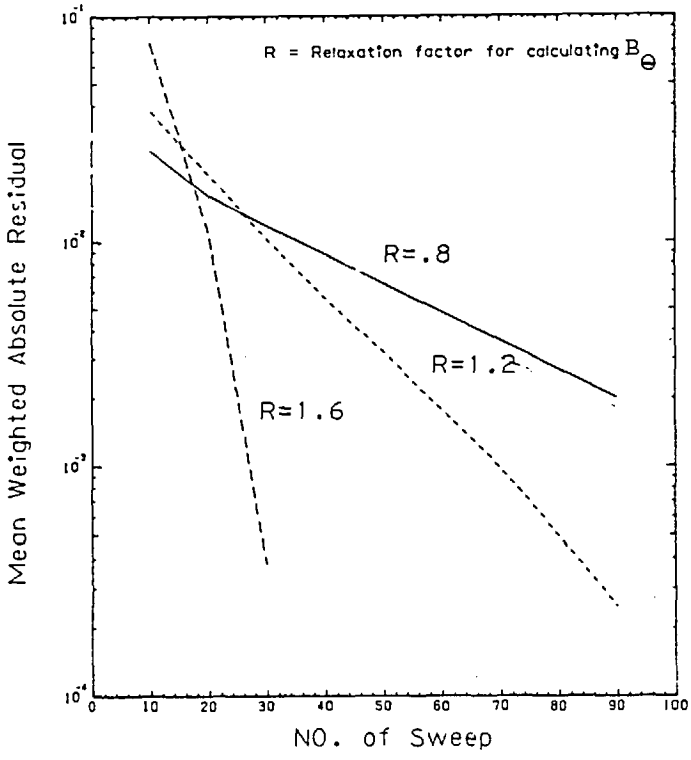

Figure 4.7 The mean weighted absolute residual VS. no. of sweep

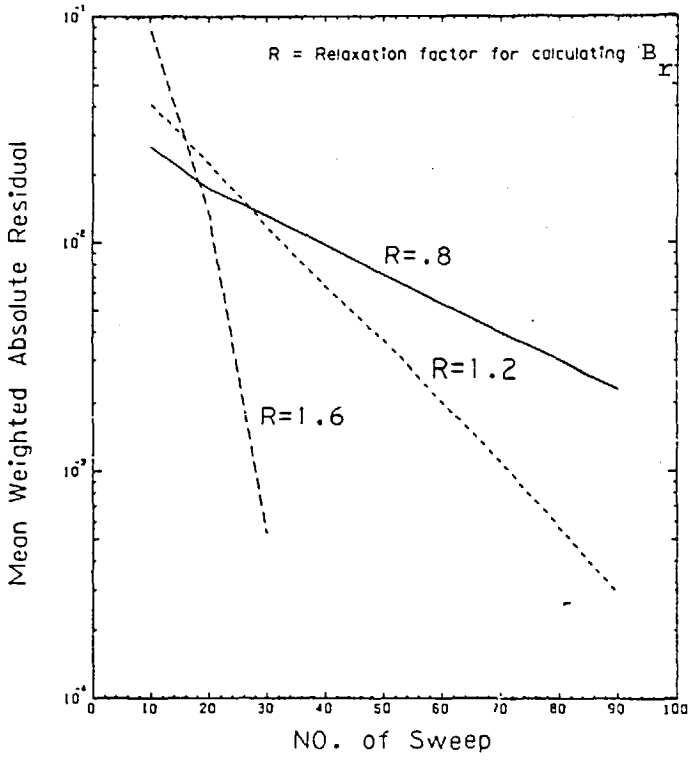

Figure 4.8 The mean weighted absolute residual VS. no. of sweep

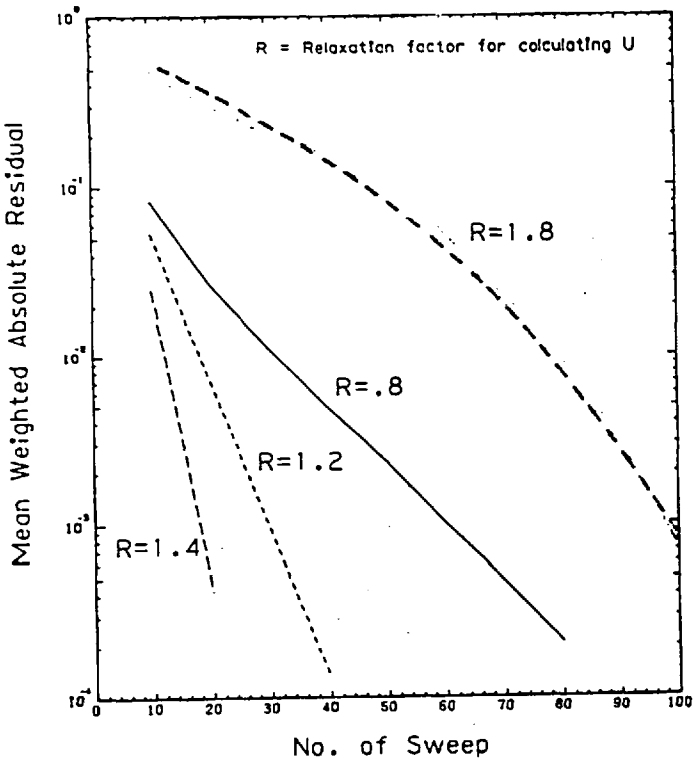

Figure 4.9 The mean weighted absolute residual VS. no. of sweep

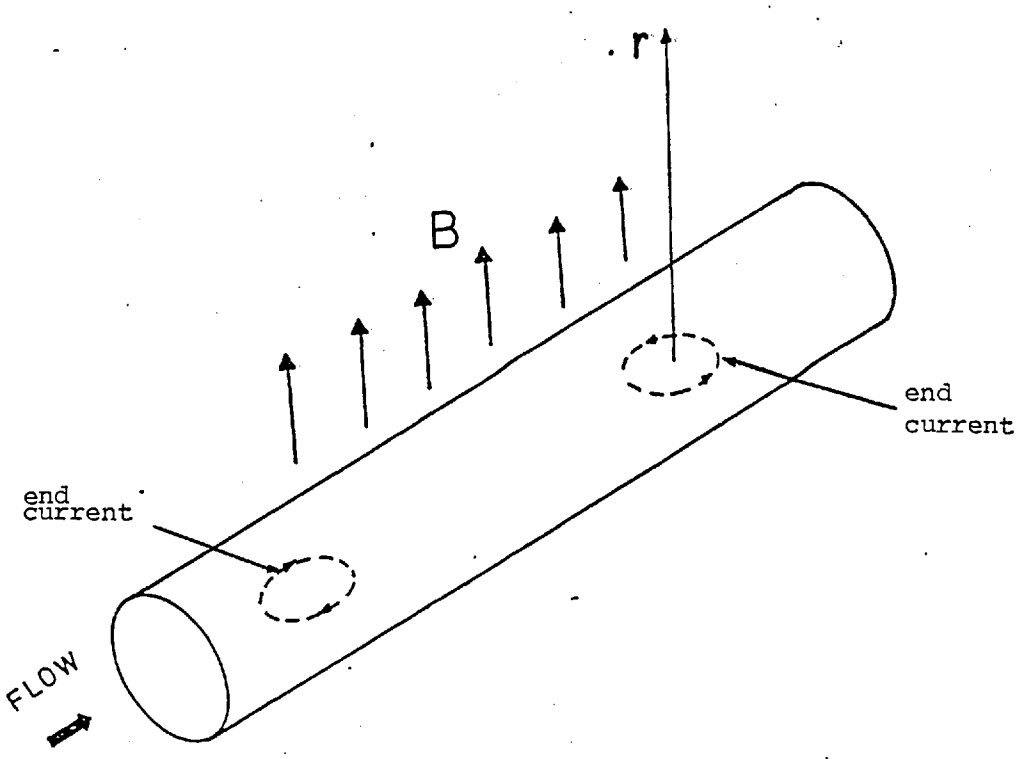

Figure 4.10 View of flowmeter showing current loop at the edges of the field.

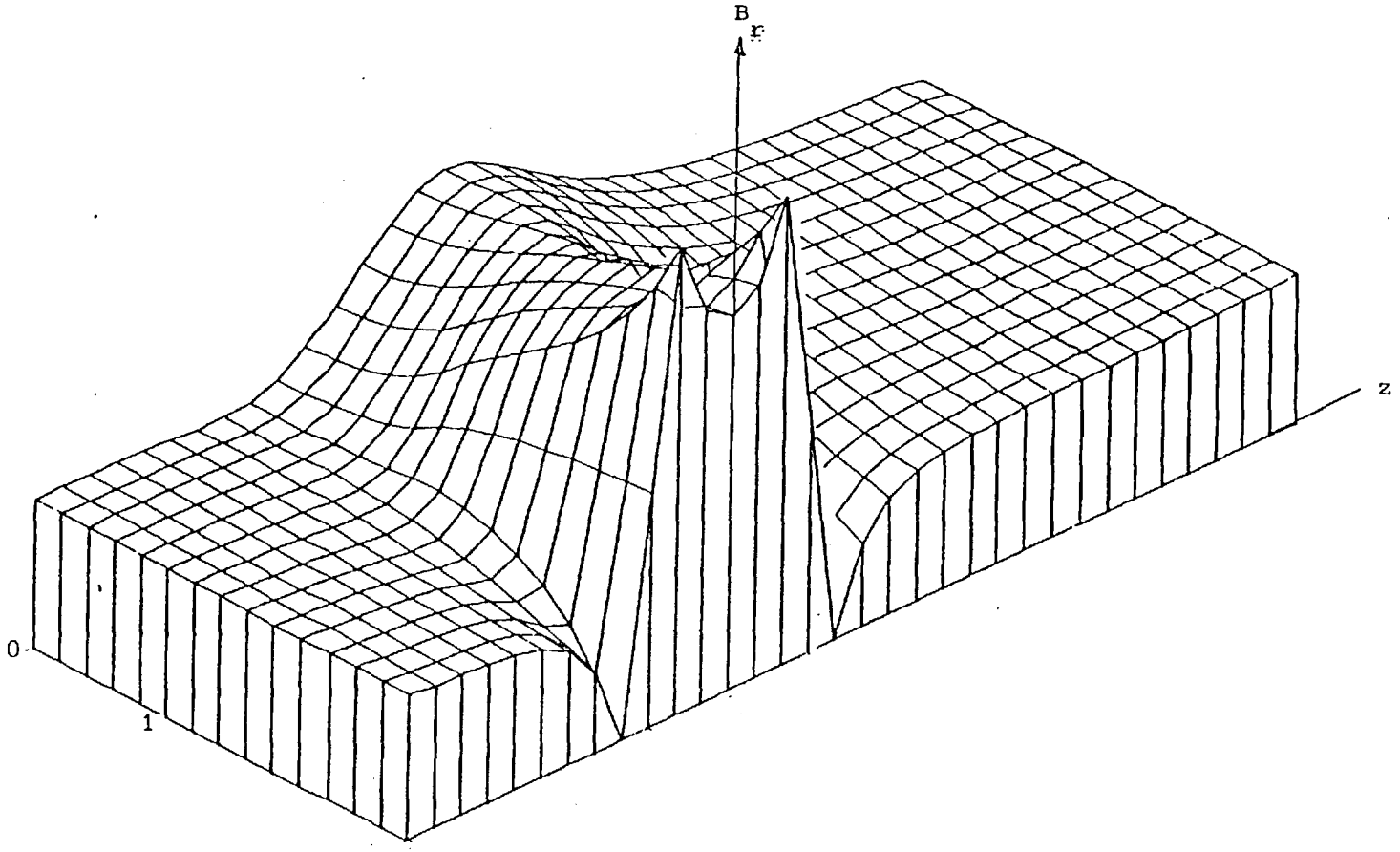

Figure 4.11 Magnetic field distribution in the plane, $\theta = 0$

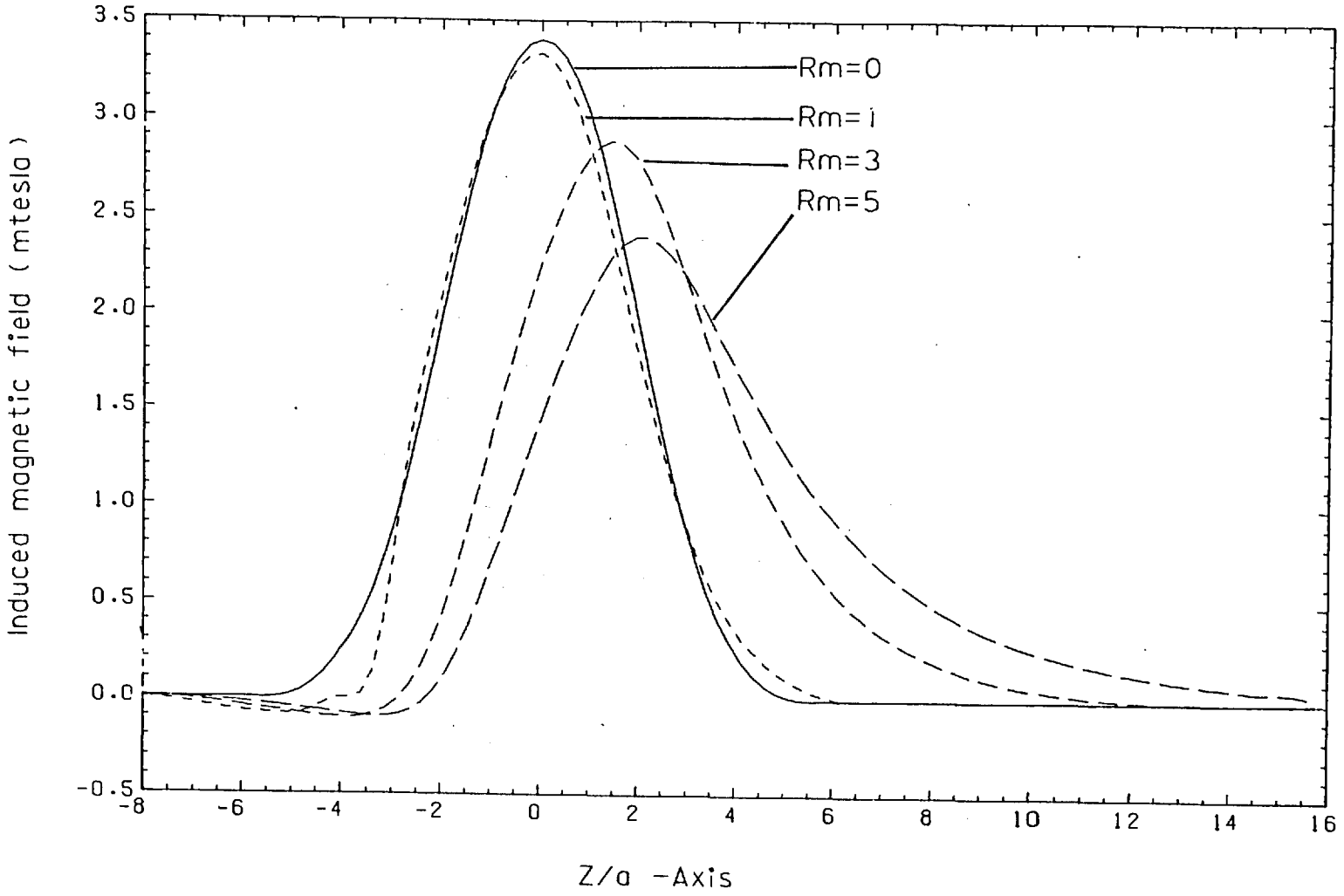

Figure 4.12 Magnetic field distribution at the centre line of pipe, uniform velocity

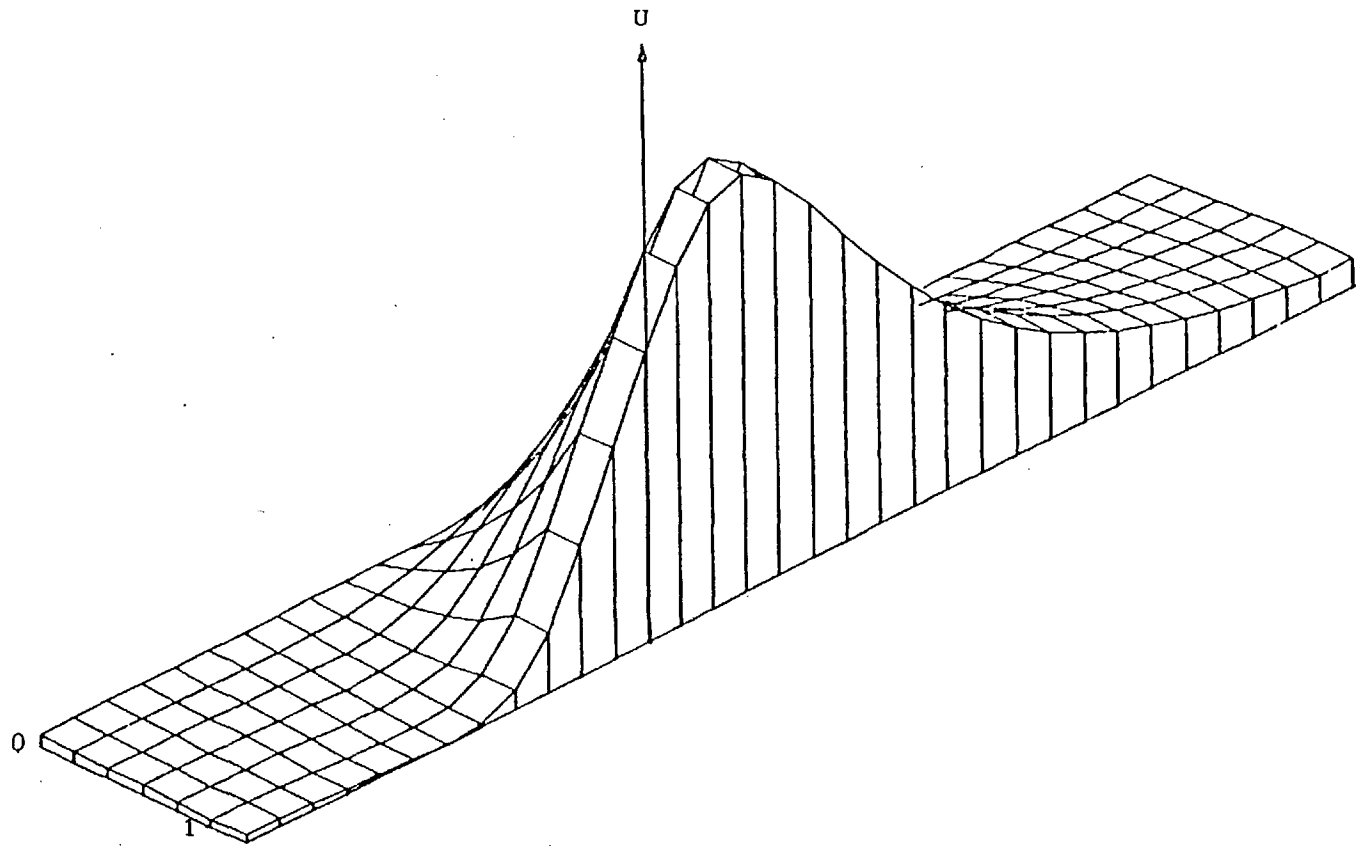

Figure 4.13 Induced voltage distribution in the plane, $\Theta = \pi/2$

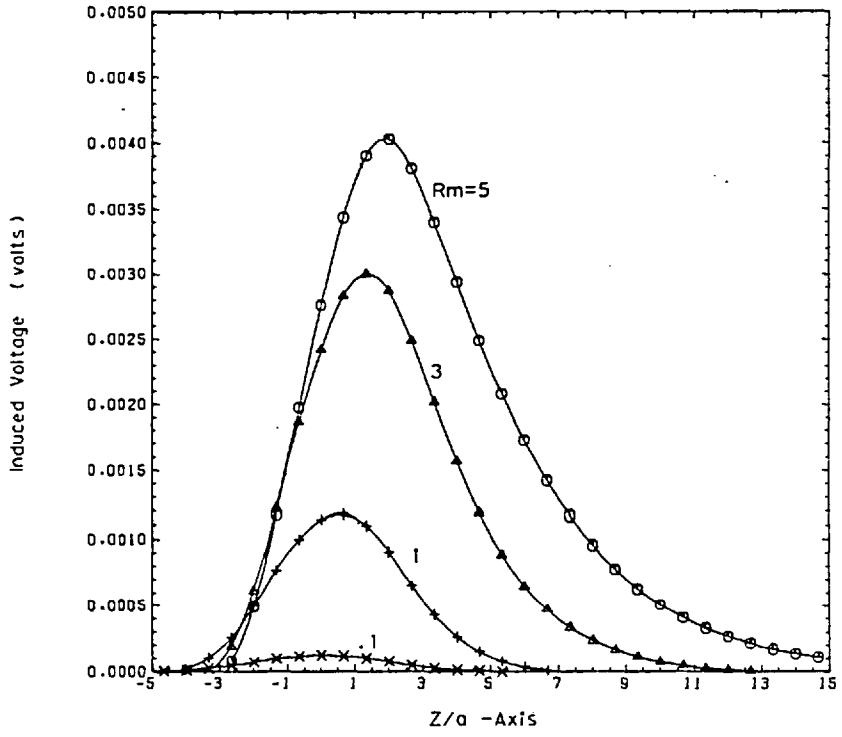

Figure 4.14 Induced voltage distribtuion along z-axis, d = .044 C_r = 0 and uniform velocity

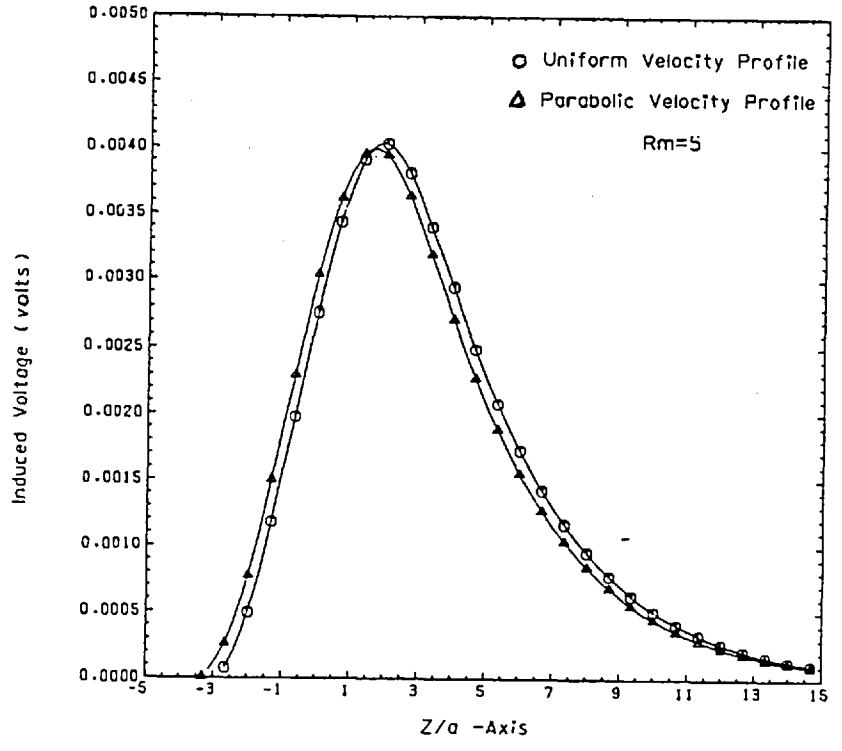

Figure 4.15 Induced voltage distribution along z-Axis, d = .044 and C_r = 0

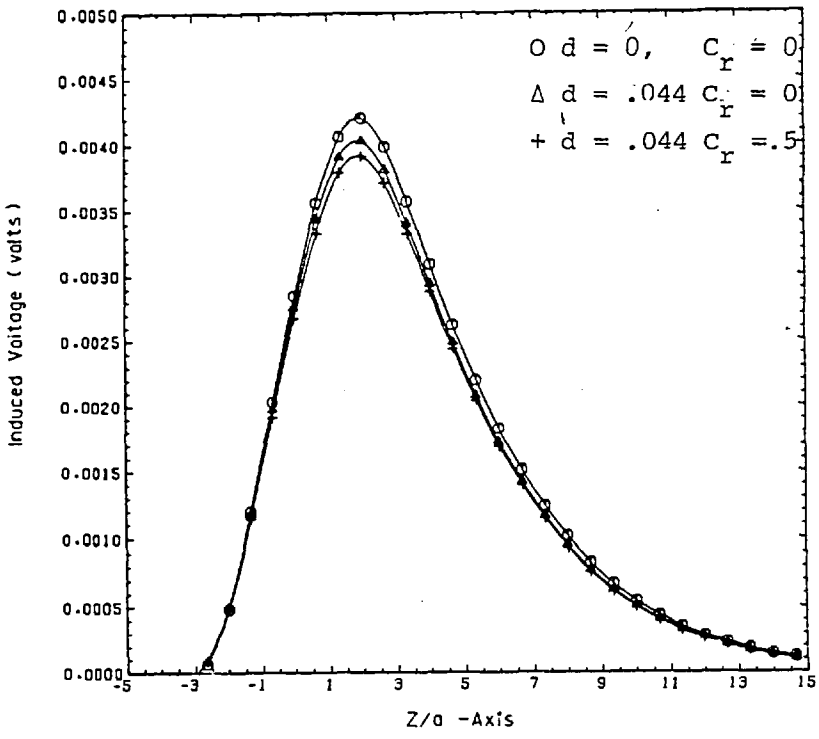

Figure 4.16 Effect of the wall conductivity no. d, and the contact resistance no. C_r on the induced voltage

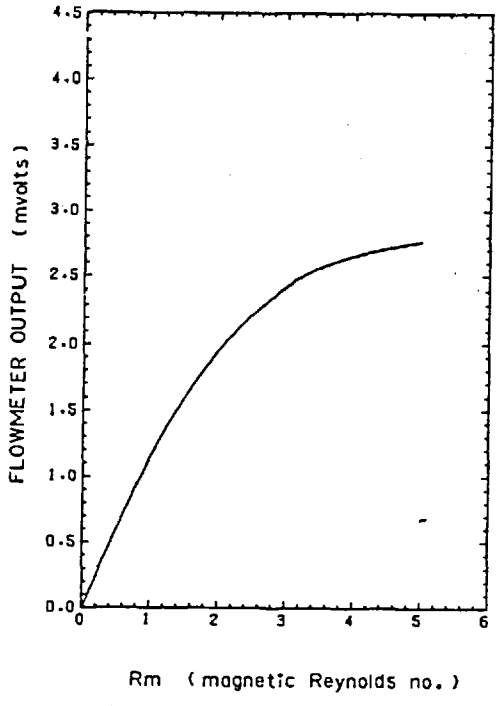

Figure 4.17 Flowmeter output from centre electrodes

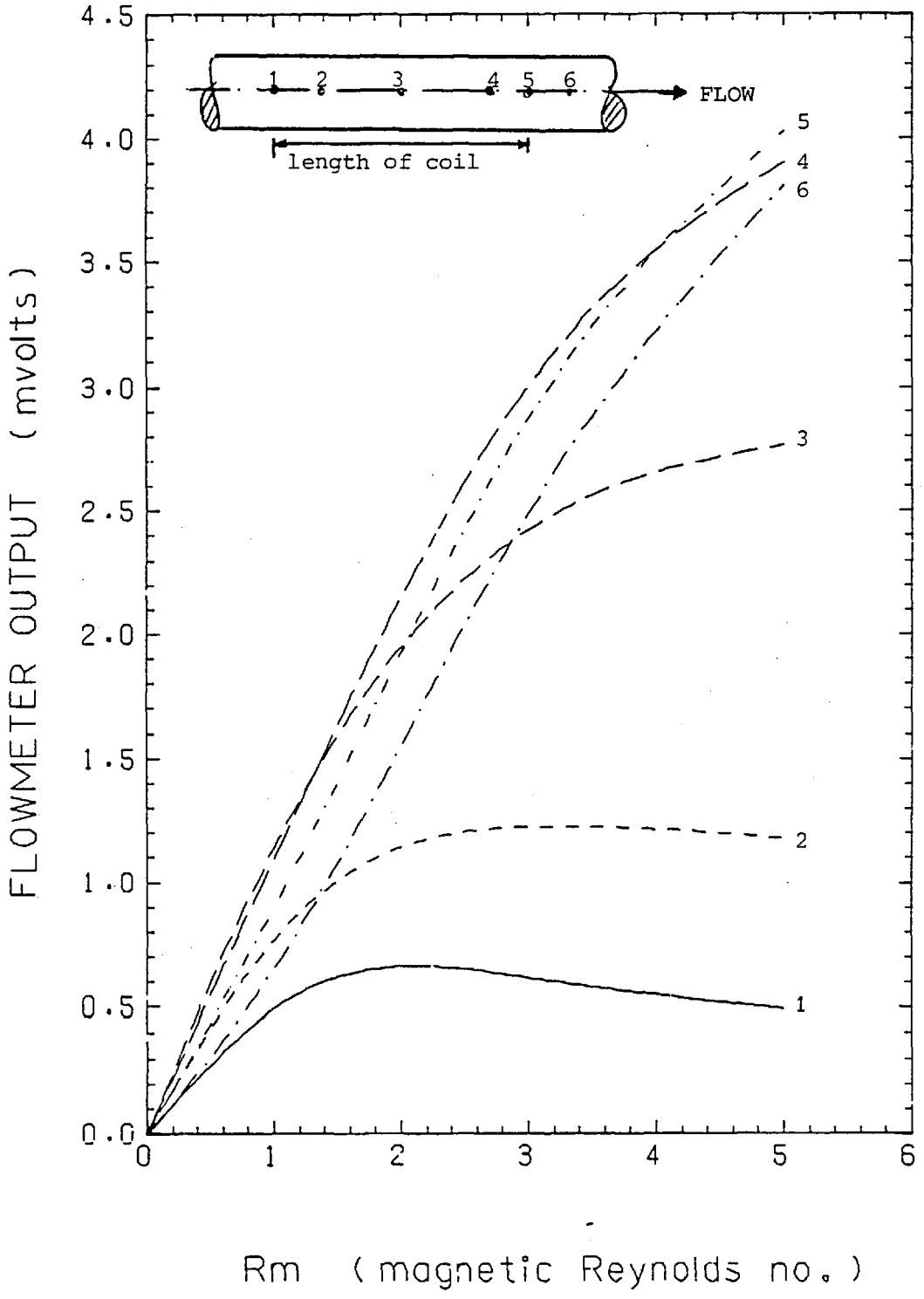

Figure 4.18 Flowmeter output from six electrode locations

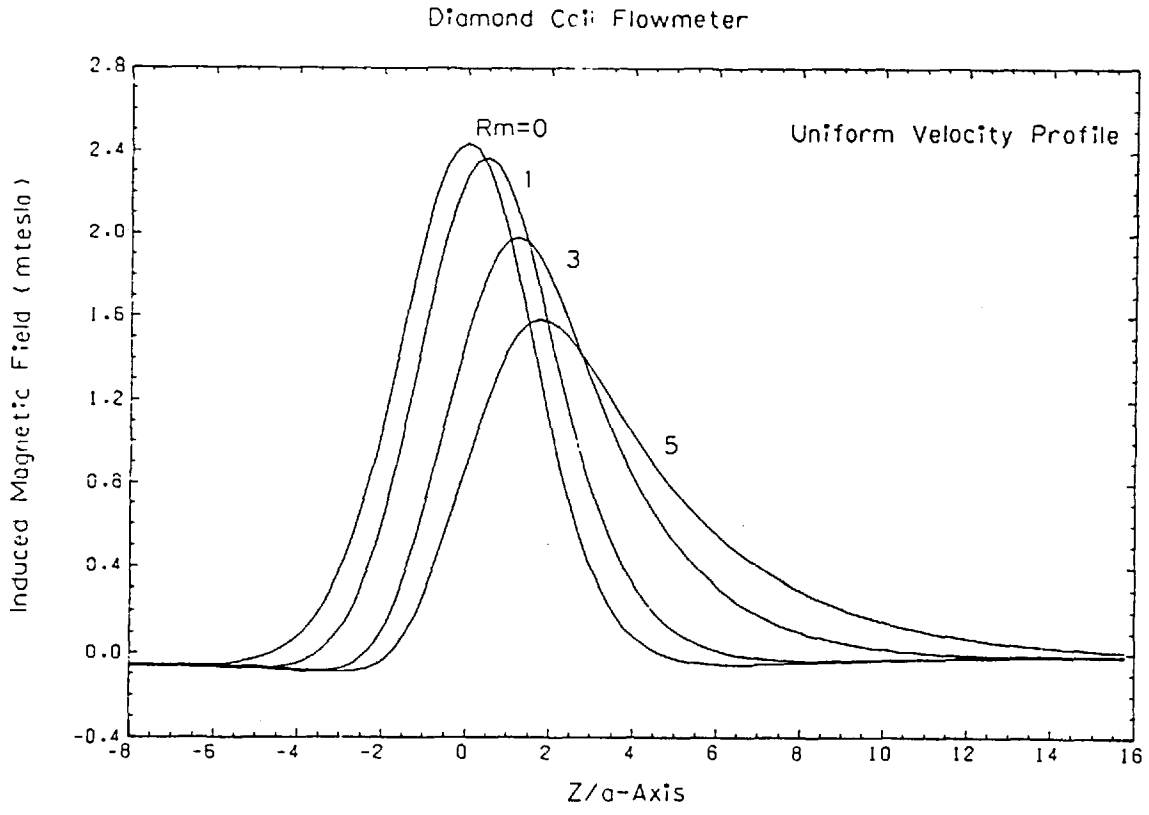

Figure 4.19 Induced magnetic field distribution along z-axis

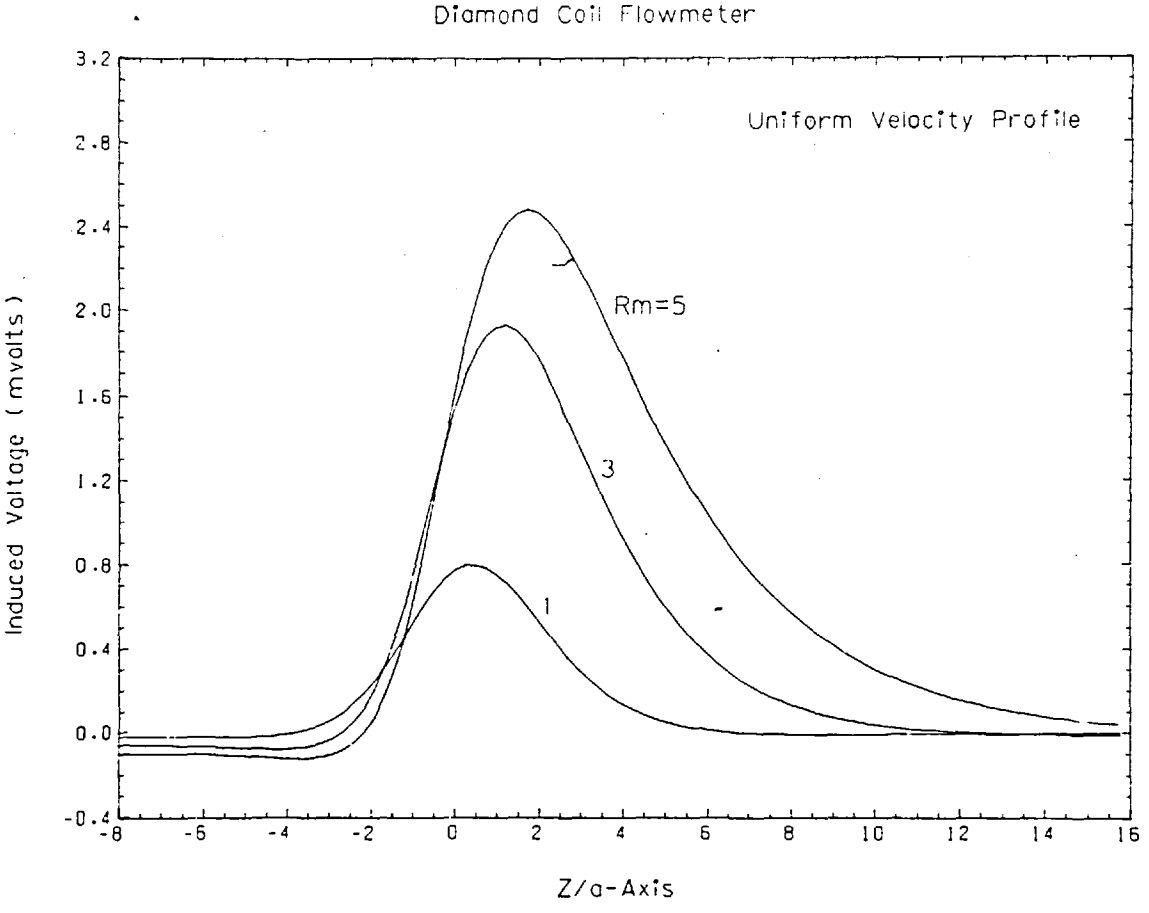

Figure 4.20 Induced voltage distribution along z-axis

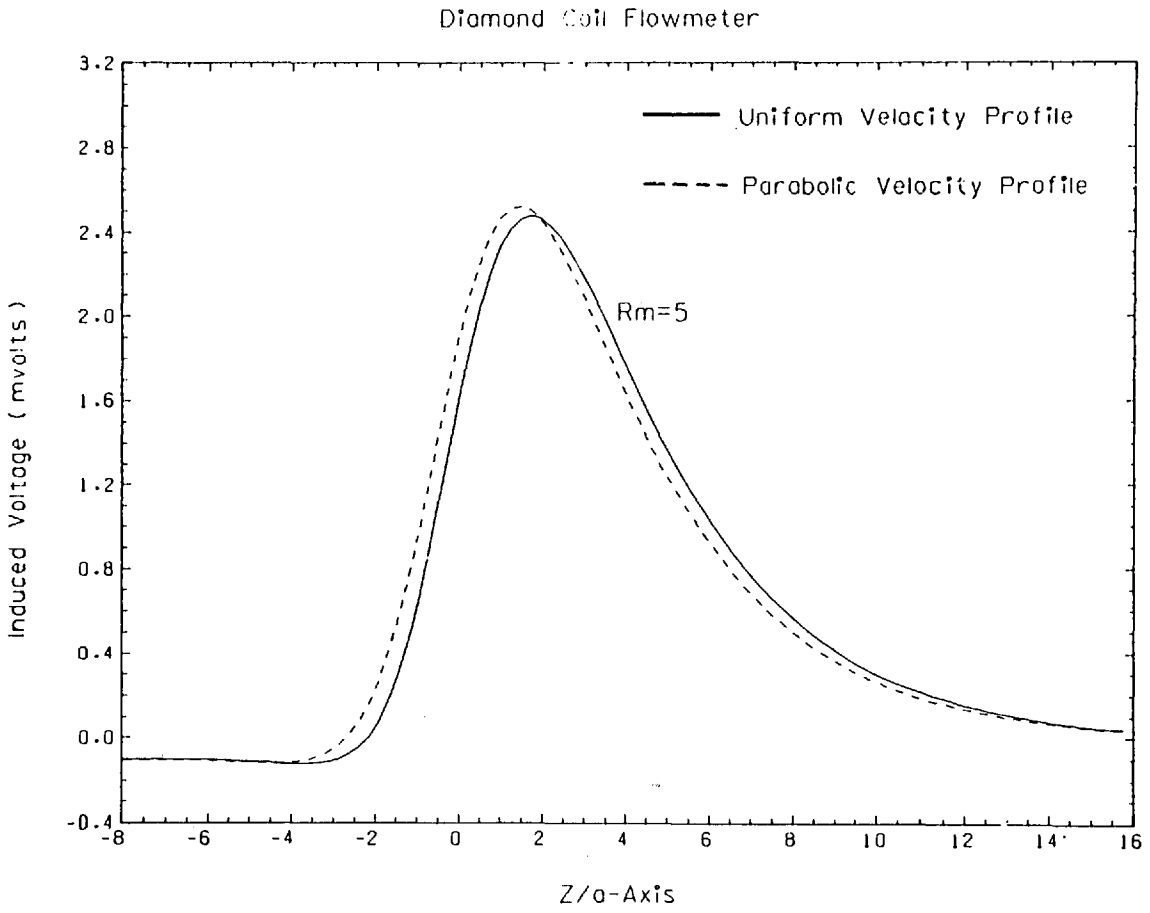

Figure 4.21 Induced voltage distribution along z-axis

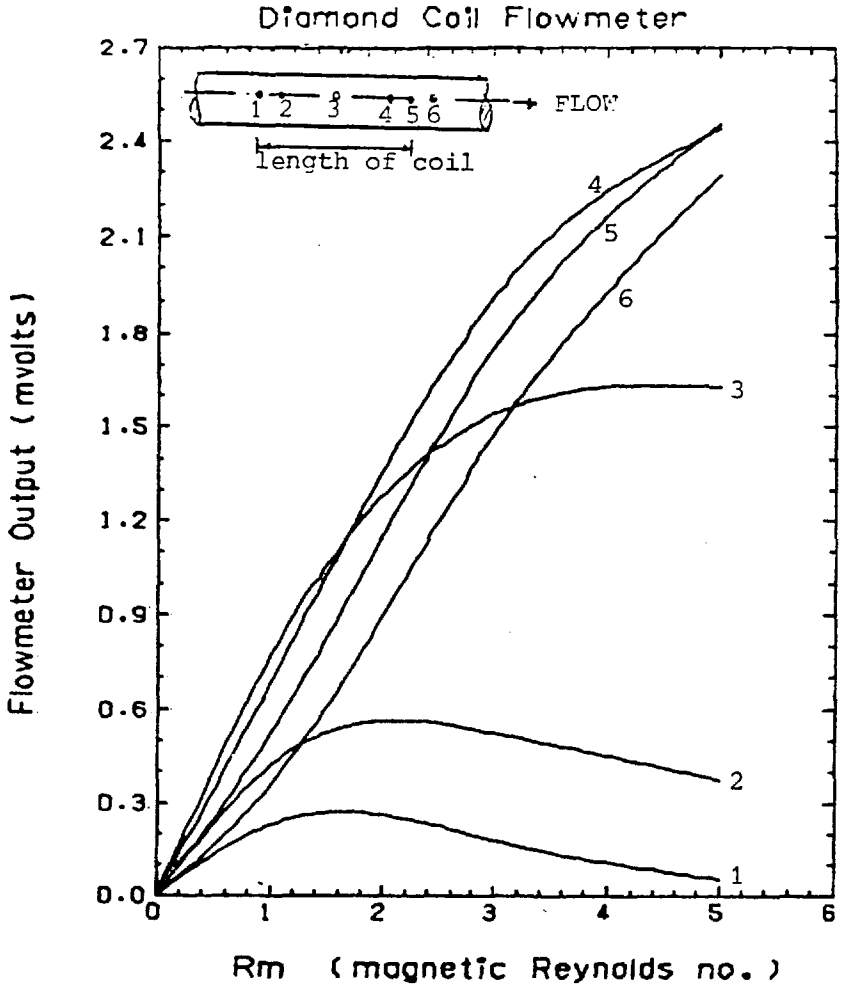

Figure 4.22 Flowmeter output from six electrode locations

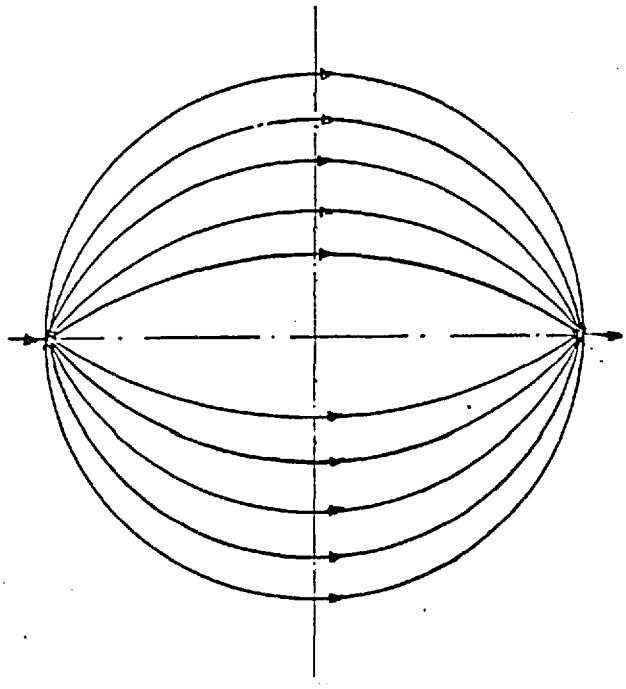

a) Section perpendicular to flow (on xx')

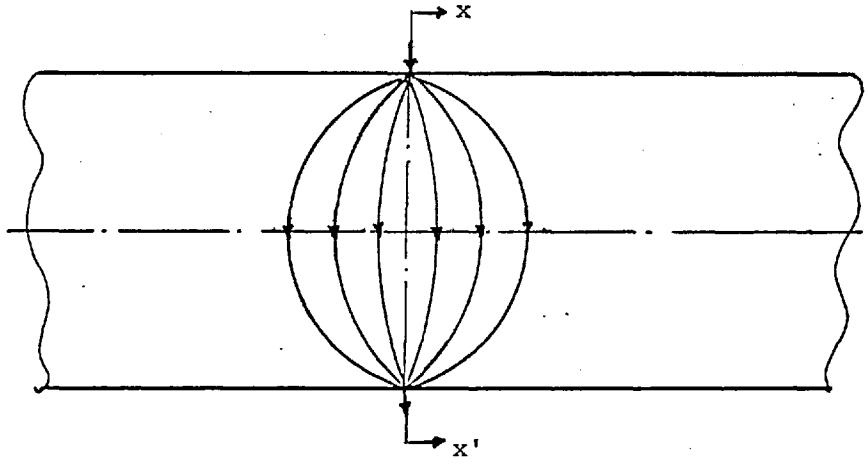

b) Section perpendicular to magnetic field

Figure 5.1 The virtual current lines for circular conducting thin wall flowmeter with point electrodes

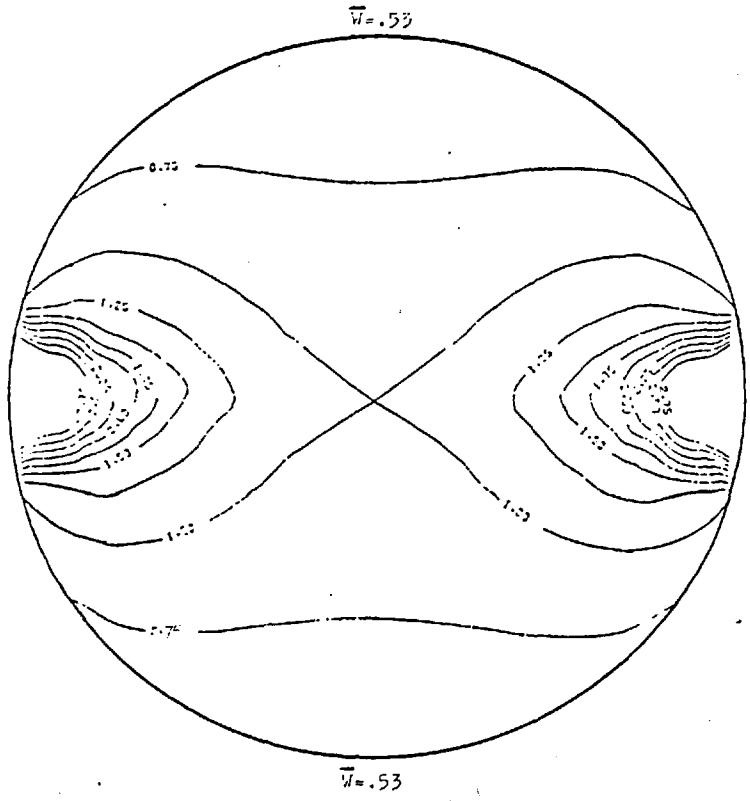

Figure 5.2 $\bar{W}$-distribution at the cross section of pipe with a saddle coil, electrode positioned at the middle, no flow (R_m = 0), wall conductivity no. = .044, and no contact resistance.

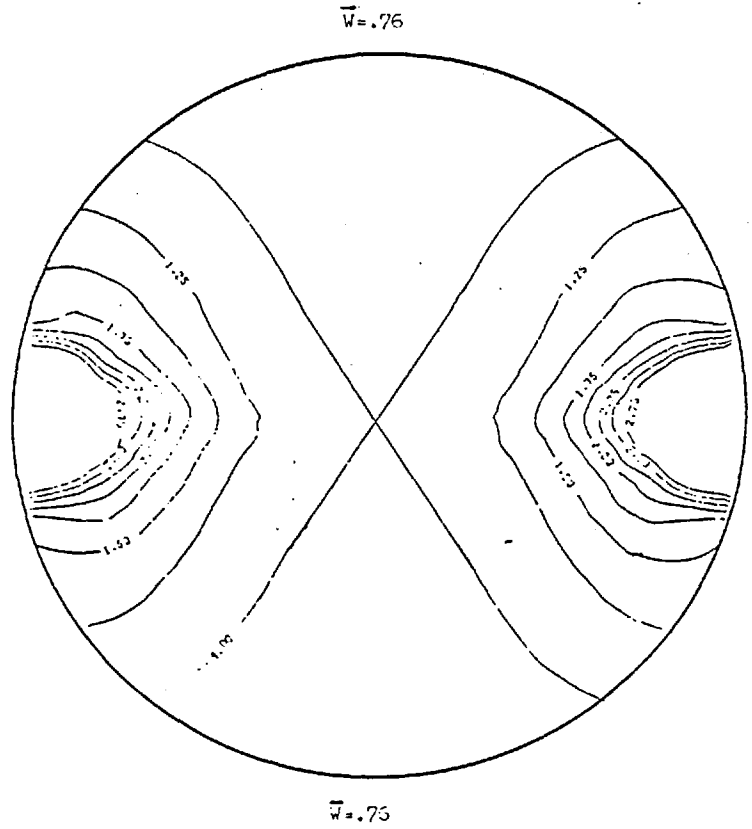

Figure 5.3 $\bar{W}$-distribution at the cross section of pipe using a saddle coil, electrode positioned at the middle, R_m = 5, wall conductivity no. = .044 and no contact resistance

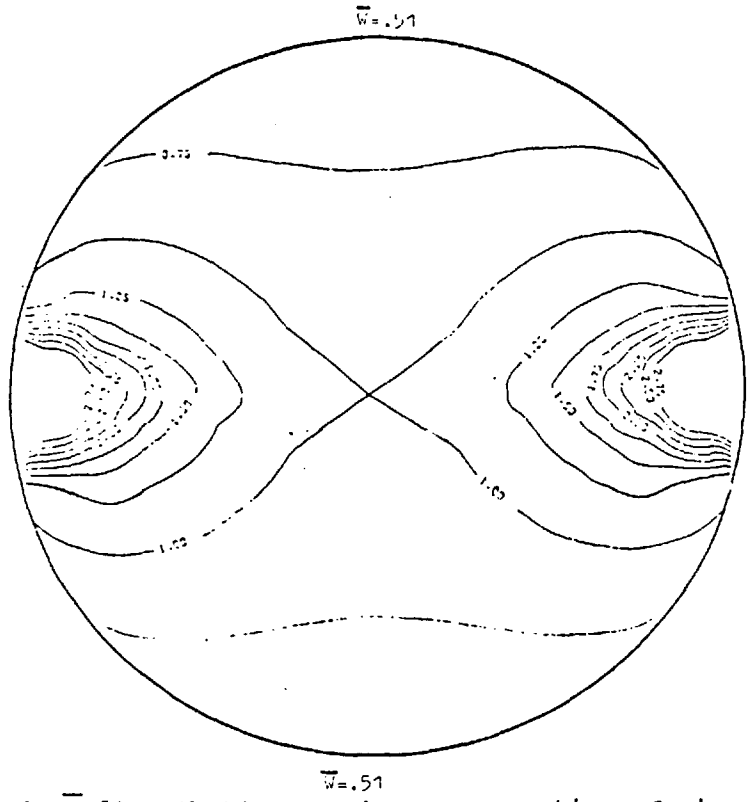

Figure 5.4 $\overline{W}$-distribution at the cross section of pipe with a saddle coil, electrode positioned at the edge of field, calculations were made for $R_m = 0$ and $R_m = 5$ and the distribution of $\overline{W}$ was the same for both, wall conductivity no. = .044 and no contact resistance

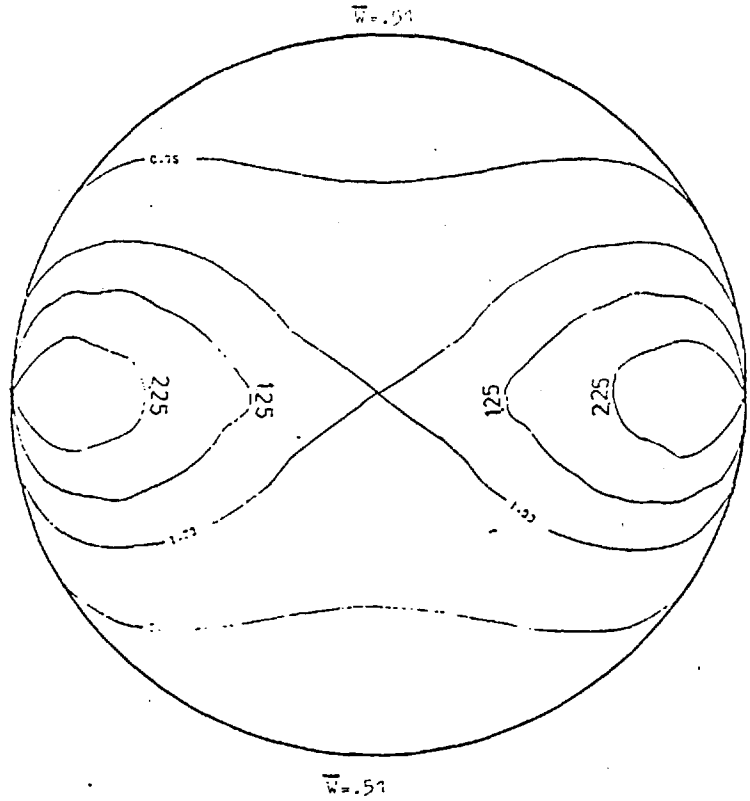

Figure 5.5 $\overline{W}$-distribution at the cross section of pipe using a saddle coil, wall conductivity no. = 0, and no contact resistance

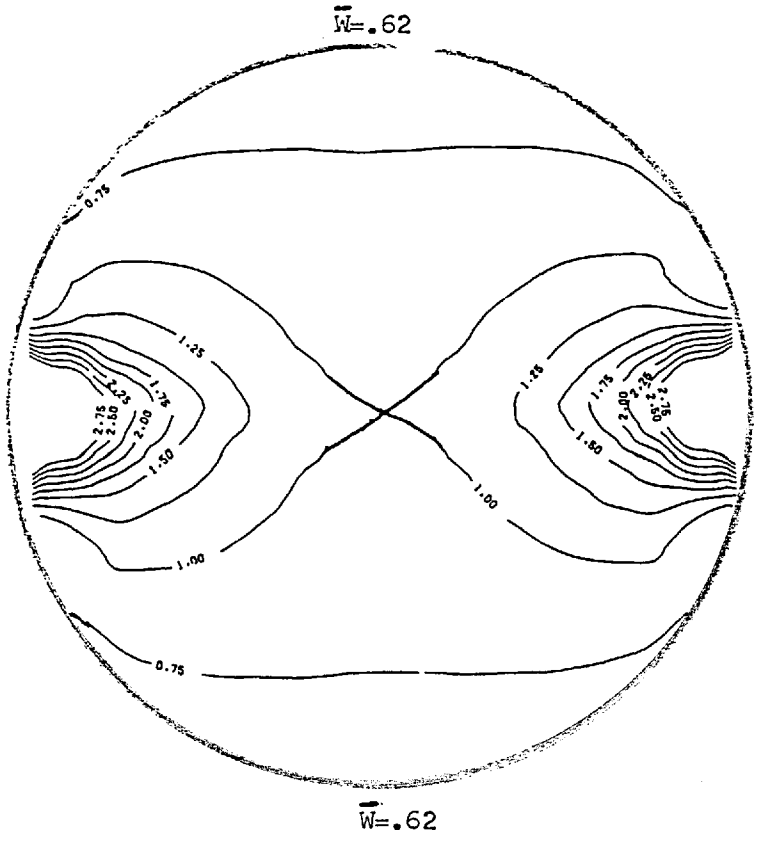

Figure 5.6 $\bar{W}$-distribution at the cross-section of pipe with a diamond coil, electrode positioned at the middle, no flow (R_m = 0), wall conductivity no. = .044, and no contact resistance.

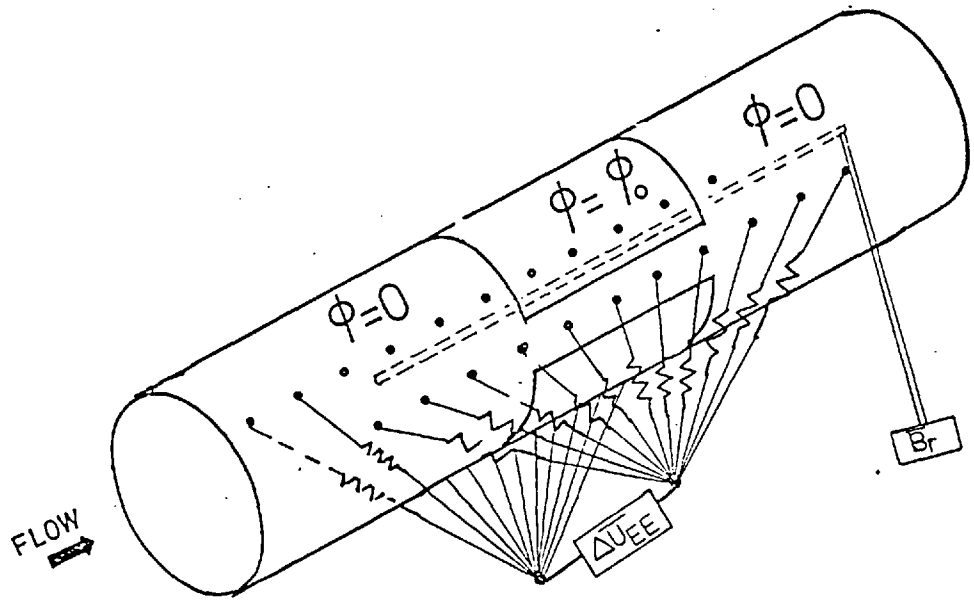

Figure 6.1 Electromagnetic flowmeter design which measures the flowrate independent of fluid properties (magnetic property and electrical conductivity)

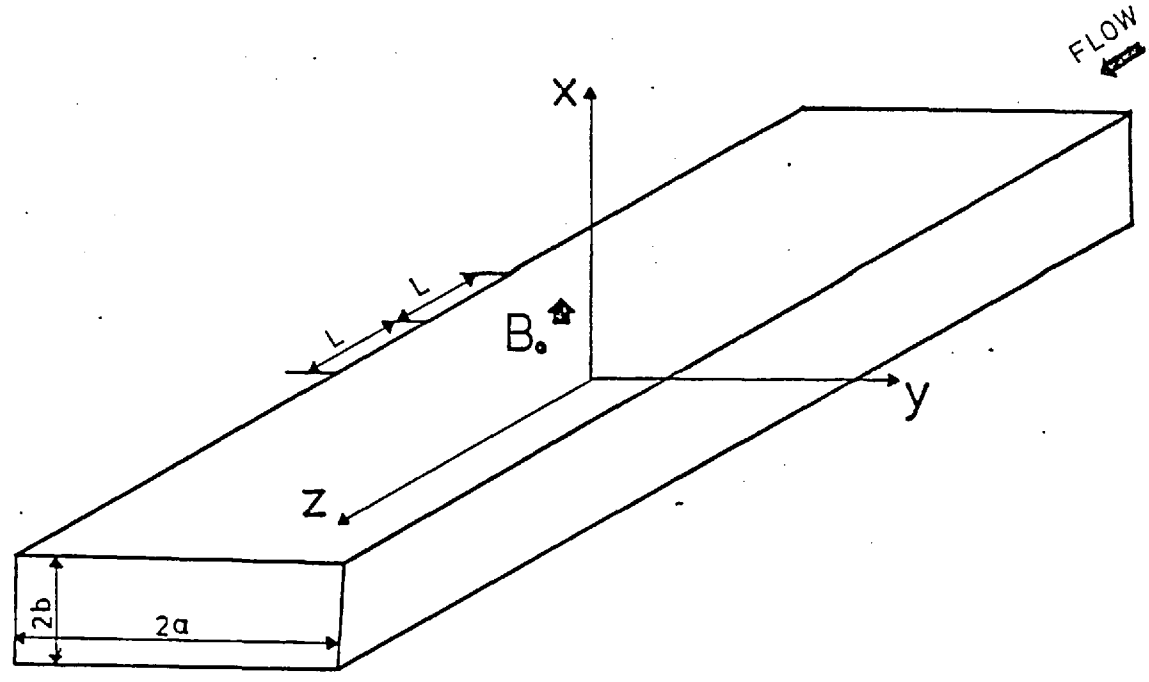

Figure 6.2 Electromagnetic flowmeter model used by Thatcher (1971)

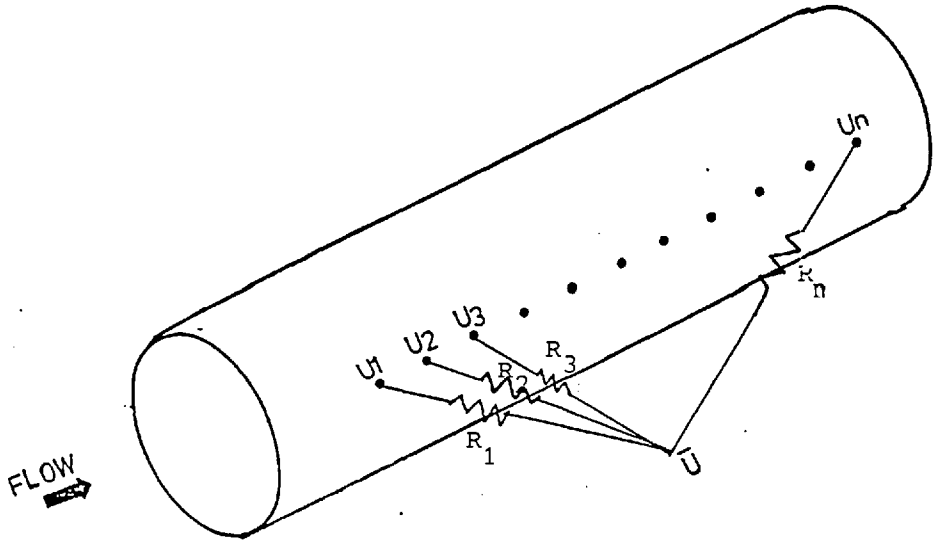

Figure 6.3 Diagram showing the resistance for integrating the signal along the pipe

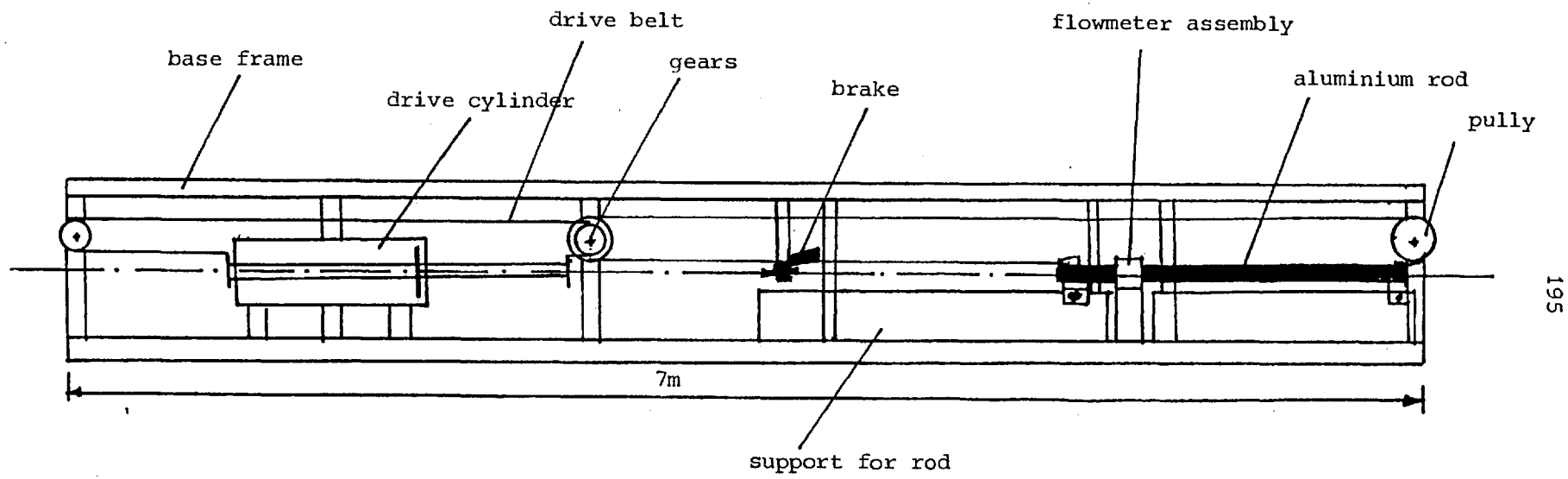

Figure 7.1 Sketch of the experimental rig

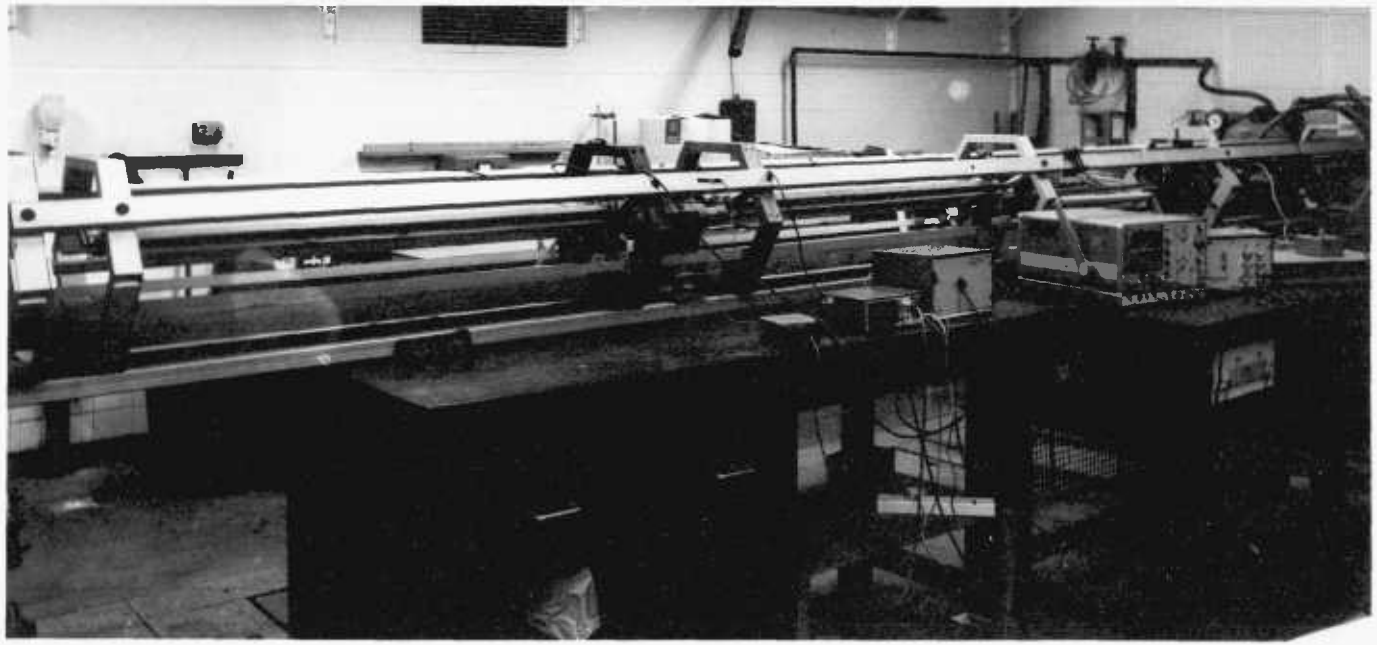

Figure 7.2 Side View of Experimental Rig

Figure 7.3 View of Gears from Drive Cylinder End

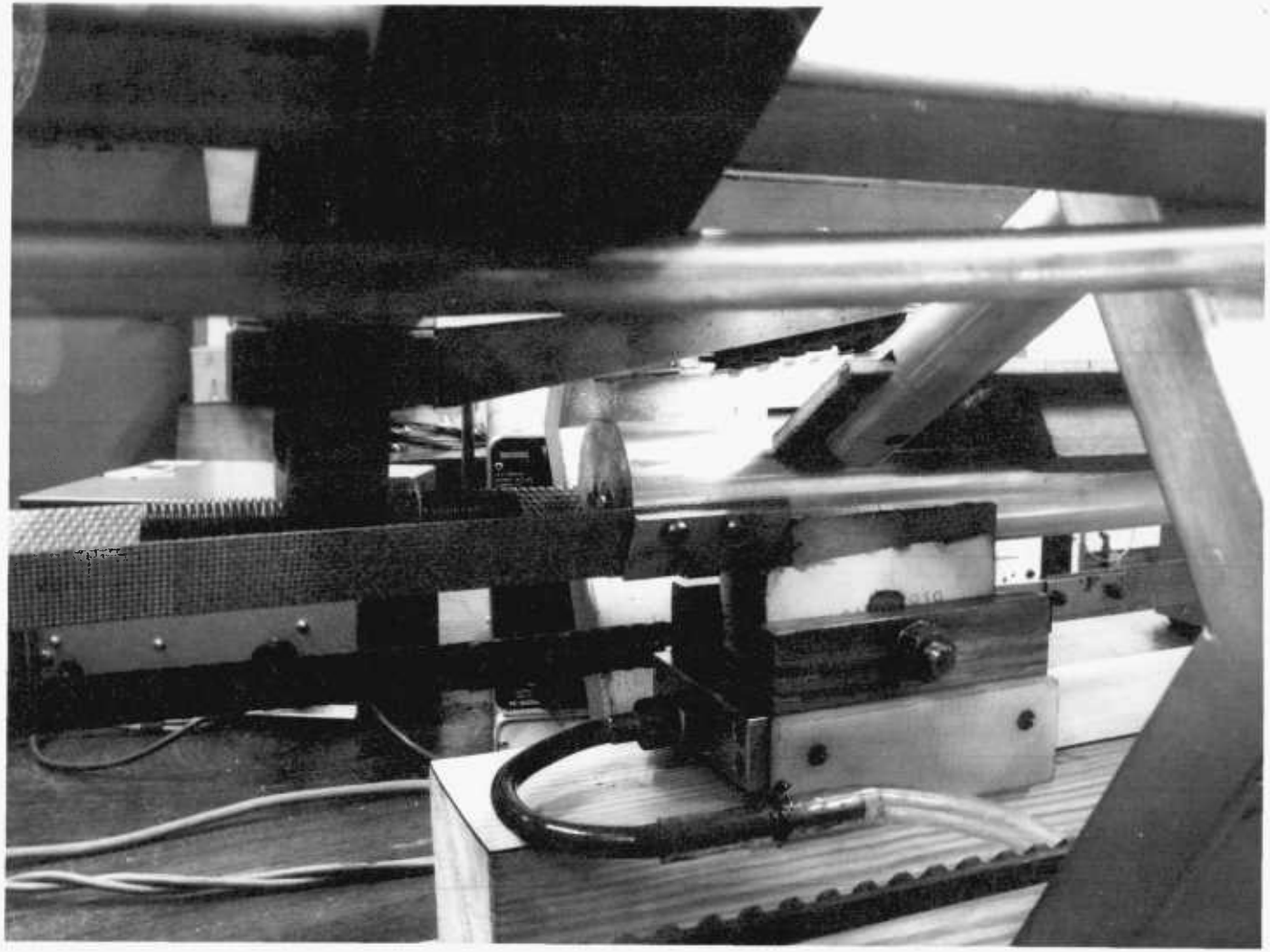

Figure 7.4 View of Braking System

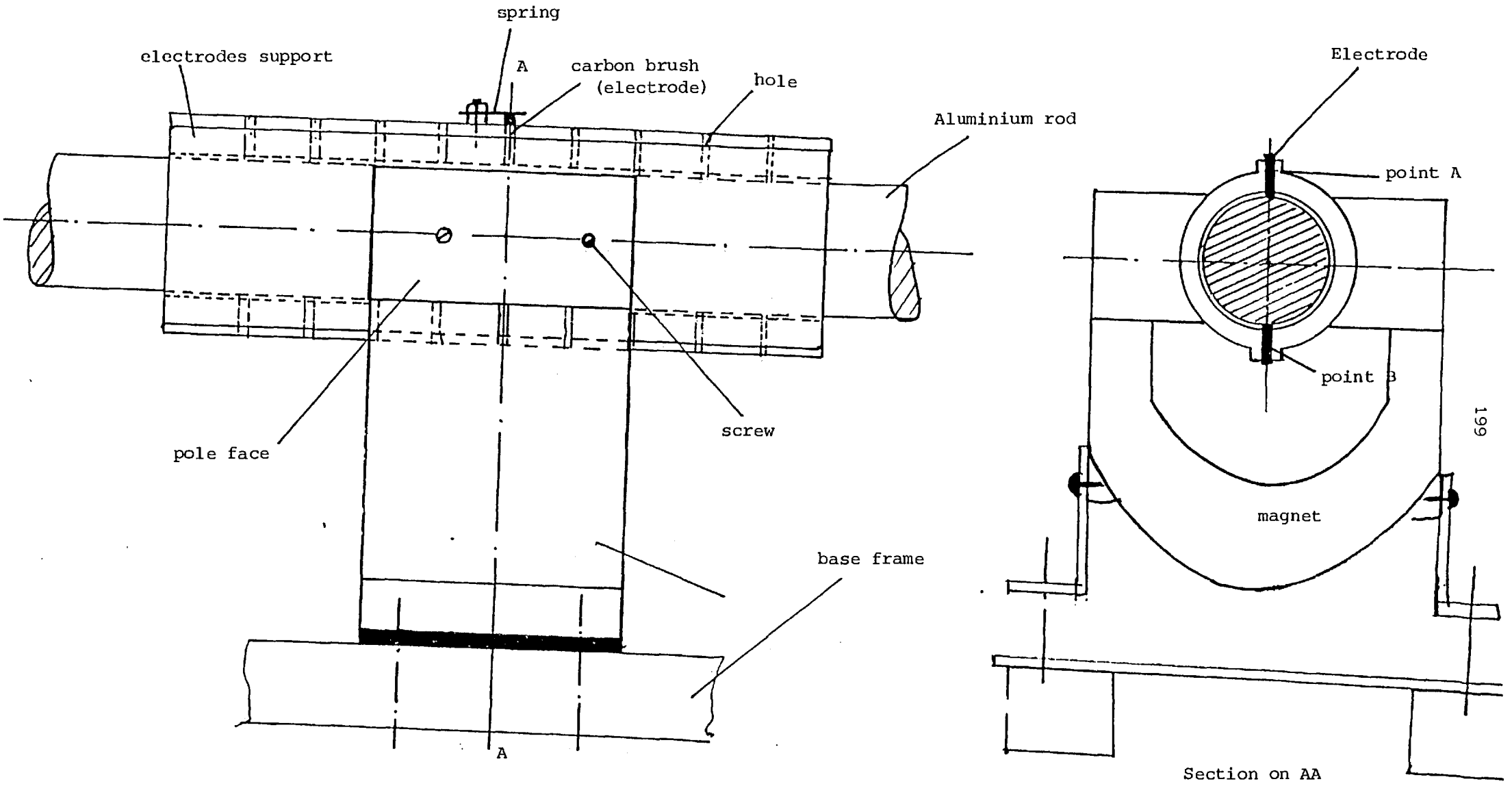

Figure 7.5 Flowmeter assembly

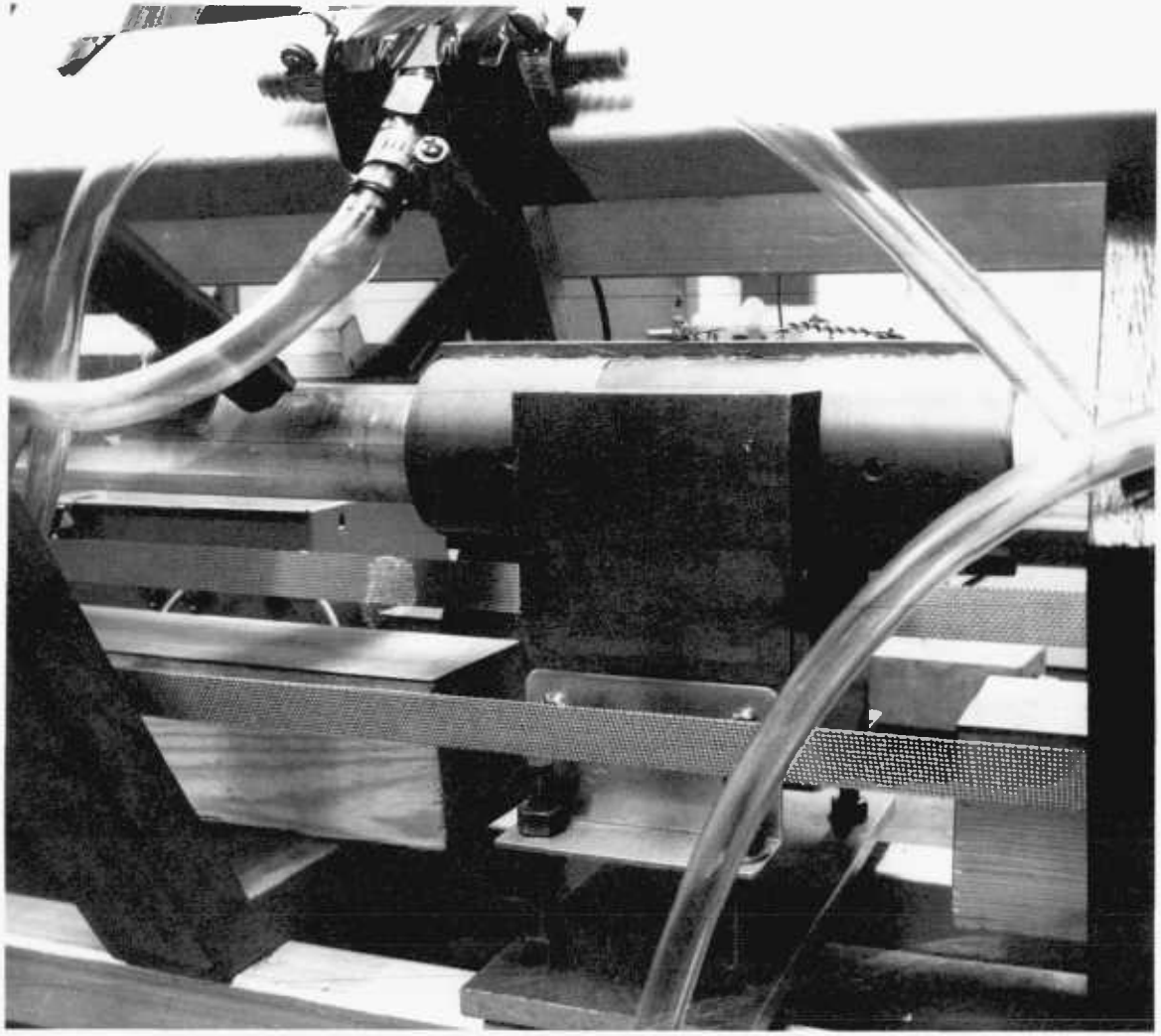

Figure 7.6 View of Flowmeter Assembly

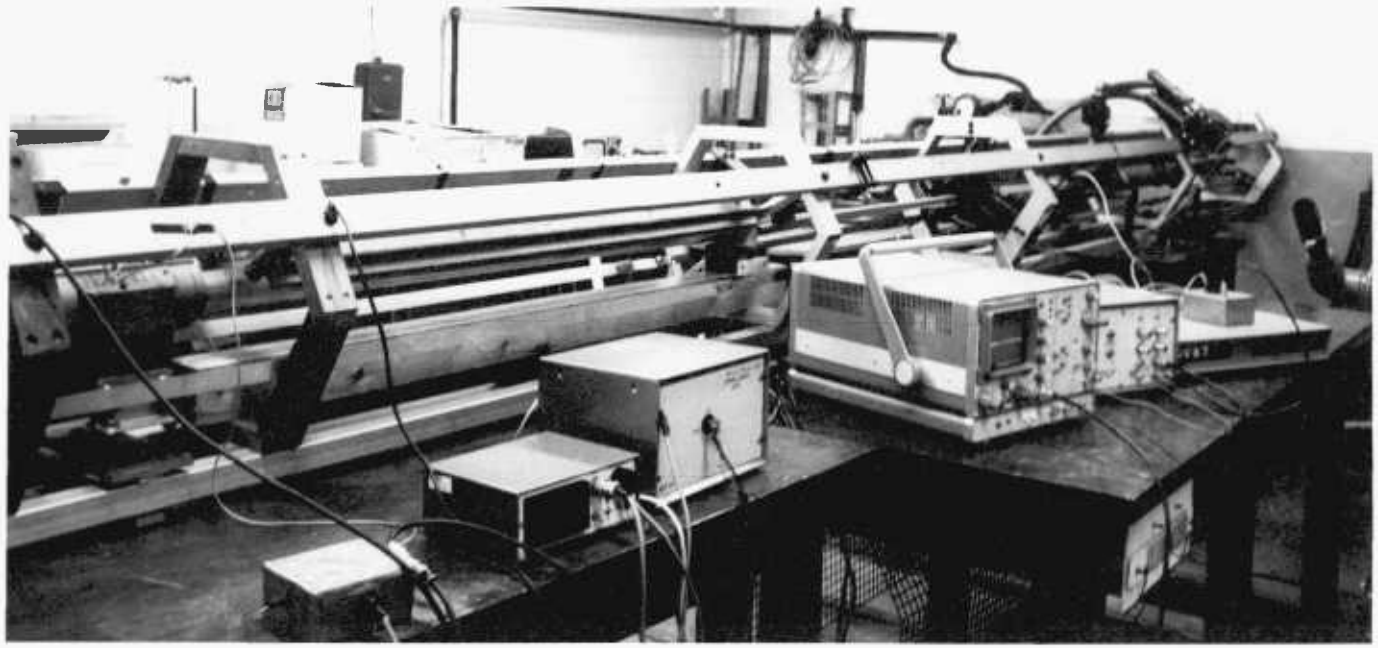

Figure 7.7 View of Instrumentation

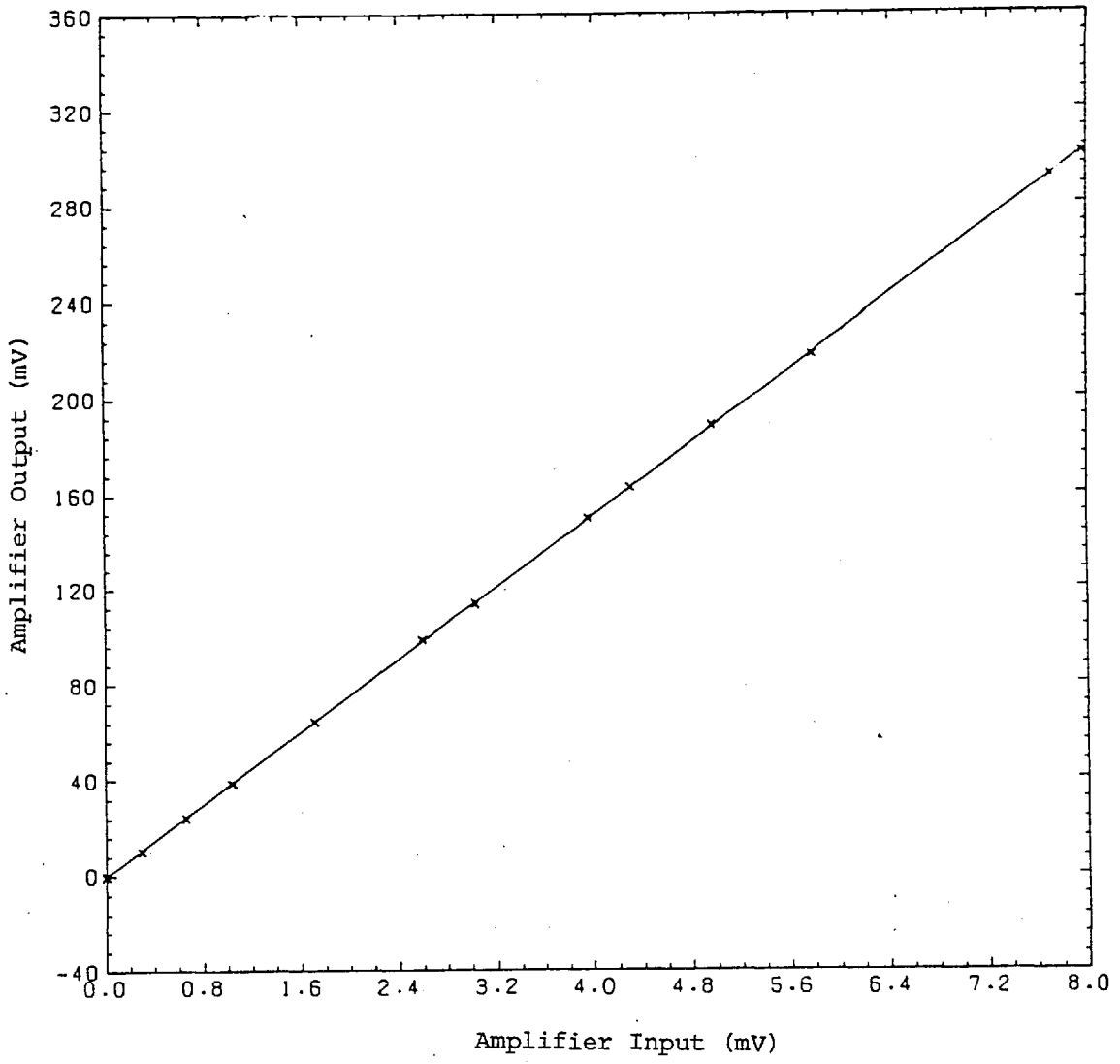

Figure 7.8 Amplifier calibration

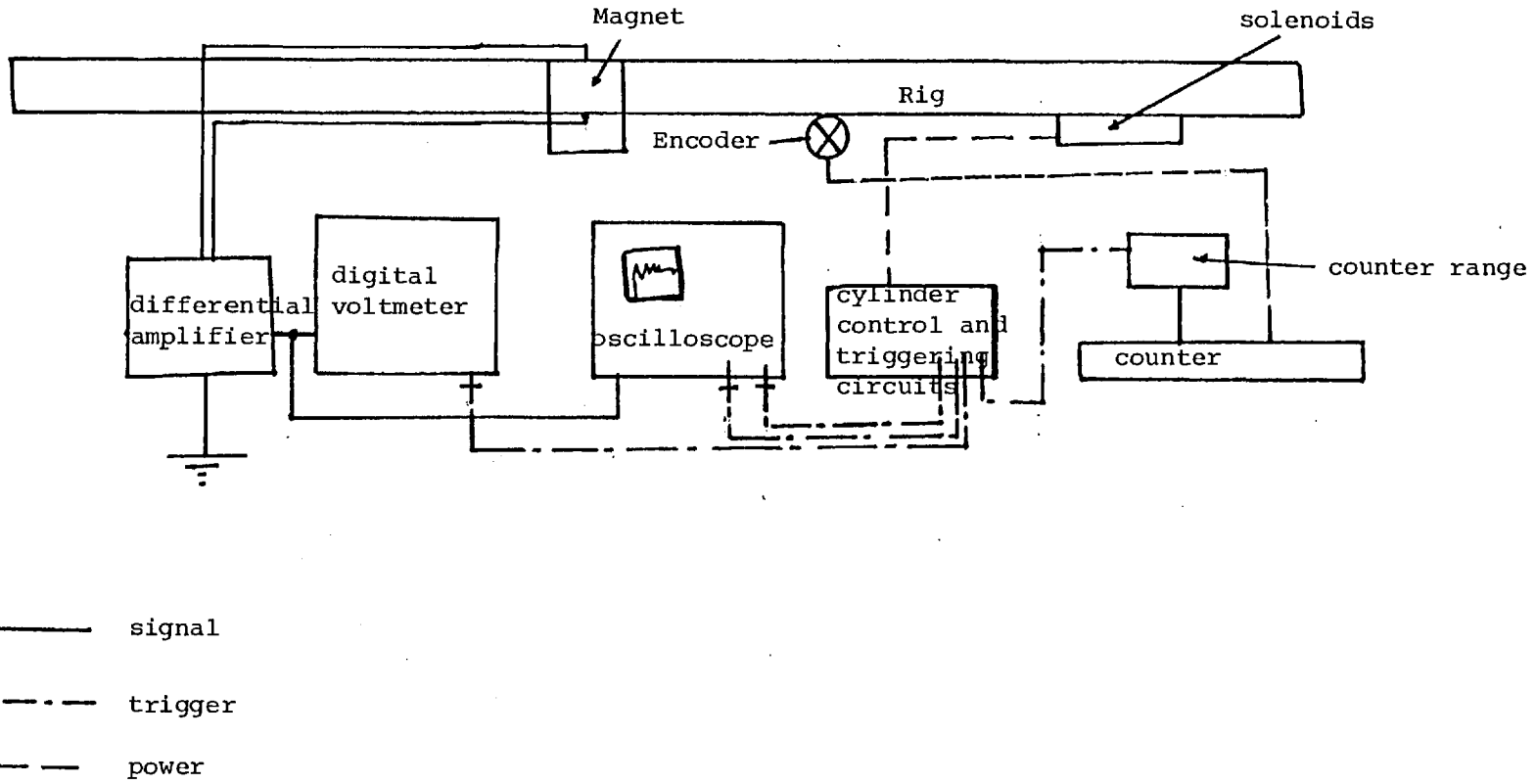

Figure 7.9 Block diagram of instruments showing earth connections

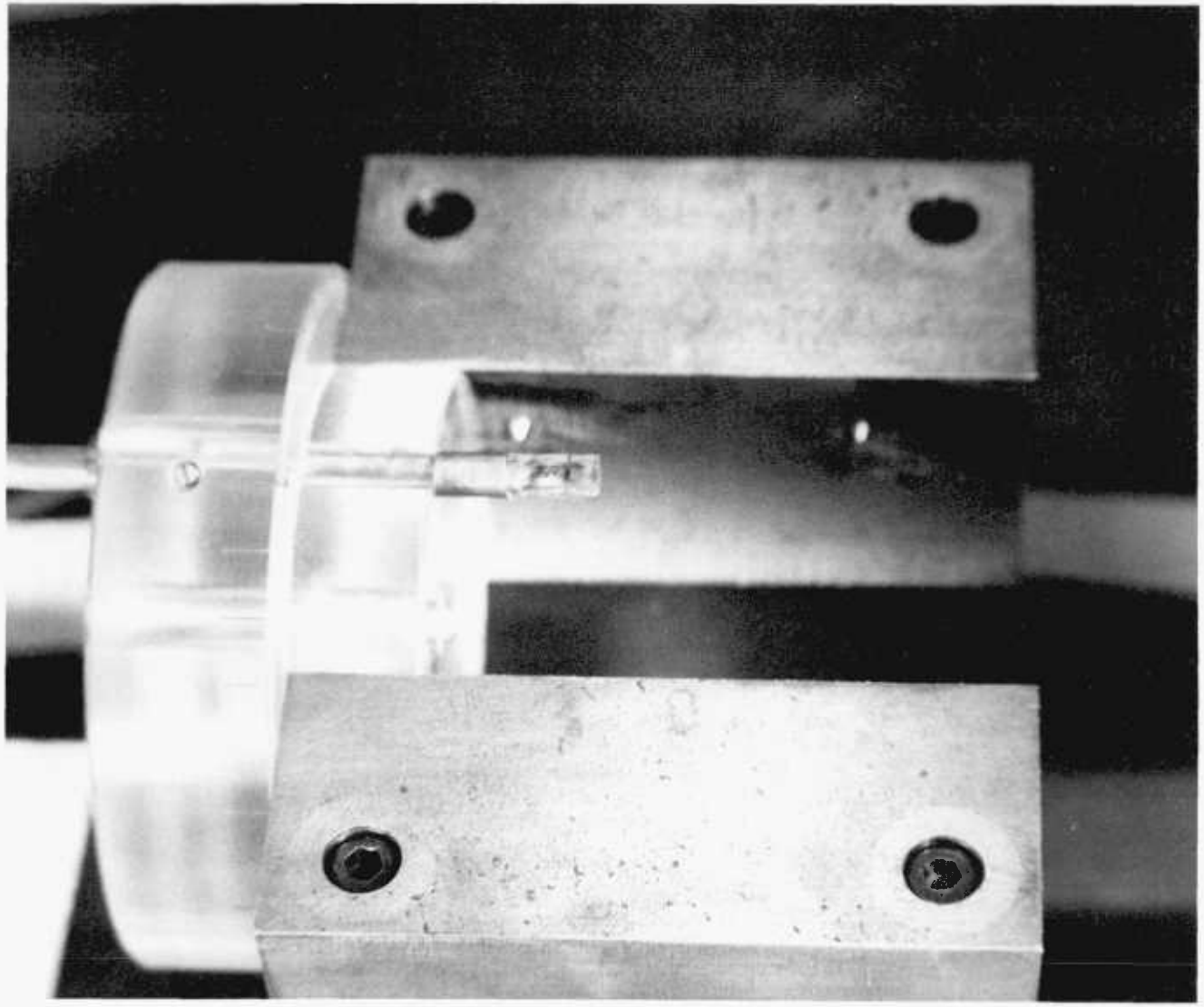

Figure 7.10 View of Permanent Magnet and Hall Probe

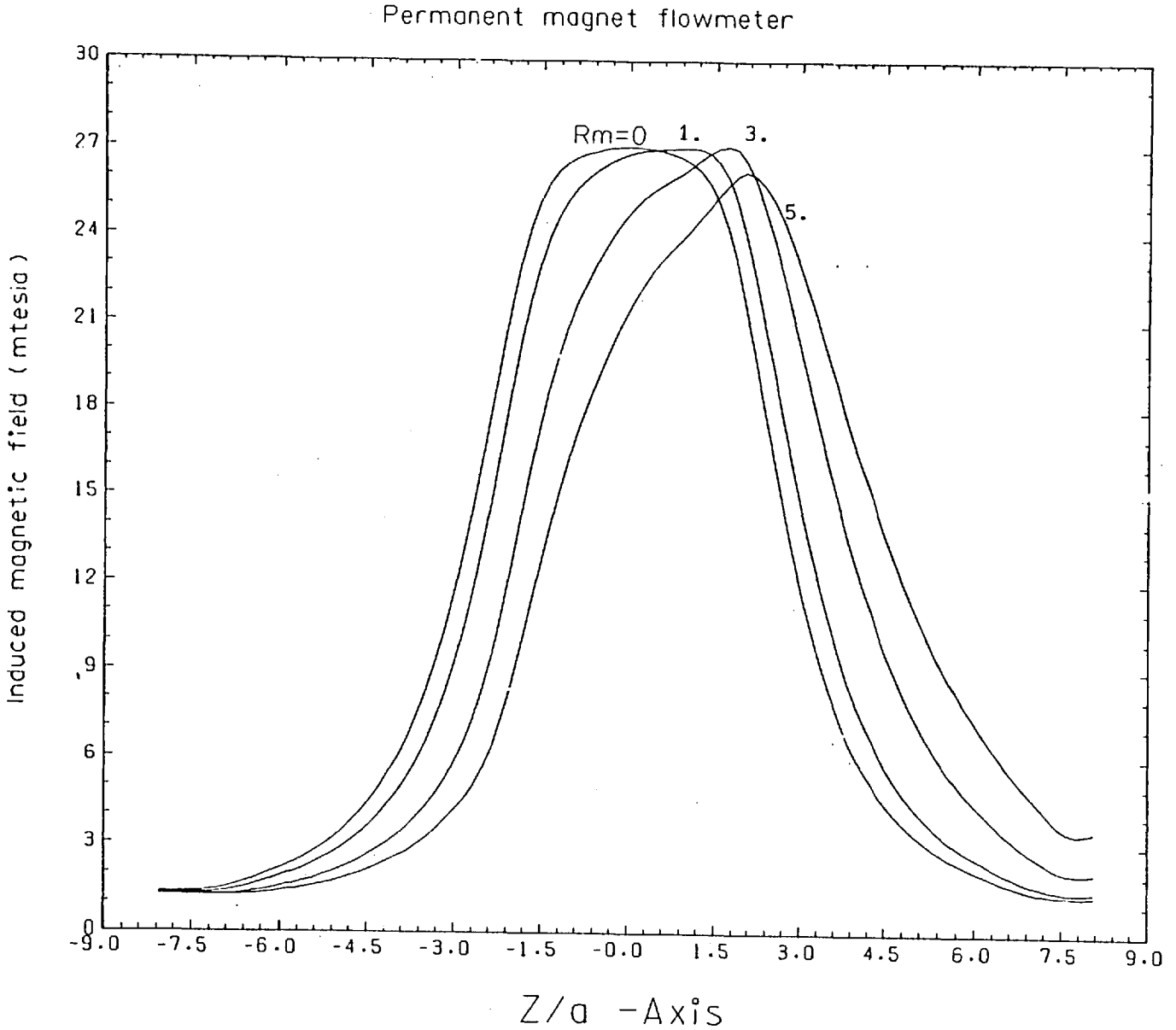

Figure 7.11 Magnetic field distribution at the centre line of aluminium rod (prediction)

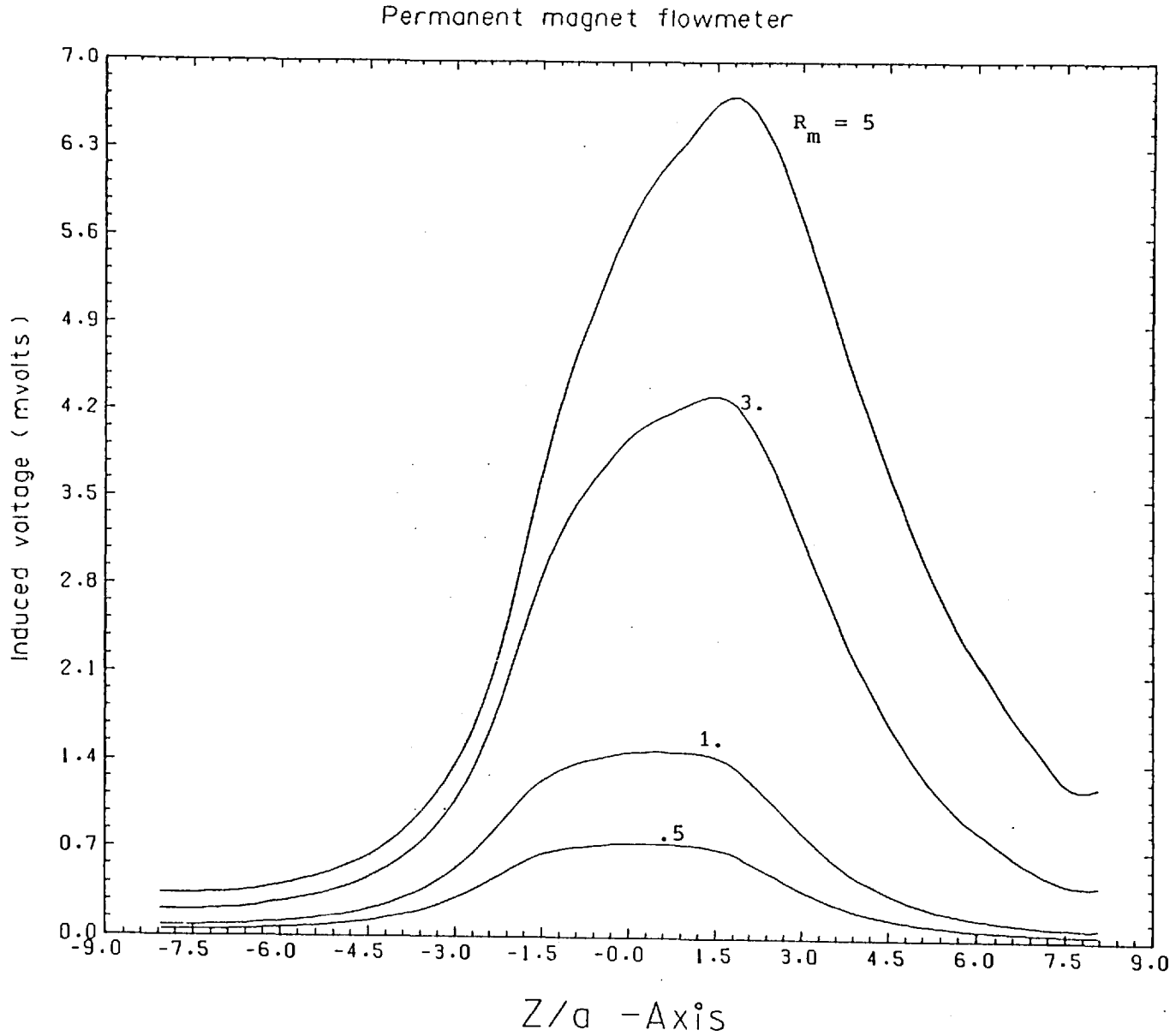

Figure 7.12 Induced voltage distribution along z-axis (prediction)

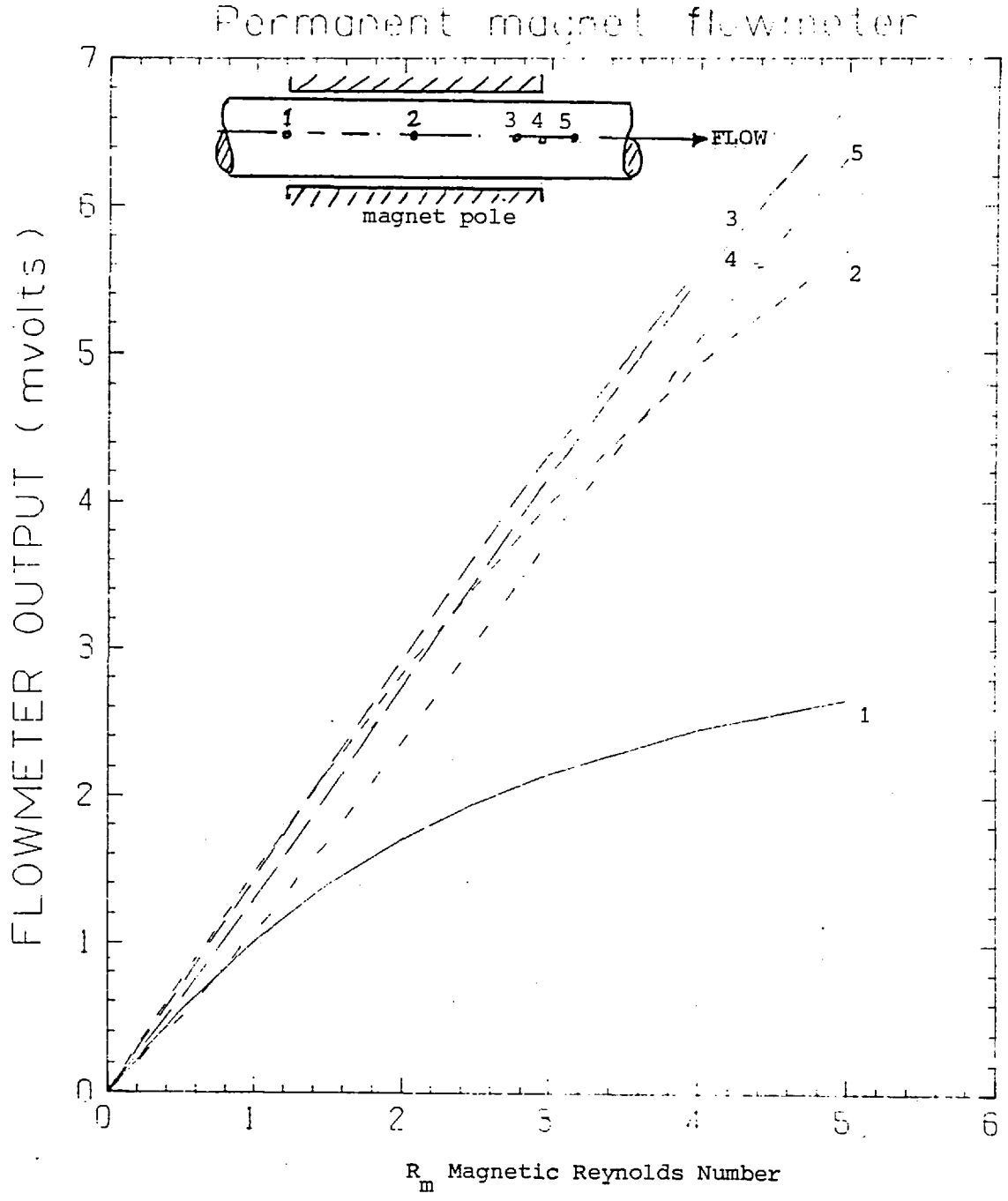

Figure 7.13 Flowmeter output for six electrode locations (prediction)

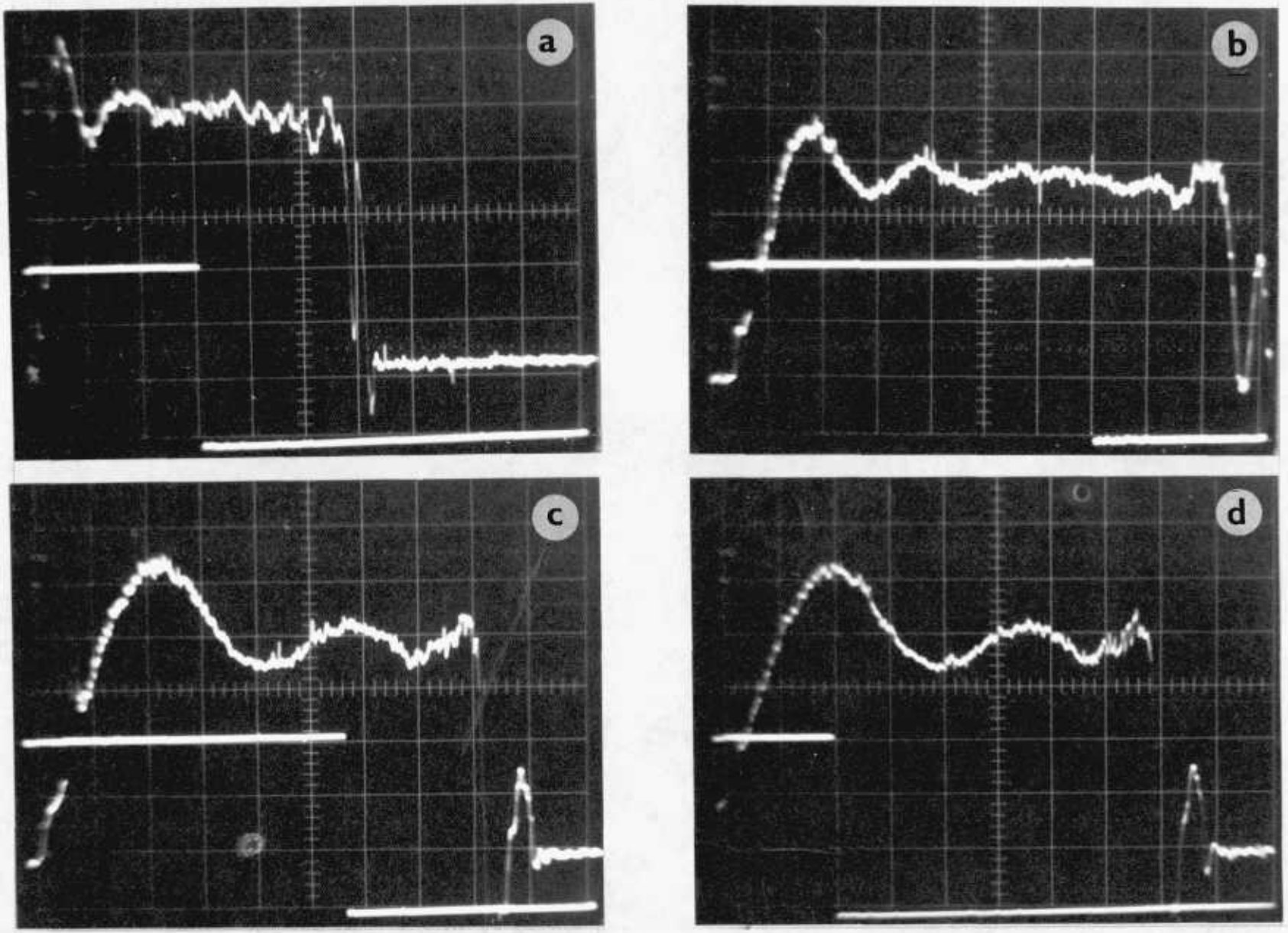

Figure 7.14 The signal displayed on the oscilloscope a) R_m = .36, Counting Period = 100mS, Scale .5S- 5mV
b) R_m = .87, Counting Period = 50mS, Scale .2S-10mV c) R_m = 1.4, Counting Period = 50mS, Scale .1S-20mV
d) R_m = 1.7, Counting Period = 25mS, Scale .1S-20mV

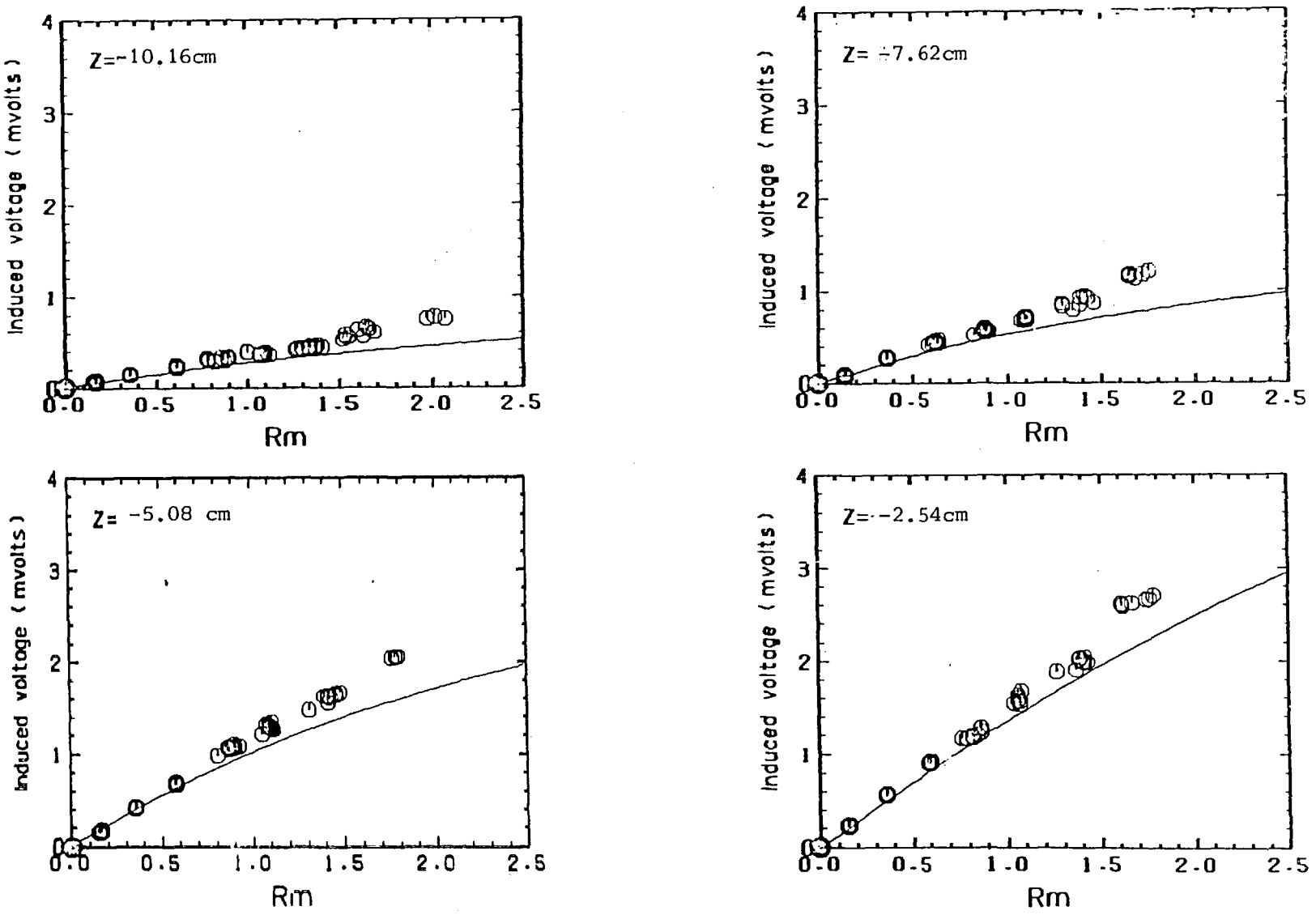

Figure 7.15 Induced voltage against magnetic Reynolds number for four location of electrodes upstream, (o experimental values, — theoretical values)

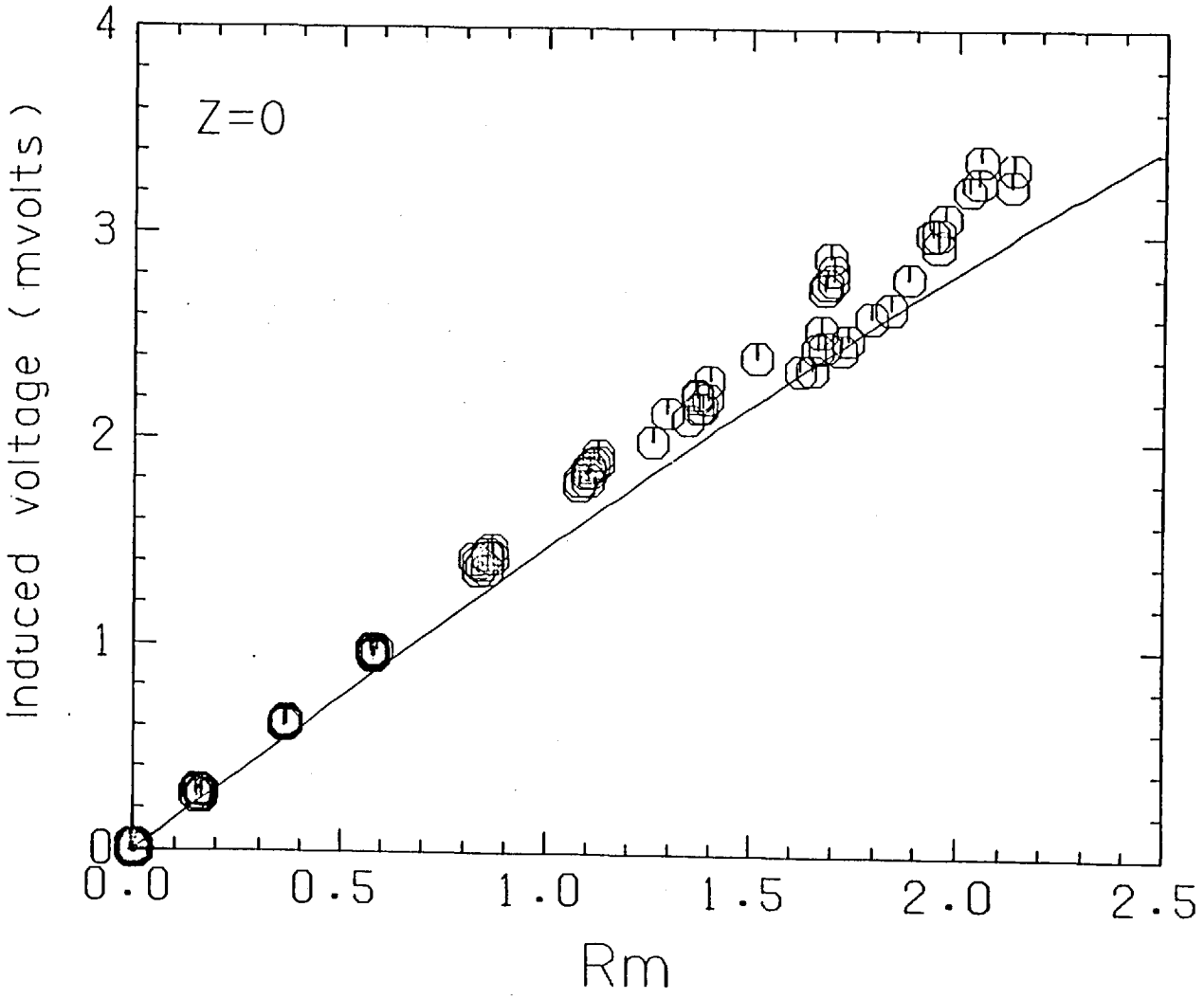

Figure 7.16 Induced voltage against magnetic Reynolds number for electrodes at the middle (O experimental values, —theoretical values)

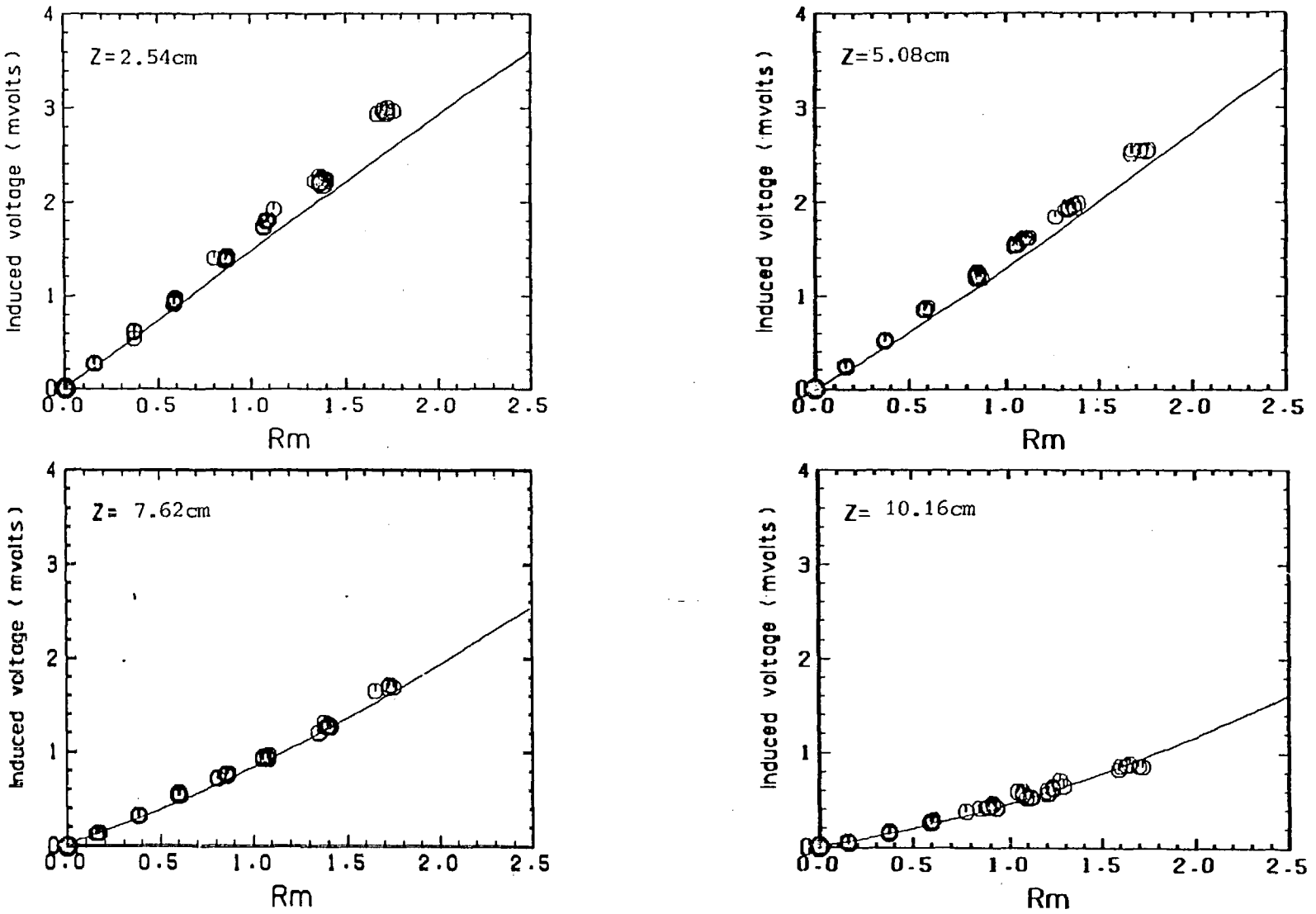

Figure 7.17 Induced voltage against magnetic Reynolds number for four locations of electrodes downstream, (O experimental values, —theoretical values.)

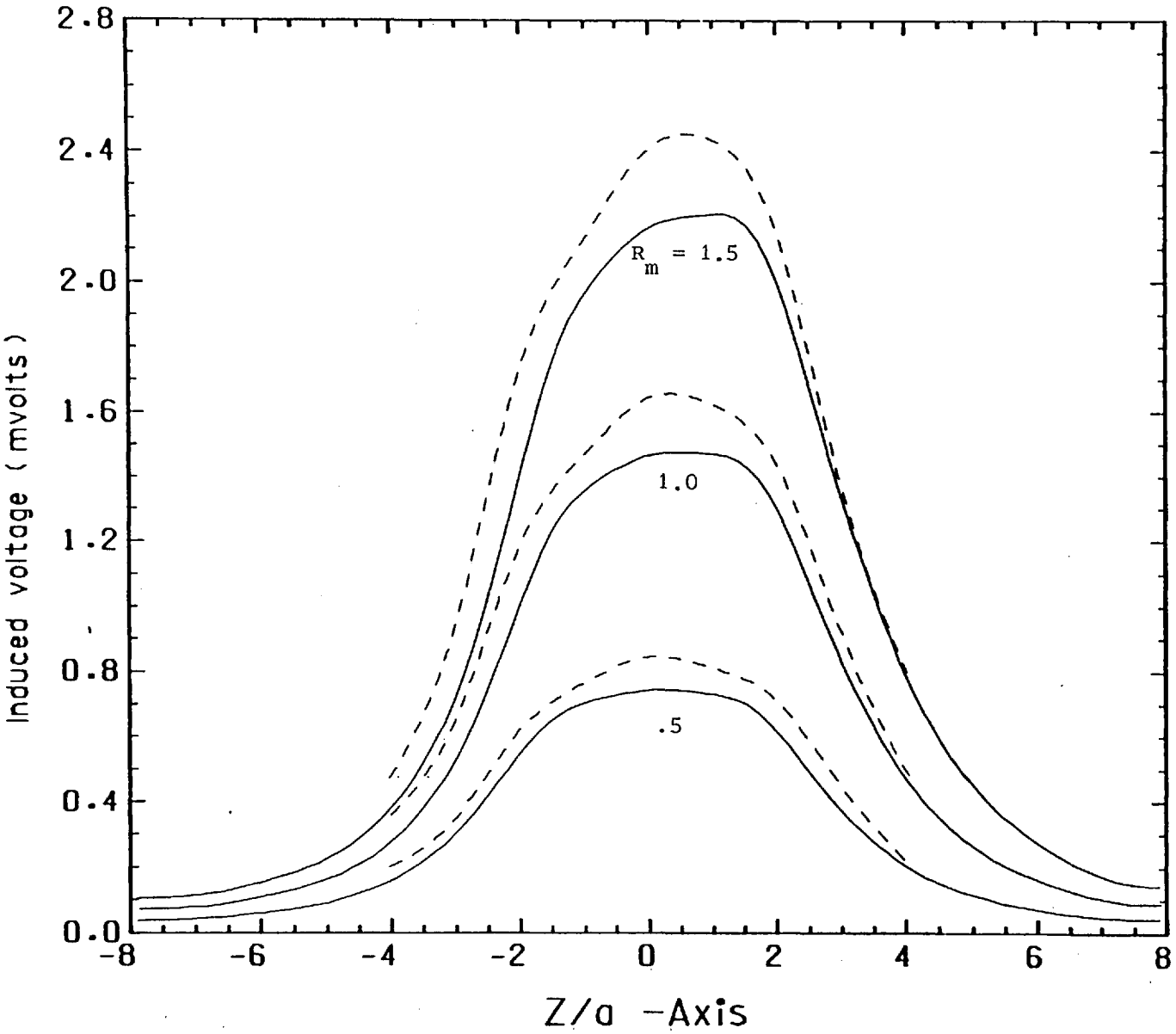

Figure 7.18 Induced voltage along the rod for electrodes at r=a and $\theta = \pi/2$, (——— theoretical values, - — — — — experimental values)

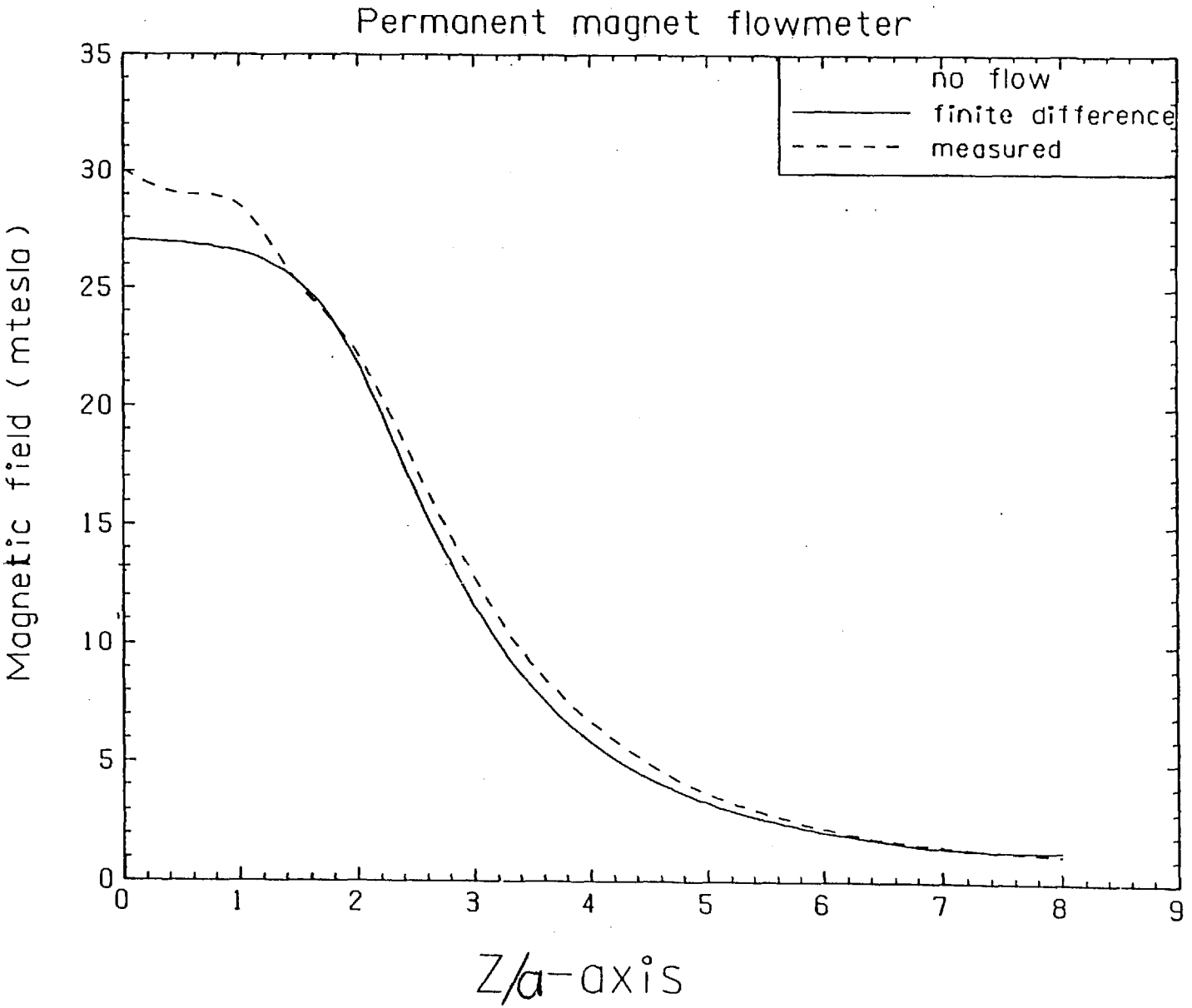

Figure 7.19 Magnetic field distribution at the centre line of rod

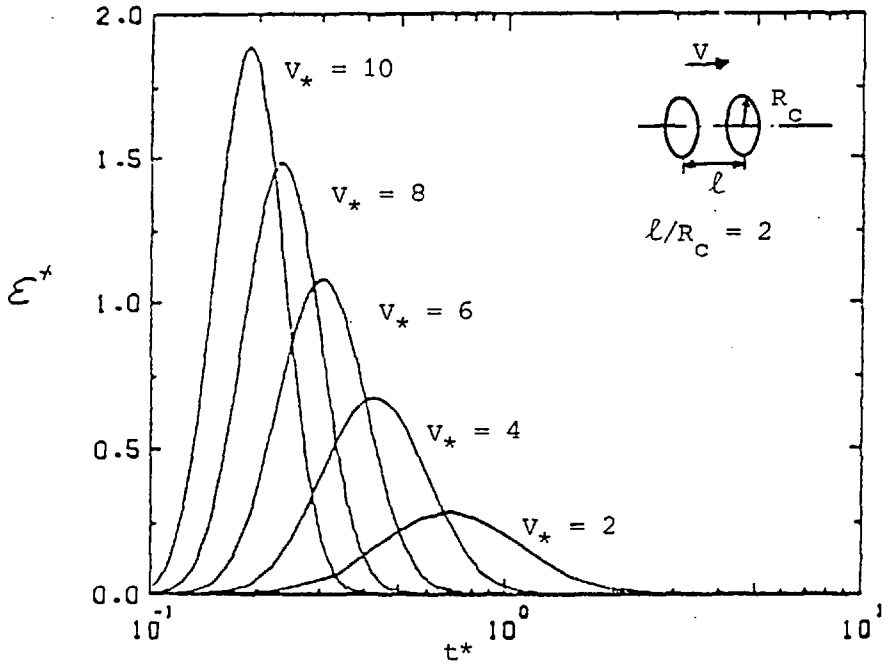

Figure 8.1 Graphs plotting the dependence of the emf as a function of time in the measuring coil when a pulse is transmitted between two circular circuits in a moving electrically conducting medium

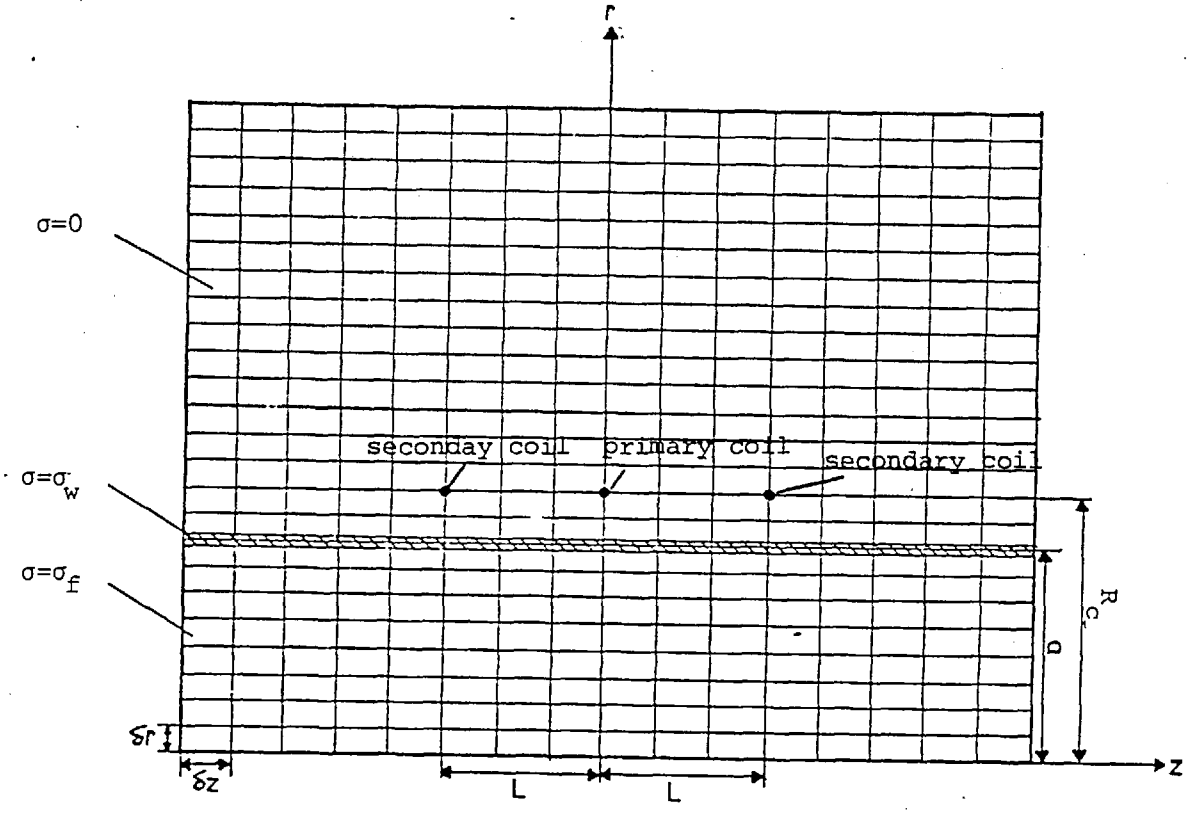

Figure 8.2 Typical lattice arrangement

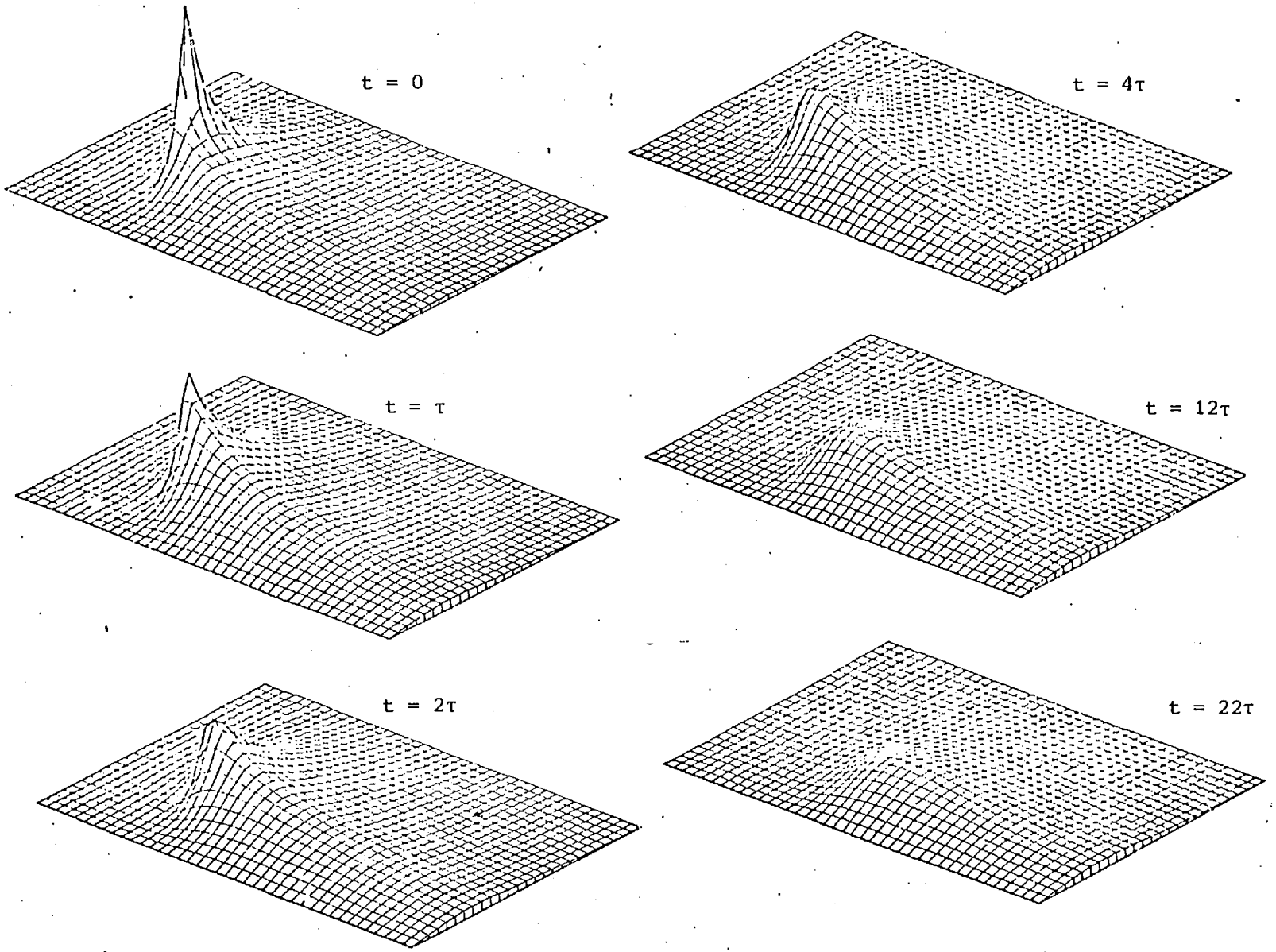

Figure 8.3 Distribution of vector potential function at different time intervals

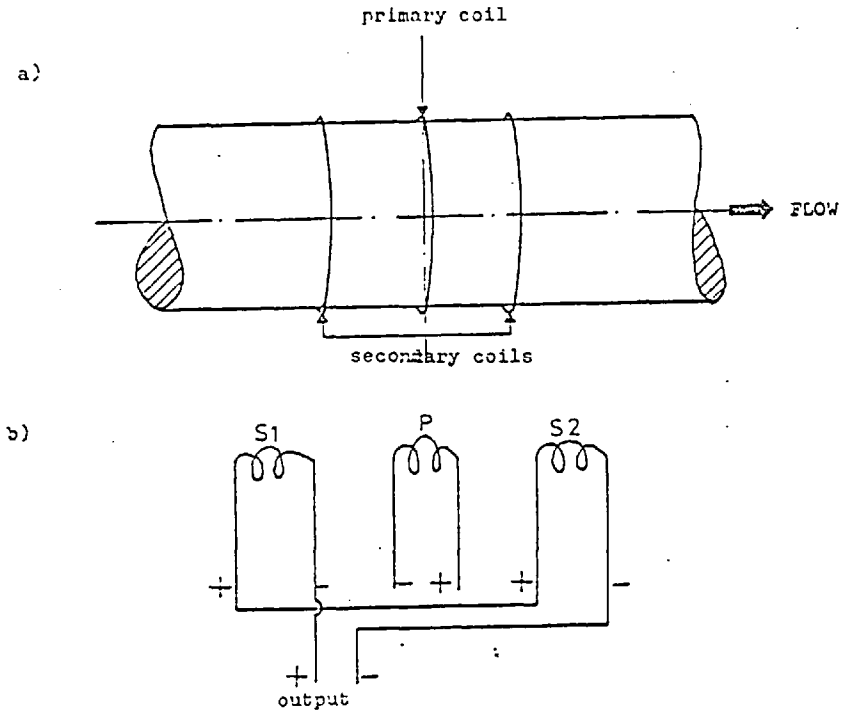

Figure 8.4 Pulsed field flowmeter, a) coil arrangements, b) electrical diagram of the differential transformer

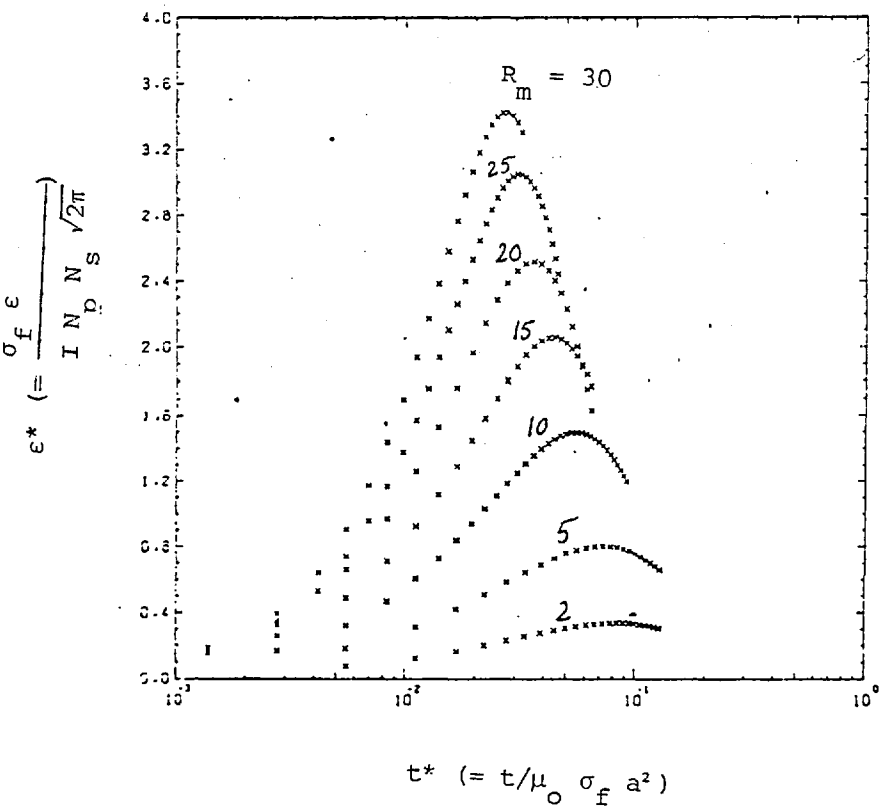

Figure 8.5 Induced signal in secondaries for uniform velocity profile

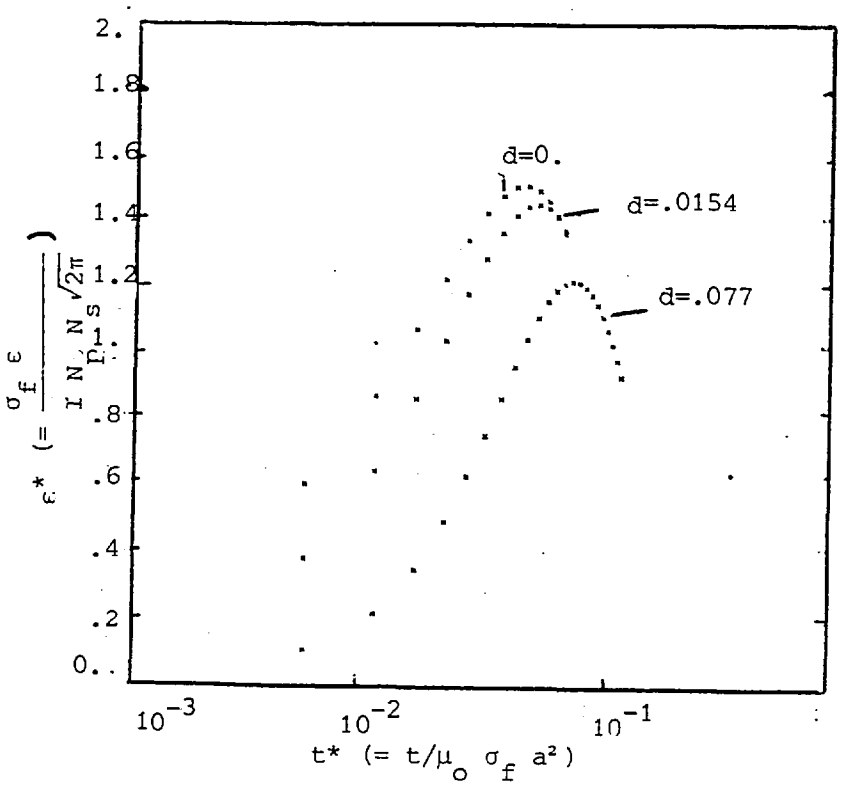

Figure 8.7 Effect of wall conductivity no. on delay time

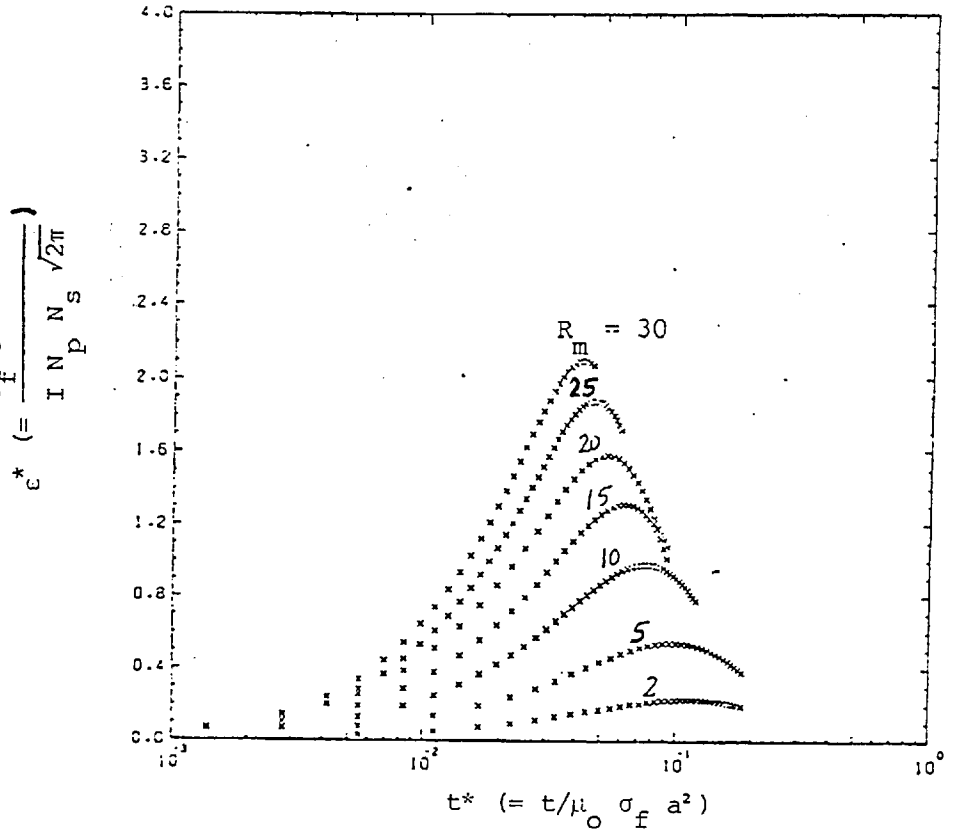

Figure 8.6 Induced signal in secondaries for parabolic velocity profile

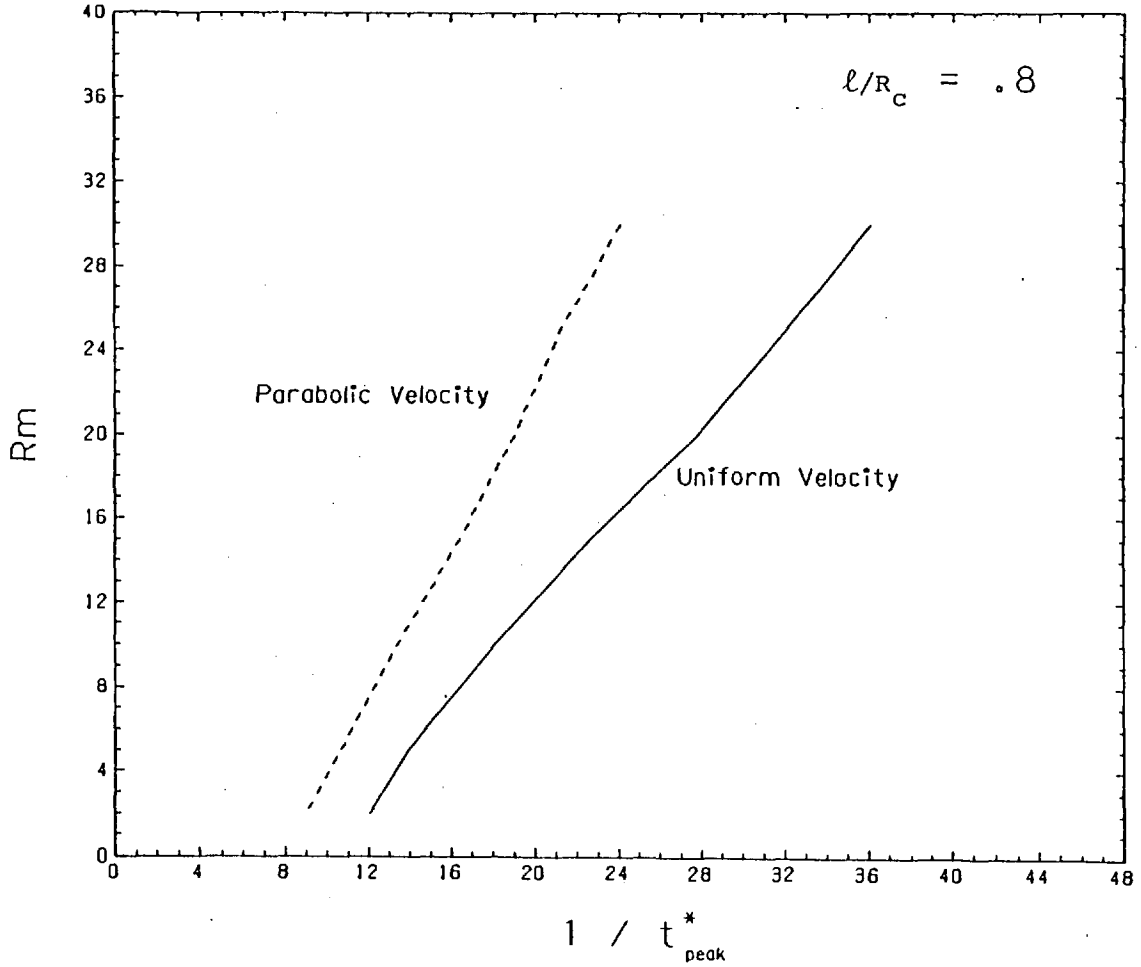

Figure 8.8 Magnetic Reynolds number plotted against t* peak (= t peak/$\mu\ \sigma_f\ a^2$)

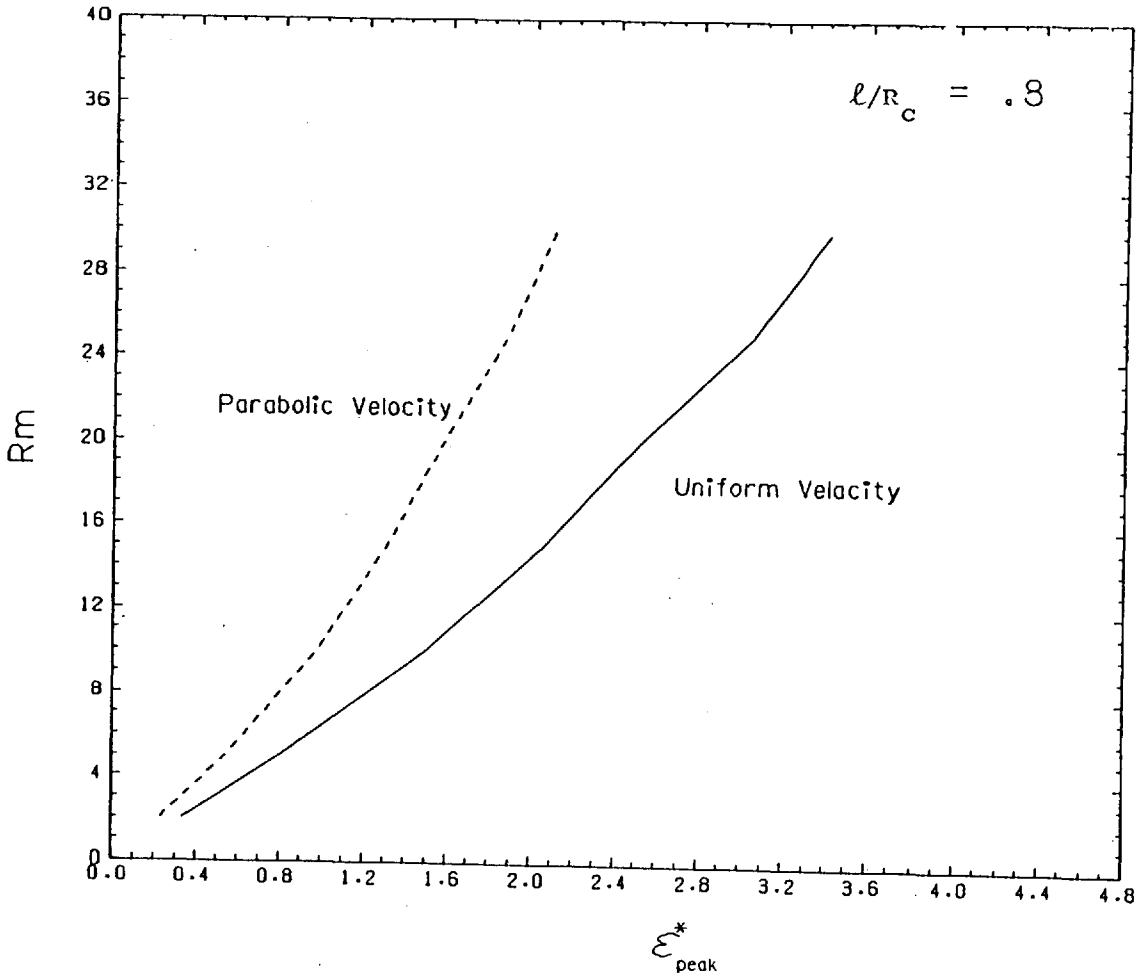

Figure 8.9 Characteristic of flowmeter with induced signal measurement

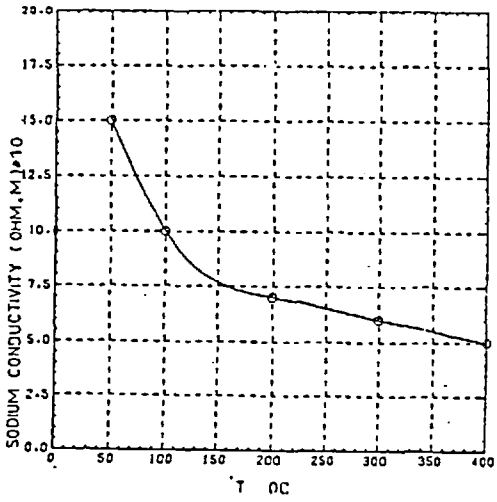

Figure 8.10 Conductivity of sodium as a function of temperature

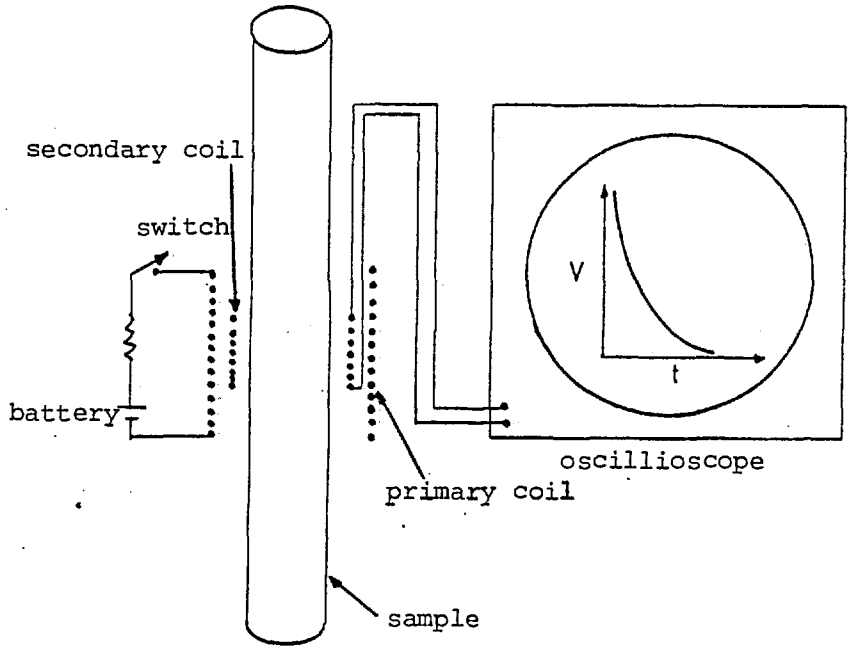

Figure 8.11 Arrangement for determining the resistivity of a metal bar - A step function current applied through the solenoid produces a magnetic field that diffuses into the bar. The resulting voltage across a secondary coil is observed as a function of time on an oscilloscope.

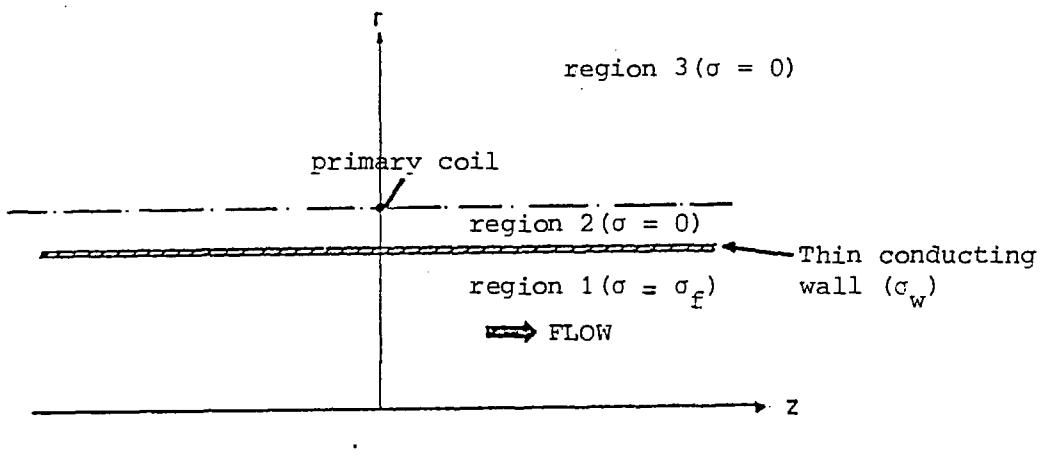

Figure 8.12 Diagram of pulsed field flowmeter showing different regions

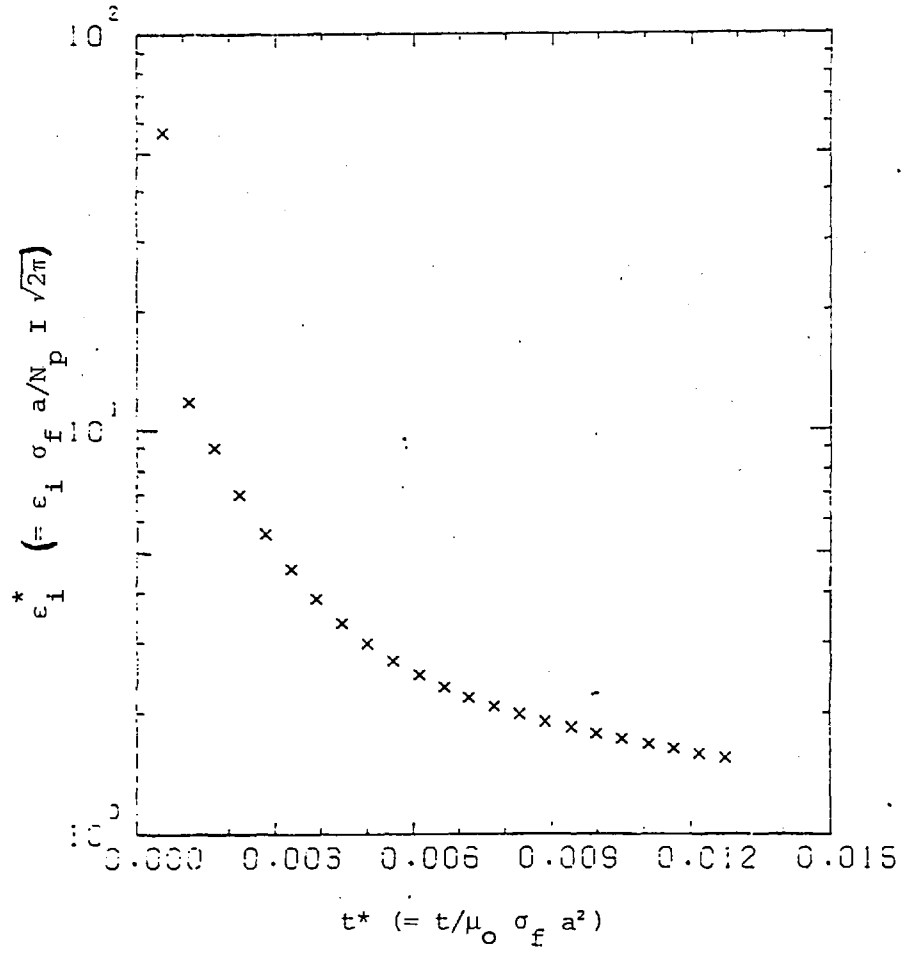

Figure 8.13 Induced voltage vs time after applying pulsed current in primary coil

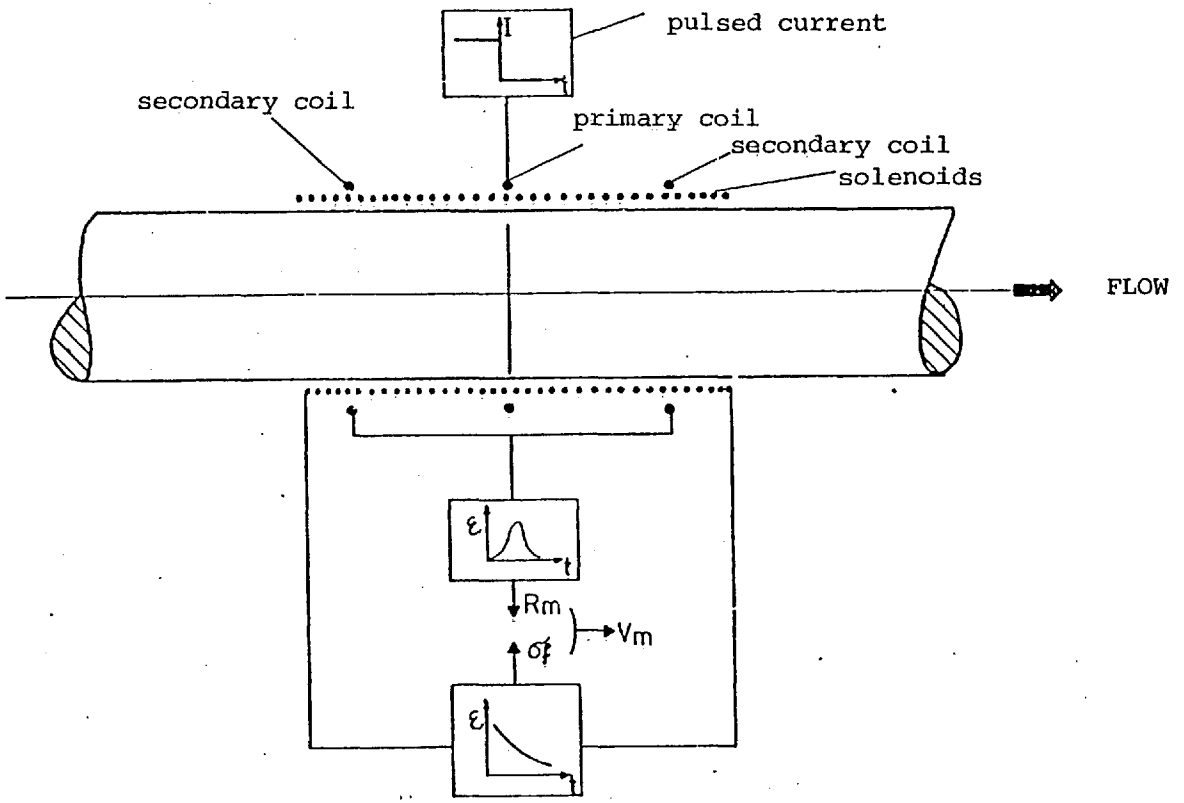

Figure 8.14 Pulsed field flowmeter for flowrate measurement

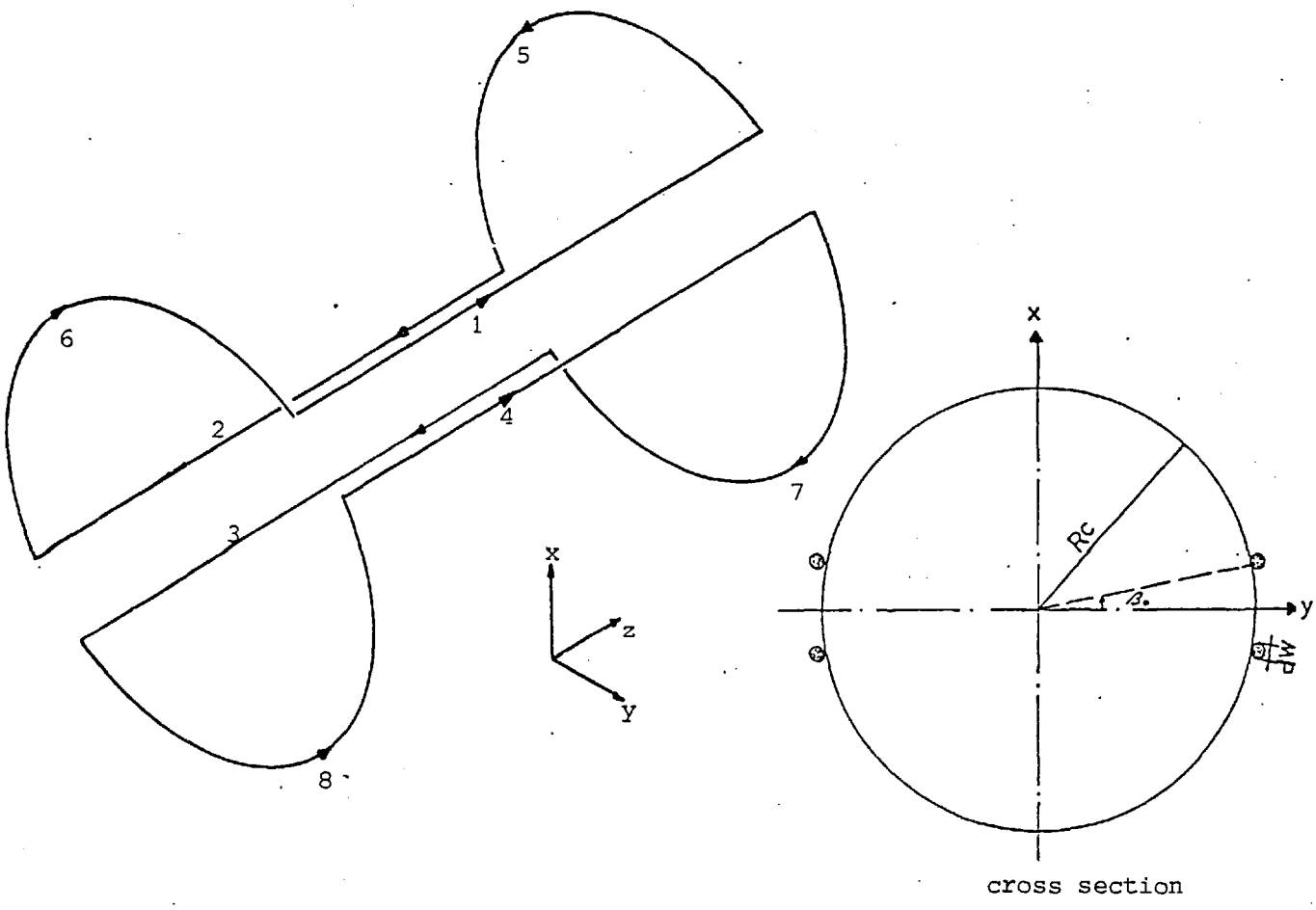

Figure A.1 Saddle type coils (concentric winding)

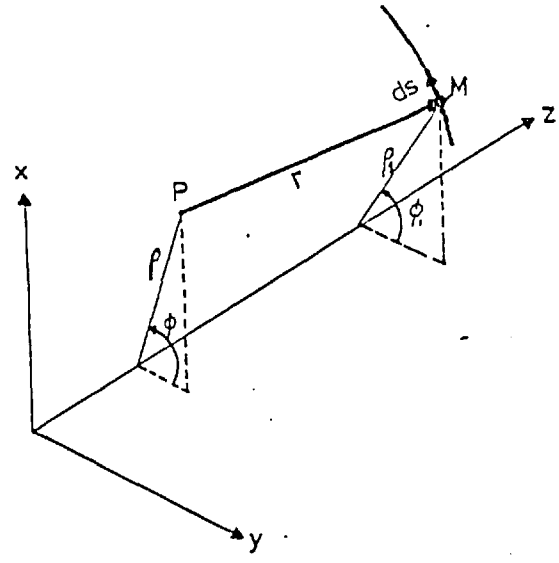

Figure A.2 Calculation diagram using Biot-Savart's Law for magnetic field of a saddle type coil.

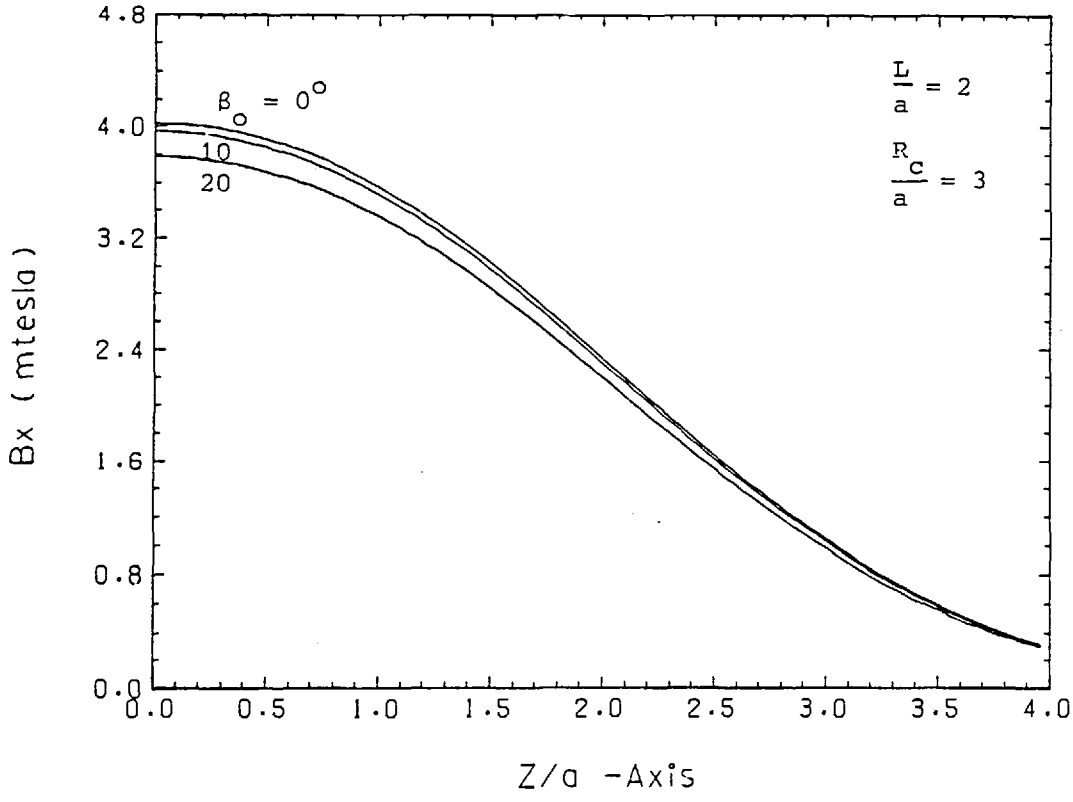

Figure A.3 Magnetic field distribution along z/a axis at the centre of saddle coil for three coil angles

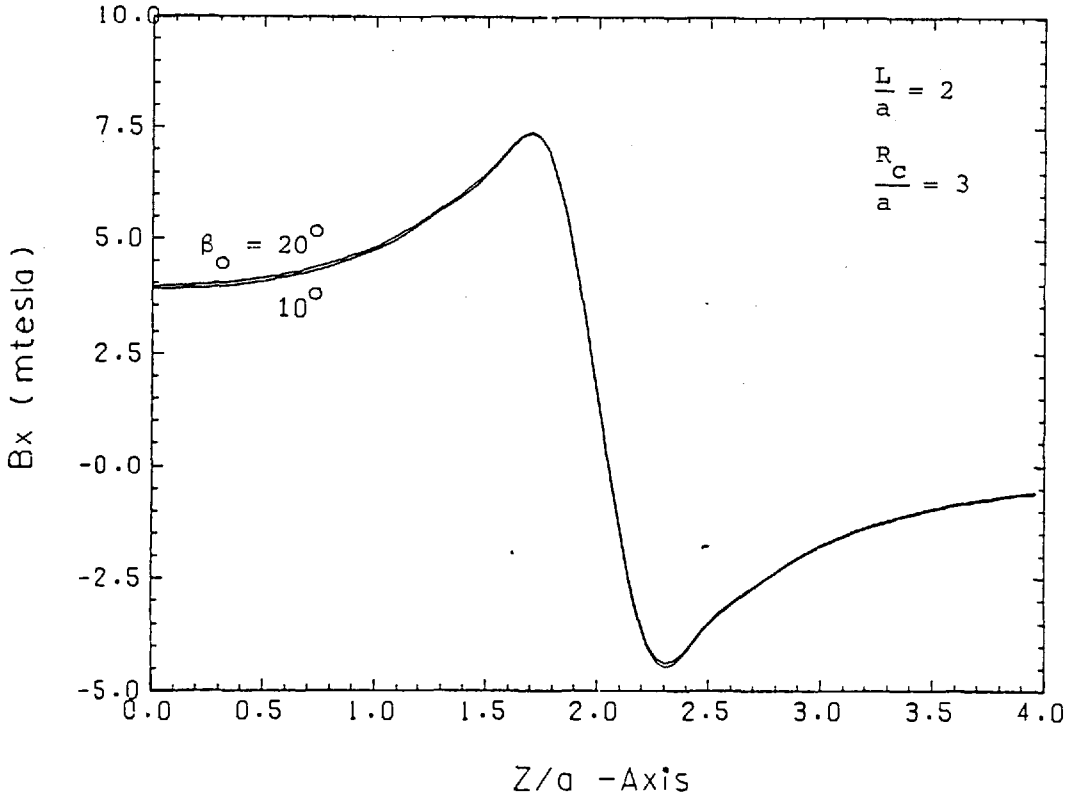

Figure A.4 Magnetic field distribution along z/a axis at R/a = 2.7 where the boundary values are calculated for finite difference calculations

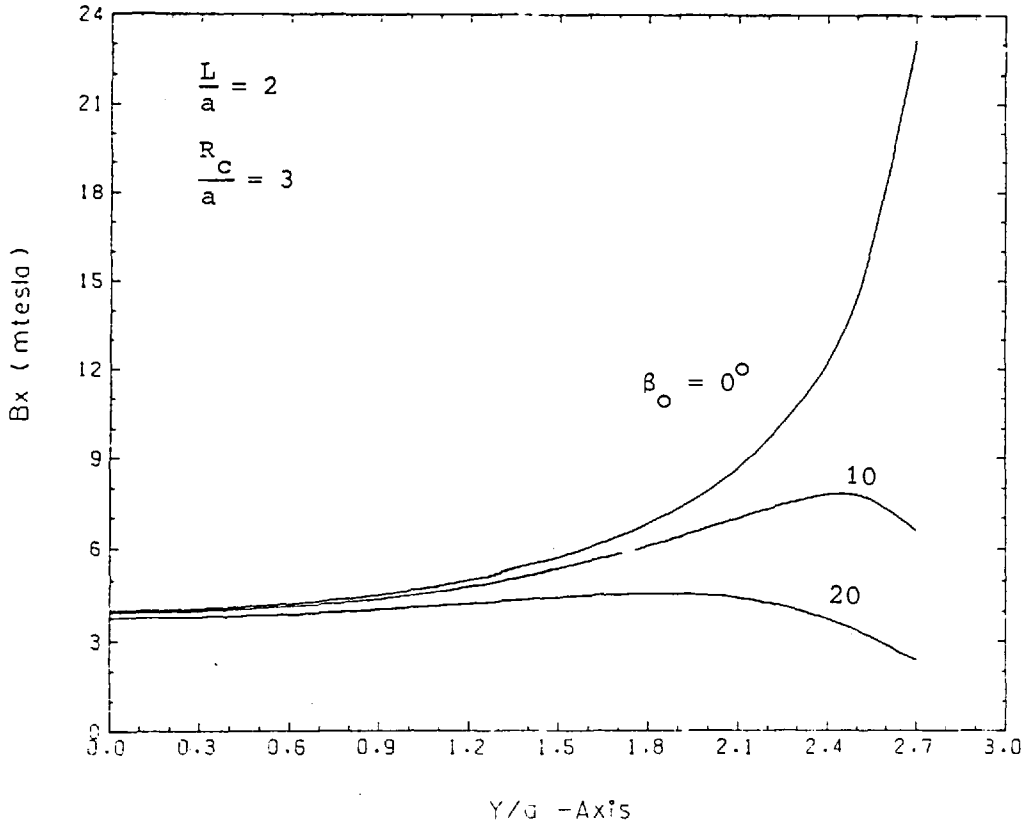

Figure A.5 Magnetic field distribution along Y/a axis at z/a = 0 and ϕ = 0 for three coil angles

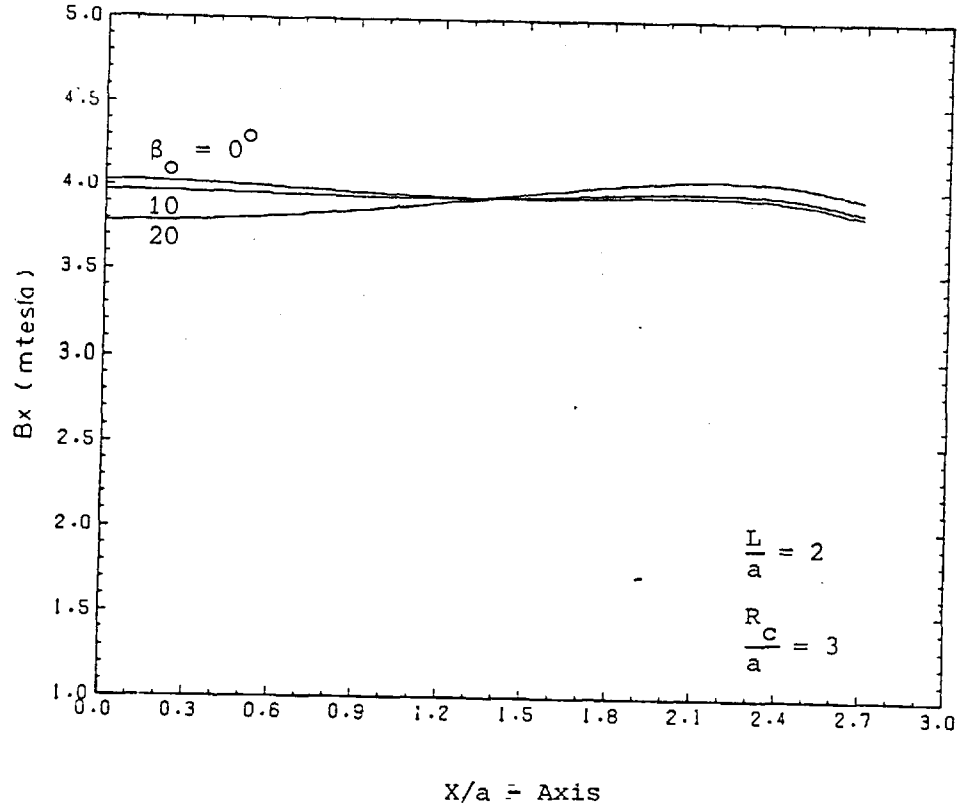

Figure A.6 Magnetic field distribution along x/a axis at z/a = 0 and $\phi = \pi/2$ for three coil angles

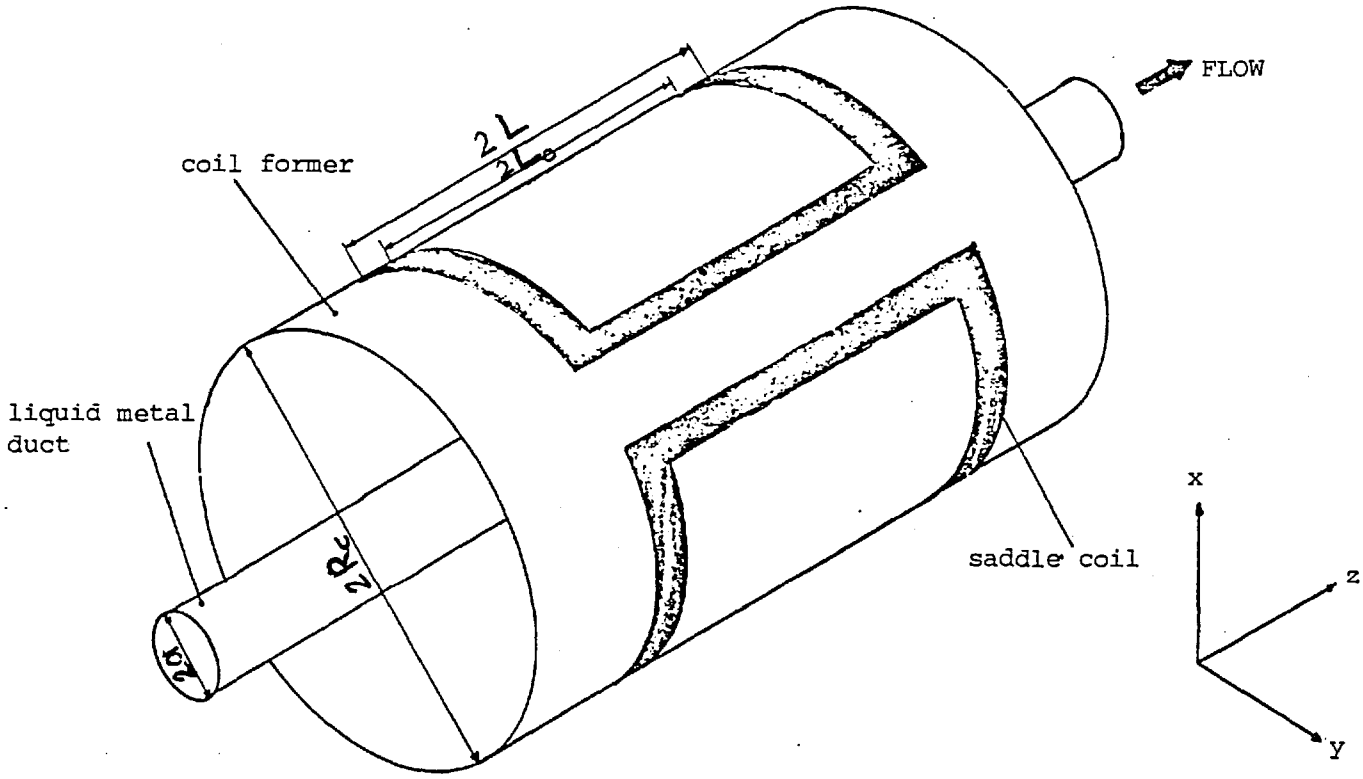

Figure B.1 Saddle-type coils flowmeter

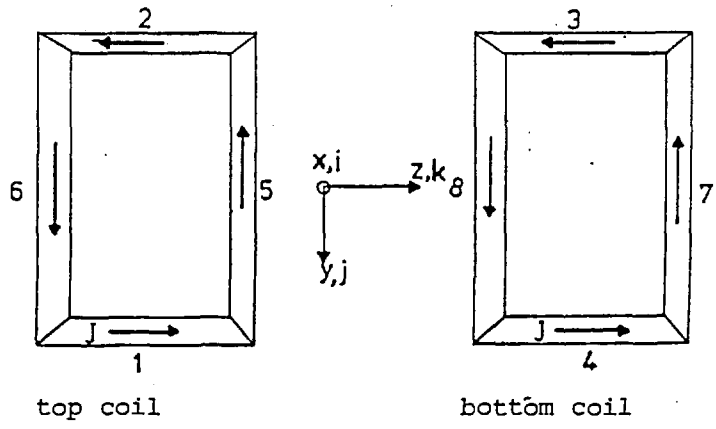

Figure B.2 Diagram of coils from top and bottom

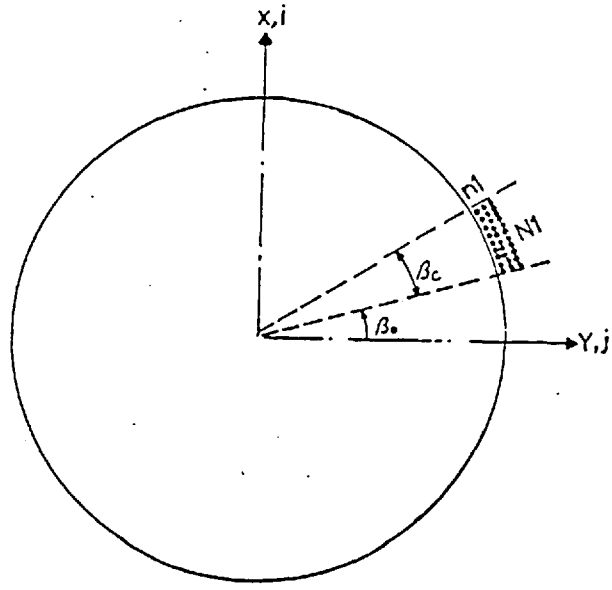

Figure B.3 Cross-section of coil showing the winding arrangement

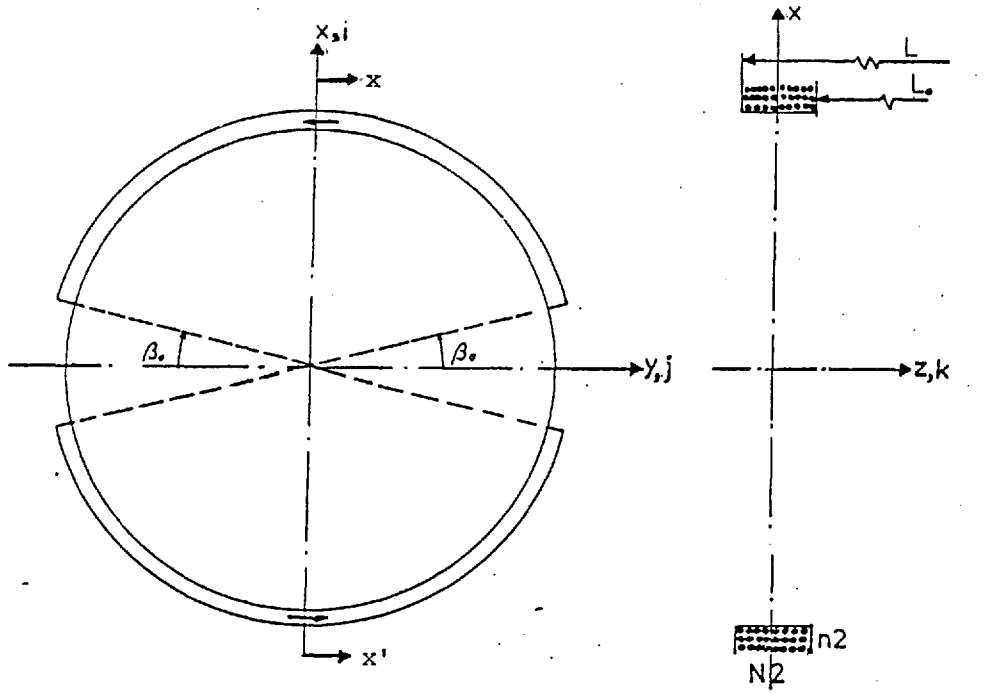

Figure B.4 Diagram of curved part of the saddle coils

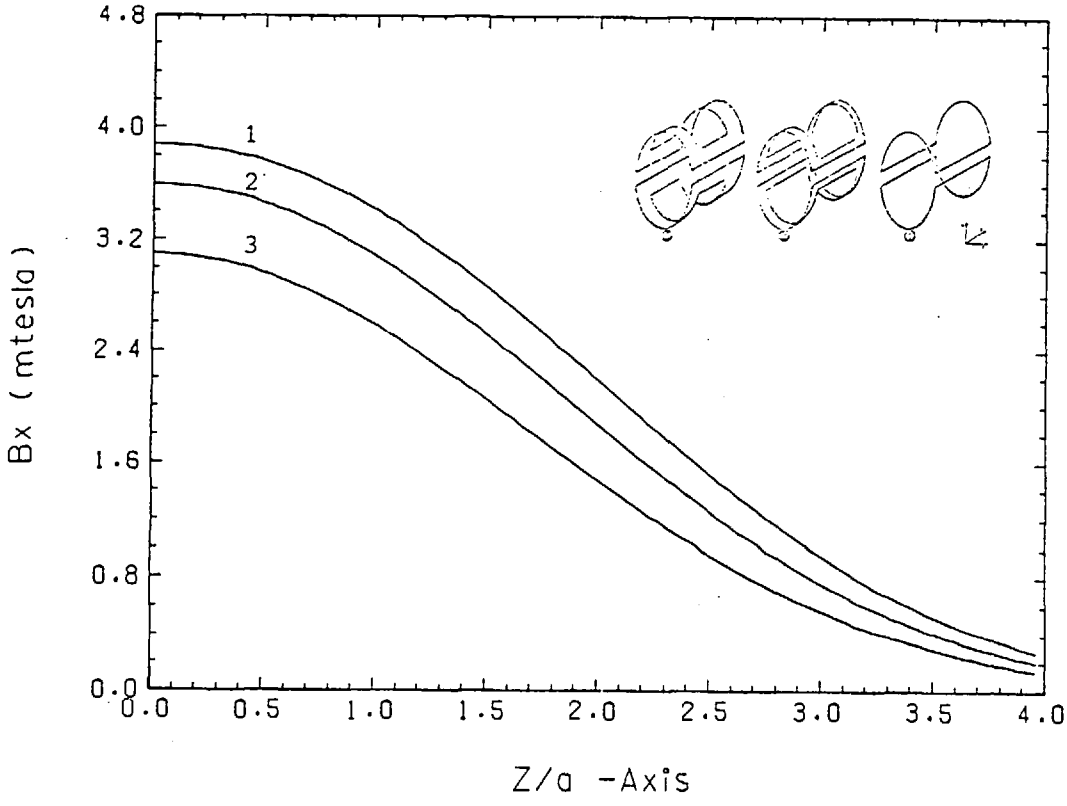

Figure B.5 Magnetic field distribution of the centre line of coil at $\phi = \pi/2$ and three different types of saddle coil windings.

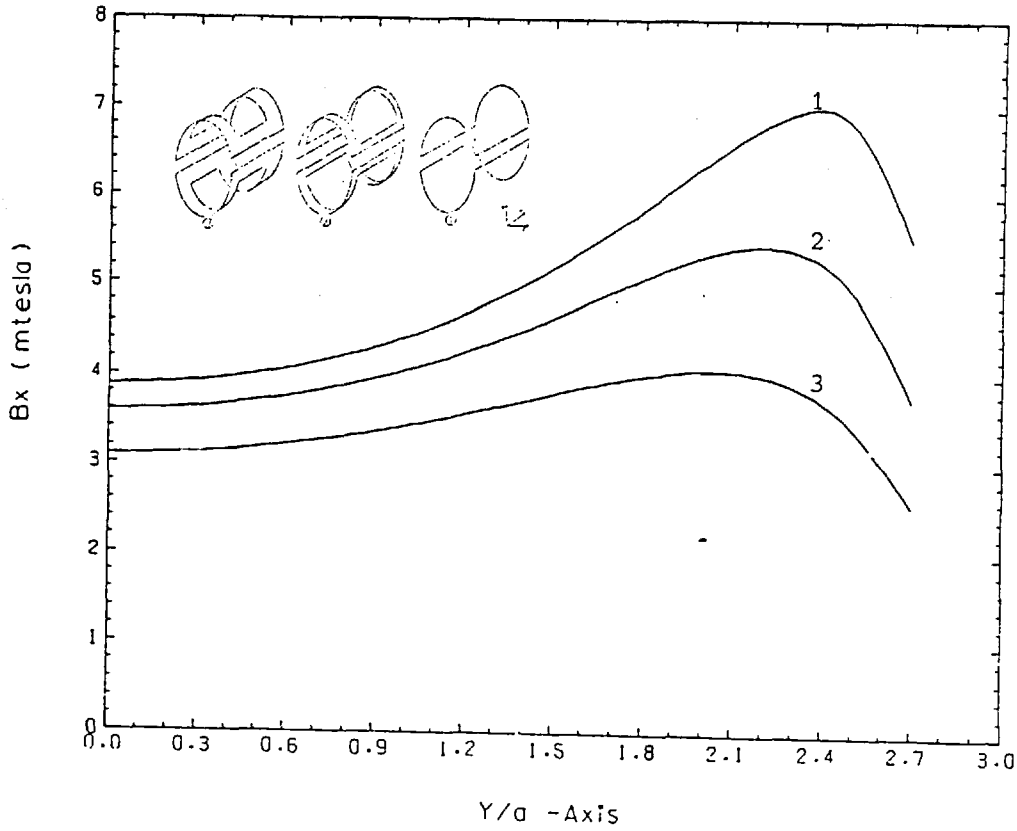

Figure B.6 Magnetic field distribution at z/a = 0, along y/a axis of coil and $\phi = 0$ and three different types of saddle coil windings

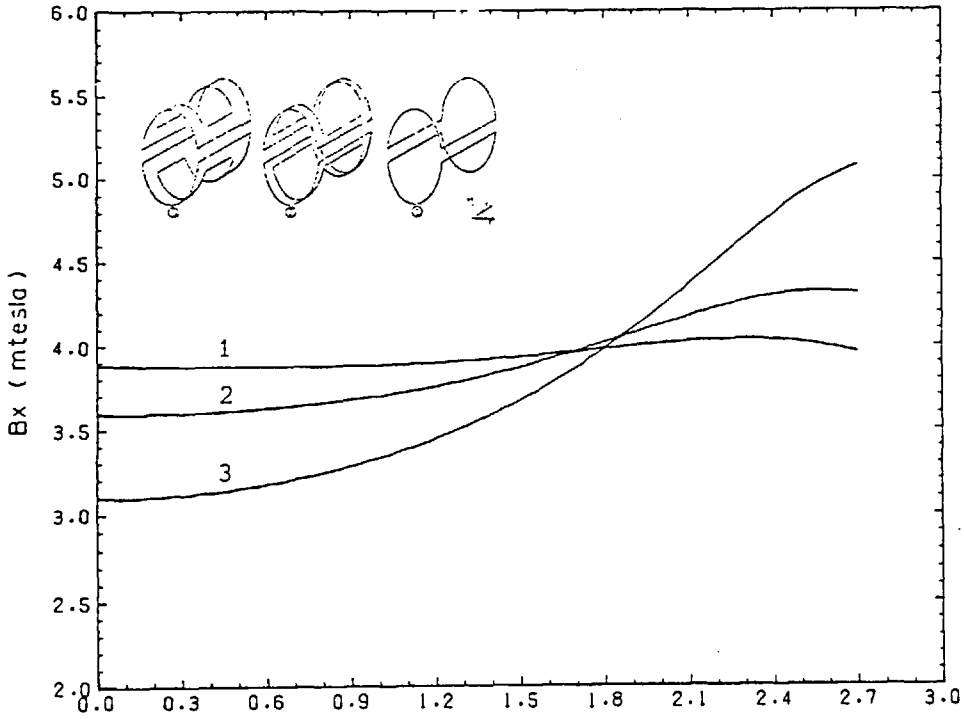

Figure B.7 Magnetic field distribution at z/a = 0 along x/a axis of coil at $\phi = \pi/2$ and three different types of saddle coil windings

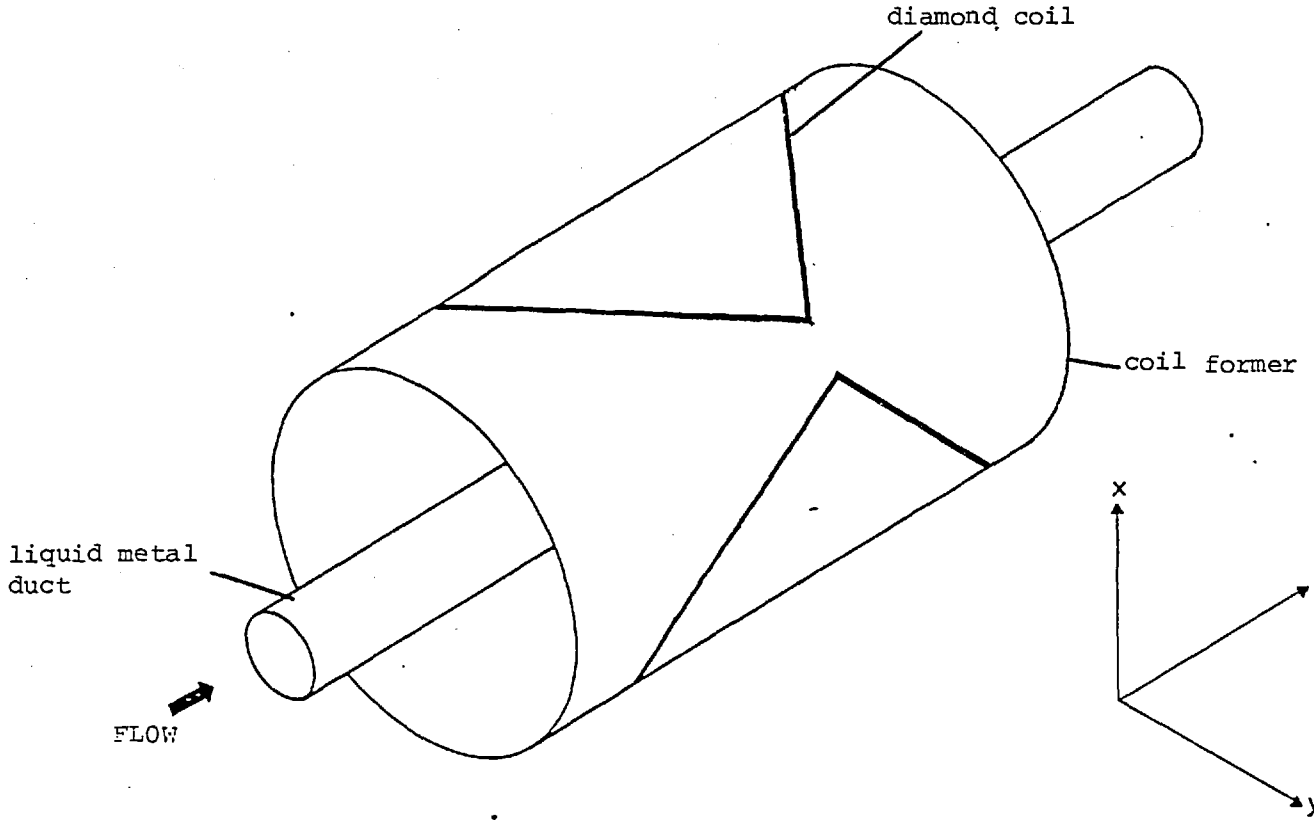

Figure C.1 Diamond-type coils flowmeter

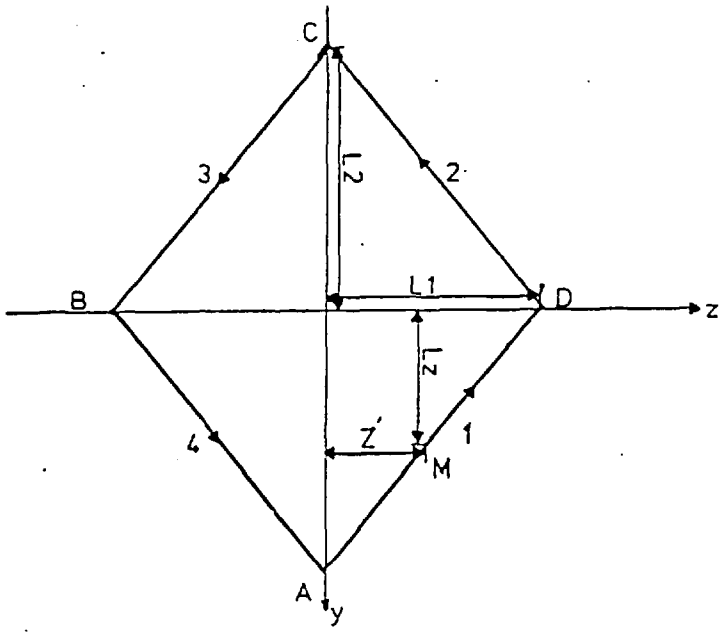

a) View of coil from top

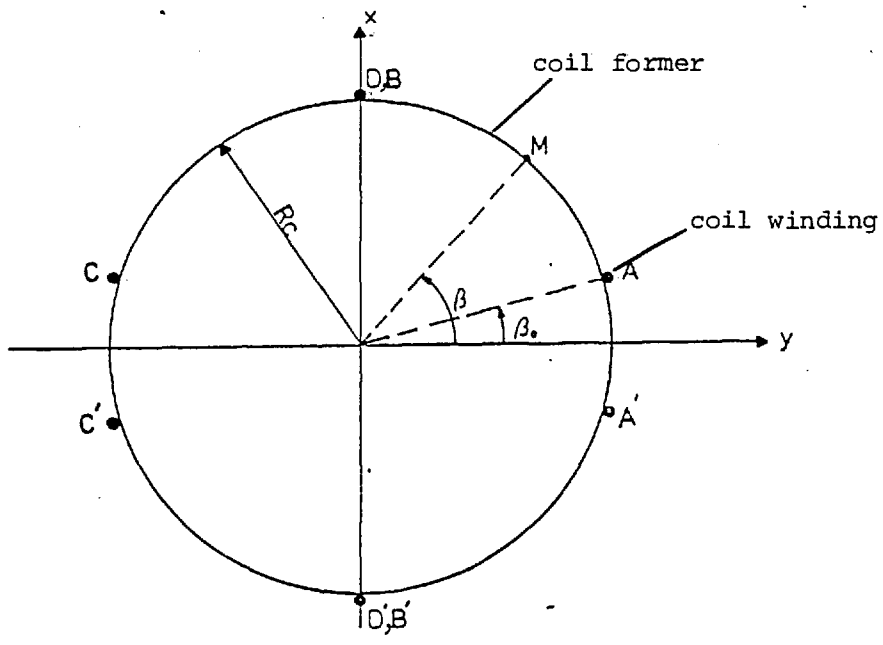

b) Cross section

Figure C.2 Plan view of diamond-type coils

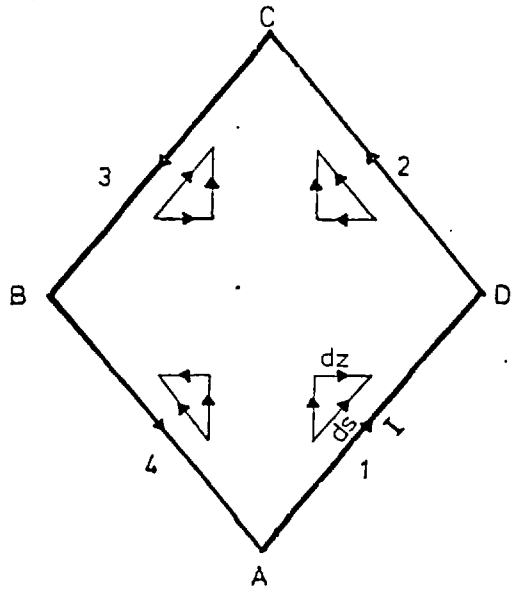

Figure C.3 Top diamond coil showing the direction of ds and dz at different sections of coil

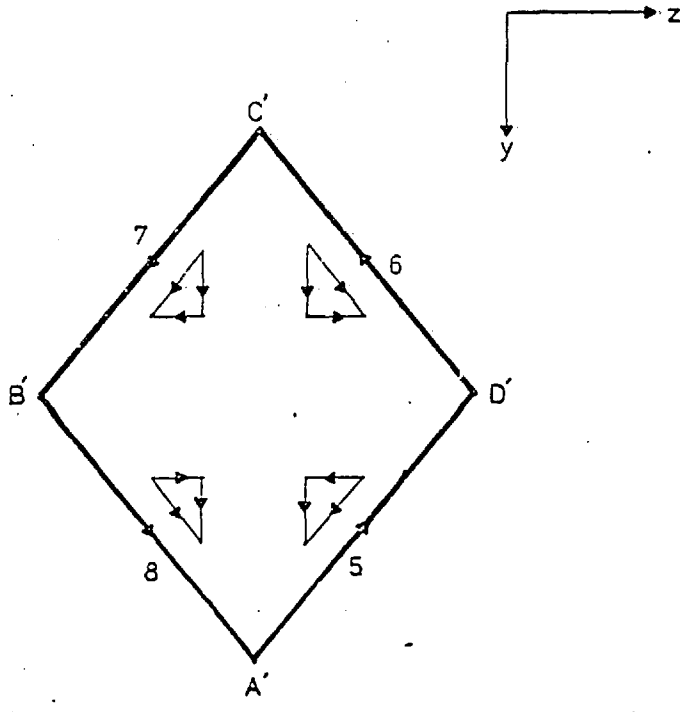

Figure C.4 Bottom diamond coil, showing the direction of ds and dz at different sections of coil

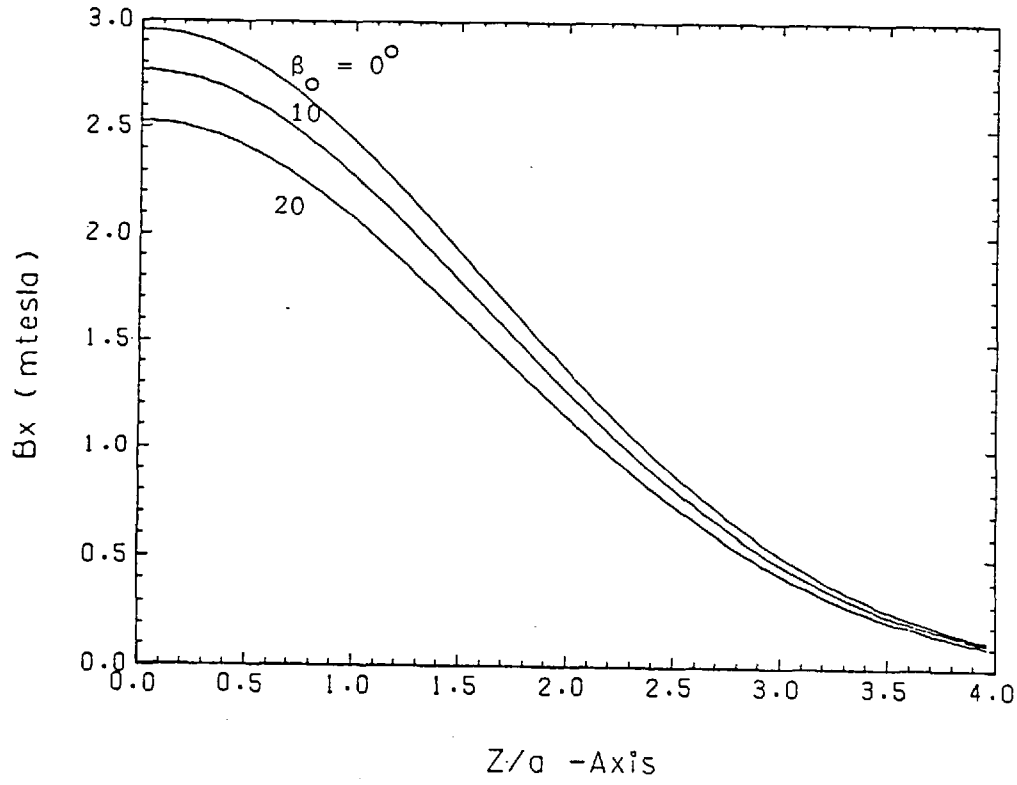

Figure C.5 Magnetic field distribution along z/a axis at the centre of diamond coil for three coil angles

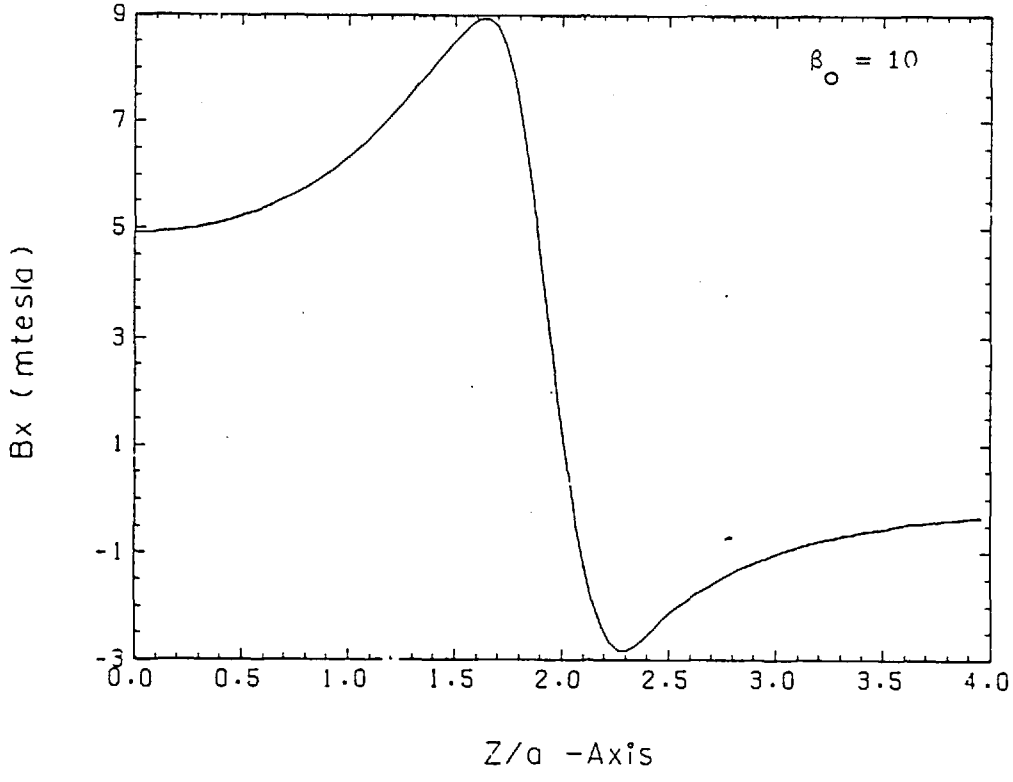

Figure C.6 Magnetic field distribution along z/a axis of diamond coil at R/a = 2.7.

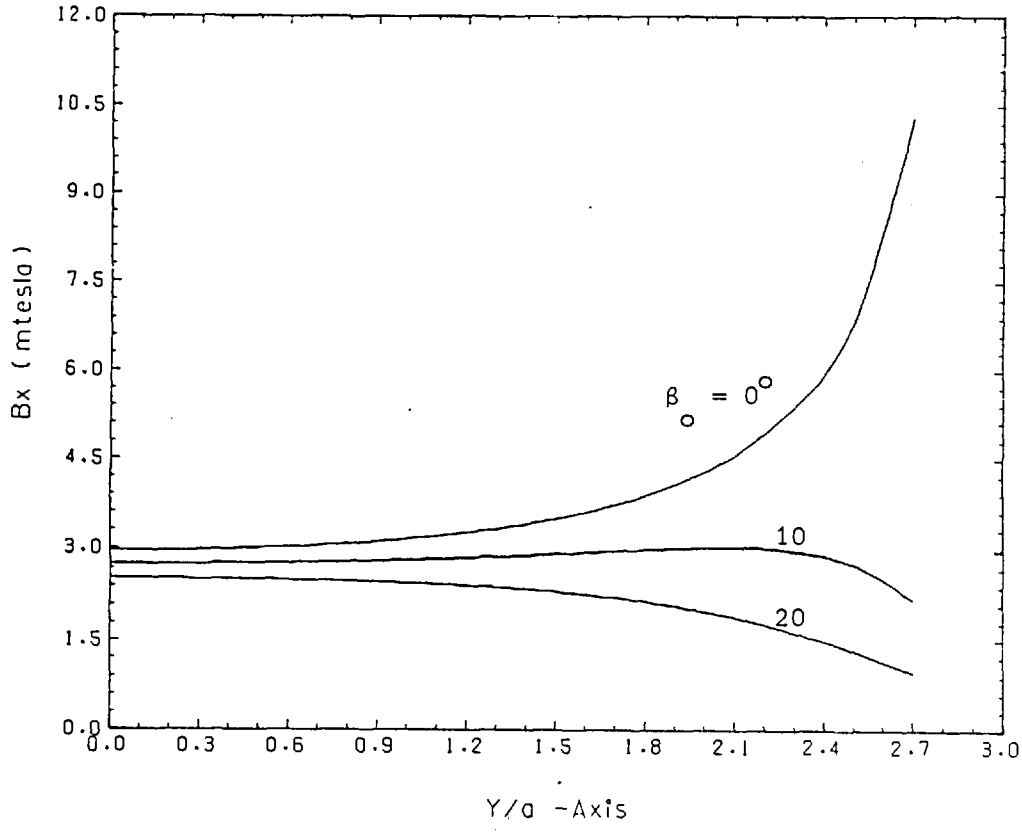

Figure C.7 Magnetic field distribution at z/a = 0 along Y/a axis of diamond coil for three coil angles

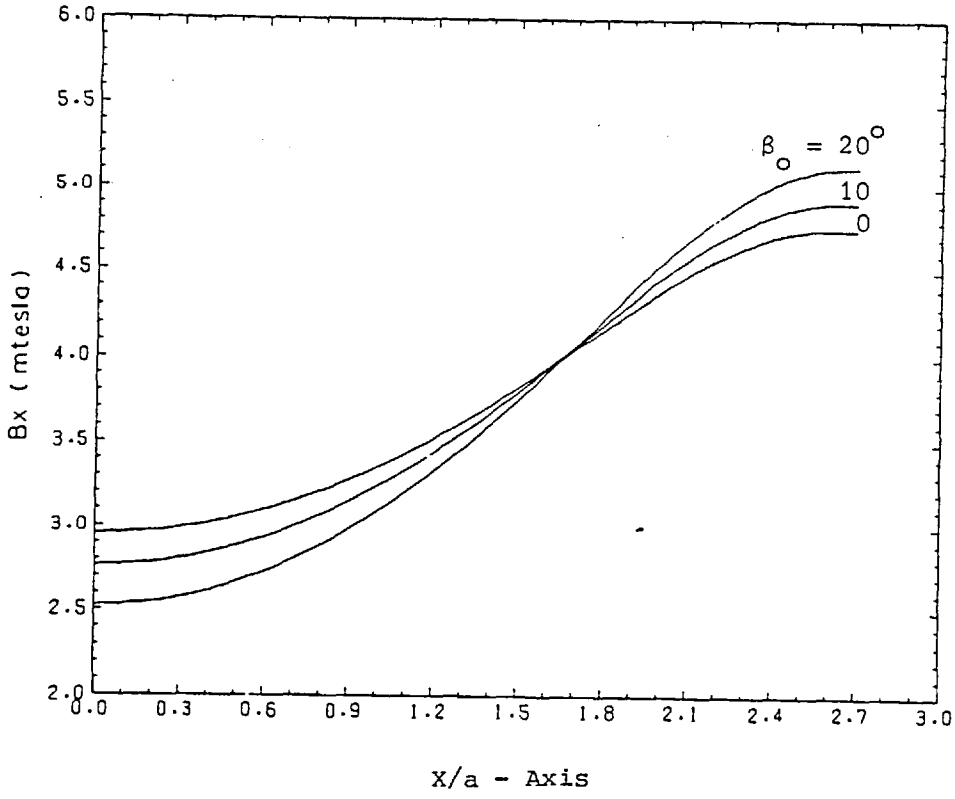

Figure C.8 Magnetic field distribution at z/a = 0 along X/a axis of diamond coil for three coil angles .

REFERENCES

1. Baker R.C. (1968a) "On the potential distribution resulting from flow across a magnetic field projecting from a plane wall." J. Fluid Mech. Vol. 33 pp.73-86

2. Baker R.C. (1968b) "Solutions of the electromagnetic flowmeter equation for cylindrical geometrics." Br.J.Appl. Phys.(J.Phys.D) SER 2 Vol.1 pp.895-899

3. Baker R.C. (1973) "Numerical analysis of the electromagnetic flowmeter." Proc. IEE Vol.120 No. 9 pp.1039-1043

4. Baker R.C. and Saunder P.M. (1974) "A numerical and experimental investigation of flux distortion flowmeters." Work undertaken for U.K.A.E.A. Reactor Group, Risley, Warrington

5. Baker R.C. (1977) "Electromagnetic flowmeters for fast reactors." Progress in Nuclear Energy. Vol. 1 pp.41-61

6. Baker R.C. and Tarabad M. (1978) "The performance of electromagnetic flowmeters with magnetic slurries." J.Phys.D. Appl.Phys. Vol.11 pp.167-175

7. Bean C.P., DeBlais R.W. and Nesbitt L.B. (1959) "Eddy-current method for measuring the resistivity of metals." J.Appl.Phys. Vol.30 No.12 pp.1976-1980

8. Bevir M.K. (1969) "Induced voltage electromagnetic flowmeters." PhD thesis, University of Warwick

9. Bevir M.K. (1970) "The theory of induced voltage electromagnetic flowmeters." J.Fluid Mech. Vol.43 pp.577-590

10. Bevir M.K. (1971) "Long induced voltages electromagnetic flowmeters and the effects of velocity profile." Q.J.Mech. and Appl.Math. Vol.24 pp.347-372

11. Boucher R.A. and Ames D.B. (1961) "End effect losses in DC MHD generators." J.Appl.Phys. Vol.32 No.5 pp.755-759

12. Campbell R.H. (1973) "Primary system design of sodium cooled fast reactors". Journal of British Nuclear Energy Society Vol.12 pp.357-365

13. Cushing V. (1958) "Induction flowmeter (for use with dielectrics)." Rev. Sci. Instrum. 29,692

14. Dean S.A., Harrison E. and Stead A. (1970) "Sodium flow monitoring." Nuclear Engineering International Vol. 15 No.174

15. Dodd C.V. and Deeds W.E. (1967) "Electromagnetic forces in conductors." J.Appl.Phys. Vol38 No.13 pp.5045-5051

16. Duncombe E. and Thomasson R.K. (1970) "Sodium process instrumentation for the Dounreay PFR." Nuclear Engineering International Vol.15 No.172 pp.714-717

17. Dwight H.B. (1961) "Tables of integrals and other mathematical data." Macmillan 4th edition

18. "Electromagnetic methods of measuring the parameters of MHD processes." Academcy of Sciences of the Latvian SSR, Institute of Physics. "Zinatne" publishers, Riga, 1968 English Translation U.K.A.E.A. Culham Laboratory. April 1977.

19. Faraday M. (1832) "Experimental researches in electricity" Vol. 1 p.55 January

20. Feng C.C., Deeds W.E. and Dodd C.V. (1975) "Analysis of eddy-current flowmeters." J.Appl.Phys. Vol.46 No.7 pp.2935-2940

21. Foster G.A. (1971) "Performance of permanent magnet flow-through-type sodium flowmeters in EBR-II instrumented subassemblies." IEEE Trans. NS18(1) pp.363-365

22. Foster G.A. (1973) "Long-term stability of Alnico 5 and 8 magnets at 700 to 1200^{o}F." Argonne National Lab. Ill(USA) Report No. ANL-CT-73-16

23. Gammerman M.Ya and Mezhburd V.I. (1971) "Weight functions of electromagnetic flowmeter in the three dimensional approximation." Magn. Gidrodin. No. 3 pp.130-133

24. Hartmann J. (1937) Math-fys. Medd. 15, No. 6

25. Hayes D.J. (1974) "Instrumentation for liquid sodium in nuclear reactors." J.Phys.E.: Scientific Instruments pp.69-75

26. Hess B. and Ruppert E. (1975) " Instrumentation for core and coolant monitoring in liquid metal fast breeder reactors (LMFBR)." Atomic Energy Review, 13, 1 pp.81-144

27. Hirayama M. (1977) "Theoretical model of an eddy current flowsensor." IEEE Trans. Vol.NS-24 No.5 pp.2021-2030

28. Kalnin R.K., Kisis A.Yu. and Sermons G.Ya (1966) "A contactless device for measuring the flow velocity of an electrically conducting fluid." Magn. Gidrodin. Vol.2 No.3 pp.150-151

29. Kemmer N. (1977) "Vector analysis." Cambridge University Press

30. Kirshtein G.Kh. and Timofeev V.A. (1975) "Effect of a magnetic field non-uniform along the stream on the characteristics of electromagnetic flowrate transducers." Magn. Girodin. No.4 pp.139-142

31. Kirshtein G.Kh. and Timofeev V.A. (1977) "Effect of magnetic field distribution on the weighting function of a conduction flowmeter for rectilinear flow." Magn. Gidrodin. No.1 pp.125-130

32. Kolin A. (1945) "An alternating field induction flowmeter of high sensitivity." Rev.Sci.Instr. Vol.16 No.15 pp.109-116

33. Komori Y., Someyana T., Iwameto S., Yamada K. and Kobayashi H. (1974) "Shimadzu electromagnetic flowmeter for liquid sodium." Shimadzu Hyoran 31, 163

34. Kormilov V.P. and Loginov N.I. (1978) "Effect of the velocity head on the output voltage of an electromagnetic velocity meter with a cylindrical magnet." Magn.Gidrodin No.1 pp.121-124

35. Korsunskii L.M.(1974) "Effect of the velocity distribution on the readings of flowmeters with a magnetic field intensity inversely proportional to the weighting function." Magn. Gidrodin. No.2 pp.125-128

36. Lehde H. and Lang W.T. (1948) "Device for measuring rate of fluid flow." U.S. Patent 2 435 043

37. Loginov N.I. (1971) "Distribution of the potentials in an electromagnetic velocity meter with a cylindrical magnet." Magn. Gidrodin No.2 pp.128-132

38. Mannherz E.D. and Schmook R.F. (1968) "Magnetic flowmeters for magnetic slurries." U.S. Patent 3 380 301

39. Meshii R. and Ford J.A. (1969) "Calibration of electromagnetic flowmeters in the Enrico Fermi atomic power plant." Nuclear Applications and Technology Vo. 7 pp.76-83

40. Meyer R.X. (1961) "Some remarks concerning magneto-hydrodynamic applications to re-entry problems." Second symposium on the engineering aspects of MHD (Columbia University Press)

41. Moore R.V. and Hurst R. (1961) "The fast breeder reactor." Journal of the British Nuclear Energy Conference Vo. 6 pp.161-165

42. Nagao A. and Ishibash R. (1976) "Resistivity measurement of NaCl solution by eddy current decay method." Japanese J.Appl. Phys. Vol. 15 No. 4 pp.627-631

43. "Non-contact control of liquid metals flow". (1968) Academy of Science - Latvia Republic of the Soviet Union, Institute of Physics, Zinatne, Riga

44. Pfister C.G. and Dunham R.J. (1957) "D-C magnetic flowmeter for liquid sodium loops." Nucleonics Vol.15 No.10 pp.122-123

45. Popper G.F. and Glass M.C. (1967) "The design and performance of a 1200^{o}F magnetic flowmeter for in-core application in sodium cooled reactors." IEEE Trans. Nuc.Sci. NS-14(1), 342

46. Rummel Th. and Ketelson B. (1966) "A non uniform magnetic field makes inductive measurements of the flowrate possible with all velocity profiles encountered in practice." Regelungstechnik, No.6 pp.262-267

47. Sermons G.Ya. (1964) "Propagation of an electromagnetic field pulse in a moving electrically conducting medium." Transactions of the Academy of Sciences of the Latvian SSR, physical and technical sciences series no.1, 33

48. Sermons, G.Ya (1966) "Theory of propagation of pulsed magnetic field in moving conducting media." In: Motion of conducting bodies in a magnetic field. Riga "Zinatne", p.135

49. Sermons, G.Ya and Zheigur B.D. (1964) "Study of the propagation of an electromagnetic field pulse in a moving medium." Problems of Magnetic Hydrodynamics, 4. Riga, Academy of Sciences of the Latvian SSR Publishers, 91

50. Shercliff J.A. (1954) "Relation between the velocity profile and the sensitivity of electromagnetic flowmeters." J.Appl.Phys. Vol.25 pp.817-818

51. Shercliff J.A. (1962) "The theory of electromagnetic flow measurement." Cambridge University Press

52. Simnad M.T. (1971) "Fuel element experience in nuclear power reactors." Gordon and Breach Science Publishers, Inc.

53. Smythe W.R. (1968) "Static and dynamic electricity." McGraw-Hill, 3rd edition

54. Thatcher G. (1971) "Electromagnetic flowmeters for liquid metals." International Conference on modern developments in flow measurement, Harwell pp.359-380

55. Thatcher G., Bentley, P.G. and McConigal G. (1970) "Sodium flow measurement in PFR." Nuclear Engineering International Vol.15 No.173 pp.822-825

56. Thürlemann B. (1941) "A method of electrically measuring the velocity of fluids." Helv.Phys.Acta., No.14 pp.383-419

57. Turner G.E. (1960) "The non-linear behaviour of large permanent-magnet flowmeters." Atomics International Report NAA-SR-4544

58. Velt I.D. and Mikaileve Yu.U. (1977) "E.M. flowmeter with a non-uniform magnetic field for liquid metal." Magn.Gidrodin, No.1 pp.131-135

59. Wenger N.C. (1971) "Effect of velocity profile distortion in circular transverse field electromagnetic flowmeters." NASA TND-6454

60. Wiegand D.E. (1967) "Summary of an analysis of the eddy current flowmeter." 14th Nuclear Science Symposium, IEEE, Los Angeles, October.

61. Wiegand D.E. (1969) "The eddy current flowmeter. An analysis giving performance characteristics and preferred operating conditions." Argone National Laboratories Engineering and Equipment. Rep. No. ANL-7554 August.

62. Williams E.J. (1930) Proc. Phys. Soc. Lond., 42, 466

63. Zheigur B.D. and Sermons G.Ya. (1965) "Pulse method of measuring the flowrate of liquid metals." Academy of Sciences of the Latvian SSR Institute of Physics "Zinatne" Publishers, Riga.

64. Yada H. (1970) "Fuji electromagnetic flowmeters for liquid sodium." Fuji Electric Journal 43, 194(24)

PUBLICATIONS

1. Baker, R.C. and Tarabad, M. (1978) "The performance of electromagnetic flowmeters with magnetic slurries." J.Phys.D. Appl.Phys., Vol. 11 pp.167-175

2. Tarabad, M. and Baker, R.C. (1979) "Electromagnetic flowmeters for sodium-cooled reactors." Proceedings of IMEKO symposium on flowmeasurement and control in industry, Tokyo, Japan, November.

3. Baker, R.C. and Tarabad, M. (1979) U.K. Patent Application No.119243.